Unsteady Boundary Layer Transition on Axial Compressor Blades

William by

W J. Solomon, B.E. (Hons.)

Department of Civil and Mechanical Engineering

Submitted in fulfilment of the requirements
for the degree of
Doctor of Philosophy

University of Tasmania

August 1996

Statement of originality and authority of access

This thesis contains no material which has been accepted for the award of any other degree or diploma in any tertiary institution. To the best of my knowledge and belief, the thesis contains no material previously published or written by another person, except when due reference is made in the text.

This thesis may be made available for loan and limited copying in accordance with the Copyright Act 1968.

William J. Solomon

Abstract

The unsteady laminar to turbulent transition of boundary layers on the blading of axial turbomachinery has been investigated experimentally. Measurements were made on and around the outlet stator row of a 1.5-stage axial compressor using thermal anemometry. Pitch-wise hot-wire probe traverses were made upstream and downstream of the blade row to define the freestream disturbance field; these clearly show the interaction of the inlet guide vane and rotor wakes. Boundary layer traverses were taken with a single hot-wire on the stator suction surface.

A blade instrumented with 61 surface hot-film sensors distributed around the surface at mid-blade height was used to obtain high frequency response skin friction measurements. High speed data acquisition triggered by a rotor angle position reference signal allowed ensembles of data to be acquired corresponding to a specific set of rotor wakes. This data was processed in a variety of ways to reveal the nature of the unsteady transition process. This work corroborates and complements that of Halstead et al. (1995) and provides a useful resource for validation of unsteady flow calculations.

A new intermittency detection algorithm has been developed to aid in the interpretation of the surface hot-film data. Intermittency is a more reliable measure of the transitional boundary layer state (and is easier to interpret) than other statistics such as skew, especially as the boundary layer nears separation. The intermittency detection algorithm has also been adapted to detect the region of relaxing flow commonly observed following turbulent spots where the skin friction relaxes from a turbulent level to the laminar level. This region is more stable and more resistant to separation than the undisturbed laminar layer and has a lower skin friction than the turbulent layer (on average). It may be possible to exploit the properties of this relaxing flow to improve blade profile designs.

The experimental data show the transition process to be periodically unsteady and dominated by the presence of turbulent spots. Not only do the transition onset and completion points oscillate markedly in stream-wise position with the passage of wakes from upstream, but small regions of boundary layer separation may appear in the transition region during certain parts of the cycle. In flows with large separations through the whole cycle, the re-attachment point has also been observed to oscillate in stream-wise position.

Using experimental data recently compiled by Gostelow et al. (1995) a new method of predicting the transition length in rapidly changing pressure gradients has been proposed and tested in typical turbomachine pressure distributions. The new method, which extends the commonly used Chen-Thyson technique, allows the spot propagation and growth parameters to respond to changes in the local pressure gradient. This can be especially important in turbine blade boundary layers where transition may

commence in a region of favourable pressure gradient and then move into a region of strong adverse pressure gradient. Only the new method is able to predict the shortening of the transition zone due to this change in pressure gradient.

Acknowledgements

Thanks are due to Dr G. J. Walker who has given excellent supervision, guidance, support and friendship throughout this project. The Mechanical Engineering technical support staff at the University of Tasmania, T. McNicol, S. Hamilton and R. Stephenson, were invaluable. Prof. J. P. Gostelow has also been a source of inspiration and support.

A most important component of this project has included regular visits to the Aerothermal Methods Department of Rolls-Royce plc. Interaction with Dr. P. Stow and Mr. J Coupland there was useful, enjoyable and interesting.

Special thanks to Christina Coe who has endured more lonely nights at home than a young girl should.

Financial support for this work was provided by the Australian Research Council and Rolls-Royce plc. Thanks also to the Aerodynamics Group at GEC Alsthom Large Steam Turbines for the use of their computing facilities in the final preparation of the thesis.

Contents

List of Figures

List of Tables

Nomenclature

a	circumferential position of stator leading edge relative to IGV trailing edge
b	axial distance from stator leading edge to probe
e	axial distance from rotor leading edge to probe
d	axial distance from IGV trailing edge to rotor leading edge
aU, U_l	spot leading edge velocity
bU, U_t	spot trailing edge velocity
c	blade chord
c_1, c_2, c_3	3 hole probe calibration coefficients
f_1, f_2, f_3	3 hole probe correlation functions
g	spot formation probability function
i	blade incidence
i^*	nominal incidence (Howell)
k	film calibration constant
n	amplification ratio;
	turbulent spot generation rate, $\mathrm{m}^{-1}\mathrm{s}^{-1}$
p_1, p_2, p_3	static pressures from 3 hole probe
p_{in}	inlet static pressure
r	radial coordinate
s	surface distance
s^*	non-dimensional surface distance from leading edge, s/S_{max}
t	time
t^*	non-dimensional time, t/T
u	local velocity
w	circumferential position of probe relative to IGV trailing edge
x	circumferential position of probe relative to stator trailing edge
x_t	transition onset location (surface distance)
x_{tw}	wake-induced transition onset location (surface distance)
y	distance normal to blade surface
x, y	blade profile definition coordinates
z	axial coordinate
C_f	skin-friction coefficient
C_1, C_2, C_3	hot-wire calibration coefficients
D	mid-blade height diameter, 914.4 mm
$D(t)$	detector function
E	hot-film anemometer output voltage
E_0	anemometer voltage at zero flow

$F(\gamma)$	Narasimha intermittency function, $[-\ln(1-\gamma)]^{1/2}$
G	Chen and Thyson [14] breakdown parameter ($= n\sigma$)
H	velocity profile shape factor, δ^*/θ
M	Mach No.
N	non-dimensional breakdown rate parameter, $n\sigma\theta_t^3/\nu$; number of blades
N_A	ratio of disturbance amplitude to freestream velocity
P	total pressure (at probe)
P_{in}	compressor inlet total pressure (upstream of IGV)
Q	total heat transfer from film gauge
Q_0	heat transfer from film gauge at zero flow
Q_s	heat transfer from film gauge to the substrate
$\overline{Re}$	rotor and stator average Reynolds number
Re_1	stator blade inlet Reynolds number, $U_1 c/\nu$
Re_{NS}	Non-steady Reynolds number (Eqn. (2.1))
Re_c	rotor blade Reynolds number, $U_{mb}c/\nu$
Re_θ	momentum thickness Reynolds number, $\theta U/\nu$
S	blade pitch
S_{max}	maximum surface distance
T	rotor blade passing period
Tu	local freestream turbulence level, %
U	freestream velocity
U_1	blade row inlet relative velocity
U_m	largest inlet velocity vector (Fig. 2.2)
U_{mb}	rotor blade velocity, at mid blade height
U_w	hot-wire measured velocity
V_a	inlet axial velocity
α	turbulent spot spreading half angle
α_3	stator row inlet air angle
β_1, β_2	blade row inlet and outlet blade angles
γ	turbulent intermittency
δ	boundary layer thickness
δ^*	displacement thickness, $\int_0^\delta (1-u/U)\, dy$
ϵ^*	nominal deflection (Howell)
θ	momentum thickness, $\int_0^\delta (1-u/U)\, u/U\, dy$;
λ	characteristic transition length, $\lambda = x\|_{\gamma=0.75} - x\|_{\gamma=0.25}$
λ_θ	pressure gradient parameter, $(\theta^2/\nu)(dU/dx)$
$\lambda_{\theta t}$	pressure gradient parameter at x_t angular coordinate; blade camber
ν	kinematic viscosity
ξ	blade stagger angle
ρ	density
σ	spot propagation parameter (dimensionless)
τ	quasi-wall shear stress; time constant
$\bar{\tau}$	long term mean quasi-wall shear stress

τ_w	wall shear stress
$<\tau(i)>$	ensemble average τ at time $t = t_0 + i\Delta t$
$<\tau(i)>_{RMS}$	ensemble random unsteadiness of τ
ϕ	flow coefficient, V_a/U_{mb}
ω	circular frequency
Δt	data acquisition sampling period
ΔT_0	temperature elevation of hot-film gauge
Ω	rotational speed, rad/s

Definition of terms used in processing periodic unsteady data

Consider a property $Q(t)$ measured at some position r, θ, z in a turbomachine at time t. If $Q(t)$ is sampled at n evenly spaced time periods (Δt) to give an array of data points $Q(i)$ (each at time $t_i = t_0 + i\Delta t$) then the *long term mean* value of $Q(t)$ is simply

$$\overline{Q} = \frac{1}{n}\sum_{i=1}^{n} Q(i) \tag{0.1}$$

The instantaneous variation from the long term mean is

$$Q'(i) = Q(i) - \overline{Q} \tag{0.2}$$

and so the *long term RMS* value of $Q(t)$ is

$$Q'_{RMS} = \left[\frac{1}{n}\sum_{i=1}^{n} Q'(i)^2\right]^{1/2} \tag{0.3}$$

Other long term statistical moments may be found similarly.

If Q is a velocity U then the *total disturbance level* Tu_D is given by

$$\mathrm{Tu}_D = \frac{U'_{RMS}}{\overline{U}} \tag{0.4}$$

Measurements of more than one velocity component were not performed in the current work and will not be considered here.

In flows with periodic unsteadiness it is necessary to distinguish between fluctuations of a periodic nature (periodic unsteadiness), random fluctuations (freestream turbulence) and the total disturbance level because of the non-stationary nature of the signals obtained. The notation and nomenclature used here is similar to that of Evans [30].

Phase-locked sampling of data allows periodic components to be resolved. Sampling is synchronised relative to a periodic event of interest which may be that of a rotor passing through some reference angle. Other workers (Gostelow et al. [39]) have done phase-locked sampling by triggering off the pulse they used to generate a turbulent spot in an otherwise steady flow. Data is acquired in a two-dimensional array $Q(i,k)$ of size $(n \times m)$ where the index k identifies the individual realisation amongst the ensemble of m realisations. Each data point $Q(i,k)$ is acquired at time $t_{i,k} = t_{0,k} + i\Delta t$ where the reference time $t_{0,k}$ (the trigger point) is different for each realisation but at the same phase of the periodic process for all realisations.

The *ensemble average* of $Q(t)$ at time $t_i = t_0 + i\Delta t$ is then

$$<Q(i)> = \frac{1}{m}\sum_{k=1}^{m} Q(i,k) \tag{0.5}$$

Now the *unsteadiness* of $Q(t)$ is defined as the excursion of the ensemble average value from the long term mean value at the given point t_i in the period and is given by

$$\widetilde{Q(i)} = <Q(i)> - \overline{Q} \tag{0.6}$$

When the property Q is velocity, the *periodic unsteadiness level* $\widetilde{\mathrm{Tu}}$ is

$$\widetilde{\mathrm{Tu}} = \frac{\sqrt{\frac{1}{n}\sum_{i=1}^{n}\widetilde{U(i)}^2}}{\overline{U}} \tag{0.7}$$

It is especially important that either many periods or an integral number of periods are used to calculate $\widetilde{\mathrm{Tu}}$ with minimum bias. This applies to the other properties to a lesser extent. Flow variations between different blade passages (caused by minor mis-alignments, small blade shape variations, or non-uniformity in the inlet flow) will increase the measured unsteadiness unless sampling is over the same blade passage(s) for each realisation.

Truly random fluctuations in the periodic signal are given by the excursion from the ensemble mean level.

$$Q''(i,k) = Q(i,k) - <Q(i)> \tag{0.8}$$

The *ensemble RMS* at time t_i in the period (i.e. square root of ensemble variance) is

$$<Q(i)>_{RMS} = \left[\frac{1}{m}\sum_{k=1}^{m} Q''(i,k)^2\right]^{1/2} \tag{0.9}$$

the *ensemble skew* is found from

$$<Q(i)>_{SKEW} = \frac{1}{m}\sum_{k=1}^{m}\left[\frac{Q''(i,k)}{<Q(i)>_{RMS}}\right]^3 \tag{0.10}$$

and the *ensemble kurtosis* is

$$<Q(i)>_{KURT} = \frac{1}{m}\sum_{k=1}^{m}\left[\frac{Q''(i,k)}{<Q(i)>_{RMS}}\right]^4 \tag{0.11}$$

Ensemble skew and kurtosis are by their definitions normalised with respect to the ensemble RMS values. Appropriate normalisation of the ensemble RMS signal may alter depending on the relative levels of the mean or ensemble mean values. This is discussed in relation to the hot-film measurements described in Chapter 8.

With Q as velocity, the *ensemble local randomness* or the *freestream turbulence* $<\mathrm{Tu}(i)>$ is defined by Evans as

$$<\mathrm{Tu}(i)> = \frac{<U(i)>_{RMS}}{\overline{U}} \tag{0.12}$$

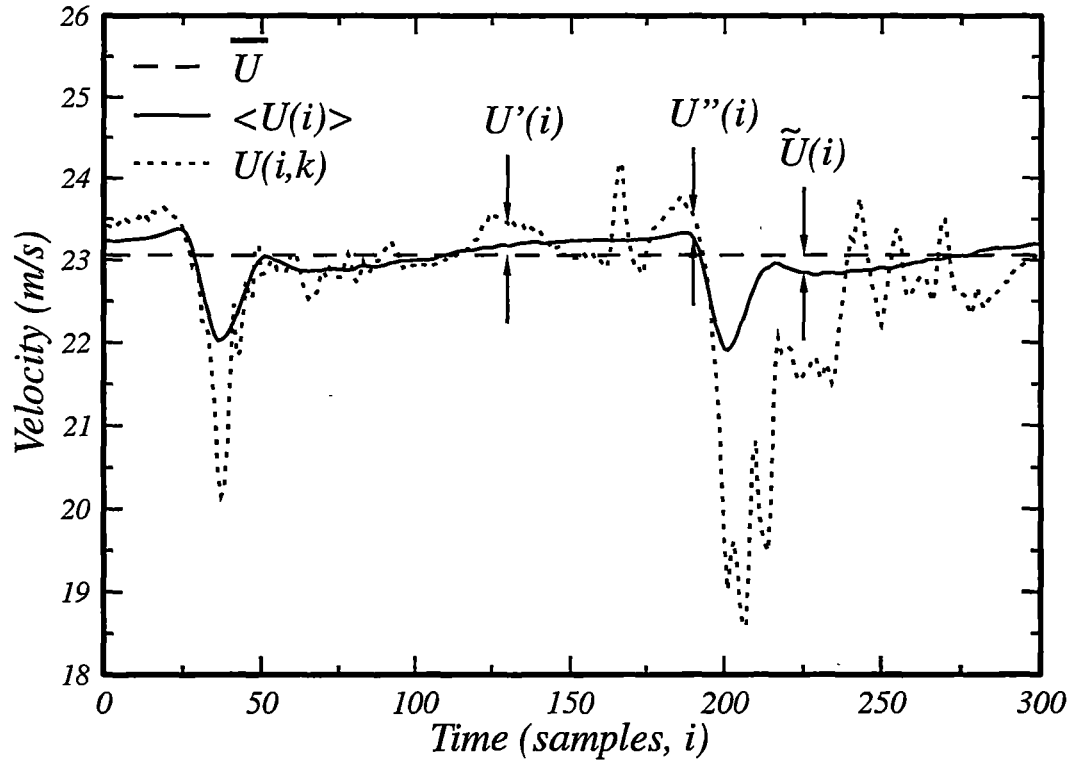

Typical long term mean, ensemble mean and instantaneous velocity traces in a turbomachine measured over two rotor passing periods

The *long term freestream turbulence* can be found by averaging the local values over an integral number of periods (or a large number of periods).

$$\mathrm{Tu} = \frac{1}{\overline{\overline{U}}}\left[\frac{1}{mn}\sum_{k=1}^{m}\sum_{i=1}^{n}U''(i,k)^2\right]^{1/2} \tag{0.13}$$

$$= \left[\frac{1}{n}\sum_{i=1}^{n}<\mathrm{Tu}(i)>^2\right]^{1/2} \tag{0.14}$$

Over the ensemble the *total disturbance level* is

$$\mathrm{Tu}_D = \frac{1}{\overline{\overline{U}}}\left[\frac{1}{mn}\sum_{k=1}^{m}\sum_{i=1}^{n}U'(i,k)^2\right]^{1/2} \tag{0.15}$$

Evans [30] shows that the total disturbance level is approximately related to the freestream turbulence and periodic unsteadiness by the following relationship.

$$\mathrm{Tu}_D^2 = \widetilde{\mathrm{Tu}}^2 + \mathrm{Tu}^2 \tag{0.16}$$

The figure shows a typical velocity trace $U(i,k)$ taken midway between the rotor and stator blade rows with a single hot-wire mounted stationary relative to the stator. The ensemble mean $<U(i)>$ and the long term mean $\overline{U}$ are shown for comparison.

Chapter 1

Introduction

Development of the axial compressor for jet propulsion was begun in England in 1936 by the Royal Aircraft Establishment (RAE). In 1937 the Metropolitan Vickers company entered into a contract with the RAE to design and develop an experimental test plant using an axial compressor. Whittle's earliest engines had been designed using centrifugal compressors. Efficient centrifugal compressors, required for the super-charging of reciprocating engines, were readily available. Availability of sufficiently efficient turbines and compressors made development of a practical turbojet engine possible. Since that time the gas turbine based aircraft propulsion systems have displaced reciprocating engines from all but the smallest of applications. Industrial gas turbines and modified aircraft turbines have also found widespread use in areas such as in gas pipeline pumping stations and for power generation. Gas turbines have been less prolific in land and sea transport applications where weight and compactness considerations do not outweigh their higher fuel consumption (especially for off-design operation) compared with diesel engines.

This thesis is concerned with flow behaviour on the blading of axial machines and all of the experimental work has been performed in an axial compressor. Axial compressors are preferred for large aircraft engines because they have a high flow rate for a relatively low frontal area. They have also undergone considerable development and can yield high efficiencies. Centrifugal compressors are often used in smaller engines (and turbochargers). These have can have a wider range of operating flow rates at a given rotational speed, are shorter in length, have fewer parts and are simpler to produce in cases where the impeller is precision cast (Cumpsty [18]). Axial and centrifugal compression stages can also be combined as in the Lycoming AGT1500 tank engine or the Rolls Royce BR505 aero-engine.

The large aircraft engine market has been highly competitive in recent times with three engine manufacturers offering engines for aircraft such as the Boeing 747 and 777. Cumpsty [19] documents a 24% improvement in the fuel mileage of the 747 since 1975, only 3% of which is attributed to aircraft drag reduction. Much of this improvement has come from improved engine aerodynamics. Improvements in compressor or turbine efficiencies have a direct effect on the overall cycle efficiency. Computational fluid dynamics (CFD) has been advanced considerably over this period and has certainly contributed to the aerodynamic improvements. But according to Cumpsty [19] CFD has not led to a greater understanding of the flow or better recognition of the design

restraints. It could be argued direct numerical simulation (DNS) has improved the understanding of turbulence at low Reynolds number but such information is still far from being useful to an engine designer. Flows which are dominated by shocks, where most of the losses arise from wave drag, are generally well predicted by the better CFD methods despite the fact that the viscous flow modelling may be poor. Despite much ongoing work (e.g. Savill [105]) accurate prediction of low Reynolds number transitional and turbulent flows still eludes commonly applied flow calculation methods.

The experimental work of this thesis aims to improve the understanding of the unsteady boundary layer transition process. As well as improving design point efficiency, better understanding of the flow should enable better predictions of off-design performance, compressor stall margin and unsteady machine phenomena. The present work confirms and complements the observation of several workers that a large fraction of the boundary layer flow on a compressor blade is transitional and dominated by the development of turbulent spots. Wakes from the upstream blade row promote intermittent breakdown to turbulence at a location upstream of the natural (undisturbed) transition onset point. Immediately following a turbulent spot is a relaxing flow region where the flow is laminar and the wall shear stress reverts to a steady laminar flow level. This relaxing flow region suppresses development of other spots and effectively delays the end of transition past that expected for the natural unperturbed boundary layer. Relaxing flow is also likely to be more resistant to separation than the natural laminar boundary layer. These observations support those of Halstead et al. [46], Cumpsty [25] and others.

The transitional state of the boundary layer has a large effect on the heat transfer coefficient. This can be very important in the case of turbine blades, although the hottest blades usually employ film cooling which further complicates the situation. Improved understanding of boundary layer transition also has important application in low Reynolds number external aerodynamics. Jang et al. [63] have shown that a good transition model is vital to correctly predicting unsteady blade boundary layer behaviour and aeroelastic phenomena. Much of the early work on unsteady turbomachinery flows was directed at predicting the unsteady forces on the blades.

Chapter 2 reviews previous work in unsteady boundary layer transition relevant to turbomachinery. Experiments have been conducted on flat plates, linear cascades and in real machines with various types of wake generating devices. Recent measurements of Halstead et al. [46] confirm the existence of a complex transition process in a multistage machine and reinforce the relevance of the current work to that environment.

The research compressor and general instrumentation is described in Chapter 3 and the experimental program is summarised in Chapter 4. Time average measurements of the stator row inlet flow velocity, angle and turbulence levels are also presented here. Chapter 5 describes the stator blade velocity distributions, which were obtained from blade pressure tappings.

A large part of this work concentrates on unsteady measurements where ensembles of data were taken with acquisition being triggered by a rotor zero marker signal. The unsteady flow-field experienced by the stator row was investigated in this way (Chapter 6). The technique helps to reveal the rotor-stator interaction. A similar set of measurements was undertaken close downstream of the stator to determine the effect of the unsteady boundary layer phenomena on the stator blade wake.

The most direct description of the transition process is given by measurement of

intermittency, the fraction of time for which turbulent flow is observed at a given point in the flow. (In unsteady flow intermittency is defined as the probability that turbulent flow exists at a point in time and space.) Chapter 7 describes the methods which have been used to distinguish between laminar and turbulent regions in measured flows. A new method developed here is successful at identifying turbulence in the surface hot-film signals over the full range of different boundary layer thicknesses, shape-factors and pressure gradients found along the whole length of the blade without requiring user intervention to adjust thresholds etc. The new intermittency detection method has also been extended to measure the probability of the existence of a relaxing flow region following a turbulent spot in the unsteady flow.

A range of hot-wire and surface hot-film measurements of the boundary layer development on the stator blade suction and pressure surfaces are described in Chapters 8 and 9. Again, ensemble averaging techniques have been widely used to resolve the phenomena in time as well as surface distance.

In external aerodynamics cases, where freestream turbulence levels are generally low, transition onset is usually the result of amplification of small disturbances and growth of Tollmien Schlichting (T-S) waves in the unstable laminar boundary layer. High freestream turbulence levels typical of turbomachinery flows generally cause transition without observable amplification processes. This has become known as bypass transition after Morkovin [87] and may also be caused by factors such as noise or surface roughness. The difficulty of predicting bypass transition has led to the widespread use of correlations for determining transition onset locations in turbomachinery. The adequacy of the commonly used Abu-Ghannam and Shaw [1] transition onset correlation is tested against the current experimental data using a quasi-steady assumption.

Transitional flow has been observed to cover more than 75 percent of the blade surface in the current machine. Clearly, flow prediction methods must provide for the transition region to obtain accurate results. Errors in the calculation of laminar or fully turbulent boundary layer flows are relatively small compared to the uncertainty in estimating transition onset and length, and regions of separated flow. Errors in the transition calculation directly affect the calculated turbulent boundary layer development.

Chapter 10 reviews some of the fundamental studies of transition and turbulent spots and the various schemes which have been proposed for the modelling of onset, transition and separation. The transitional region is usually modelled using the Narasimha [89] or Chen and Thyson [14] intermittency functions. These describe the growth of intermittency in transitional boundary layer and are predominately based on zero pressure gradient data.

Calculation of separated flow regions is especially difficult, requiring either an inverse boundary layer model coupled to an inviscid flow solver or some form of computationally expensive viscous flow solver. For design purposes it is common to resort to correlation methods such as that of Horton [58] or Roberts [101]. None of these methods are capable of capturing the physics of a wake-influenced re-attaching transitional flow as observed in the current measurements. Chapter 10 considers some options for improving the design methods to account for such effects where necessary, and discusses the possibility of optimising designs to benefit from unsteady phenomena.

Neither the Narasimha nor the Chen-Thyson model allow for changes in the physics of turbulent spot propagation which occur in different pressure gradients. Using a recent

compilation of turbulent spot propagation data of Gostelow et al. [40], an improved transition length calculation scheme has been developed. Chapter 11 discusses this method and tests its performance.

1.1 Supporting publications

Some of the intermittency detection techniques used in the current work were described in papers Walker and Solomon [137] and Solomon and Walker [119]. The first of these relates to the hot-wire boundary layer traverse data processing, while the second presents the method used for the surface hot-film data.

The hot-wire boundary layer investigation of Chapter 9 was first reported in Walker et al. [139]. Some further work with this data was presented (figures and abstract only) in Walker and Solomon [138].

The presentation of the surface hot-film data (Chapter 8) has spanned several publications. Solomon and Walker [120] investigates the effect of Reynolds number on the observed flow distribution and evaluates alternative data processing techniques. Effects of changing incidence were presented in Solomon and Walker [118] with slight improvements to the intermittency processing technique. The development of phase-locked average intermittency for the test case with a rotor blade removed was compared with the development of an isolated triggered turbulent spot in Gostelow et al. [42] and Solomon et al. [122].

Gostelow et al. [40] present a compilation of turbulent spot propagation and spreading rate data and the correlation curves for these parameters used in Chapter 11 were first presented in that paper. The new method for using this data to improve transition calculation in flows with changing pressure gradient from Chapter 11 is also described in Solomon et al. [121] and Gostelow et al. [41].

Chapter 2

Unsteady transitional flow in turbomachinery

2.1 Introduction

Early axial compressor design methods relied on correlations such as deviation angle vs. incidence angle to obtain the expected performance for a particular blade profile. These correlations were based on a large amount of measurements from two dimensional cascade testing. Flow in these cascades was inherently steady (moving bars have only recently been used to simulate wakes in cascades) and for the purpose of developing correlations the state of the blade surface boundary layers was not usually measured in detail. It was considered preferable to test in the region where the loss vs. Reynolds number curve is flat and large boundary layer separations are avoided (Lieblein [74].)

During the late 1970's and early 1980's huge improvements in the speed and affordability of computer hardware occurred (and still continue). Together with improved computational methods this made it possible to move away from the well tested profile shape families towards tailored profiles. Sanger [103] describes the use of optimisation techniques to design "controlled diffusion" compressor blading. By controlling the velocity diffusion on the suction surface and hence the boundary layer growth it is hoped to achieve higher blade loadings while avoiding boundary layer separation. In the case of transonic blading the profile shape must be chosen to minimise shock losses as well as boundary layer losses. This is referred to as "supercritical blading". The results achieved in these design methods depend heavily on the assumptions made in the flow calculation procedures and some of the largest uncertainties lie in the boundary layer behaviour. Sanger found no agreement in the literature about even the initial state of the boundary layer - whether laminar or turbulent. Sanger assumed transition would always occur by means of laminar separation with turbulent re-attachment at the next calculation point.

In a multi-stage machine all blade rows excepting inlet guide vanes experience periodic disturbances from the upstream rows. Neglecting the important effects of three dimensionality, there exists a complex set of interactions between the blade rows. As the downstream row moves through the potential flow field of the row immediately upstream it experiences changes in apparent flow angle and velocity. This is the potential flow interaction (Hodson [52]). The viscous wake from the upstream row also causes

an unsteady perturbation of the flow experienced by the downstream row. This wake disturbance comprises variations of turbulence level and length scale apparent to the downstream row and a change in mean velocity caused by the wake deficit. Wakes also cause relative local flows into or out of the boundary layer as they pass the blade. This cross-passage transport of fluid is known as the jet-wake effect (Meyer [86], Smith [117], Kerrebrock and Mikolajczak [67]). Other rows further upstream also leave wakes which can alter the disturbance field experienced by the downstream row depending on their relative position. Lockhart and Walker [76] have examined the influence of rotor wake / stator wake interactions on the time-mean and unsteady flow fields downstream of an axial compressor stage. All of these effects influence the unsteady boundary layer development and transition.

Potential flow effects decay much faster than wake effects as distance from the blade row is increased. At the axial spacing for the current work of around one blade chord the potential flow interaction is very small and is not expected to influence the stator blade boundary layer development except possibly at the leading edge.

A comprehensive review of the role of the transition process in turbomachinery (with an emphasis on turbine flows) was made by Mayle [80]. Squire's review [123] of wake-boundary layer interaction also includes a section on turbomachinery. These two reviews conclude that the jet-wake effect has an insignificant effect on the unsteady transition process. Walker's discussion of Mayle's review [135] questions this assumption. Similar uncertainty exists over the relative importance of turbulence and pressure gradients in fixing the transition locations.

The jet-wake effect

Fig. 2.1 shows the direction of the relative flow due to a wake as it passes over the suction and pressure surfaces of turbine and compressor blades. Flat plate experiments with wakes have usually been designed so that the strongest wakes produce a positive or impinging jet corresponding to the turbine suction surface case. Meyer [86] calculated the likely effect of wakes on the unsteady (potential flow) velocity distribution around a downstream blade. Kerrebrock and Mikolajczak [67] studied the implications of transport of rotor wake fluid across a compressor stator passage on performance. Higher entropy fluid associated with the wake was found to build up on the pressure surface of the compressor blade studied. Hodson [52] observed a similar phenomenon in a turbine rotor passage where the relative loss (compared to flow without wakes) was higher on the suction side of the blade because of the accumulation of high entropy rotor wake fluid there. Recent experimental work of Curtis et al. [21] shows an opposite behaviour (i.e. a relative increase of downstream total pressure at the suction surface of the turbine blade.) The computational analysis of Hodson and Dawes [57] shows that this behaviour can occur simultaneously with an increase in entropy at the suction surface in the special case where the large unsteady pressure fluctuations over the turbine blade suction surface cause *energy separation*. Here the unsteady pressure fluctuations are biased so that the stagnation enthalpy rises. In an unsteady isentropic flow this must be accompanied by an increase in stagnation pressure. This behaviour is not expected to be significant on compressor blades where the distortion of the wake as it traverses the blade passage is smaller.

An unsteady calculation performed by Ho and Lakshminarayana [51] clearly shows

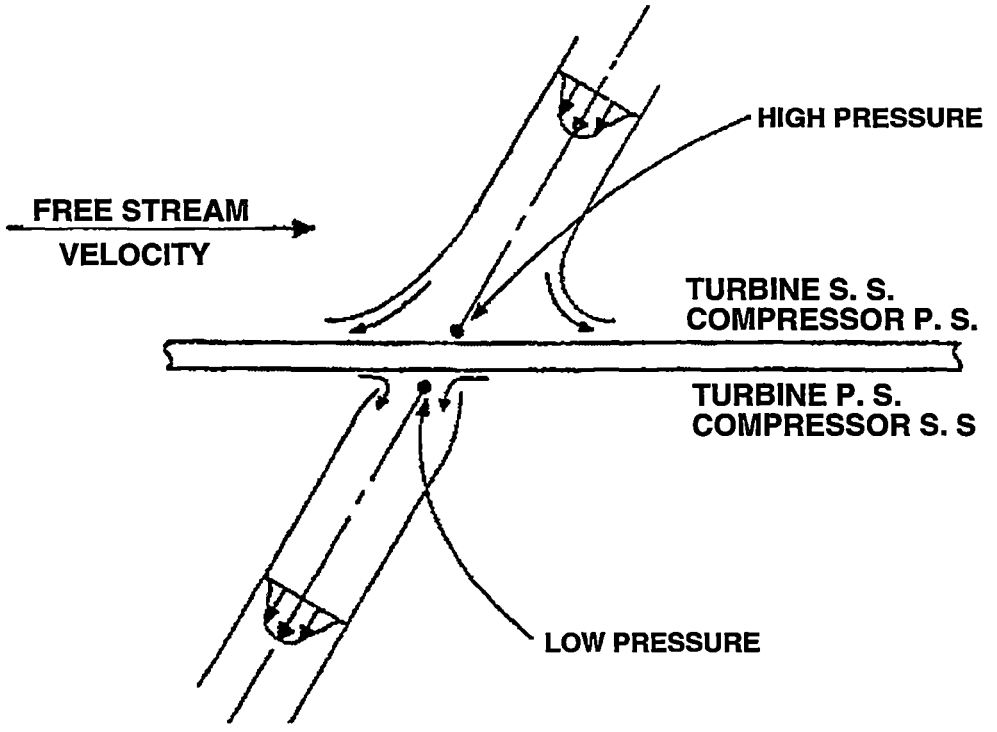

Figure 2.1: Direction of relative flow caused by a wake passing a surface. (Adapted from Hodson [52])

the jet-wake effect on the flow around a compressor blade (Fig. 2.2). The largest velocity perturbation vectors shown in the vicinity of the blade are of the order of 4% U_m (the largest velocity at inlet). Hodson [54] demonstrated similar features in a calculation of a turbine blade flow with an imposed wake disturbance. In both cases continuity requires that the flow caused by the jet-effect is replaced from elsewhere. This sets up a system of vortices on either side of the wake.

The modes of transition

In steady flow boundary layers with low disturbance levels (and assuming is no concave curvature induced Taylor-Görtler instability) the transition process commences with the growth of primary instabilities in the form of T-S (Tollmien-Schlichting-Schubauer) viscously tuned vorticity waves (Morkovin [88]). The growth of these primary instabilities is relatively slow and is affected by the shape of the velocity profile. Against this new background of periodically varying base flow many possible secondary instabilities are predicted by Floquet theory. These three dimensional secondary instabilities appear in the form of regular span-wise arrays of vortical structures such as the Klebanoff type instability. At points of very high local vorticity, breakdown to turbulence occurs with the formation of turbulent spots. Subsequent growth and merging of these regions of

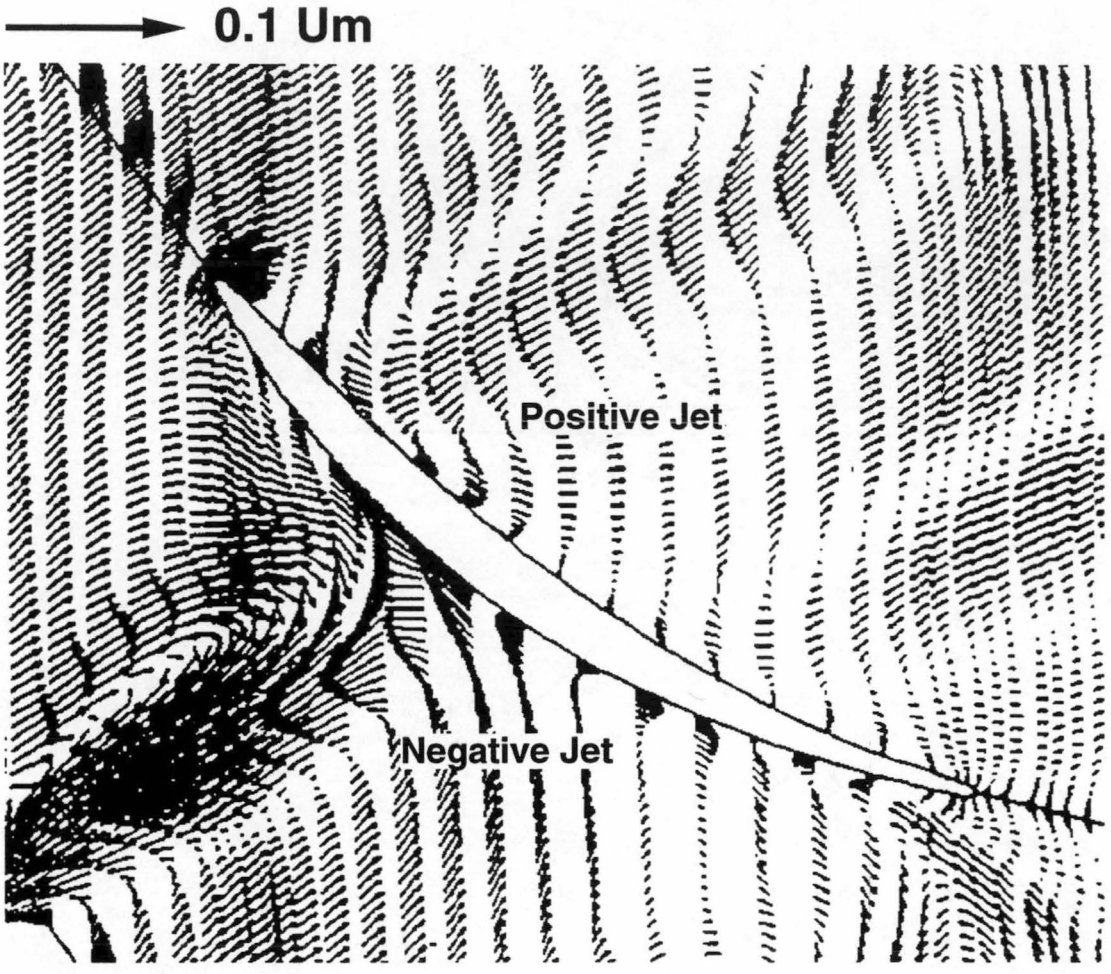

Figure 2.2: Results of an unsteady calculation of flow through a compressor blade passage by Ho and Lakshminarayana [51]. Vectors show the difference between the instantaneous and time-mean velocities. U_m is the largest vector at inlet.

turbulence may eventually result in a fully turbulent boundary layer. The mechanism described above is commonly referred to as *natural transition.*

In flows with high freestream turbulence and/or surface roughness, onset of turbulent flow has been observed to occur without evidence of the amplification of T-S waves. This is known as *bypass transition* (Morkovin [87]). The dominant mode of transition on turbomachinery blading is usually expected to be bypass because of the high levels of freestream turbulence associated with the wakes. Transition in a turbomachine is often accompanied by laminar separation which may persist over the wake passing period or may be periodically suppressed. Separated flow transition is often regarded as a distinct transition mode (Mayle [80]) although freestream disturbances can change the length of separated flow transition. Other factors such as noise and vibration can also influence boundary layer transition.

Dong and Cumpsty [25] observed amplified Tollmien-Schlichting waves in the inter-wake region on their compressor blades, indicating that stability theory may not be irrelevant in this region. The results of Walker and Gostelow [136] indicate that ad-

verse pressure gradients such as those experienced on a compressor blade cause T-S waves to have increased amplitude and frequency compared to those observed in zero pressure gradient. They also found that the transition process starts and ends earlier in the adverse pressure gradient. It cannot automatically be assumed that only the bypass mode is important to compressor blade boundary layers. Mayle [80] refers to the possibility of more than one type of transition process in an unsteady flow as *multimoded* transition. Mayle concludes that bypass transition may be predicted without reference to linear stability theory. At lower freestream turbulence levels (around 0.65%) Suder et al. [125] found that bypass mode transition was affected by the dominant frequencies of the external disturbance. Frequencies causing earlier transition correlated with frequencies in the linear stability curve. Blair [10] found no significant preferential amplification of disturbances with frequencies in the unstable range predicted by stability theories (160 to 620 Hz in this case) although his results show a strong streamwise increase of power in the 300 to 2000 Hz range.

The current work aims to resolve some of these questions and thereby allow better predictive techniques to be developed. Ensemble-averaging techniques and multi-element surface mounted hot-film arrays offer the means to measure the state of the boundary layer in the time-space plane. In this thesis these techniques have been coupled with intermittency and relaxing-flow detection algorithms to improve and simplify the interpretation the data obtained.

2.2 Some experimental investigations of unsteady boundary layer development

A brief review of steady transition processes and the development of turbulent spots, including some of the more commonly used correlations, is given in Chapter 10. Some experimental observations of unsteady boundary layers are discussed below. They are loosely classified according to the level of experimental simplification made in simulating the wake-boundary layer interactions of a multistage turbomachine.

Oscillating flows

The first evidence of the periodic-unsteady nature of the wake-induced transition process on a compressor blade was presented by Walker [133]. Inspired by the similarity of these transition measurements with results obtained in oscillating flow (with low freestream turbulence) by workers such as Obremski and Fejer [92], Walker proposed a tentative model of unsteady transition on compressor blades (Fig. 2.3). Here the effect of the wake unsteadiness is assumed to periodically alter the stream-wise position of the neutral stability point and the amplification rates of disturbances in the boundary layer. The decelerating part of the wake passing cycle makes the boundary layer less stable and increases the amplification rates. The acceleration part of the cycle has the opposite effect.

Obremski and Fejer [92] had found that certain levels and frequencies of sinusoidal oscillation of the freestream velocity promoted periodic transition to turbulence. They

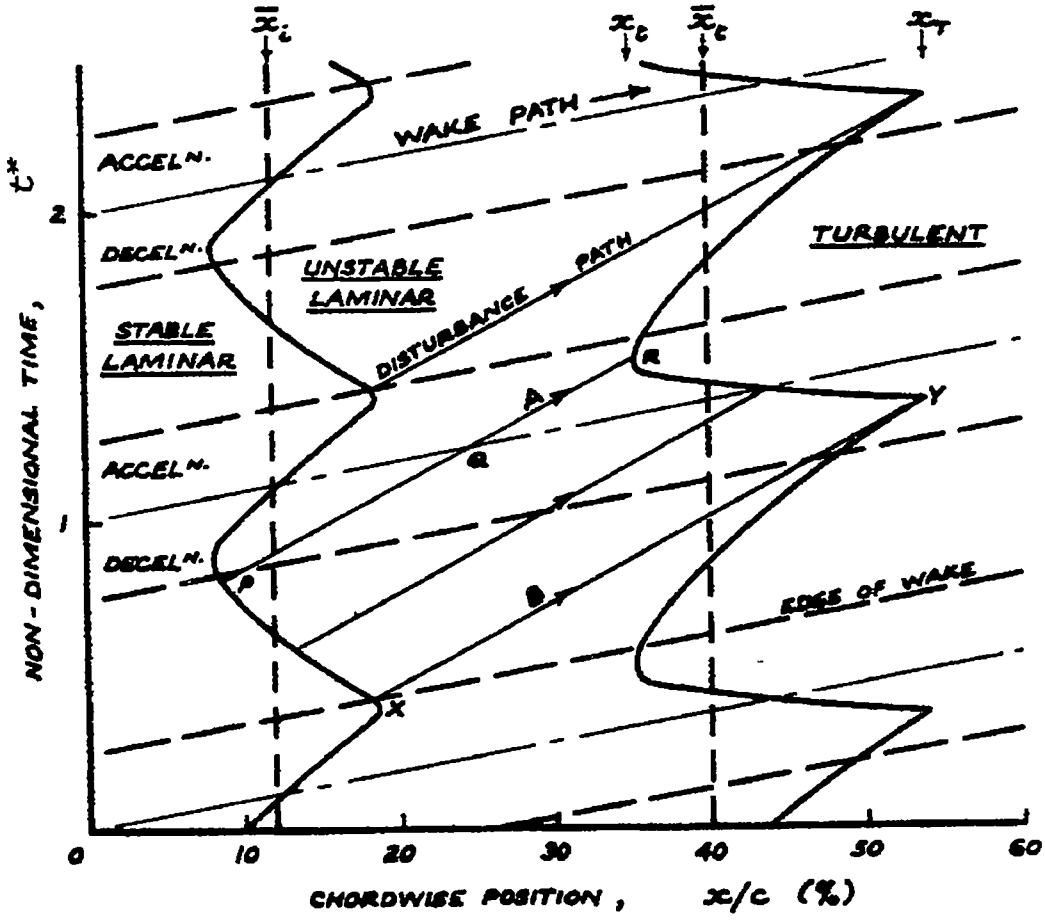

Figure 2.3: Walker's 1974 model [133] of unsteady transition on a compressor blade

quantified these effects in terms of a non-steady Reynolds number

$$Re_{NS} = \frac{U^2 N_A}{\omega \nu} \tag{2.1}$$

where N_A is the ratio of the disturbance amplitude to the freestream velocity and ω is the circular frequency of the oscillation. In zero pressure gradient flow the amplitude of the disturbance did not alter the transition onset point until Re_{NS} exceeded 27000. In their adverse pressure gradient study Obremski and Fejer observed a non-steady Reynolds number of 6000.

A review of transition in oscillation boundary layer by Loehrke et al. [77] thoroughly discusses the work of Obremski and Fejer and others but warns that designers should consider the presence of possible bypass mechanisms. They attributed an inconsistency between the observations of Obremski and Fejer and previous work of Miller and Fejer to a bypass caused by periodic venting of static pressure leads.

One bypass mechanism not considered in Walker's model was freestream turbulence. Later workers, notably Addison and Hodson [2] and Dong and Cumpsty [25], criticised this omission from Walker's model in the light of more recent experimental evidence.

Both of these papers suggest that the turbulence of the wake is the only factor of first-order importance to the unsteady transition process on a turbomachine blade. One of the arguments to support this view is the fact that the non-steady Reynolds number in these experiments (including Walker's) is typically below 1000. Actually if the estimate of Re_{NS} is based on the period of the wake disturbance instead of the blade passing period then Re_{NS} may even be 5–10 times lower. The disturbances typical of turbomachinery wakes apparently do not give sufficient time for Obremski-Fejer breakdowns to occur through amplification of T-S waves to a critical level during a single cycle of the freestream oscillation.

Only a limited range of pressure gradients were covered in the work of Obremski and Fejer and to the author's knowledge there have been no experiments of this type performed at raised freestream turbulence levels. Both of these factors may have significant effects on the non-steady Reynolds number required to cause breakdown.

Flat plates with incident wakes

Several alternative methods for simulating turbomachine blade wakes in a wind tunnel or cascade have been proposed. The simplest experimental approach is to design a mechanism to generate wakes which can pass over a flat plate installed in an existing wind tunnel. This approach allows more flexibility than testing in a real machine and allows models of larger physical dimensions to be used. The Reynolds number of the flow and the wake passing period can be changed independently. The wake defect amplitude can also be altered without changing the pressure distribution (Pfeil et al. [96].) Obvious shortcomings of the technique are the difficulty in applying a realistic pressure gradient (if this is attempted at all) and problems in modelling the wakes of a lifting cascade.

Usual practice has been to simulate blade wakes by using circular cylinder (or rod) wakes. Raj and Laksihminarayana [98] measured the wake behind a cascade of lifting airfoils. The wake was found to be asymmetric and two different scaling lengths (one for each blade surface) were required to obtain similarity of the wake velocity profiles. The distribution of turbulence intensity was also found to be asymmetric in the range of testing ($0 < x/c < 0.72$, where x is the streamwise distance behind the trailing edge of the cascade.) Testing in the current machine (Chapter 6) has revealed the additional phenomenon of periodic variations in turbulence intensity within rotor wakes. Despite these reservations Rodi et al. [102] find that circular cylinder wakes are an adequate representation of real blade wakes. In a multi-stage compressor Halstead et al. [46] replaced one rotor blade by various rods. This enabled direct comparison of rod and airfoil generated wakes and the effects of each wake on the unsteady boundary layer transition in the following blade row. Here it was found that matching the turbulence level in the wake is far more important than matching the velocity defect. Halstead et al. warn that a choice of rod dimensions based on velocity defect alone can lead to turbulence levels which are too high, and can give a misleading picture of wake-induced effects. Schulte [112] selected bars on the velocity defect criterion and measured peak turbulence intensities of 13 % in the simulated wakes compared with 11 % in a turbine.

Pfeil et al. [96] studied the formation of wake-induced turbulent spots in a flat-plate laminar boundary layer. The background turbulence level was around 0.6% (according to Orth [95]). Despite the abovementioned problems with this type of simulation the

observed transition processes largely agree with later observations made on real blades disturbed by real wakes such as Halstead et al. [46] and the current work. Pfeil et al. proposed a transition model where the high levels of turbulence associated with the passing wakes caused transition at a forced transition onset point some distance upstream of the natural transition point. Turbulent spots initiated under the wakes at the forced transition point grow in the otherwise laminar flow, eventually merging to form a fully turbulent boundary layer. It was also recognized that this picture could be altered if the natural transition point was upstream of the merging point of the wake-induced spots. The unsteady transition points observed by Pfeil et al. were not consistent with the work of Obremski et al.

Pfeil et al. [96] observed a region of becalmed or relaxing flow which follows a spot. Like Schubauer and Klebanoff [110] they suggest that the becalmed region exists because the trailing edge of the turbulent spot travels faster than Tollmien Schlichting (T-S) waves, thus forming a region in x-t space which is inaccessible to T-S waves propagating from upstream. In this work formation of T-S waves was observed in the boundary layer between the wake-induced patches. If the wake-induced turbulent patches had not merged by the natural transition point then natural transition would occur and start to contaminate the becalmed region due to the higher leading edge propagation rate of these new spots compared with the propagation rate of the trailing edge of the becalmed region. These authors were not able to determine the relative importance of the wake turbulence or periodic velocity defect on the transition process.

Experiments using squirrel-cage wake generators such as Orth [95] and Pfeil et al. [96] produce two sets of wakes: one set is generated by the bars travelling upwards and one by the downwards travelling bars. The sign of the jet-wake effect is opposite for these different wakes. Pfeil et al. did observe disturbances from the two different kinds of wakes but did not find a significant difference in character except that the upwards wake disturbance had a lower amplitude because it was generated further upstream. Orth was able to apply ensemble averaging techniques to the flow and clearly showed the developing spot to lag behind the wake which caused it. Both the upwards and downwards wakes caused spots, but the upwards wake was slower to cause transition than the downwards wake in Orth's experiment. The spot generated by the weaker wake seems to lag the wake by a slightly larger amount than the spot from the strong wake. These apparent differences may be due either to the different relative strengths of the two wakes or by the differing sign of the jet-wake effect. Walker [135] (in published discussion to this paper) suggests that one of Orth's figures shows a spot growing with no direct connection to its associated wake, possibly indicating an indirect spot formation mechanism. Funazaki [34] however concluded that the turbulence from Orth's weaker wake did directly cause a spot but that this spot was slower to grow because of the lower turbulence level in that wake.

Results of Liu and Rodi [75] in a similar experimental configuration are also confused by the presence and interaction of primary and secondary wakes generated by the squirrel cage. They chose to investigate flow cases where the primary and secondary wakes converge in the boundary layer region. The disturbance then is not a single wake but two wakes with opposite jet-wake signs superimposed.

Alternatives to the squirrel cage which avoid the secondary wake problem have been tried by several workers. Dong and Cumpsty [25] used rods mounted on moving belts to simulate wakes in a linear cascade. The rods returned on the downstream side of

the blade so that no secondary wakes impinged on the blade. Doorly and Oldfield [26] and Funazaki et al. [35] both used a spoked wheel arrangement to generate wakes. Only spokes on one side of the wheel pass through a slot in the tunnel wall to generate wakes - all travelling in the same direction (although only parallel to the plate at one position.)

Linear cascades with moving bar wakes

In these experiments the complications of real blade pressure gradients and curvature are introduced. Bars are still used to generate the wakes so they are still not truly representative of wakes from a cascade of lifting aerofoils.

Doorly and Oldfield [26] studied the combined effects of wakes and shock waves passing over a linear cascade of turbine rotor blades at Mach and Reynolds numbers representative of those found in the first stage of an engine turbine. They observed separate turbulent patches, one arising from the effect of the shock on the boundary layer and a second wake-induced turbulent patch. They found that the leading edge of the turbulent patch remained beneath the path of the wake in the freestream. In this work no significant lag time between the arrival of the wake on the blade and apparent development of a self-sustaining turbulent spot in the boundary layer was observed. This contrasts with the observations of Hodson and Addison [56] and [2] where long stripes of wake-disturbed laminar boundary layer were observed prior to the final breakdown to turbulent spots. In discussion of later work from the same facility reported by LaGraff et al. [72], Hodson, Addison and Walker suggested that the lag time (if it existed) was much shorter in this instance because of the higher Reynolds number.

The observations of Hodson and Addison show that bypass transition under the wake path does not occur from the leading edge but must wait until Re_θ is high enough to permit a self-sustaining turbulent spot. Pressure fluctuations due to the wake turbulence will be felt at the surface but these may not influence boundary layer stability until the thickness of the Stokes layer associated with the pressure fluctuations becomes comparable with the height of the critical layer.

Other workers such as Dullenkopf et al. [27] and Han et al. [47] have used a cascade and rotor combination in a similar arrangement to Doorly and Oldfield. Measurements of time mean heat transfer coefficient over the whole turbine blade show that an increase in the wake frequency causes the heat transfer rate to rise at earlier and earlier points on the suction surface. This strong effect of the wakes is less pronounced on the turbine pressure surface. The pressure surface boundary layer is more stable than the suction surface layer and under the influence of a negative jet which carries turbulent wake fluid away from the blade.

Dong and Cumpsty [25] measured the unsteady boundary layer on a supercritical-type compressor blade with incident wakes. Strong wake-induced turbulent spots were observed on the suction surface and relaxing flow persisted following the spot for a considerable portion of the blade passing period. Breakdown in the inter-spot area was associated with T-S waves and intermittent laminar separation. The spots on the pressure surface were found to be quite similar to those on the suction surface except near the freestream. The apparent similarity of spots on the two surfaces was taken as evidence of the irrelevance of the sign of the jet-wake effect on the boundary

layer behaviour. Results of the current work contradict this finding: new spots on the pressure surface of the University of Tasmania compressor form over a wider range of non-dimensional times than on the suction surface and are generally less well-defined. This is probably caused by the very different pressure distributions on the two surfaces, but it is not yet possible to rule out the jet-wake effect.

Dong and Cumpsty also found that differences in blade performance with and without wakes were smaller in the case of the compressor blade compared to differences observed by Hodon [52] for turbine blades. With wakes the transition started earlier but the relaxing flow region caused stabilised flow to persist longer on the blade than in the undisturbed case. These compensating factors yielded little overall change in performance.

Schulte and Hodson [113] have measured the boundary layer on a turbine blade where a separation bubble causes transition. In this case the effect of wakes was to significantly reduce the loss. In this work a strong interaction between the negative jet of the wake and the separation bubble was observed. Later Schulte [112] concluded that the marked alteration of the separation bubble by the jet wake was a consequence of the close proximity of the bubble to the throat of the cascade.

Schulte [112] has made a detailed experimental survey of wake-induced transition in a turbine cascade using a range of wake passing reduced frequencies. The cascade in this work shows a large steady flow separation bubble. Wake-induced turbulent spots and their associated relaxing flow regions are largely able to suppress the separation. Schulte demonstrates that an optimum wake passing reduced frequency can be determined where the additional loss incurred by the wake-induced turbulent spots is less than the reduction of loss obtained through the reduction in size of the separated flow area.

Annular cascades and turbomachines

Measurement in an actual turbomachine ensures a realistic wake structure and inlet flow-field for the blade row in question. However, a new range of difficulties are introduced, including effects of three dimensionality, restricted operating flow conditions and increased expense. Even in large low-speed research machines, where blade chords are of the order of 100 mm, detailed boundary layer traverse measurements require great care. As the boundary layer thickness is of the order of the length of a hot-wire sensor only single wire measurements are usually possible. The minimum possible axial blade-row spacing in a research machine may restricted to a value larger than would be used in a production machine by the requirements of providing probe access space.

Early workers such as Evans [30] restricted themselves to measurement in the freestream. At this time it was hoped that wake passing effects could be adequately accounted for in a design scheme if a representative turbulence level which included the wake-induced unsteadiness was known. The measurements of Walker [132, 133], introduced above, revealed the transitional nature of the wake-affected boundary layer on an axial compressor blade.

Comparison of aerodynamic efficiency of an axial turbine with an expected aerodynamic efficiency derived from measurements on equivalent cascades by Hodson [52] showed a 50% increase in rotor profile loss in the presence of unsteady wakes. In the cascade the boundary layer was found to be laminar for 78% surface distance followed by complete laminar separation. In the turbine, no separation was observed on the ro-

tor. Although the wakes promoted an earlier transition and suppressed the separation, there was a significant loss penalty in this case.

Valuable information regarding the state of the unsteady boundary layer was obtained by Hodson through the use of surface mounted hot-film sensors and phase-lock averaging. This technique offers relatively high frequency response measurement of wall shear stress (although direct calibration is not usually attempted). Several sensors can be arranged in an array on an airfoil surface to allow simultaneous measurements at different positions. Other workers to apply this technique to turbomachinery include Halstead et al. [46] and the current work. Similar results in unsteady flow have been obtained with thin film heat transfer gauges by Doorly and Oldfield [26]. A significant development of the current work is the automated extraction of unsteady turbulent intermittency information from a surface hot-film array.

The four paper collection of Halstead et al. [46] is one of the most recent and most comprehensive experimental investigations of wake-induced turbomachine blade boundary layer transition. This work includes measurements made in both compressor and turbine facilities. These workers clearly showed that the wake-induced turbulent strip is initially transitional, i.e. not every wake necessarily induces a turbulent spot and not all wake-induced turbulent spots have the same stream-wise onset point. The importance of the calmed region in suppressing separation and delaying the completion of transition is also demonstrated. The machines in the Halstead study were a four stage compressor and a two stage turbine. Even in the third stage of the compressor, flow between the wakes was transitional as far back as 80% of blade surface distance. This confirms that observations of transitional flow made in the current 1.5 stage machine are relevant to conditions which may be expected in the embedded stages of a multi-stage machine.

With reduced Reynolds numbers Halstead et al. found a reduction in the strength of the wake-induced transitional strips. For the compressor, laminar separation eventually spreads to the whole wake-passing period at low Reynolds numbers. These authors warn that measurements should be taken at Reynolds numbers above the critical Reynolds number to obtain behaviour relevant to engine design point operation.

Wakes from blade rows further upstream

Thus far only wakes from the blade row immediately upstream have been considered. In a multi-stage machine there also exist wake disturbances from the other upstream blade rows. The significance of such effects has been clearly demonstrated by Binder et al. [8] who measured a strong twice-per-revolution variation in velocity and turbulence measurements downstream of a turbine stage. The stage in question had rotors with blade counts differing by two. Binder et al. concluded that the flow on the downstream rotor may either be attached or separated depending on the relative position of the wake from the upstream rotor. Further measurements downstream of rotors in the same machine by Arndt [5] clearly show the footprint of the upstream nozzle wakes at certain circumferential positions. Halstead et al. [46] measured a variation in the transition pattern on the suction surface of a downstream nozzle with relative circumferential position of the upstream nozzle row in an LP turbine stage.

Walker [131] notes that since the circumferential wake transport is different at the hub and tip, the relative positions of the upstream rotor wake and the downstream

rotor would vary at different radial positions. Thus the phase angle of the nodes in Binder's observed flow pattern may be expected to vary with radial position.

2.3 Summary

The unsteady boundary layer transition in a turbomachine is a complex process. Truly representative prediction methods need to encompass the most relevant phenomena for the application to be considered.

For calculating a given unsteady transitional flow it is necessary to know the following:

- location of transition onset point in steady and unsteady flow, both attached and separated
- length of transitional flow (or time-space footprint in unsteady flow)
- extent of the calmed region in the time-space plane
- effectiveness of calmed region in delaying separation and transition.

A generally applicable prediction method must variously be able to determine the influence of freestream turbulence level (in and out of wake), pressure gradients, roughness and other external parameters on these factors.

Existing transition length and onset correlations have been developed for steady flows. It is necessary to know if these correlations can be applied to unsteady flow on a quasi-steady basis.

Recent useful progress has been made by Schulte [112] who has demonstrated that the relaxing flow region in an unsteady transitional flow can be predicted by a conventional unsteady boundary layer calculation if a suitable (time and space varying) intermittency distribution is prescribed.

Chapter 3

The research compressor

3.1 Introduction

This chapter describes the experimental facility used for the current work. The physical dimensions of the machine and a typical blade are presented here along with a summary of the instrumentation and machine operating conditions. The various modifications made to the hardware and software associated with the tunnel during the course of this project are also discussed.

The research compressor is a 1.5-stage axial machine comprising inlet guide vane (IGV), rotor and stator rows. It was designed and built at the Aeronautical Research Laboratories (ARL) in Melbourne Australia in the 1950's. The machine was developed as part of a long term investigation into compressor aerodynamics undertaken by the ARL and the University of Tasmania with the aim of improving compressor blade performance through the use of prescribed velocity distribution design techniques. Detailed descriptions of the research compressor facility are given in Oliver [94] and Walker [132]. Relevant details are repeated here for completeness with conversion to SI units applied where appropriate.

3.2 Description of the tunnel

Fig. 3.1 shows a longitudinal section of the machine. The tunnel is of flow-through type with exit air re-circulating through the laboratory before returning to the tunnel inlet.

The contraction inlet constructed from plywood turns the incoming air from a nearly radial direction through 90° to an axial direction. The entry to the contraction is 610 mm wide and has a diameter of 2134 mm. The annulus at the start of the working section has a 686 mm inside diameter and a 1143 mm outside diameter. This gives an inlet contraction area ratio of 6.2:1. A wire gauze is used to cover the inlet and increase flow uniformity. The wire also acts as a coarse filter to help protect hot-wire probes used in the compressor.

The inlet section together with the inlet guide vane row can be unbolted from the rest of the machine and wheeled back on rollers to allow easy access to the rotor and stator rows. One disadvantage of this arrangement is that a long motor drive shaft from the outlet end of the machine is needed. Steps in the casing flanges ensure accurate alignment of the two sections. Good alignment of the hub at the join relies on the inlet

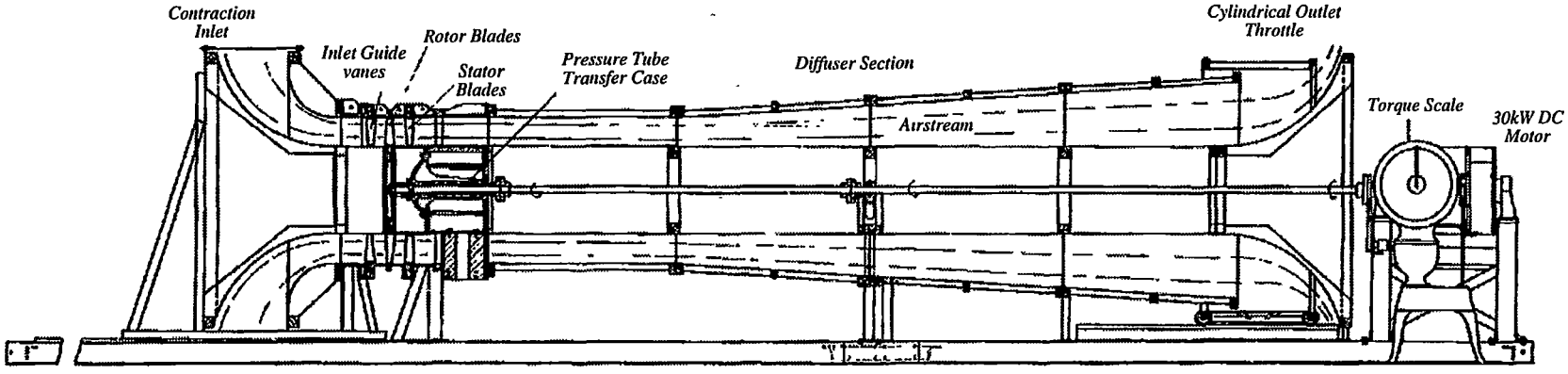

Figure 3.1: Longitudinal cross-section of research compressor

section hub part remaining centred relative to the casing. To improve this aspect of the design the old plywood cylindrical hub section upstream of the rotor was replaced by a machined aluminium section prior to the start of this project.

A brief investigation of the vibration levels using a single accelerometer showed resonances at 200, 230 and 330 rpm. These were audible and easily avoidable in the selection of test operating points. Above 700 rpm a vibration spectrum with a fundamental frequency at the shaft speed was observed at a level of about 10 mm/s rms. This rose to above 20 mm/s rms at 750 rpm; hence long duration testing at speeds above around 720 rpm was avoided.

The working section where the blade rows are mounted is 1143 mm long with parallel walls. A further parallel section of about 1.25 diameters long joins the working section to a diffuser section about 4 diameters (4572 mm) long. The diffuser has a cylindrical core and conical outer shell with an included whole angle of 7°. At the outlet, the inner wall of the tunnel is flared outwards to turn the exit air to a nearly radial direction.

A cylindrical sliding throttle at the outlet controls the through-flow and hence the compressor operating point. A motor driven chain turns three sprocketed screws which drive the throttle along its rails. A simple position sensor was fashioned from a 10-turn potentiometer driven by a toothed belt. With a 12-bit ADC, this system gives a resolution of ±0.15 mm but with a non-linearity of approximately ±1.5 mm over a 600 mm scale. Since the flow coefficient control algorithm does not require accurate knowledge of the absolute throttle position, this non-linearity is acceptable.

A 30 kW D.C. motor drives the compressor. A thyristor controller allows the speed to be controlled to an accuracy of around ±0.1 rpm at 500 rpm. Speed was measured using a 6000 pulse per rev. shaft encoder. An external counter and timer converted the signal from the encoder to a binary coded decimal speed value at a selectable rate of either 1 Hz or 10 Hz. A small tacho-generator was initially used to provide the thyristor controller with a feedback signal. Part-way through the project the tacho-generator developed a fault, and was replaced by a voltage derived from the shaft encoder signal. This returned the speed stability to better than ±0.1 rpm.

3.3 Details of the compressor

The compressor consists of a 38 blade inlet guide vane row, a 37 blade rotor and a 38 blade stator row, all mounted in a cylindrical annulus with hub and tip diameters of 685.8 mm and 1143 mm respectively. This gives a hub-tip ratio of 0.6. A C4 blade section with a constant chord of 76.2 mm and an aspect ratio of 3.0 was used. The blades are machined from aluminium at a tolerance of 0.09 mm (0.001″ per 1″ chord, Oliver [94]). The mid-blade space/chord ratios are 0.99 for the stationary blades and 1.02 for the rotor. A complete description of the blade profile and sensor locations is given in Appendix A.

The blade angles (Table 3.1) were originally selected using the data of Howell [60] to give a free vortex design with 50% reaction at mid-blade height. An error in assembly (see Appendix A) resulted in a change in rotor blade stagger of 2° from the design condition for the current work. Consequently the design conditions of 50% reaction and free vortex flow will no longer be exactly fulfilled. Correction must now also be made when comparing the present work with that previously performed with this

machine. Using the actual blade angles and Howell's correlation, nominal incidence i^* and nominal deflection ϵ^* values for the machine have been calculated. Results are shown in Table 3.2 for the machine with unmodified (Rotor 1) and modified (Rotor 2) rotor blade stagger angles.

Table 3.1: Blade angles, Oliver [94].

		Hub	Mid	Tip
IGV	θ	34.4°	27.8°	24.3°
	β_1	0.0°	0.0°	0.0°
	β_2	34.4°	27.8°	24.3°
	ξ	17.2°	13.9°	12.1°
Rotor[1]	θ	52.5°	31.1°	19.1°
	β_1	30.5°	45.0°	51.7°
	β_2	-22.0°	13.9°	32.6°
	ξ	4.2°	29.5°	42.2°
Rotor[2]	θ	52.5°	31.1°	19.1°
	β_1	28.5°	43.0°	49.7°
	β_2	-24.0°	11.9°	30.6°
	ξ	2.2°	27.5°	40.2°
Stator	θ	32.9°	31.1°	29.4°
	β_1	53.7°	45.0°	39.8°
	β_2	20.8°	13.9°	10.4°
	ξ	37.2°	29.5°	25.1°

[1] Rotor design values (for comparison with previous work)
[2] Rotor settings as installed for current work (see Appendix A)

Table 3.2: Nominal conditions at mid blade height

	i^*	ϵ^*
IGV	0.0	22.6°
Rotor[1]	-0.1°	22.3°
Rotor[2]	+0.6°	23.2°
Stator	0.0°	22.6°

The change in rotor blade setting angle has effectively increased the rotor incidence by two degrees. Hence the rotor would be expected to stall at a higher flow coefficient than observed in the previous studies.

Fig. 3.2 shows the rotor blade attachment detail. A similar arrangement exists for the stator blades. This particular arrangement allows accurate adjustment of the blade angles at the expense of reduced tip clearance setting accuracy. Average clearance is about 0.3% of blade height (0.75 mm) with a typical variation of ±0.25 mm. Blade angle setting accuracy is discussed in Appendix A.

The blades in the stationary rows are fixed to rings at the tip and are free at the hub. Each blade row can be traversed independently in the circumferential direction by rotating these rings. Although this arrangement adds mechanical complexity, the

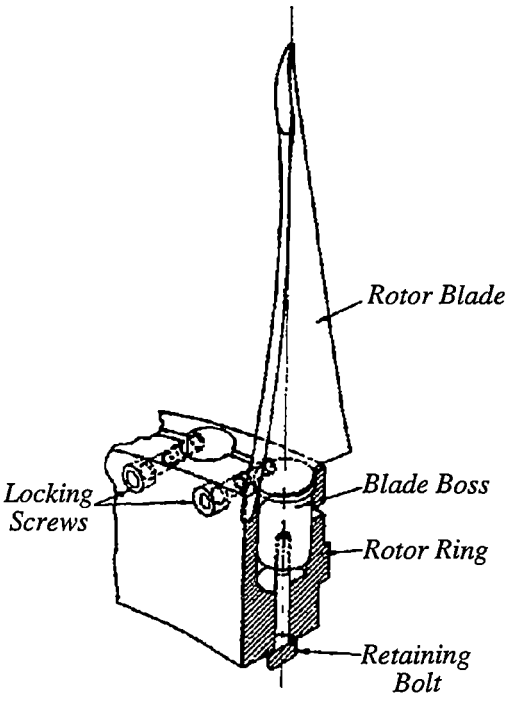

Figure 3.2: Cross section of variable-stagger rotor blade assembly

problem of sealing the probe insertion point is now trivial as the probe is fixed relative to the casing while circumferential traverses across the blade row are taken. One of the probe insertion points is visible in Fig. 3.6 with the end of a probe support rod protruding.

The screw with handle visible at the top of Fig. 3.6 acts against a bracket fixed to the stator blade retaining ring, thereby changing the circumferential position of the stator blades relative to the rest of the machine. A stepper motor (out of picture) is also connected to the screw to allow automated traversing. The IGV blade row is equipped similarly. Both stepper motors are controlled by a digital output signal from the compressor controller PC. A linear potentiometer on each traversing screw is used by the control system to find the blade row circumferential position to an accuracy of around ± 0.2 mm when referenced back to the mid-blade height, depending on the screw position. More accurate differential positioning can be achieved with the stepper motor drive and a digital dial gauge.

The blade rows are positioned so that the blade roots of neighbouring rows have an axial spacing of two chord lengths. The resulting machine geometry at mid-blade height is shown in Fig. 3.3. Actual values for the given dimensions varied slightly for different re-builds and different probe positions. The dimension d varied from 87.0 to 88.5 mm and dimension b was between 39.5 mm and 45.0 mm. w and a varied as the IGV blade row was traversed although $w+a$ was kept constant at 43.7 mm for pressure measurements and 0.0 mm for the upstream hot-wire traverse. The reference relative circumferential IGV-stator position gave $a/S = 0.50$. In that position the blade roots are at the same circumferential position.

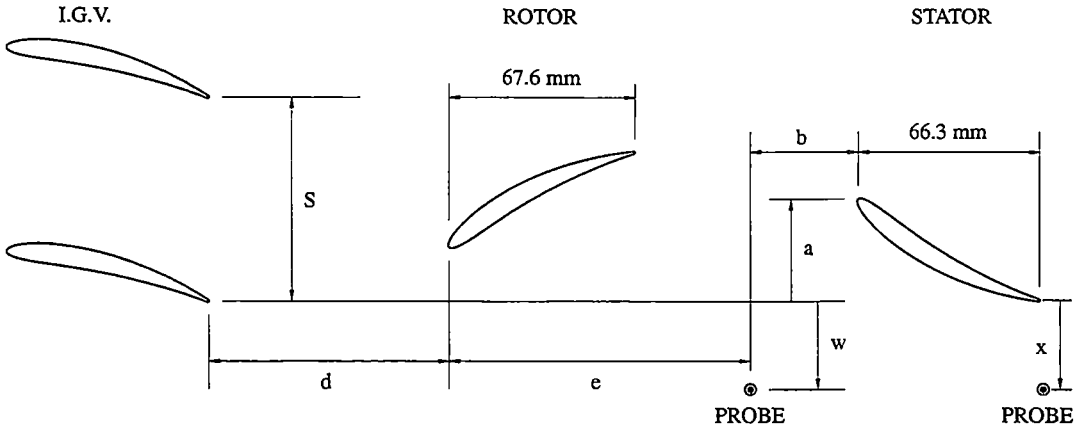

S	circumferential blade spacing $\pi D/N$
w	position of upstream probe relative to IGV trailing edge
x	position of downstream probe relative to stator trailing edge
a	position of stator row relative to IGV trailing edge
b	position of upstream probe relative to stator leading edge
d + e + b	237.1 mm

Figure 3.3: Compressor geometry at mid-blade height

3.4 Overview of instrumentation

Inlet air temperature is measured by a Stow Laboratories platinum resistance thermometer inserted through the casing 130 mm upstream of the centre of the IGV row at the top of the machine. This thermometer was compared against a mercury in glass thermometer and found to agree to better than ±0.2 °C. The manufacturer quotes an accuracy of $\pm 0.15°C$ or ±0.2% of reading.

Two Datametrics brand pressure transducers and signal conditioners were used, one absolute transducer (1000 torr range) for atmospheric pressure and one for differential pressure (±100 torr range). Accuracy information for the pressure transducing system is given in Appendix D. Both transducers are referenced to the inlet static pressure obtained from an inlet pitot-static tube. A Scanivalve rotary pressure switch is used to automatically step the (externally-mounted) differential transducer between the various pressure tappings.

The 4 mm o.d. inlet pitot static tube was mounted with its stem 115 mm upstream of the centre of the IGV row. The measuring head was inserted 100 mm from the casing into the flow in a circumferential position midway between the top and bottom of the machine on the probe insertion side. The wake from the inlet pitot tube is clear of the stator blade passages where measurements were taken.

Ambient relative humidity of the return air is measured by a Vaisala humidity sensor suspended from one of the instrument racks outside the tunnel. Accuracy for this gauge is given as ±2% RH depending on the calibration reference.

A Mitutoyo digital dial gauge with 30 mm travel and ±0.002 mm accuracy was

mounted so as to measure the stator row circumferential position over a small range with sufficient accuracy for boundary layer traversing. When referenced to the mid-blade position, the circumferential position of the stator blade row is measured to an accuracy of about ± 0.001 mm. This gauge was read by the data acquisition system via an RS232c connection. For the early boundary layer traverses (as reported in Walker and Solomon [137]) a mechanical dial gauge was used (accuracy 0.003 mm or $0.0001''$). The stepper motor and drive screw system has a resolution in the range 1.4–1.6 μm per step (at mid blade height) depending on which end of the screw the actuator is at.

Most of the anemometry work was undertaken using TSI IFA-100 type anemometers of which up to 5 were available. A pair of DISA 55M10 anemometer bridges were also available and were used in the early hot-wire work (Walker and Solomon [137]). The TSI system was favoured for the later work because of the convenient signal conditioners included in that system rather than any inherent superiority over the DISA system. The actual hot-wire and surface hot-film gauges used are discussed in the relevant chapters. A Yokogawa DL1200a digital oscilloscope was found to be very useful for checking anemometer output in real time.

3.5 Control and data acquisition system

A schematic showing the layout of the compressor instrumentation is shown in Fig. 3.4. Two IBM-compatible personal computers (PC's) are used to control the system. The Compressor Control PC controls the tunnel operating point and does all the low speed data acquisition. The Data Acquisition PC takes the high speed data from the anemometry system and co-ordinates the system by RS232c communication with the Compressor Control PC. The current system has undergone almost continuous revision as new hardware, instrumentation and software has been introduced during the project. The system allows the software on the Compressor Control PC to remain unchanged while the Data Acquisition PC is re-programmed when a new testing schedule is required.

In normal operation the Compressor Control PC runs a `TurboPASCAL` based application program. This software samples the analogue input ports to measure inlet dynamic pressure, atmospheric pressure, temperature and relative humidity at regular intervals. Running averages of air density, kinematic viscosity and inlet axial velocity are calculated. The optical shaft encoder output signal is hardware processed to provide compressor speed in a binary coded decimal (BCD) format for the data acquisition system. From this information flow coefficient ϕ and Reynolds number based on chord and rotor mid-blade velocity Re_c are calculated and displayed in real time.

Tunnel speed is primarily controlled by an analogue control loop built into the motor drive unit. The Compressor Control PC continuously adjusts the analogue loop set-point signal through a 12-bit D/A converter to maintain speed at the required value. The software varies the set-point as required to maintain either constant speed, Reynolds number or Mach number. The speed error is determined digitally by comparison of the BCD speed value and the computed set-point value. This extra loop of control corrects for long term changes in Reynolds number (or speed or Mach number) as atmospheric conditions change or as changes in mains voltage, mains frequency, the analogue electronic control system or the mechanical bearing resistances occur. In steady operation the Compressor Control PC makes a small adjustment to the set point

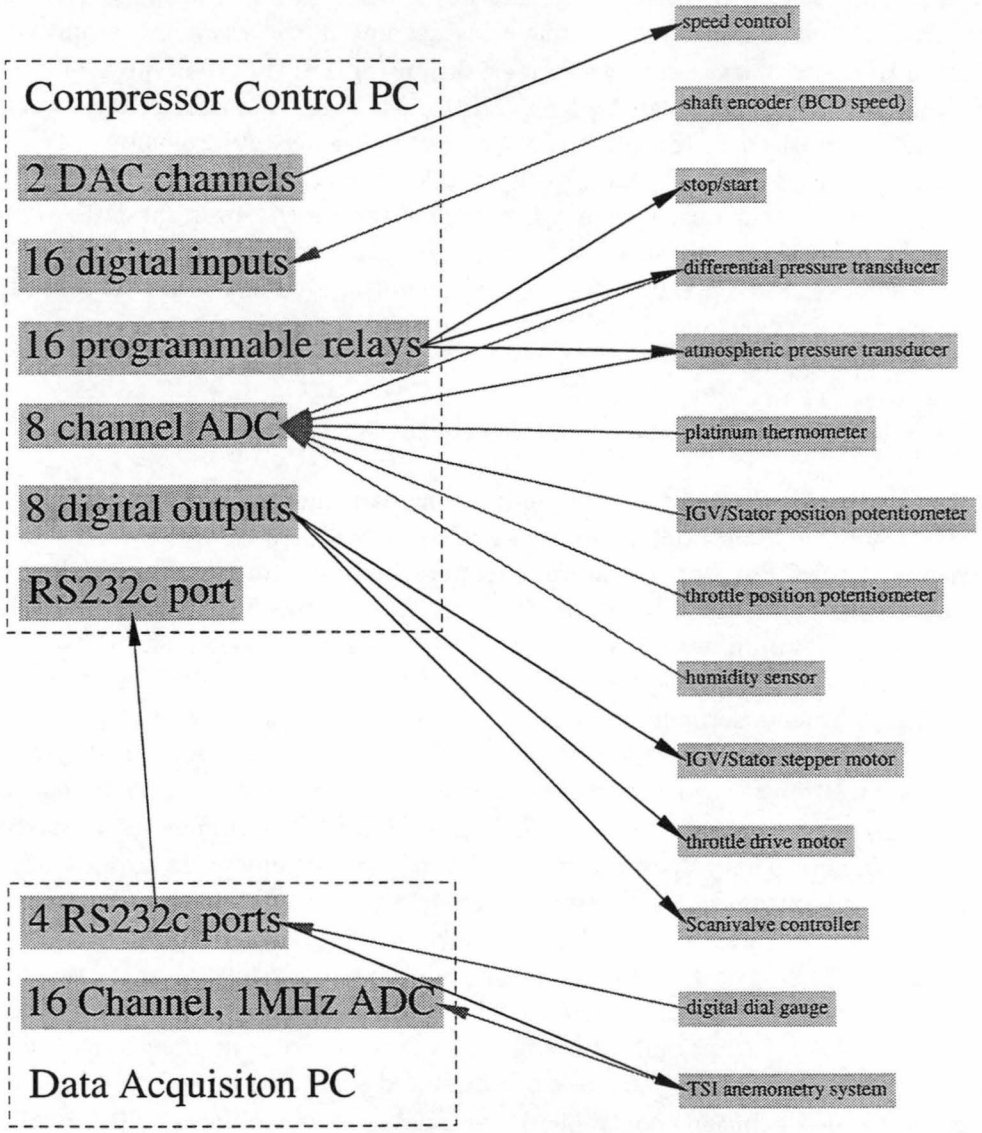

Figure 3.4: Simplified instrumentation layout

typically once every 5 seconds. Speed errors are typically below ±0.1 rpm.

In principle the flow coefficient is continuously controllable in a similar manner; however some practical difficulties have prevented this to date. First the throttle position motor has considerable switching noise which was found to cause large spikes in the anemometer signal. Secondly, the throttle position control process is quite slow because of the on-off nature of the position motor. A third difficulty is that the flow coefficient varies with a period of around 30 seconds even with the throttle position fixed (see below). The current practice is to allow the Compressor Control PC to set the flow coefficient automatically at the start of a test run and from then on operate with a fixed throttle position until a new flow coefficient set point is required.

Unsteady data was obtained by triggering the data acquisition system on a zero marker signal provided by the optical shaft encoder. This was open to error from the shaft encoder being at the far end of the long drive shaft away from the rotor. Any fluctuations in shaft or coupling twist may have caused variability in the synchronisation and hence extra jitter in the ensemble averaged data. Recent work by Hughes [62] involved the addition of a new optical sensor to the machine which was triggered directly off one of the rotor blades through a hole in the casing. Hughes found the relative timing of the two signals at a given operating point had a standard deviation equivalent to less than 0.8% of a blade passing period. There was a small change in the relative timing of the signals across the speed range attributed to steady shaft and coupling twist. No consistent trend was observed as the aerodynamic loading was changed at constant speed.

The Data Acquisition PC is currently programmed with `LabView`. An RS232c link to the Compressor Control PC allows the Data Acquisition PC to set test-points and read the current operating conditions. New test sequences can be set up on the Data Acquisition PC without needing to re-program the Compressor Control PC. This has been found to work quite well but in the future it is likely that all of the control and acquisition functions will be performed by a single computer.

3.6 Machine operating conditions

Reynolds number

The maximum comfortable Reynolds number for testing without unduly high vibration levels was $Re_c = 170000$, where Re_c is based on rotor mid-blade velocity and chord. At a flow coefficient of 0.7 this corresponds to a stator blade Reynolds number based on inlet velocity Re_1 ($= Re_c\phi/\cos\alpha_3$) of 169000 where α_3 is the stator row inlet air angle. Re_1 rises to 182000 at a flow coefficient of 0.84. These values are somewhat lower than commonly used in more modern research compressors. Halstead et al. [46] used a stage average Reynolds number (based on inlet velocity and suction surface length) of the order of 3×10^5 and suggested that this value should be exceeded to give conditions representative of engine operating conditions.

Hourmouziadis [59] plots the Reynolds number distribution for a typical medium sized by-pass engine at cruise altitude. In the LP (low pressure) compressor Reynolds numbers are in the range 0.7–1 $\times 10^6$, rising to over 1×10^6 in the HP (high pressure) compressor. Through the HP and LP turbines Reynolds numbers are lower due to higher temperatures. A minimum Reynolds number in the LP turbine of around

1×10^5 is shown. Similar numbers are quoted by Mayle [80]. Engine Reynolds numbers fall with decreasing engine size and increasing altitude. Hourmouziadis describes the dramatic rise in loss levels associated with complete laminar separation when the Reynolds number has fallen too far, but points out that the design requirement for minimum weight demands small aerofoils and hence low Reynolds number.

Lieblein [74] has plotted loss coefficient against Reynolds number for a number of two-dimensional-cascade blade sections. Lieblein observes that there is no single value of limiting Reynolds number for all blade shapes but suggests a typical value of around 2.5×10^5. Lieblein defines the limiting Reynolds number as the value below which losses increase rapidly. Lieblein also shows that the limiting Reynolds number for a given cascade decreases as the freestream turbulence level is increased. Roberts [101] uses the term critical Reynolds number to describe the point below which losses increase and notes that its value depends on the cascade geometry, freestream turbulence level, Mach number and temperature.

Blight and Howard [11] and Crooks and Howard [17] tested six L–series cascades which were designed by the Lighthill method and compared them with a C4 cascade, designated S1, which is identical to the mid-blade section of the research compressor rotor and stator (at the design settings). The C4 cascade was found to have a critical Reynolds number around 1×10^5, below that of the L3 and L6 sections which had values of 2.5×10^5 and 2×10^5. These workers also found a reduction in critical Reynolds number to 1.5×10^5 for the L3 cascade when the turbulence level was increased. These 'Lighthill' sections were designed to have a region of constant velocity over the front part of the suction surface to promote laminar flow and then a linear decrease in velocity to the trailing edge. The L3 was designed for constant velocity over 50% of the surface and the L6 for 28%. These profiles were successful in reducing losses over a small range of incidence values but the stronger adverse pressure gradient over the rest of the blade caused poor behaviour off design and the observed increase in the critical Reynolds number. Results of Rhoden [100] presented by Cumpsty [18] for another C4 cascade suggest a critical Reynolds number in the $1–2 \times 10^5$ range.

In general, profiles such as the C4 where the suction surface velocity peak is close to the leading edge can be expected to have lower critical Reynolds numbers than blades which allow less surface length for the deceleration. This is because the suction surface boundary layer is better able to resist separation at low Reynolds numbers due to the more gentle adverse pressure gradient.

The maximum Reynolds number obtainable in our facility is below that commonly considered to be critical for many possible blade surface velocity distributions. It is however in the supercritical range quoted in the literature for a C4 section especially considering the higher turbulence levels in our machine compared to those commonly used in cascade testing. Laminar separation without re-attachment was not observed on the present blades over the range of conditions tested. In any case, low Reynolds number behaviour is important for low pressure turbines, high altitude operation and smaller engines, and should not necessarily be considered uninteresting.

It will be shown later that results from our machine are similar in character to those observed at higher Reynolds number by Halstead et al. [46]. The low Reynolds number in our facility is beneficial in providing thicker boundary layers which facilitate detailed surveys. The other useful consequence of low Reynolds number is that the length of the transition region, which was the main focus of the current study, is maximised.

Flow coefficient

The stalling flow coefficient has been slightly increased over that observed in previous work on this machine due to the increase in rotor incidence. A measured (see Chapter 4) decrease in stator incidence as the flow coefficient was decreased from 0.6 to 0.55 indicates the onset of stall below $\phi = 0.6$. (Oliver [94] observed stall onset at $\phi = 0.55$ for the machine in standard configuration). The increased rotor incidence is promoting rotor blade stall and hub wall boundary layer separation at a higher flow coefficient.

In developing a flow coefficient control algorithm some difficulty was encountered due to a low frequency variation in flow coefficient with a period of the order of 30 seconds. A short series of measurements of the inlet dynamic pressure was undertaken to quantify this effect. For these measurements the frequency response of the pressure transducing system was determined by measuring the transducer step response and found to be 0.4 sec. A reasonable sampling time for the phenomena of interest was considered to be 10 minutes and so a sampling frequency of 6 Hz was used to limit the amount of data acquired. The sampling frequency was well above the approximate Nyquist frequency of 0.8 Hz although a 3 Hz low pass filter was used to eliminate any electrical noise.

Fig. 3.5 shows a section of a typical record of inlet dynamic pressure and the autocorrelation of the signal. This data was taken at $Re_c = 120000$ and $\phi = 0.7$. The standard deviation of the signal in this case was 1.4 Pa. The pressure scale is exaggerated and in fact 95% of the measured values lie within $\pm 1.6\%$ of the mean value. This corresponds to a variation in inlet velocity of $\pm 0.8\%$ or a flow coefficient of $\phi = 0.700 \pm 0.006$.

Peaks in the autocorrelation at 30, 60 and 90 sec indicate periodicity in the signal. A spectral analysis (not shown) confirmed the presence of a power peak at 0.035 Hz (28.6 sec). It is thought that this periodicity may be caused by either large scale eddies in the return air or a Helmholtz style resonance in the room or the diffuser. All subsequent pressure readings were averaged over periods of between 60 and 180 seconds to minimise any bias from this source.

Deviations from two-dimensional flow

Walker [133] studied the deviation from two-dimensional flow in the compressor at the mid-blade height by comparing the measured boundary layer momentum thickness with values calculated using the two-dimensional momentum integral equation and the measured blade surface pressure distribution. At 500 rpm the deviations were below 5% over 80% of the suction surface for incidence values below 2.9°. At high positive incidence the hub wall boundary layer grows and eventually separates causing deviations from two-dimensional flow as high as 15% at an incidence of 4.7°. Comparison of the measured blade surface velocity distributions with a two-dimensional calculation in Chapter 5 confirms the near two-dimensionality of the flow.

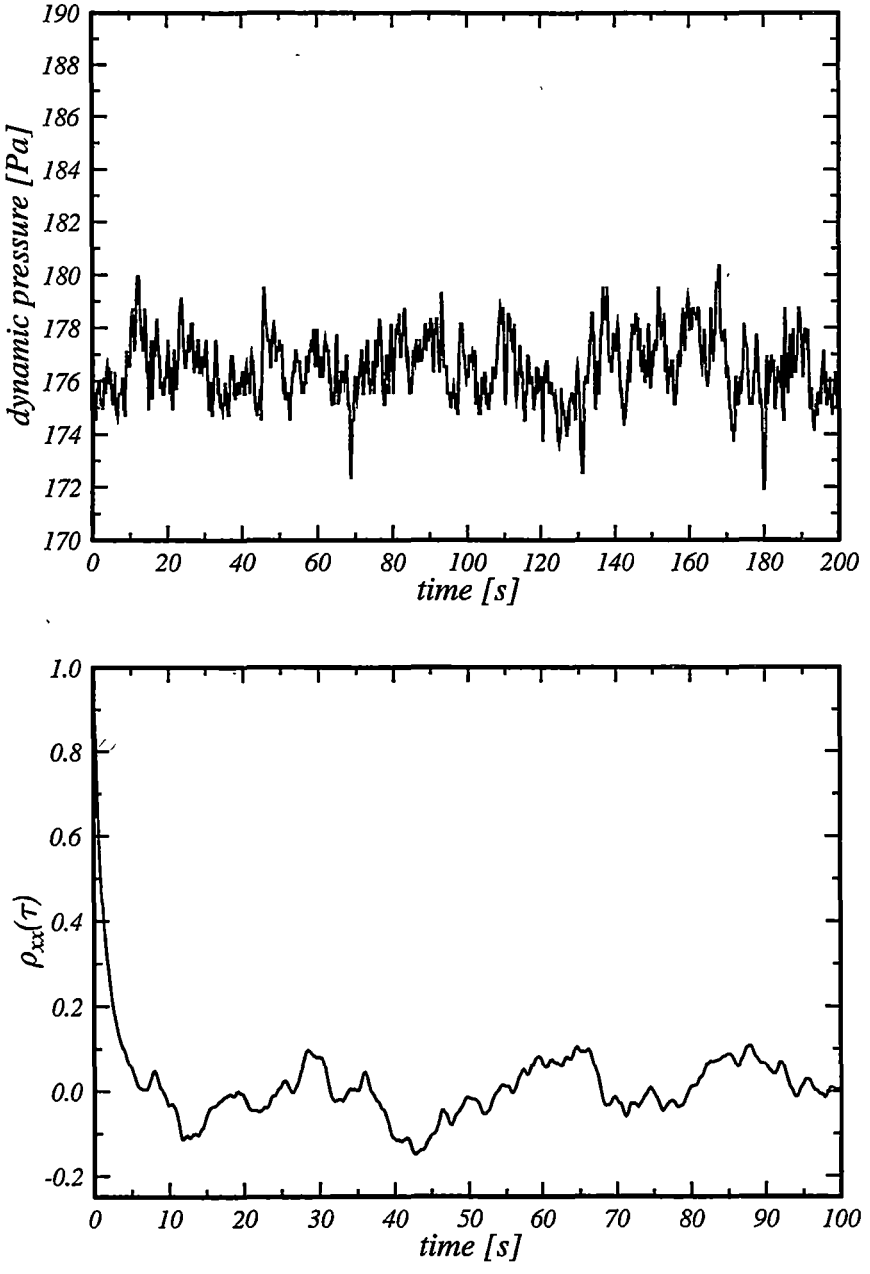

Figure 3.5: Variation of inlet dynamic pressure with time: raw signal $[Pa]$ and auto-correlation $\rho_{xx}(\tau)$.

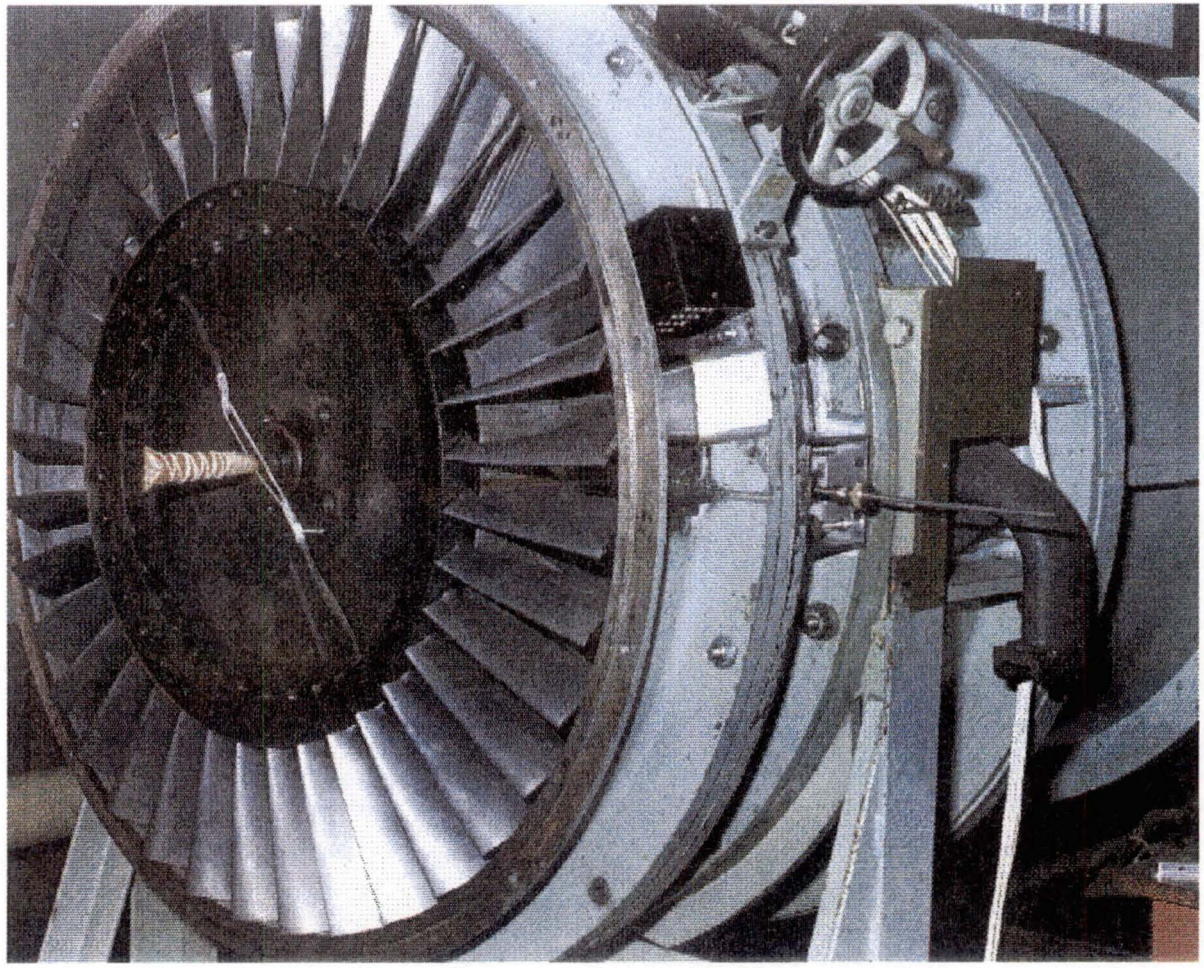

Figure 3.6: View of tunnel, open at rotor

Chapter 4

Summary of experimental investigation

4.1 Introduction

The current experimental investigation concentrates on the stator blade boundary layer flow at mid blade height. The stator row has two blade rows upstream and is influenced by the relative position of the IGV wake street as well as by the passing wakes from the rotor. The stator flowfield has all the important characteristics of the flowfield experienced by an embedded stage in a multi-stage machine. As mentioned in the previous chapter the axial spacing of the blade rows in this test rig is larger than would be expected in a typical machine where overall length is minimised for weight and vibration reasons. Consequently wakes experienced by our stator row are more diffuse than those which may be found in practice. Large axial spacing has also minimised the interaction of the rotor potential flow field with the two stationary rows.

This chapter summarises the testing which has been done during the project. Most measurements were made on the stator blade surface. A series of measurements were also made at a plane midway between the rotor and stator rows to investigate the disturbance field experienced by the stator row. At this upstream position measurements of total pressure, dynamic pressure and flow angle have been made using a 3 hole probe. The total pressure measurements from the 3 hole probe are compared with Kiel probe measurements. A single hot-wire was used to measure the steady and unsteady velocity and turbulence field.

Available facilities precluded measurements in the rotating reference frame. However, the work of Halstead et al. [46] indicates the boundary layer behaviour on rotors and stators in multi-stage machines to be essentially similar. This is supported by earlier surface flow visualisation studies of Walker [132] in the present facility.

4.2 Summary of test cases

The test points for the current work have been defined in terms of a Reynolds number Re_c and a flow coefficient ϕ. Before the start of any testing an automatic control routine was run to adjust the throttle so that a 60 sec average of ϕ fell within ± 0.005 of the required flow-coefficient. The throttle was not subsequently adjusted during

testing. The compressor was run at constant Reynolds number, with Re_c preferred as the reference over the more conventional Re_1 during the early part of the current work while the exact flow-angles were still unknown. Running at constant Re_c is also closer to the constant speed case. Note that at constant Re_c the stator row inlet Reynolds number Re_1 changes with varying inlet flow angle (and hence varies with ϕ – see Table 4.2). In previous work this machine has been run at constant speed Ω and constant throttle. Assuming standard atmospheric conditions (101.325 kPa and 288.15 °C) an approximate conversion between Re_c and Ω is given by

$$Re_c = \frac{U_{mb}c}{\nu} = \frac{\Omega D c}{2\nu} = \Omega \times 2385 \text{ where } \Omega \text{ is rotor speed in rad/s} \qquad (4.1)$$

The throttle position for each flow coefficient varies slightly with speed (some typical values are given in Table 4.1.)

Table 4.1 summarises most of the experimental work undertaken. In selected cases a series of measurements were made at the same Re_c and ϕ set point for a range of different relative circumferential positions of the stationary rows or of the probe and the IGV row. By traversing the IGV row relative to the probe a circumferential traverse of the inlet flow field seen by the stator was obtained. By changing the relative position of the stationary blade rows the effect of the IGV wake position relative to the stator blade was investigated.

4.3 Three hole probe measurements

A three hole probe with the plane of angle measurement perpendicular to the probe shaft was inserted radially into the machine with the sensing holes at mid blade height. The commercially available probe (United Sensor 2-dimensional cobra probe type CA120, 1/8 inch diameter sensing head) consisted of three tubes each with outside diameter 0.75 mm joined together side-by-side and set in-line. The ends of the two outside tubes were ground at 45° to form the probe.

The position of the three hole probe in the machine as defined in Fig. 3.3 is given by the following parameters

$a = 37.9$ mm (in ref. position, blade roots axially aligned)
$b = 41.0$ mm
$d = 88.5$ mm
$w = 5.6$ mm (in ref. position, blade roots axially aligned)

The probe was inserted $0.54c$ upstream of the stator leading edge.

The effect of any radial variation of stream tube height has been neglected but is expected to be small at the mid-blade position. A circumferential traverse of the flow field at the probe position was made by indexing the IGV row over a range of w/S values. For these measurements the three hole probe and stator row were fixed relative to each other and the machine casing to give a constant value of $a + w$ throughout the traverse. This means that these measurements do not reflect variations of the stator potential flow field across the passage, only effects from the upstream rows.

The pressure transducing system and its accuracy is discussed in Appendix D. A time constant of $\tau = 1.0$ sec for the pressure transducer was found by directly measuring

Table 4.1: Summary of experimental testing

Re_c $\times 10^{-3}$	Flow coefficient ϕ Throttle position ["] (approx.) 0.840 13.0	0.790 10.3	0.750 8.2	0.730 7.7	0.700 7.0	0.675 6.4	0.60 5.1	0.550 4.8
36	BP, K		BP, K			BP, K	BP, K	BP, K
50					BP, BL60	BP, BL60		
60	BP, K, 3H		BP, K			BP, K, HF, 3H, HWUS	BP, K, 3H	BP, K
90		BP, K, BL60	BP, K, BL60	BP, BL60	BP, BL60, HF		BP, BL60	
120	BP, K, HF, 3H, HWUS, ST, HWDS		BP, K, 3H		3H	BP, K, HF, 3H, HWUS, ST, HWDS	BP, K, HF, 3H, HWUS, ST, HWDS	K, 3H
130					BP, BL60, 3H			
170	BP, K, 3H		BP, K, 3H		3H	BP, K, HF, 3H, HWUS	BP, K,3H	3H

BP	Stator blade surface pressure tappings (Chapter 5)
BL60	Boundary layer traverse at 60% chord on stator suction surface (Chapter 9)
HF	Stator blade surface hot-film survey (Chapter 8)
HWUS	Single hot-wire probe measurements midway between rotor and stator (Chapter 6)
HWDS	Single hot-wire probe measurements close downstream of the stator (Chapter 6)
K	Kiel probe measurements midway between rotor and stator (Chapter 4)
ST	Stethoscope investigation of transition locations on stator (Chapter 9)
3H	3 hole probe measurements midway between rotor and stator (Chapter 4)

the step response. Ports were stepped using the Scanivalve and an exponential curve was fitted to the resulting pressure trace. This gives a 99.9% settling time of 7.2 sec for the complete system including connecting tubes. An actual settling time of 10 sec was allowed for each port. Pressure readings for each port were taken at 6 Hz and averaged over 30 sec.

Calibration of 3 hole probe

A closed circuit wind tunnel with an octagonal working section of 615 mm width was used to calibrate the three hole probe. Alignment of the probe head with the probe reference bar was checked by inserting the probe from either side of the tunnel in turn. (This was necessary since the exact angle of air at the probe location in the working section was initially unknown.) A protractor with a vernier scale was used to position the probe and a small spirit level used as a reference. For this probe the deviation between the probe axis (where the side tapping pressures were equal) and the reference bar was found to be $90.0 \pm 0.2°$.

A pitot-static tube was placed in the tunnel with its static holes at the same axial position as the three hole probe and used as a reference. The three hole probe pressure tappings were numbered 1 through 3 with 1 at the centre.

By considering the potential flow around a cylinder as an ideal case the following three functions, f_1, f_2, f_3, can be shown to depend only on the flow angle α relative to the probe head and the probe geometry. In a real fluid there may also be a Reynolds number effect caused by changes in the viscous flow behaviour.

$$f_1(\alpha, \text{geometry}, Re) = \frac{p_2 - p_3}{p_1 - p_3} \tag{4.2}$$

$$f_2(\alpha, \text{geometry}, Re) = \frac{p_1 - p_3}{\frac{1}{2}\rho U^2} \tag{4.3}$$

$$f_3(\alpha, \text{geometry}, Re) = \frac{P - p_1}{\frac{1}{2}\rho U^2} \tag{4.4}$$

P is the total pressure at the probe and U is the velocity at the probe. If only one probe is used the geometry unknown is eliminated and the form of f_1, f_2 and f_3 may be found at a given Reynolds number by measuring over a range of flow angles.

A typical calibration result is shown in Fig. 4.1. Curve fits were made with data for all velocities lumped together as no significant Reynolds number effect was detected over the velocity range tested (10 to 28 m/s). Evidently the sharp edges of this particular probe prevent the separation location from changing. Fourth order polynomials were fitted to the f_2 and f_3 data and an expression of the following form was fitted to f_1:

$$f_1 = c_1 \tan\left(\frac{c_2}{\alpha + 90°} + c_3\right) + c_4 \tag{4.5}$$

The scatter in the f_3 data suggests an uncertainty of the order of 0.5% which is close to the uncertainty expected from consideration of the pressure instrumentation accuracy and measured standard deviations of individual pressure signals (see Appendix D).

In the compressor all probe pressures were measured relative to the inlet static pressure p_{in}. With the probe in an unknown flow $p_2 - p_3$, $p_1 - p_3$ and $p_1 - p_{in}$ were

Table 4.2: Circumferential mean stator incidence angle $i°$ and Reynolds number Re_1 at mid-blade height from three hole probe

		ϕ					
Re_c		0.550	0.600	0.675	0.700	0.750	0.840
60000	$i°$		2.97	0.23			-7.64
	Re_1		54000	58000			63000
120000	$i°$	3.85	4.11	1.24	0.01	-2.31	-6.11
	Re_1	100000	110000	117000	119000	122000	130000
130000	$i°$				-0.36		
	Re_1				128000		
170000	$i°$	3.98	4.30	1.41	0.35	-2.17	-6.54
	Re_1	143000	156000	166000	169000	174000	182000

determined. The flow angle α was found from the f_1 calibration function. A dynamic pressure coefficient, Cp_{dyn} was found from the f_2 probe calibration function.

$$Cp_{dyn} = \frac{(p_1 - p_3)}{f_2(\alpha)(P_{in} - p_{in})} \tag{4.6}$$

$$= \left(\frac{U}{V_a}\right)^2 \tag{4.7}$$

A total head coefficient was also found using the f_3 curve.

$$Cp_{tot} = \frac{f_3(\alpha)\frac{1}{2}\rho U^2 + (p_1 - p_{in})}{P_{in} - p_{in}} \tag{4.8}$$

$$= \frac{P - p_{in}}{\frac{1}{2}\rho V_a^2} \tag{4.9}$$

Measured flow angles

Flow angles were measured at each test point for 31 different IGV positions covering one whole blade pitch. w/S ranged from 0.08 to -0.93 for the three hole measurements. It was necessary to assume periodicity for the purposes of comparison with the Kiel probe and hot wire measurements because the probe mounts used did not allow measurements over exactly the same circumferential span with all probes. The origin for circumferential position corresponds to a probe location at the same circumferential position as the IGV trailing edge ($w = 0$.)

Axial and radial velocity component measurements from the three hole probe were each mass averaged across the traverse. The average flow angle and average flow velocity was thus obtained. Average flow angles and the resulting Re_1 values for each test case are given in Table 4.2. These results have been found to agree reasonably with the results of Walker [132] after allowance has been made for the change in rotor stagger. Linear interpolation from Walker's results gives $i \simeq 2.9°$ at $\phi = 0.6$ and $Re_c = 120000$. Using Howell's off-design correlation the change in i due to the change in rotor stagger was 0.85°. Hence the incidence angle predicted is 3.75° compared with the actual measured value of 4.11°.

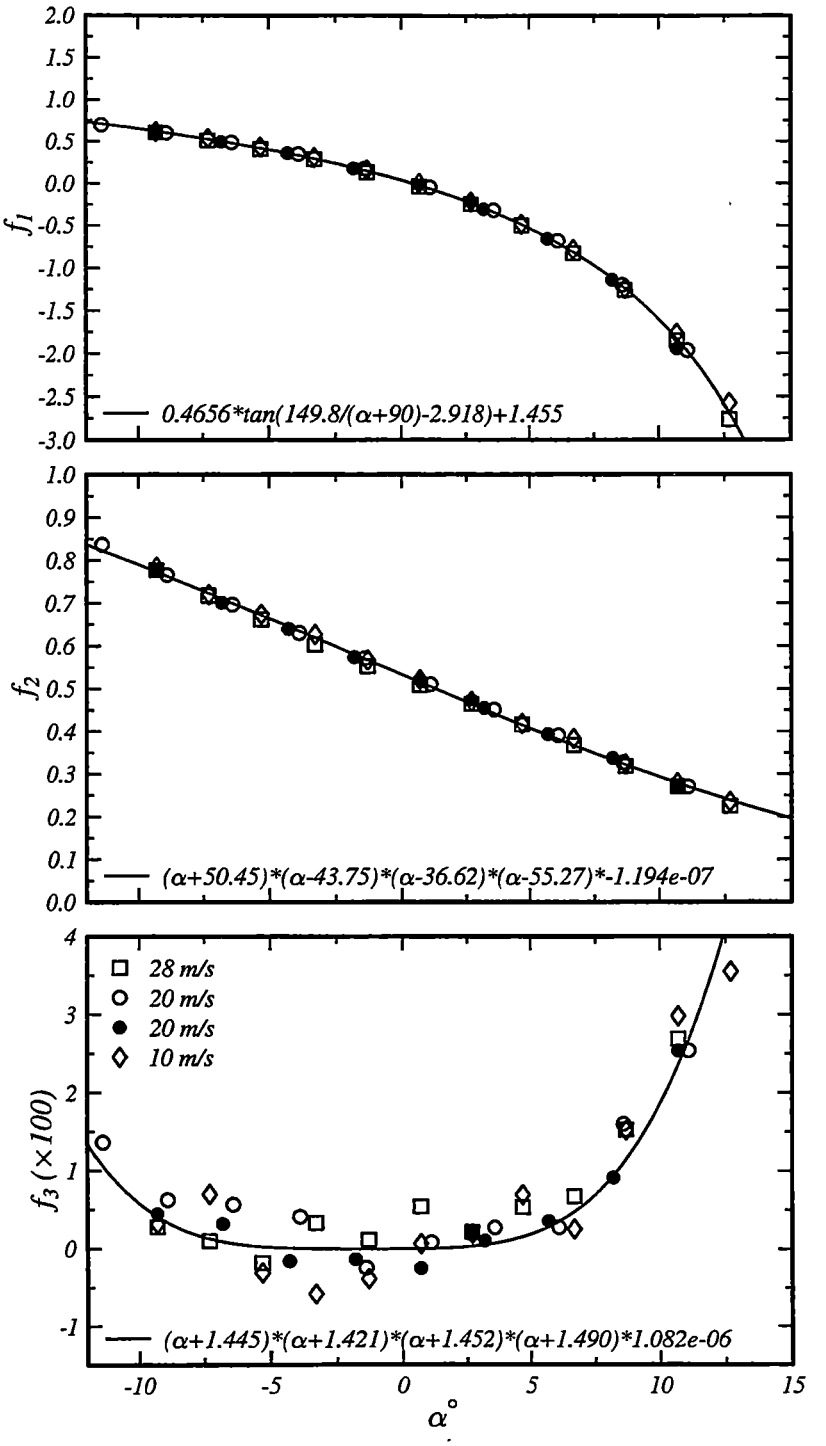

Figure 4.1: Three hole probe calibration results

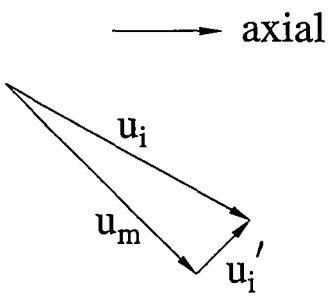

Figure 4.2: Definition of the local time-mean velocity defect vector

Circumferential variation of flow angle over one blade pitch

A measurable variation in flow angle in the circumferential direction has been observed at a position 0.54c upstream (axial direction) of the stator leading edge (Fig. 4.3). Ignoring the circumferential variation of the the stator potential flow field (which is not included in these measurements because the probe was always in the same position relative to the stator), no circumferential flow variation would be expected in the stationary frame of reference if the inlet guide vanes were not present. In that case the rotor wakes would be averaged out by the pressure transducing system. Part of the observed variation is caused by the mixing out of the inlet guide vane wake street itself which is still detectable downstream of the rotor although in a somewhat altered form. The dispersion of the IGV wakes is significantly affected by the rotor as described by Lockhart and Walker [76]. Part of the observed circumferential periodicity may also be due to the fact that the rotor is passing through flow periodically disturbed by the IGV wake street. As a rotor blade passes through regions of different turbulence level, flow angle and velocity, the amount of turning done by the rotor will vary periodically. This in turn will register as a circumferential variation in flow observed in the stationary reference frame downstream of the rotor.

Observed variations of flow angle across the passage are typically larger than 0.5°. Errors in these measurements may be around 0.4% (uncertainty in f_1) or 0.05° (uncertainty in α) with a (constant) reference angle uncertainty of $\pm 0.2°$. The magnitude of the observed variations exceeds the measurement uncertainty. The cause of this variation will be examined further in the Chapter 6.

Total and dynamic pressure measurements

Total and dynamic pressure coefficients were also obtained from the three hole probe. These results are shown in later sections in comparison with Kiel probe and hot-wire measurements.

Defect velocity vector from three hole measurements

The three hole probe results give the magnitude (relative to V_a) and direction of the time mean velocity at each circumferential position in the measurement plane. This

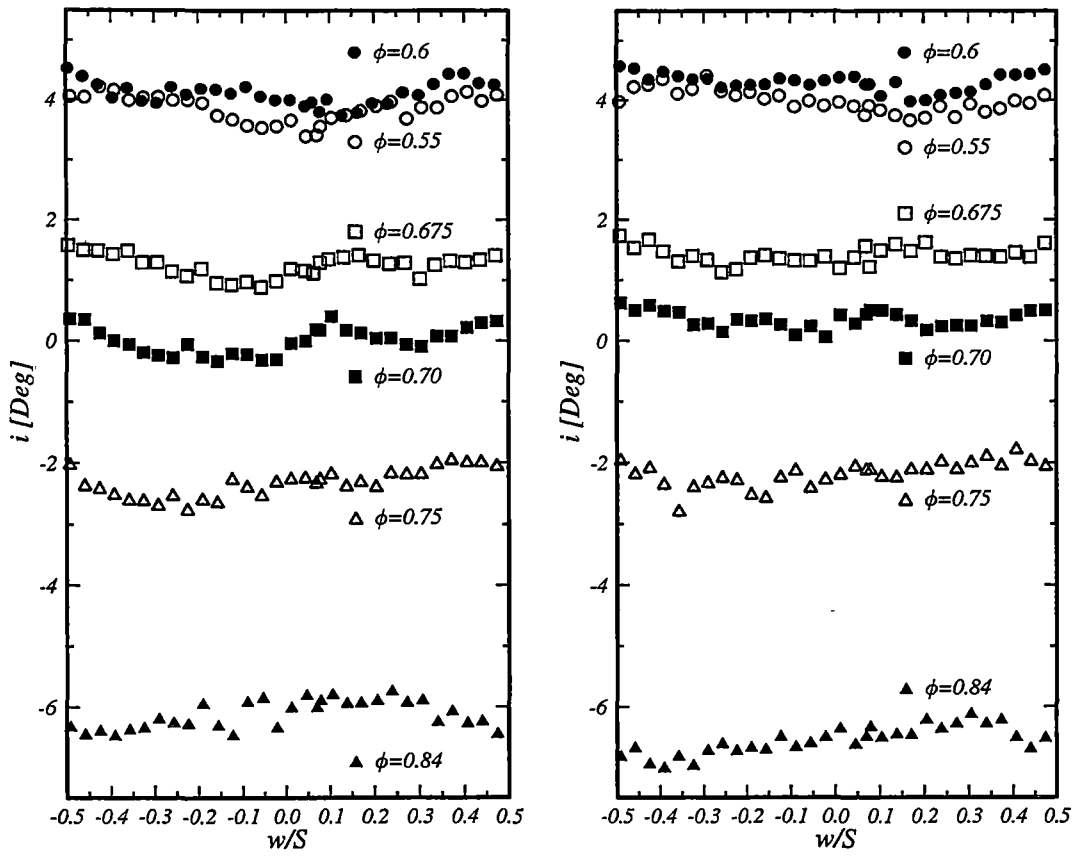

(a) $Re_c = 120000$ (b) $Re_c = 170000$

Figure 4.3: Variation of stator blade incidence ($i°$) with IGV position over a range of flow coefficients and Reynolds numbers. $i°$ measured $0.54c$ upstream of stator leading edge. $(a + w)/S = 0.575$

data can be represented in vector form as $\overrightarrow{u_i}$. A mass-averaged vector mean relative velocity across the passage $\overrightarrow{u_m}$ can also be determined.

A defect velocity vector $\overrightarrow{u_i}'$ can now be calculated from the three hole probe results.

$$\overrightarrow{u_i}' = \overrightarrow{u_i} - \overrightarrow{u_m} \tag{4.10}$$

Ho and Lakshminarayana [51] presented computational results in a similar manner by defining a fluctuating velocity vector. Note that $\overrightarrow{u_i}'$ is the difference between the time mean velocity at the local circumferential position and the passage mean velocity vector, whereas Ho and Lakshminarayana calculated the difference between the local instantaneous velocity and the time mean. Fig. 4.2 shows the definition of $\overrightarrow{u_i}'$.

4.4 Kiel probe measurements

Prior to the three hole probe measurements a Kiel probe had been used to find the total pressure upstream of the stator row for calculation of blade surface velocity from

the measured surface pressure distributions. A United Sensor type KBC Kiel probe with a 1/8 inch diameter sensing head was used. The probe was placed in a similar position to the three hole probe and the same pressure transducing system was used. Again, only the IGV row was clocked during the traverse.

$a = 37.7$ mm (in ref. position, blade roots axially aligned)
$b = 38.0$ mm
$d = 87.0$ mm
$w = 6.2$ mm (in ref. position, blade roots axially aligned)

This corresponds to a position $0.50c$ upstream of the stator leading edge. For comparison purposes this will be assumed to be the same as the axial position of the three hole probe.

A total pressure coefficient is defined as per the three hole probe results. Fig. 4.4 compares Cp_{tot} measured by the Kiel probe with results from the three hole probe. Typical uncertainty levels in Cp_{tot} (as defined in Appendix D) were 0.25% for the Kiel probe and 0.5% for the 3 hole probe. The 3 hole and Kiel probe results are generally in very good agreement except at a few circumferential positions where odd 3 hole results show larger than average scatter.

4.5 Hot-wire measurements upstream of stator

A single hot-wire was placed in the rotor–stator gap at a similar axial position to the Kiel and three hole probes. The probe was a DISA type 55P01 straight general-purpose type with gold-plated ends. The Pt-plated tungsten wire has a 5 μm diameter and 1.25 mm sensitive length. Overall wire length including the gold plating is 3 mm. The probe was mounted on a 215 mm straight support which was inserted through a stator row passage at mid blade height and approximately aligned with the mean flow direction. The wire itself was aligned in the radial direction and hence was not sensitive to flows in that direction.

A comprehensive investigation of the turbulence properties would require measurement of the fluctuations in the radial direction as well as in the circumferential and axial directions. The single wire has however proven useful in estimating overall turbulence levels and in gaining insight into the unsteady IGV-rotor blade wake interaction, as will be discussed in Chapter 6.

Details of the hot-wire calibration and data processing procedure are given in Appendix C. Approximate corrections to the temperature and pressure values at the wire were made to account for the rise of these values through the rotor (actual measurements of temperature and pressure were only made at inlet.) The circumferential span of the hot-wire probe measurements was different from that of the other two probes because a different mounting scheme was used. Comparison can still be made by assuming circumferential periodicity.

$a = 37.8$ mm (in ref. position, blade roots axially aligned)
$b = 45.$ mm
$d = 88.5$ mm
$w = -37.8$ mm (in ref. position, blade roots axially aligned)

Again, the slight shift in axial position (now at $0.59c$ upstream of the stator leading edge) has been neglected for the purposes of comparison with the three hole probe results.

Average bridge voltage was recorded from the IFA 100 front panel digital meter. An Analogic DP100 $5\frac{1}{2}$ digit digital multimeter was used to measure the AC voltage output from the anemometer bridge. The AC meter was set to average over 5 seconds. At best only 3 significant figures were considered useful from this meter.

The anemometer output was also sampled by the digital system. Sampling was at a rate of 50 kHz and triggered by the rotor zero marker signal. The signal was filtered at 20 kHz to avoid aliasing and was AC coupled. The IFA signal conditioner was used with a gain of 60–70 to improve the signal to noise ratio. At the lowest compressor speed 2048 samples were taken (to cover at least five blade passages); 1024 consecutive samples were taken at the other speeds. At each of 16 circumferential positions the sampling operation was repeated 512 times to provide sufficient data for ensemble processing. Results of these unsteady measurements are presented and discussed in Chapter 6.

Probe calibration

For this set of hot-wire measurements the probe was first calibrated in a small recirculating wind tunnel and then moved to the compressor. Prior to taking the turbulence measurements the probe was moved to a reference position in the compressor and U_w/V_a was measured for a range of Reynolds numbers at a reference throttle position where U_w is the indicated time-mean hot-wire velocity. This test was repeated after the turbulence measurements were taken and any differences were attributed to drift of the probe calibration coefficients with aging of the wire and dust accumulation. It was assumed that the calibration remained unchanged as the wire was transfered from the calibration tunnel to the compressor.

A small drift was observed (C_1 changed from 0.358 to 0.333). As discussed in Appendix D the drift in this parameter alone would cause errors of 6% if not corrected for. Correction was made by allowing for a linear variation of the correlation parameters over the measurement points.

Unfortunately a comparison of the hot-wire results with the three hole probe results still showed unacceptably large differences (of the order of 10%) even after making the drift correction. The most probable cause of these errors was a change in the probe lead connection resistance which occurred when the probe was moved to the compressor from the calibration tunnel. A check of the wire cold resistance when assembled in the tunnel would have revealed this problem but was not made in this instance.

An increase in the assumed cable resistance from 0.68Ω to 0.75Ω proved sufficient to account for the deviation in results. In effect then the hot-wire results have been calibrated against the three hole probe readings. Since the hot-wire results were primarily intended for turbulence measurement this approach should be acceptable.

Dynamic head coefficient

A dynamic head coefficient $Cp_{dyn} = (U_w/V_a)^2$ has been calculated from the hot-wire results for comparison with the three hole probe results. The hot-wire results have

been shifted to better agree with the three hole measurements by changing the cable resistance assumed in the processing.

Fig. 4.5 compares the dynamic head coefficient as measured by hot-wire with that measured by the three hole probe for a range of flow coefficients at $Re_c = 120000$. Scatter in the hot-wire results is larger than for the three hole probe, but both probes suggest a similar pattern of variation across the passage. Uncertainty in the Cp_{dyn} results from the 3 hole probe (as defined in Appendix D) is typically $\pm 0.5\%$.

Turbulence upstream of stator

Data from the single hot-wire probe has been used to estimate the turbulence levels as defined in the nomenclature. The single wire was not rotated and hence was not capable capable of measuring fluctuations in the radial direction, or distinguishing the direction of the streamwise fluctuations. Despite this, the term total disturbance level has been used below to distinguish it from periodic unsteadiness and freestream turbulence.

The *total disturbance level* Tu_D was obtained from the measured RMS bridge voltage by assuming

$$U' = \frac{dU}{dE} E' \tag{4.11}$$

where E is the bridge voltage and $\frac{dU}{dE}$ is obtained from the calibration curve.

These values are shown in Figures 6.4–6.8. Note that the total disturbance level varies with circumferential position even though these measurements are not synchronised with rotor position. This variation is due to the presence of the IGV wakes themselves and the periodic effect they have on the development of the rotor boundary layers and wakes.

The total disturbance level was also estimated from the ensemble averaged data using Eqn. (0.15) given in the Nomenclature. This was found to be consistently between 5 and 10 percent below the value obtained from the RMS voltmeter. This is probably because the ensemble averaged data was only taken over about 5 blade passages and hence does not include unsteadiness arising from blade to blade variability over the other 32 blades which the RMS meter will see. The RMS voltmeter is also more susceptible to noise in the signal because a gain of 1 was used instead of the 60 or 70 used in the ADC data.

4.6 Hot-wire measurements downstream of stator

A second set of measurements with a single hot-wire was taken at a position close downstream of the stator blade. Measurements were taken at 36 positions across the passage by traversing the IGV and stator rows simultaneously. These measurements were unevenly spaced across the passage to better resolve the stator wake; maximum spacing was 4.9% S and minimum spacing 0.8% S. These measurements were intended to provide information about the unsteady variation of the stator wake thickness and so DC coupling of the hot-wire signal was used. This reduced the possible gain to around 10. The number of traces in each ensemble, the data sampling rate and the low-pass filter cut-off frequencies were as for the upstream turbulence measurements.

The wire was inserted on the same sting as for the upstream measurements at an axial position further downstream. The angle of the wire support to the flow was approximately 10°. There was an axial gap of 1.2 ± 0.2 mm between the wire and the trailing edge of the stator blade. Other relevant dimensions for these measurements are;

$a = 37.8$ mm (all IGV-stator positions, blade roots axially aligned)

$d = 88.5$ mm

$x = 9.96$ mm (in ref. position)

The reference position here corresponds to stator and IGV row circumferential position vernier readings of $6.160''$.

As in the case of the upstream measurements an in-situ calibration approach was used. This time a slightly different reference position was used and care was taken to re-check the cable resistance after moving the wire between the calibration tunnel and the compressor. At the end of the series the wire was re-checked in the calibration tunnel and the calibration coefficients found to be in very good agreement with those predicted by the in-situ calibration procedure.

Results of the upstream and downstream turbulence measurements are presented and discussed in Chapter 6.

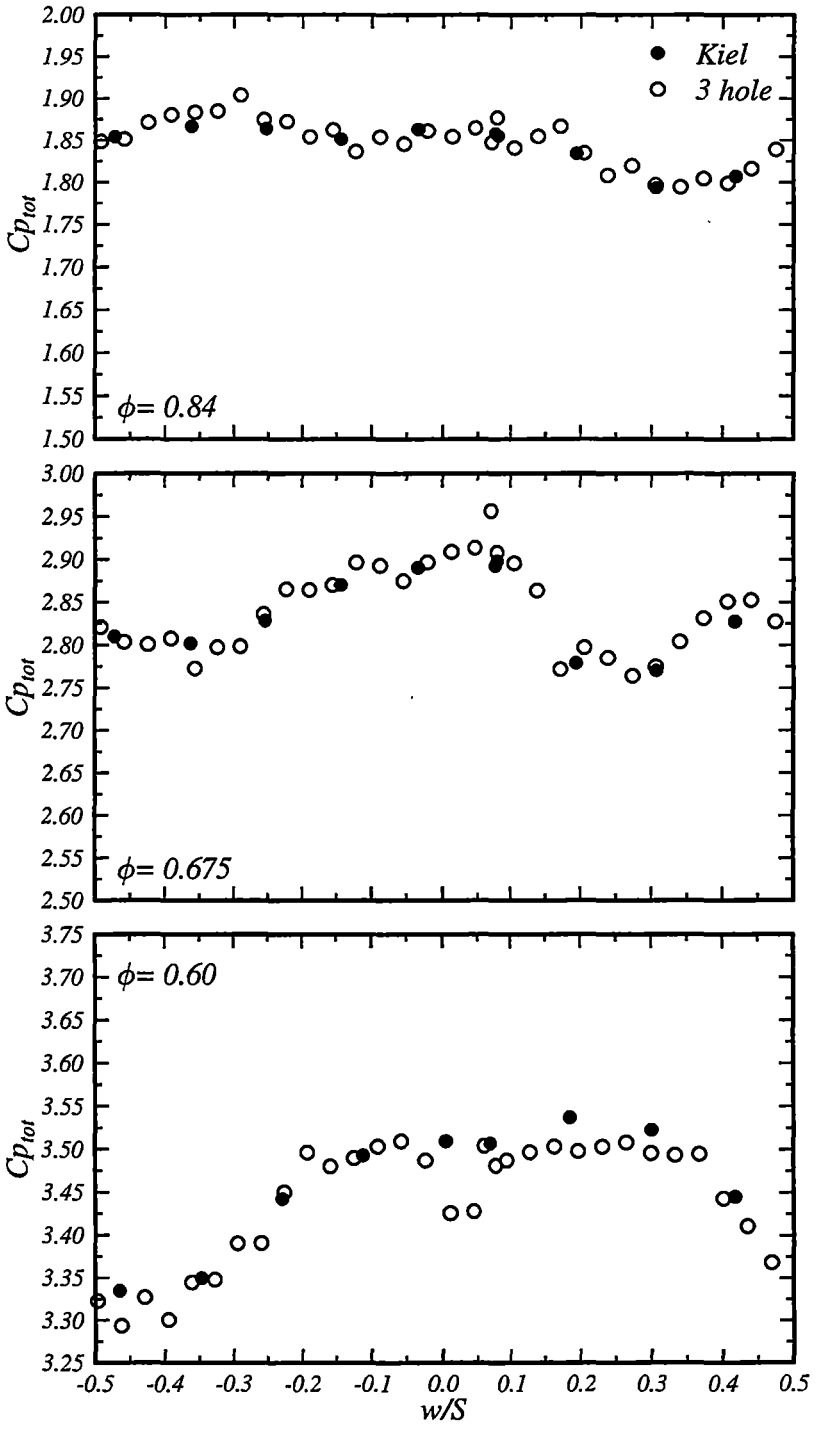

Figure 4.4: Total pressure coefficient Cp_{tot} from Kiel probe at $(a+w)/S = 0.581$ and three hole probe at $(a+w)/S = 0.575$ compared for three different flow coefficients. Axial position relative to stator leading edge was 38.0 mm for Kiel probe and 41.0 mm for the three hole probe. $Re_c = 120000$

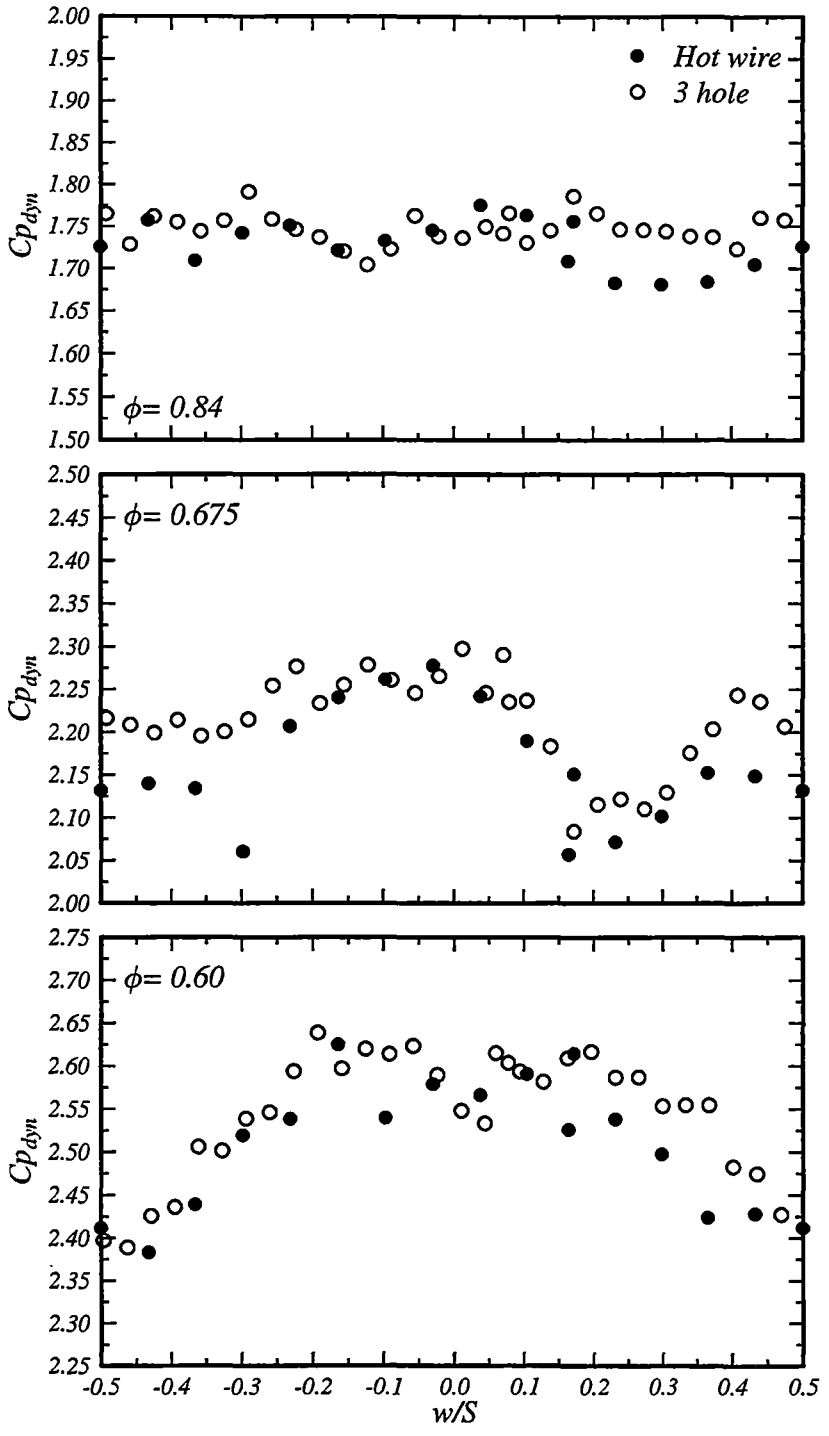

Figure 4.5: Dynamic pressure coefficient Cp_{dyn} from hot-wire and three hole probe compared at three different flow coefficients. Axial position of probe relative to stator leading edge was 45.0 mm for the hot-wire and 41.0 mm for the three hole probe. $Re_c = 120000$

Chapter 5

Stator blade surface pressure distribution survey

5.1 Introduction

Stator blade surface velocity distributions have been calculated from static pressure measurements for the tunnel operating conditions described in Table 4.1. Total pressure on the stagnation streamline was estimated using the 3 hole and Kiel probe results. The effects of Inlet Guide Vane (IGV) wake disturbance on the possible stator blade velocity distribution were investigated by taking measurements over a range of IGV-stator relative blade row circumferential positions. All measurements were confined to mid-blade height.

A simple two dimensional vortex element potential flow calculation method using coupling coefficients of Lewis [73] shows reasonable similarity to the measured results. This calculation was repeated for a profile modified to simulate the surface displacement caused by wrapping the hot-film array of Chapter 8 around the blade.

5.2 Stator blade pressure tappings

Two of the stator blades were drilled with pressure tappings: one on the suction surface, the other on the pressure surface. These blades were arranged so that the measurement surfaces bound the same flow passage. Each blade was drilled at five spanwise stations from hub to tip. For this work only the mid-blade tappings were used (the others were sealed with cellotape).

In the streamwise direction there are 14 tappings each of about 0.5 mm diameter. These start at the leading edge and progress in 5% chord steps up to 40% chord and then in 10% chord steps to 90% chord. Position coordinates and surface distances are reported in Appendix A. Fig. 5.1 shows the pressure tapping distribution on a typical profile.

5.3 Blade pressure coefficient distribution

The pressure transducing system, Scanivalve and data acquisition system are described in Chapter 3. Care was taken to eliminate leaks from the array of pressure tubes. By

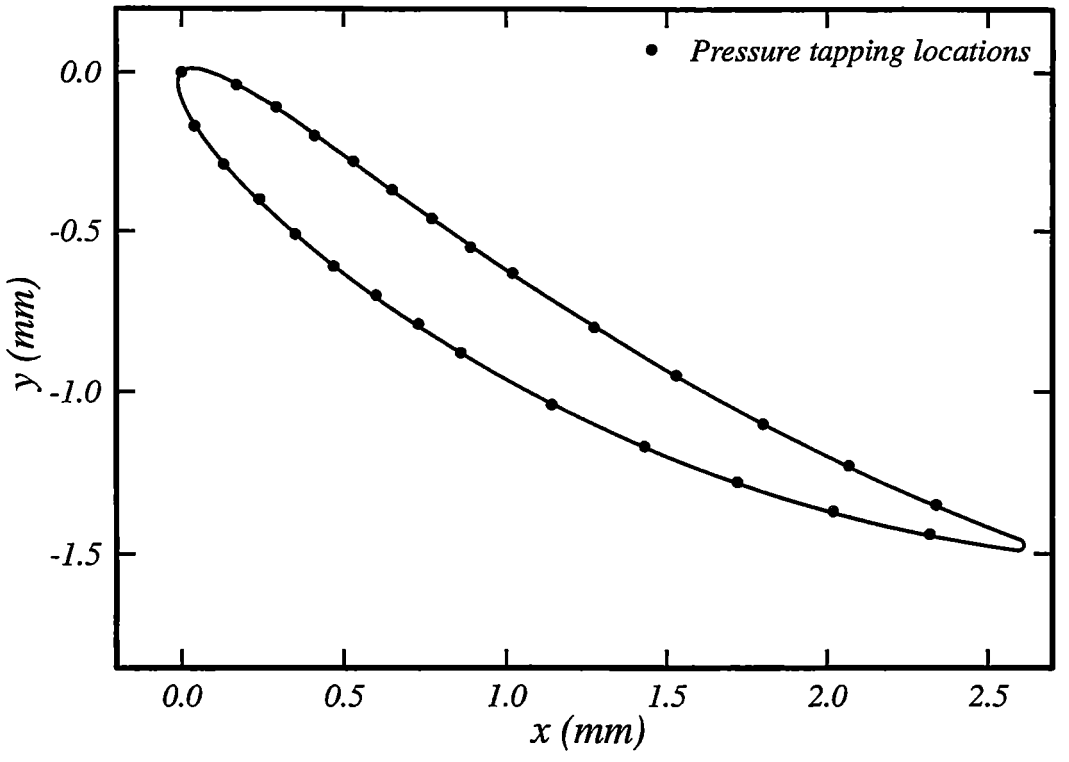

Figure 5.1: Distribution of pressure tappings around the stator blade profile at mid blade height

observing the transducer output as the Scanivalve was stepped between ports with different applied pressures the system time constant was measured and a suitable settling time chosen.

During a sweep the pressure on each port was read 30 times at a rate of 6 Hz and the average and RMS values were recorded. To minimise the effects of the long term (30 second period) fluctuation of inlet pitot pressure 12 sweeps were done and the results averaged. The experimental uncertainty was determined by combining the instrumentation uncertainty with the standard deviation of the set of readings (see Appendix D). For the case $Re_c = 120000$, $\phi = 0.675$ the uncertainty was in the range 0.1-0.2% over the pressure surface and 0.1%-0.4% on the suction surface except at 40% chord where the error was 1.7%. This position shows a large percentage error because the mean differential pressure is close to zero.

The pressure transducer system was initially used with its auto-ranging function enabled. This was found to cause erroneous measurements if a range change occurred during a set of readings. A test was subsequently incorporated into the data acquisition software to detect this condition and repeat the readings if necessary with auto-ranging disabled.

The surface pressures p_i were measured relative to the inlet static pressure p_{in} and

are expressed as pressure coefficients Cp_i relative to the inlet dynamic pressure:

$$Cp_i = \frac{p_i - p_{in}}{P_{in} - p_{in}} \tag{5.1}$$

Note that the subscript *in* here refers to the compressor inlet, not the stator row inlet.

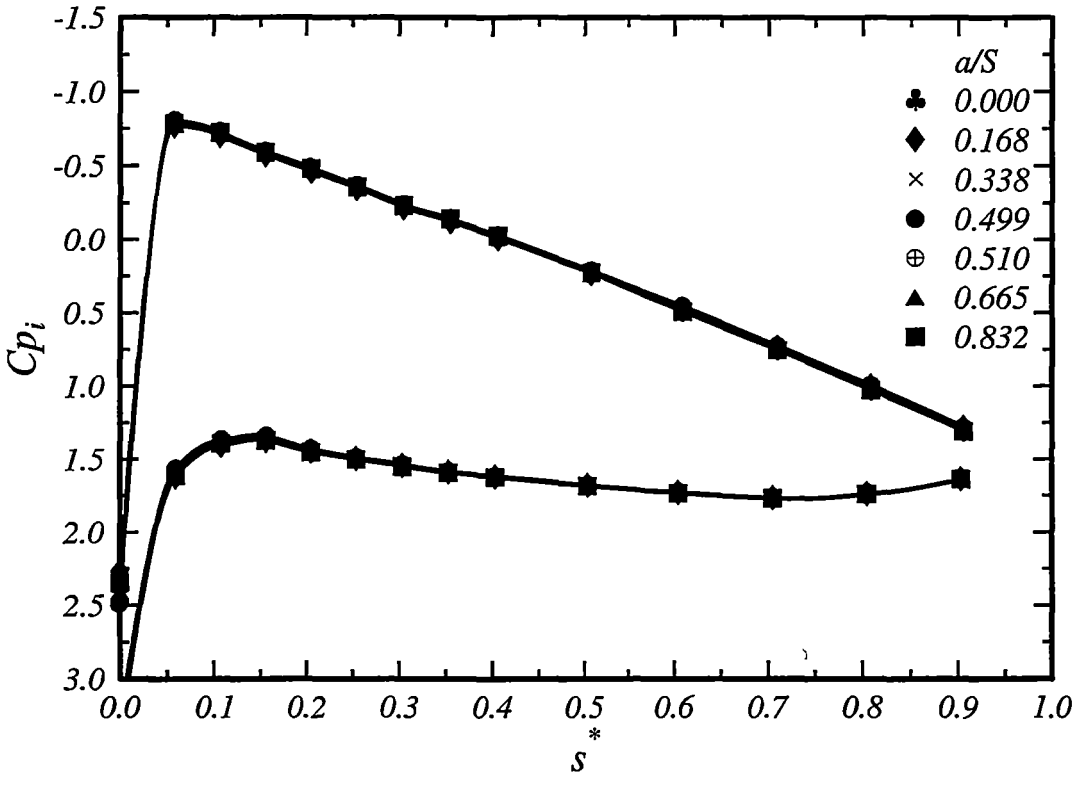

Figure 5.2: Pressure coefficient distribution over the stator blade at mid blade height for a range of relative circumferential IGV positions (a/S). $Re_c = 120000$, $\phi = 0.675$

Fig. 5.2 shows the variation of Cp_i as the IGV row is clocked relative to the stator row. On the suction surface the surface pressure coefficient rises to a maximum around 5% chord and then decreases approximately linearly towards the trailing edge. The pressure surface has accelerating flow from the leading edge to $s^* = 0.15$ then a gentle deceleration through to 70% chord and then a final acceleration towards the trailing edge.

The relative position of the IGV wake (a/S) has a small effect on the stator blade surface pressure distribution. The scale of Fig. 5.2 obscures any trend in the variation which is largest at the leading edge.

Table 5.1: Error ϵ° in stagnation streamline position caused by streamline curvature

	ϕ			
Re_c	0.600	0.675	0.750	0.840
36000		0.0	0.9	
60000		0.1	1.0	
120000		-0.1		
170000	-1.5	-0.7	0.4	1.4

5.4 Surface velocity distribution

Location of stagnation streamline

In order to calculate the blade surface velocity distributions the total pressure on the stagnation streamline P_{st} is required. This was first measured using the Kiel probe and then verified using the 3 hole probe (see Chapter 4). The flow angle is required to locate the stagnation streamline.

A series of calculations with the MISES two-dimensional flow solver of Youngren and Drela [144] were performed to obtain estimates of the amount of curvature of the stagnation streamline between the pressure probe traverse station and the stator leading edge. This code performs fully simultaneous viscous-inviscid interaction over a streamline grid. The position of the stagnation streamline at the Kiel probe insertion position relative to the stator blade leading edge was measured directly from the program output and expressed as an angle α so that

$$\tan\alpha = d/x \tag{5.2}$$

Where d is the circumferential offset of the streamline from the stator leading edge and x is the axial distance from the probe to the blade leading edge.

The angle α may then be calculated from

$$\alpha = \beta_1 + i - \epsilon \tag{5.3}$$

where β_1 is the blade leading edge angle, i is the incidence determined from the pressure probe measurements and ϵ is the error caused by curvature of the streamline. The calculated ϵ values are presented in Table 5.1.

The errors in locating the stagnation streamline directly from the blade row inlet air angle are seen to be below 1.5° for the cases of interest. This would cause an error in a/S at the probe insertion point of 0.013. Peak variation in the total head coefficient across the passage (Fig. 4.4) $\Delta Cp_{tot}/(w/S)$ is approximately 0.8. So the maximum likely error in determining Cp_{tot} using Eqn. (5.3) with $\epsilon = 0.0$ would be 0.01 or 0.3%.

Calculation of surface velocity distribution

Once the correct Cp_{tot} value is known the surface velocity distribution is calculated as

$$\frac{U}{U_{mb}} = \phi\sqrt{Cp_{tot} - Cp_i} \tag{5.4}$$

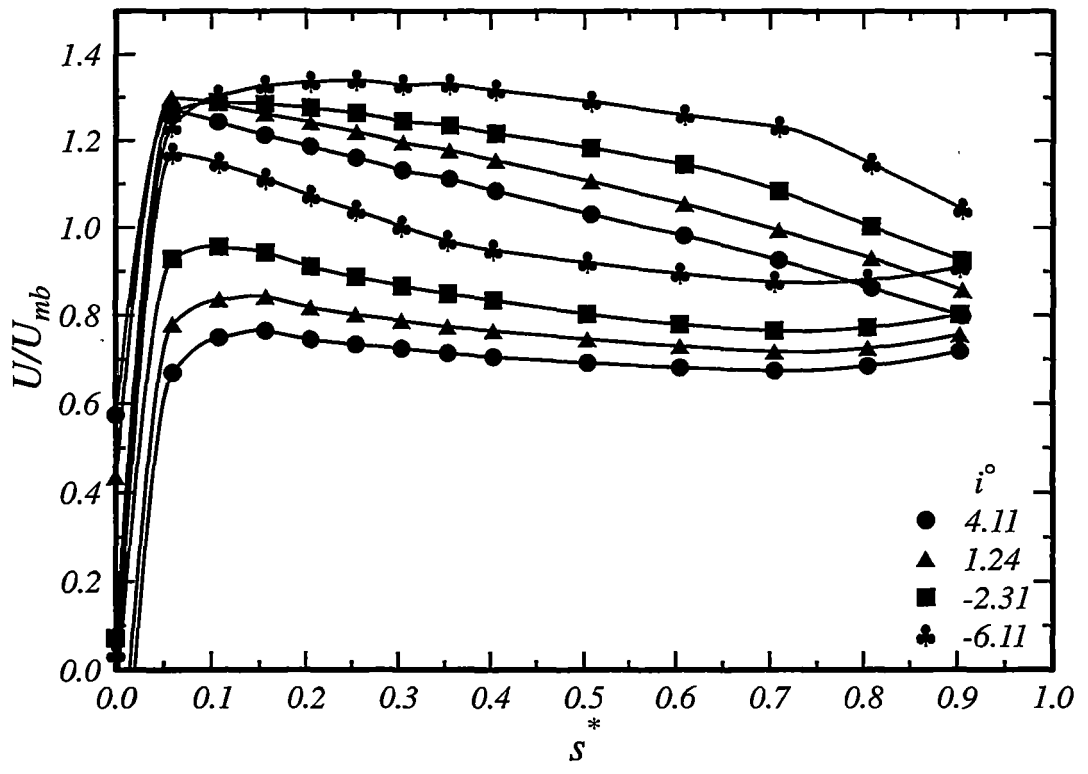

Figure 5.3: Stator blade surface velocity distributions at mid blade height over a range of incidence values for $Re_c = 120000$ (IGV and stator at reference position. $a/S = 0.5$)

Fig. 5.3 shows the effect of incidence on the blade surface velocity distribution at constant Re_c. For the positive incidence cases the suction surface velocity rises to a peak at 5% chord and then linearly decelerates towards the trailing edge. As the incidence is reduced the amount of deceleration on the suction surface reduces and at $i = -2.3°$ the velocity distribution has become convex. The change of slope between 60 and 70% chord indicates a laminar separation bubble here. The separation is more distinct in the $i = -6.1°$ case. On the pressure surface the velocity rises to a peak and then relaxes towards around 70% chord followed by a short acceleration towards the trailing edge. The pressure surface velocity peak becomes sharper and closer to the leading edge as the incidence reduces.

Fig. 5.4 shows the velocity distributions for a range of Reynolds numbers at constant flow coefficient; variation between the traces is partly due to slight changes of incidence that the changes of Reynolds number cause. The two higher Reynolds number velocity distributions are very similar (the $Re_c = 120000$ data is the same as the $i = 1.24°$ case of Fig. 5.3). At $Re_c = 60000$ the peak and slope of the suction surface velocity distribution are reduced and the curve shows a change in slope around 65% chord; a reduction in blade circulation is also evident. These effects indicate that the Reynolds number has fallen to (or slightly below) the critical value where separation bubble phenomena become apparent.

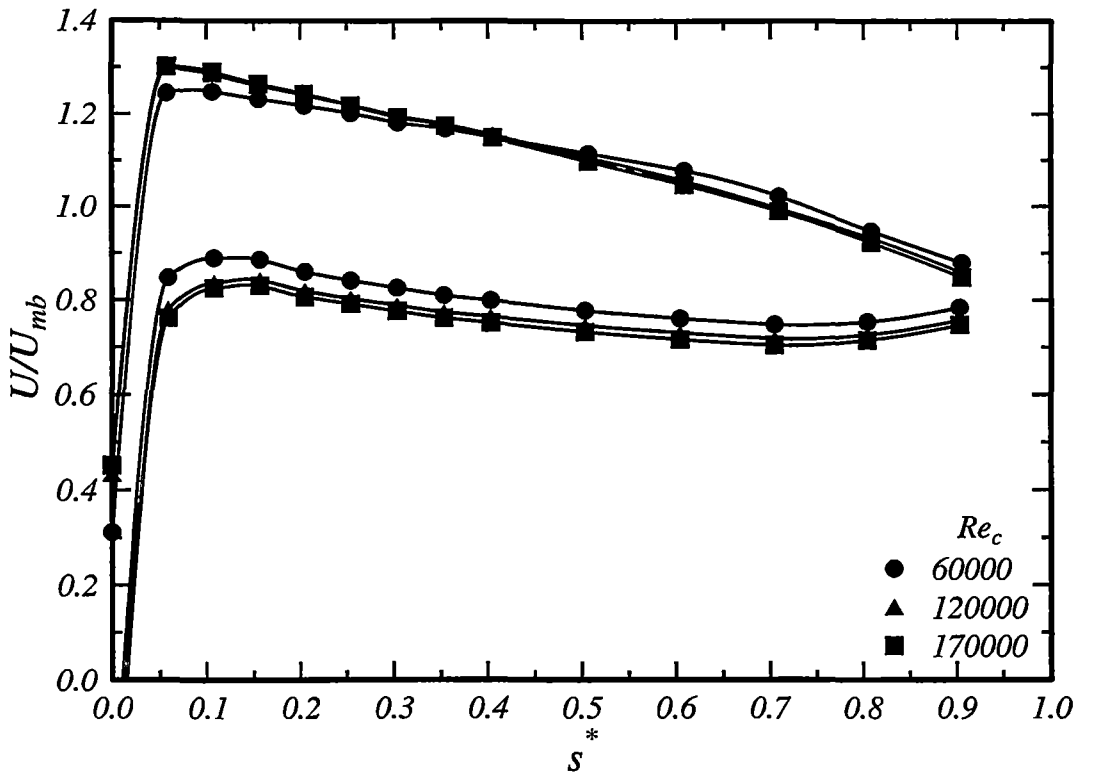

Figure 5.4: Stator blade surface velocity distributions at mid blade height over a range of Reynolds numbers at $\phi = 0.675$ (IGV and stator at reference position; $a/S = 0.5$)

The uncertainty in the surface velocity distribution U/U_{mb} values is thought to be no more than 0.9%.

A small kink in the surface velocity distribution is consistently observed at the 30% chord pressure tapping. At 30% chord there is a discontinuity in the rate of change of blade surface curvature where the two defining polynomials of the C4 section meet. Korakianitis and Papagiannidis [68] found that such discontinuities can cause undesirable perturbations in blade velocity distributions. Alternatively an irregularity in this particular blade pressure tapping may have caused this perturbation.

Effect of relative IGV position on stator surface velocity distribution

Measurements taken at seven different relative IGV circumferential positions (a/S values) have been made to test for any significant effects on the long term average velocity distribution. As shown on Fig. 5.2 the variation is small. To show these trends more clearly the percentage change in suction surface U/U_{mb} from the value at $a/S = 0.499$ has been calculated and plotted in Fig. 5.5 for the case $i = 1.24°$ and $Re_c = 120000$. This figure shows variations of suction surface velocity as large as 4% towards the trailing edge (significantly exceeding the expected measurement uncertainty of 0.9%).

The variations shown in Fig. 5.5 partly reflect the periodic changes in Cp_{tot} caused by the relative circumferential position of the IGV row. If the variations were due

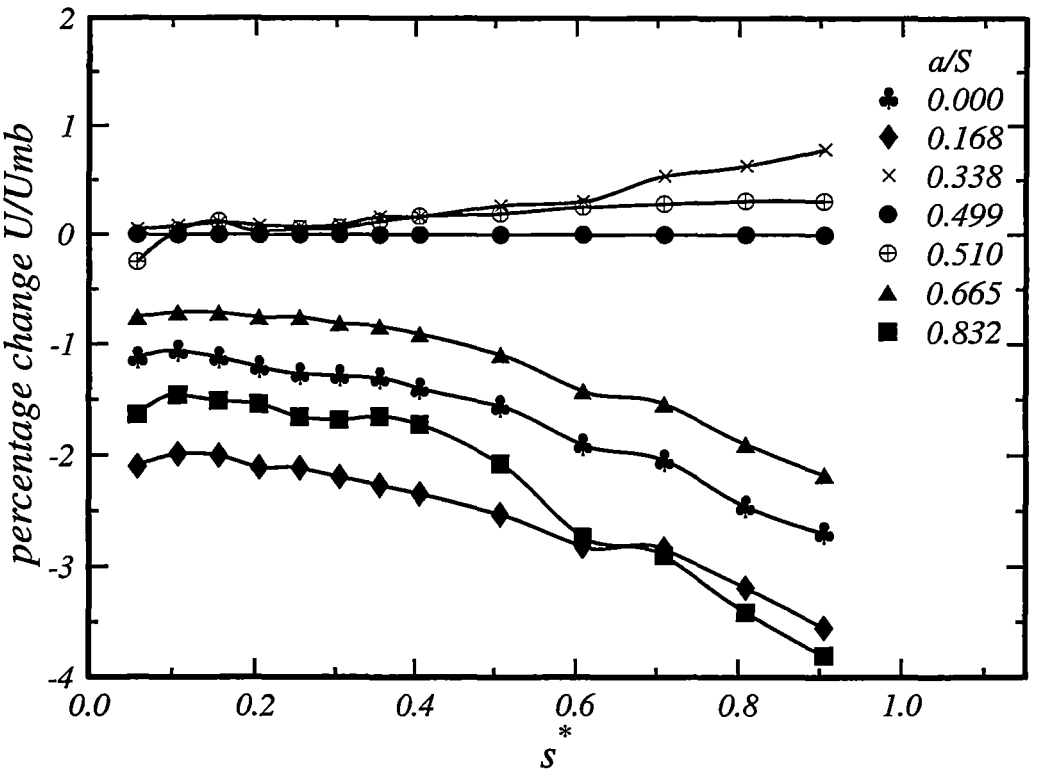

Figure 5.5: Effect of relative IGV circumferential position a/S on the mid blade height stator suction surface velocity distribution for $i = 1.24°$, $Re_c = 120000$

to this factor alone then the curves in Fig. 5.5 should all have nearly the same slope. The evident changes is slope may be due to circumferential variations of flow angle causing changes in loading at different a/S values. The circumferential distribution of turbulence level and length scale might also affect the boundary layer development. At $s^* = 0.6$ there seems to be an additional amount of perturbation, especially on the $a/S = 0.832$ line. This extra amount of change is probably caused by a separation bubble (possibly intermittent) around this location. At different a/S positions the separation bubble either grows or is suppressed depending on the disturbance field and pressure gradient experienced.

Data from Fig. 5.5 at $s^* = 0.4$ and $s^* = 0.9$ has been replotted against w/S in Fig. 5.6 to allow comparison with measurements of the inlet disturbance field presented in Chapter 4 and Chapter 6. Conversion from a/S to w/S was made using Eqn. (5.2).

With the IGV and stator at the reference relative position $a/S = 0.499$, the flowfield measured on the stator blade stagnation streamline is that found from Fig. 6.5 at the corresponding w/S position, 0.93. This position gives close to the minimum freestream turbulence and maximum freestream velocity. The trend in Fig. 5.6 is similar in shape, although inverted, to the observed Cp_{dyn} distribution in Fig. 4.5 (assuming periodicity to compare values at $w/S > 0.5$) which confirms that much of the variation in velocity distribution observed is caused by the change of stator blade stagnation pressure as the

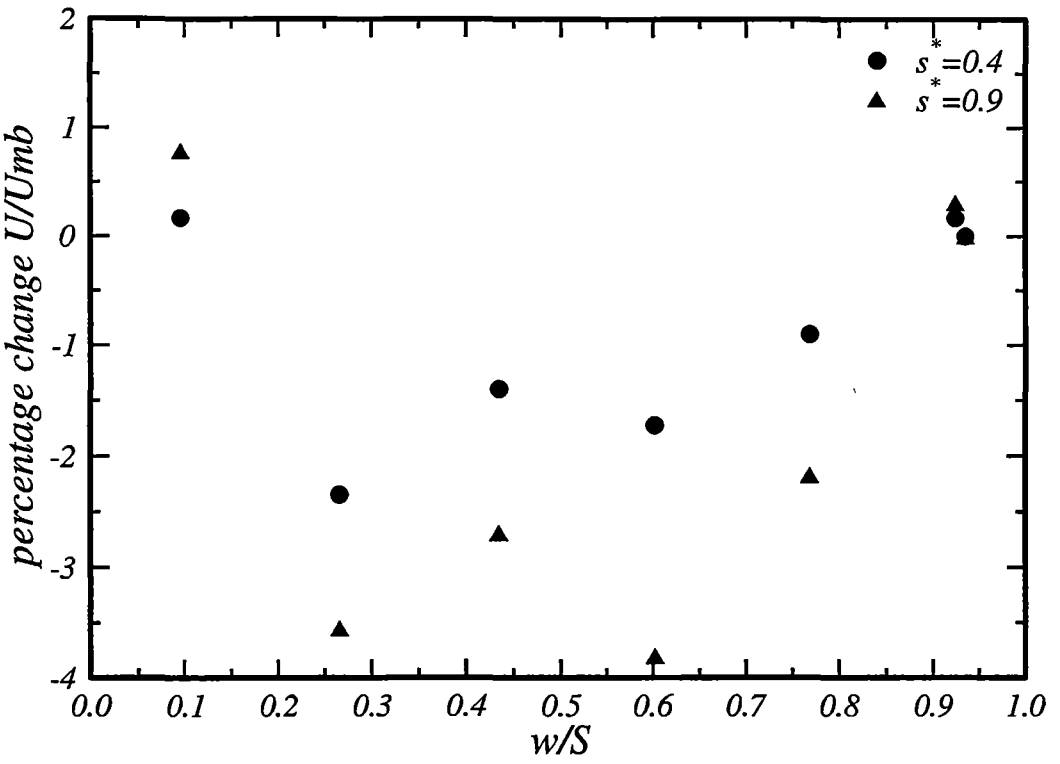

Figure 5.6: Effect of relative IGV circumferential position on stator blade suction surface velocity at two s^* positions, $i = 1.24°$, $Re_c = 120000$

IGV is clocked.

The points at around $w/S = 0.95$ and $w/S = 0.0$ show similar percentage changes at both streamwise positions indicating that the slope of the velocity distribution is unchanged from the reference position. At $w/S = 0.5$ the $s^* = 0.9$ velocity has dropped by almost twice the $s^* = 0.4$ amount indicating an increase in the deceleration on the suction surface or an increase in loading. According to Fig. 6.5 this w/S position corresponds to the point where the IGV wake street lies on the stator blade stagnation streamline. The point of maximum turbulence level occurs at $w/S = 0.2$ where the rotor wakes are the thickest. The high turbulence here has also increased the slope of the stator suction surface velocity distribution although by a slightly lesser amount. The thiner rotor wakes in the presence of higher (IGV wake) background turbulence seem to be more successful in increasing stator blade loading than the thicker rotor wakes with low background turbulence.

5.5 t-s trajectory calculation

For the unsteady work in later chapters it is useful to consider the trajectory of a particle moving at freestream velocity (and at certain fractions of freestream velocity) in the time-distance (t-s) plane. These trajectories were estimated using the velocity

distribution data presented above.

A particle starting at point s_1^* on the blade surface at the non-dimensional time t_1^* will arrive at point s_2^* at time t_2^* given by

$$t_2^* = c_1 \int_{s_1^*}^{s_2^*} \frac{1}{u^*} ds^* + t_1^* \tag{5.5}$$

where $u^* = U/U_{mb}$ and c_1 is a constant arising from the non-dimensionalising parameters used, given by

$$c_1 = \frac{S_{max}}{TU_{mb}} = \frac{37S_{max}}{\pi D} \tag{5.6}$$

Eqn. (5.5) cannot be used if $s_1^* = 0$ because u^* is zero at the leading edge. Instead, the following approximation was made for the first point on each surface:

$$t^* = c_1 \frac{\Delta s^*}{u_{ave}^*} \tag{5.7}$$

where u_{ave}^* is half the velocity at the second point on the surface. Although this method gave good results it was later decided to start the trajectories from the observed wake centers at the ±5% chord points. It was felt that ensuring the trajectory coincided with the wake at $s^* = 0.05$ would give a trajectory location which more accurately tracked the position of the wake in the t-s plane towards the rear of the blade.

5.6 Inviscid calculation

A Martensen type vortex element code with modifications due to Lewis [73] was written to calculate the inviscid flow over a two-dimensional cascade. No attempt has been made to account for boundary layers or changes in axial velocity - density ratio through the blade row. The code was run using 98 elements distributed around the blade in a half-cosine distribution. The Kutta condition was applied at the trailing edge. The circumferential mean incidence angle was used rather than the value for the particular circumferential position. For an incidence angle of 1.41° the code predicted an outlet flow angle of 21.2°. For the -7.64° incidence case the code gave an outlet flow angle of 20.8°.

Fig. 5.7 compares results of the inviscid calculation with the measurements for two different cases. Except at the trailing edge where the boundary layers are thickest and deviations from two-dimensionality the largest, the calculations are in reasonable agreement with the code. The odd spikes in the calculation at the leading and trailing edges are probably due to numerical problems caused by the close proximity of panels on the opposite surface in these regions. The measurements for the low Reynolds number, negative incidence case show evidence of a separation bubble around 60-90% chord on the suction surface. The slope of the measured velocity distribution deviates from the inviscid calculation in this region.

Effect of wrapping a surface hot-film array

The vortex element code was also used to investigate the effect on the blade surface velocity distribution of wrapping the surface hot-film array (Chapter 8) around the

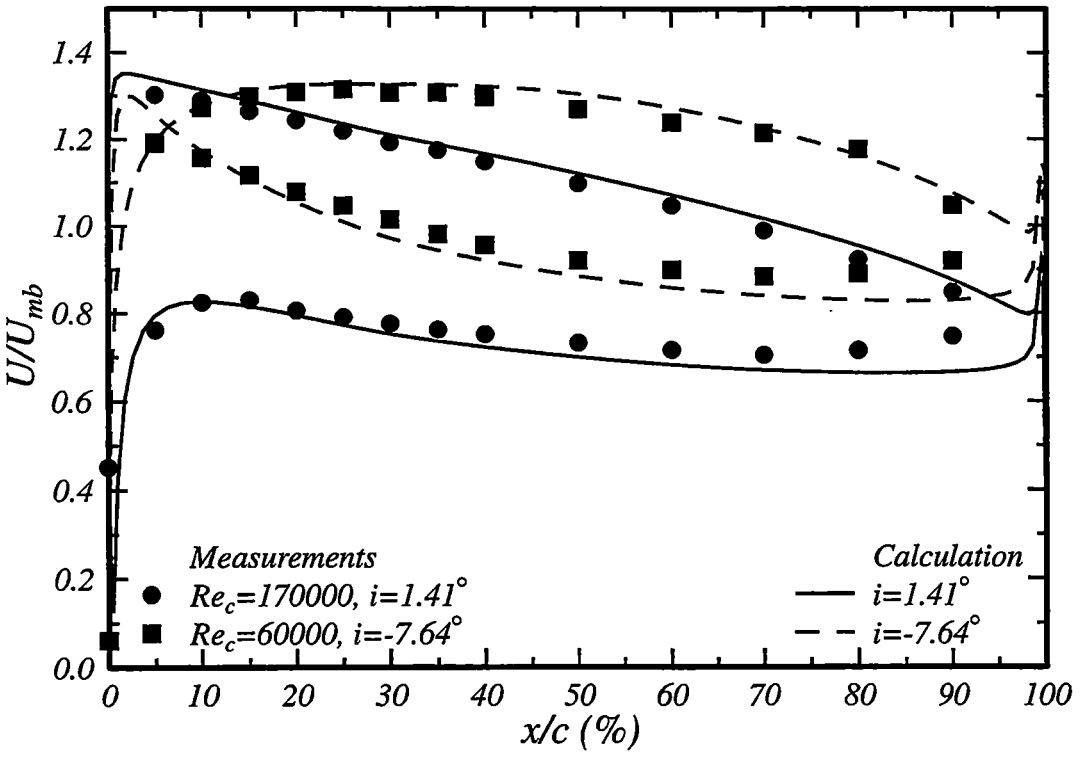

Figure 5.7: Comparison of measured velocity distributions with results from inviscid flow solver

blade. Calculations were performed for a blade which had been enlarged in the direction perpendicular to the blade surface by 0.06 mm (the thickness of the polymide film array substrate.) This enlargement allows 0.01 mm for a glue layer.

As shown in Fig. 5.8 the extra thickness added to the blade surface has a minimal effect on the blade surface velocity distribution and is not expected to significantly alter the boundary layer development. The calculation shows the largest effect at the trailing edge where the wrapped case gave an outlet air angle of 20.9° (a change of 0.3°.)

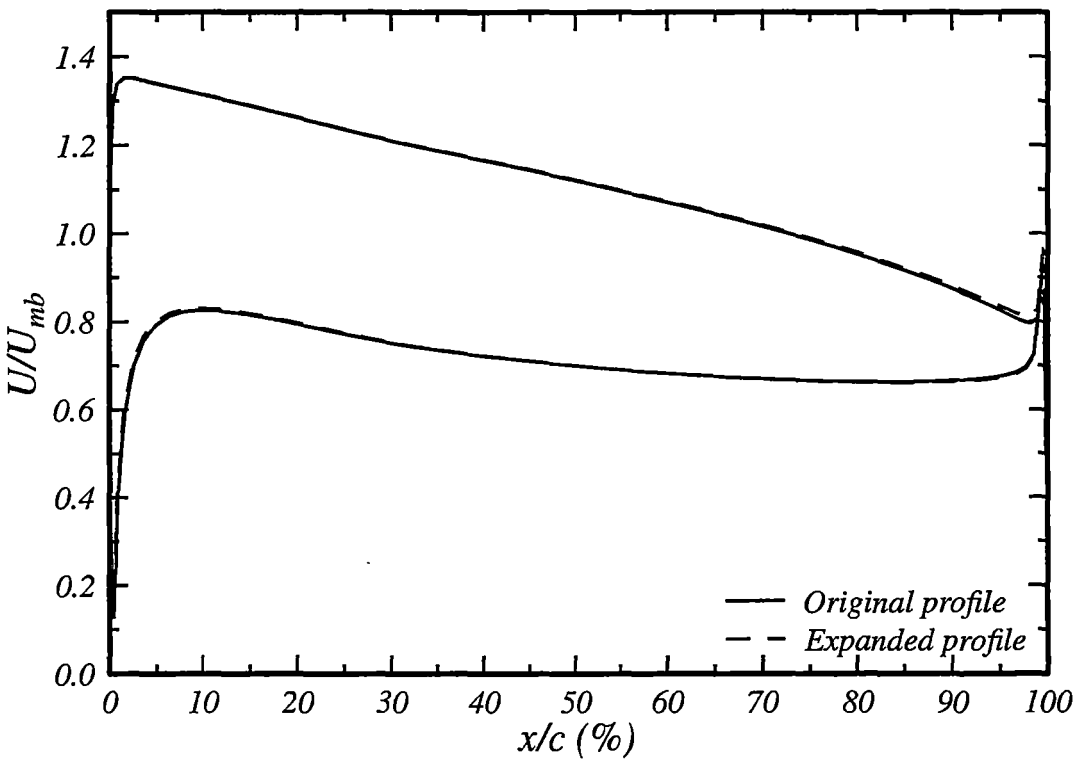

Figure 5.8: Calculated change in blade surface velocity distribution before and after wrapping the surface hot-film array

Chapter 6

Rotor – IGV wake interaction, and stator wake traverse

6.1 Introduction

Detailed knowledge of the inlet flow field is vital to the successful prediction of boundary layer transition on turbomachinery blading. As well as mean inlet velocities and angles, boundary layer transition analyses require (at least) the inlet freestream turbulence level. For design purposes a single representative freestream turbulence level is commonly assumed. In order to consider unsteady transition effects the variation of freestream turbulence level (and possibly flow angle and velocity) over a blade passing cycle is needed. Halstead et al. [46] show a close correlation between inlet freestream turbulence and the phase-locked average transition onset location for turbine blades. Measurements of phase-locked average inlet turbulence in multi-stage machines are relatively few. In their compressor Halstead et al. measured inlet turbulence levels ranging from 2% between the wakes from the upstream blade row to 6% within the wake of the upstream blade row. This was measured at a stage average Reynolds number of 3.4×10^5 at the inlet to the third stage rotor with five blade rows upstream.

Results of unsteady measurements of the stator inlet and stator outlet flow fields for the present study are presented in this Chapter. Both sets of measurements were taken with a single hot-wire in the stationary reference plane. The first series was taken at an axial position approximately midway between the plane of the rotor trailing edge and the stator leading edge. The second series was taken at a position of 1.5% chord downstream of the stator trailing edge. At the upstream station variation of the mean velocity across the passage was relatively small and so unsteady measurements were only made of the fluctuating component of the signal. Downstream of the stator there was a large velocity defect in the wake and so unsteady measurements including the DC component of the hot-wire signal were made. Both sets of results show significant time-unsteady variation of the thickness of the wake from the immediate upstream blade.

6.2 Wake-blade and wake-wake interaction

In Chapter 2 the jet-wake effect was introduced and the influence of upstream rotor wakes on the flow through a downstream rotor also discussed. Interaction of wakes from an upstream blade row with the following blade row causes periodic fluctuations in lift and aerodynamic moment experienced by a blade row. Meyer [86] modelled the unsteady pressure distribution of a turbomachine blade influenced by passing wakes using an inviscid theory. Lockhart and Walker [76] investigated the viscous interactions of wakes in the current machine and observed a circumferential variation of rotor wake decay (measured in the stationary frame of reference.) In high Mach number compressors blade row interaction has been found to cause non-uniformity of stagnation temperatures downstream of a stator row (Kerrebrock and Mikolajczak [67]); losses in the stator row higher than would be expected with a uniform inlet flow have been observed by Okiishi et al. [93].

Smith [117] observed that the wake from the upstream blade row is not only chopped up by the following row but is also skewed. The skewing is a result of the wake segment (which is transported at approximately the local freestream velocity) being slowed at the end near the pressure surface and accelerated at the end near the suction surface on the other side of the blade passage by the effects of blade circulation. Smith also notes that if the vorticity of the wake segment is conserved then its strength will change inversely with its length as it is skewed and passes through the passage. Typical instantaneous wake positions in the current compressor, showing faster wake convection on the rotor and stator suction surfaces, are sketched in Fig. 6.1.

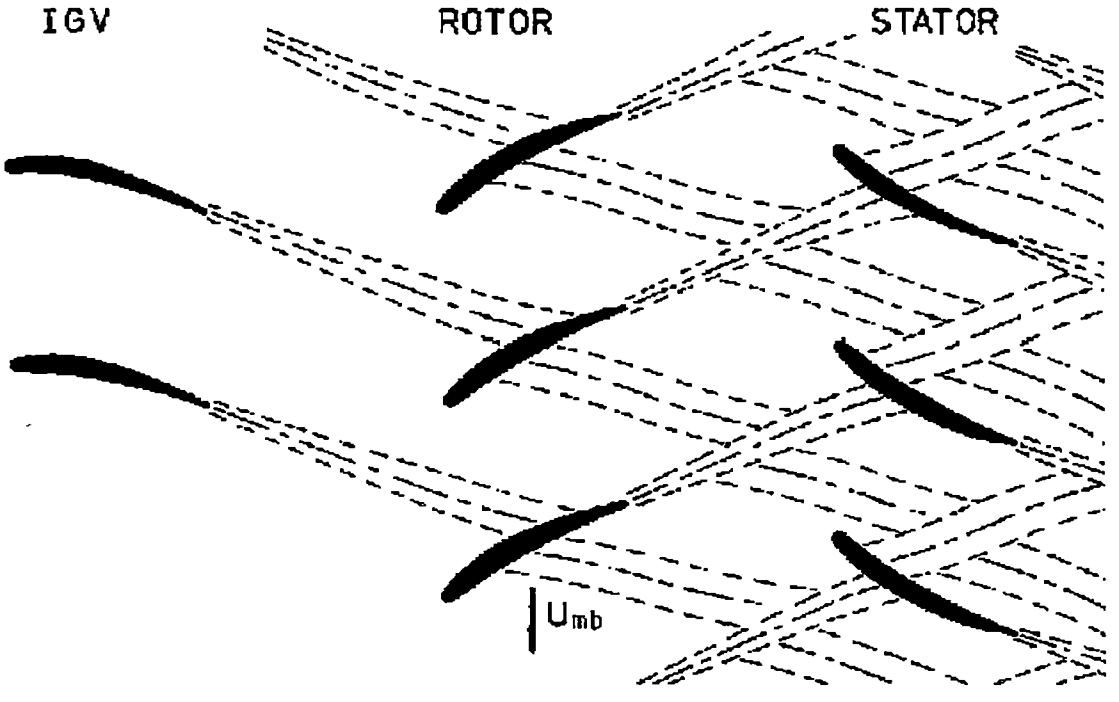

Figure 6.1: Cross-section of compressor blading, showing typical instantaneous wake dispersion

As a wake is convected through a blade row the jet wake effect leads to a redistribution of high entropy fluid (Kerrebrock and Mikolajczak [67], Hodson [52]). In the case of a compressor a build up of high loss fluid on the pressure surface of the blade and removal from the suction surface of the blade is predicted by this mechanism. When the blade boundary layers are transitional the wakes from upstream also have a direct effect on the development of the blade surface boundary layers through wake-induced variations of the transition onset and completion points. In the case of a stator blade the upstream rotor has a dominant effect on transition. The wake from the preceding stator changes the background turbulence level seen by the stator in question and the transition start and end locations on the downstream stator may be modified according to the relative location of the upstream stator wake. Binder et al. [8] observed a more extreme form of this phenomenon in the case of rotor blades in a turbine. Here the upstream rotor wakes either caused or suppressed separation on downstream rotor blades depending on their location across the downstream rotor passage.

In addition to blade-wake interactions, Lockhart and Walker [76] found that wakes interact with each other as they are convected. The mechanism is similar to the jet-wake effect except that instead of high loss fluid building up against a blade the buildup occurs against another (older) wake. In the case of wakes in the rotor-stator gap of the current machine shown in Fig. 6.1 the IGV wake turbulence from upstream has a mixing effect and can lessen the cross-passage transport of the rotor wake fluid.

These mechanisms together lead to complex unsteady flowfields downstream of both the rotor and stator rows of the current machine. Representation of the unsteady flowfield with a single inlet freestream turbulence number is inadequate if consideration of unsteady effects is required.

6.3 General picture of stator inlet flowfield

Measurements of the inlet flowfield at a station close to the centre of the rotor-stator gap have been taken at three different Reynolds numbers and at three different flow coefficients giving a total of five test cases (Figs. 6.4 to 6.8). Steady and unsteady hot-wire measurements are plotted for each circumferential traverse and the time-mean defect velocity vector described in Section 4.3 from the three hole probe measurements is included for comparison. The data has been plotted over two blade pitches by assuming pitch-wise periodicity. The long term turbulence level (or total disturbance level) from the hot-wire velocity data was measured at different circumferential positions across the passage and is plotted at the left of these figures. Ensemble average freestream turbulence is presented in colour-contour form. t^* is time normalised by the rotor passing period and has been plotted from right to left so that the rotor wakes appear in the same orientation as shown in Fig. 6.1 (In comparison with Fig. 6.1 the IGV wakes do not change circumferential position because the measurements were taken at a single axial position.) The vectors shown in these figures indicate local time mean deviation from the passage mass-averaged flow velocity and angle obtained from the three hole probe.

The data in these figures has been time-shifted so that the rotor-IGV relative circumferential position is constant at the trigger time $t = 0$ for each w/S probe position. This was necessary because the IGV was clocked relative to the trigger point which

was fixed relative to the machine and the probe.

In all these figures the relatively strong rotor wakes are visible travelling down from top right to bottom left against a background of varying turbulence levels associated with the IGV wake street. The top part of the rotor wakes in these figures are from the suction surface of the rotor blades. The lowest flow coefficient case, shown in Fig. 6.4, has the highest long term turbulence levels across the passage and the thickest rotor wakes. (Note that a different scale has been applied to the unsteady turbulence data in this figure.) The peak levels of time-average turbulence across the passage are at $w/S = 0.5$. This does not correspond to the average position of the IGV wake but is close to the position of minimum mean velocity indicated by the vector plot. A significant variation in thickness of the rotor wake is observed. Note that the peak value of total disturbance level is associated with a strong periodic disturbance component arising from the rotor wake disturbances. The slope of the rotor wake trajectory also reflects the change in local flow velocity and fluctuating rotor blade lift associated with IGV wake chopping; it is noticeably lower around $w/S = 0.25$ to $w/S = 0.5$.

The higher flow coefficient cases in Fig. 6.5 and Fig. 6.6 show a general reduction in turbulence levels. In these cases two peaks are clearly visible in the long term turbulence plots, a smaller one corresponding to the centre of the IGV wake street and a larger one at the circumferential position where the rotor wake is thickest. At the highest flow coefficient the circumferential variation of mean velocity and flow angle is small and the vector plot is difficult to interpret. In this case there is an unsteady thickness variation of the rotor wake, but there does not seem to be a significant variation in the wake velocity (slope of the rotor wake trajectory).

In all cases the results of the IGV wake chopping and skewing are visible. The circumferential location of the thickest part of the rotor wake relative to the IGV wake position is different in each case. It is notable that there are significant regions in the time-space contour plots where the ensemble average turbulence in the core flow is below 0.5% even though the minimum long term average turbulence level across the passage is typically 2.5%. Halstead et al. [46] show ensemble average turbulence levels between wakes of between in the range 2–3% measured at the inlet of a third stage compressor stator. This is comparable to the observed value for the current work in the IGV wake street. Halstead et al. did not report circumferential variation of the stator inlet ensemble average turbulence intensity but did observe a significant clocking effect in the LP turbine case.

The higher Reynolds number case Fig. 6.7 is generally similar to the medium Reynolds number case at the same flow coefficient Fig. 6.5. There is a slight reduction in the circumferential variation of turbulence levels and mean velocity. At low Reynolds number Fig. 6.8 shows a marked increase in the circumferential thickness variation of the rotor wake. The increase in the unsteady rotor wake thickness variation with a drop in Reynolds number suggests the phenomena may be associated with an intermittent rotor blade boundary layer separation.

Significant variations in the rotor wake thickness are apparent in the measurements discussed above. Peak time-average turbulence corresponds to the thickest part of the rotor wake. A second smaller peak is measured in the IGV wake street. Almost all of this thickness variation must be due to the interaction of the rotor blade and the rotor wake with the viscous flow field of the IGV wake street. The rotor is also traversing the IGV potential flow field but since the row spacing is large the potential effects

are small. Unsteady variation of incidence experienced by the rotor blade may cause loading fluctuations. The relative w/S position of the thickest part of the rotor wake and the mean IGV w/S position changes with loading but stays constant with Reynolds number. At the two higher flow coefficient values the thinnest rotor wake coincides with the IGV wake position suggesting that the raised freestream turbulence in the IGV wake street may be due to the suppression of a separation bubble on the rotor blade. This hypothesis is not well supported by Fig. 6.4 where the thickest part of the rotor wake coincides with the IGV position. The jet-wake effect, and wake-wake interaction must also be present to some degree. Interpretation of these figures is further complicated by the skewing of the IGV wake by the blade circulation. The different transport times of wakes which are carried at the freestream velocity and wake-induced boundary layer effects which are convected at some fraction of the freestream velocity also confuses the situation.

6.4 Wake measurements downstream of stator row

To better understand the rotor wake thickness variations which were observed in measurements upstream of the stator, a short series of tests were performed using a single hot-wire inserted 1.5% chord axially downstream of the plane of the stator trailing edge. At this position there will be no significant rotor wake-stator wake interaction but jet-wake and unsteady boundary layer transition (and possibly separation effects) will still be present. The close proximity of the probe to the stator trailing edge also allows these results to be compared with the surface hot-film measurements of the blade surface boundary layer development. These measurements also allow an approximate estimation of the unsteady blade loss. Schulte and Hodson [114] obtained useful information about the unsteady variation of suction surface boundary layer loss on their LP turbine blade cascade through unsteady measurement of the boundary layer momentum thickness at the trailing edge. In the current work, measurement of the unsteady stator blade wake momentum thickness has been attempted.

A single hot-wire probe was traversed across one blade pitch at mid-blade height. Both rotor and stator rows were clocked at the same rate and the probe was held at a constant position relative to the annulus wall. The relative circumferential IGV-stator position was held constant at $a/S = 0.5$ for this series of measurements. As the blade-passage was traversed, the angle of the wire relative to the blade surface changed slightly; this effect was not accounted for in the analysis. A total of 36 measurement stations were used across the passage and these were spaced more closely in the region of the stator blade wake.

This series of measurements was taken at a constant Reynolds number, $Re_c = 120000$ and at three different flow coefficients, $\phi = 0.600, 0.675$ and 0.840.

Processing

In the case of the downstream traverse there are significant variations in the time mean velocity $\overline{U}$ across the passage because of the close proximity of the stator blade trailing edge. For this reason it was decided to calculate a passage average velocity (average in time and space) and reference the turbulence measurements to this. This distinction is not important for the upstream results because the mean velocity defect in the rotor

wake has decayed significantly and is time averaged at any stationary measurement station. Mass-averaging was not possible here because no flow angles were available downstream of the stator. The passage average velocity U_{ave} was determined as

$$U_{ave} = \frac{1}{S} \sum_{j=1}^{l} \overline{U_j} \Delta w_j \tag{6.1}$$

where $\overline{U_j}$ is the longterm average at traverse point j and w_j is the circumferential distance from the probe to the IGV trailing edge. l is the number of traverse points across the passage, 36 in this case.

As in the case of the upstream data a time-shift has been applied so the $t^* = 0$ corresponds to the same rotor-IGV (and hence same stator-IGV) position at each traverse point w/S. Note that the downstream measurements have circumferential positions x/S expressed relative to the stator blade trailing edge position instead of w/S (relative to the IGV trailing edge position) which was used for the measurements upstream of the stator (see Fig. 3.3)

An estimate of the variation of unsteady blade profile loss has been made by measuring the unsteady wake momentum thickness. This process is complicated by the lack of a uniform freestream velocity to which the momentum loss can be related. The phase-locked average freestream velocity varies across the passage due to stator potential flow field effects, the rotor-blade wakes and the remnants of the IGV wake street. The current simple method of estimating the wake momentum thickness was to first find the point of minimum ensemble averaged velocity across the passage corresponding to the centre of the stator blade wake. The wake was then treated in two halves. Working from the centre of the wake the data reduction code searched for the first velocity peak across the passage and integrated to that point using the peak ensemble average velocity value as the effective freestream velocity. On a few occasions this method failed because at some parts of the cycle the velocity increased continuously across the passage. In these situations limits were placed on the estimated wake width based on the extreme values in cases where velocity peaks were found successfully.

6.5 Results

The measurements taken downstream of the stator blade row are shown in Figures 6.9 to 6.11. In these plots the colour contours represent phase-locked average velocity relative to the passage average value. Contours of phase-locked turbulence level (relative to passage average velocity also) have been overlaid and some contour levels are labeled (in percentage). There is a slight shift in scale for the velocity contours in Fig. 6.11 relative to the other two cases.

At the left of each figure the time-average velocity and turbulence levels have been plotted. The stator blade wake is clearly visible in these time-mean values close to $x/S = 0.0$. The suction surface half of the stator blade wake extends in the increasing x/S direction, that is towards the bottom of the figure from the wake centre. The suction surface half of the stator blade wake is thickest in Fig. 6.9 at $\phi = 0.600$ and decreases as the flow coefficient rises which is consistent with the change in blade loading. Turbulence levels away from the stator blade wake also decrease as flow coefficient

is increased. The time-average velocity measurements in Fig. 6.9 show a strong asymmetry of the time-average wake which is clearly much thicker on the suction surface side.

The phase-locked average results clearly show the time-varying relationships between the rotor wake segments, the IGV wake street and the stator blade wake. The location of the IGV wake street in-between the stronger rotor and stator wakes is given by locally raised turbulence levels and reduced velocity levels. Measurements were taken at a fixed axial position and so as in the case of the upstream measurements the IGV wake appears as a horizontal band across each figure. The IGV wake street appears in the band $-0.6 < x/S < -0.1$ in Fig. 6.10 and at $0.1 < x/S < 0.4$ in Fig. 6.11. Precise location of the IGV wake street in Fig. 6.9 is more difficult. By using the stator row flow inlet angles and the known position of the IGV wake at the upstream station (from Fig. 6.4), the location of the IGV wake street at the stator row inlet can be estimated. Assuming that the IGV wake fluid is guided through the blade passage and maintains a similar position relative to the stator blade puts the centre of the IGV wake street at about $x/S = -0.1$. Hence, for Fig. 6.9, the IGV wake street overlaps the stator blade position and extends over the region $-0.6 < x/S < 0.4$. The shift in IGV wake street position with changing flow coefficient in Figs. 6.9 to 6.11 is consistent with the trend observed in the upstream results. The varying IGV wake street position relative to the stator results from maintaining a constant relative IGV-stator circumferential position (a/S) while the stator inlet flow angle is changing with flow coefficient.

For the surface hot-film work in Chapter 8 a constant a/S value was also maintained for all test cases. This current set of measurements (which was obtained after the hot-film work) suggests that it may have been better to clock the IGV to maintain constant IGV wake street position relative to the stator row for the different flow coefficient test cases so that the blade surface boundary layers would see a consistent freestream disturbance field.

The unsteady rotor wake position is most clearly given by the ensemble average freestream turbulence contour lines. High turbulence levels associated with the rotor wake segments stretch in bands diagonally across the contour plots from the top right to bottom left of each blade passage. Transport of low energy fluid by the jet-wake effect is in this direction, i.e. towards the pressure surface. There are significant variations in wake thickness and intensity across the passage. In Fig. 6.10 for example there is a mild buildup of low velocity fluid where the wake impinges on the blade pressure surface (close to where the 4% turbulence label is placed). In the middle of the wake passage there is a light blue area where another accumulation of low velocity fluid in the wake exists. This may be the remains of the thickest part of the wake shed from the rotor blade. However, since this buildup coincides with the top of the IGV wake street, it may also be caused by the blocking effect of the IGV turbulence, as observed by Lockhart and Walker [76]. In Fig. 6.11 all the buildup is around the stator blade, mostly at the pressure surface. In this case the top IGV street is close to $x/S = 0.1$ so that any buildup of low energy fluid caused by IGV wake mixing (Lockhart and Walker mechanism) would occur in the region of the stator blade, which is not inconsistent with the measurements. Fig. 6.9 also shows the largest buildup at the stator blade pressure surface and thickening of the rotor wake at the top of the IGV street is not clear.

The most obvious feature of the unsteady contour figures is the stator blade wake

itself which stretches in a blue line horizontally across the figures close to $x/S = 0.0$ and $x/S = \pm 1.0$. The thickness variations of the stator wake are partly obscured by the turbulence contours. These were not plotted for levels over 9% to minimise this problem. In these figures the stator wakes seem to be thinner at t^* values where the rotor wake segment coincides with rear of the stator suction surface. At these positions, however, the velocity defect spreads further into the freestream because of the presence of the wake itself. Between rotor wake segments the stator wake itself becomes thicker; but the freestream velocity near the blade surface shows a relative increase partly because of the displacement effect of the thicker wake and partly because of the absence of a rotor wake. In each case the stator wake starts to decrease in thickness prior to the next rotor wake reaching the probe position near the stator trailing edge. These details will be examined further in conjunction with the surface hot-film measurements of Chapter 8.

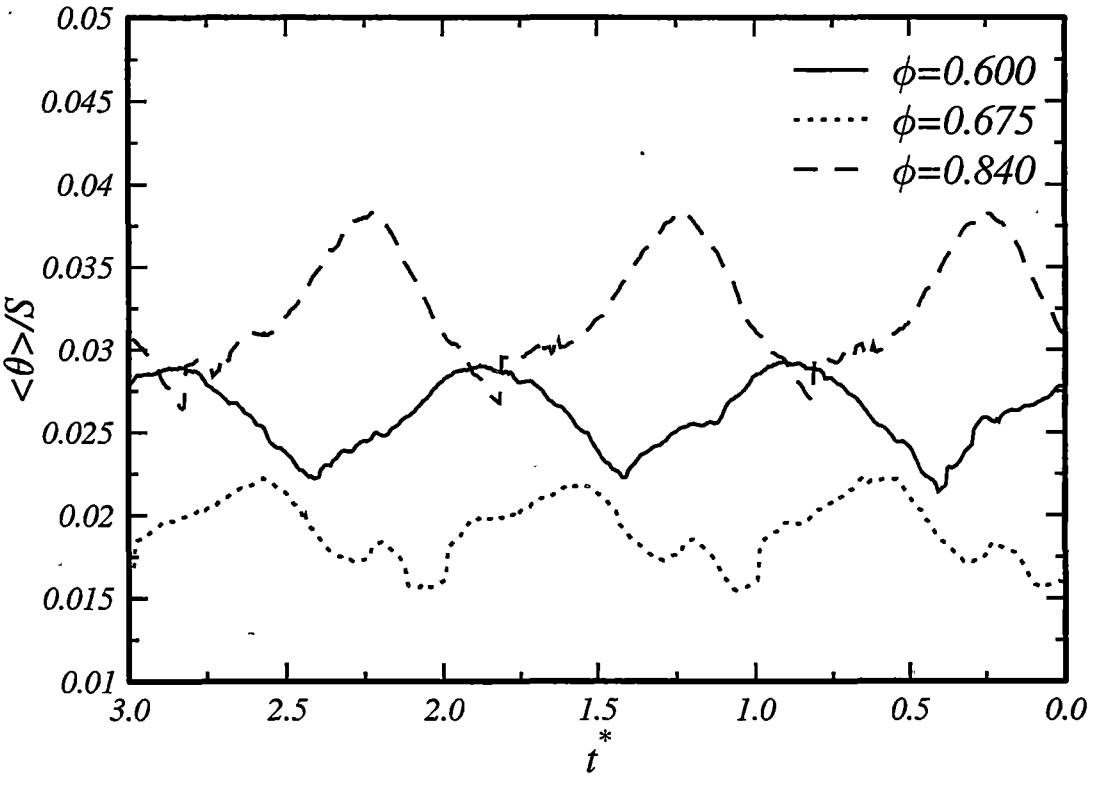

Figure 6.2: Approximate measurements of ensemble averaged stator wake momentum thickness 1.5% chord axially downstream of the stator blade trailing edge. Re_c = 120000

Fig. 6.2 shows the measurements of stator blade wake momentum thickness obtained from the ensemble-averaged single hot-wire measurements downstream of the stator blade row. As mentioned above, some uncertainties exist in these measurements because of difficulties in defining and locating the cross-passage extent of the unsteady wake and in determining appropriate freestream velocities. Also note that no allowance was made for variations in flow angle which were not available from the single hot-wire used.

Typically 15-24 measurement points were located in the region identified as stator wake.

The unsteady wake momentum thickness measurements show peak to peak unsteady variations of the order of 30 percent of the time-mean values. The $\phi = 0.675$, mid flow coefficient case shows the lowest time mean value; this case is close to the compressor design point. The higher and lower flow coefficient cases show increased wake momentum thickness values. The variation of time mean velocity across the passage shown in the previous set of figures suggested that the wake would be thickest for $\phi = 0.600$. However, Fig. 6.2 shows a higher unsteady wake thickness in the $\phi = 0.840$ case over almost the whole wake passing period. This could be because the increased rotor wake defect at $\phi = 0.600$ causes incorrect interpretation of the stator wake location or alternatively may be a result of the very low pressure surface wake thickness in this case. Because these measurements were made by considering the stator wake in two halves, the thickness of each half is available. Plotting of these results in Fig. 6.3 provides an alternative explanation for the high levels of wake thickness of the $\phi = 0.840$ case.

Fig. 6.3 shows that the wake halves from the two surfaces have a significantly different character. The suction surface wake half is far more asymmetrical, especially at $\phi = 0.600$, showing a rapid fall followed by a slow recovery. The peak values of suction surface momentum thickness and pressure surface momentum thickness are out of phase in the $\phi = 0.600$ case, leading to a lower total value and slightly smaller variation over the whole cycle. At $\phi = 0.840$ the peak momentum thickness values of the two halves of the wake are in phase causing a large peak total value and slightly larger variation. There is also clearly a large peak in the pressure surface wake momentum thickness for the $\phi = 0.840$ case, probably associated with an intermittent separation there.

6.6 Conclusions

Unsteady measurements of velocity and turbulent fluctuation have been presented downstream of the rotor and stator blade rows. The disturbance field at the inlet to any embedded blade row in a multi-stage machine will be primarily influenced by the wake from the blade row directly upstream. Wakes from further upstream can also be easily detected and will have a continuing secondary influence on boundary layer transition. Background turbulence levels in the regions between wakes in a multi-stage machine can be relatively low (very low in the current machine) and this can delay transition between the wakes leading to intermittent boundary layer separation which would not be predicted if time-average turbulence levels were assumed for design purposes.

The unsteady wake measurements have shown significant wake thickness variations even at the large inter-row spacing of the current machine where potential flow effects would be expected to be small. Three mechanisms have been considered as a explanation for the wake thickness variations. Evidence for the existence of the jet wake effect was found in the form of a buildup of low velocity fluid on the pressure surface of the stator blade. A tendency for an analogous buildup against the IGV wake as suggested by Lockhart and Walker [76] was also detected in some of the test cases. All test cases downstream of the stator show a strong variation in the thickness of the blade surface boundary layers at the blade trailing edge. The relationship of this variation to the

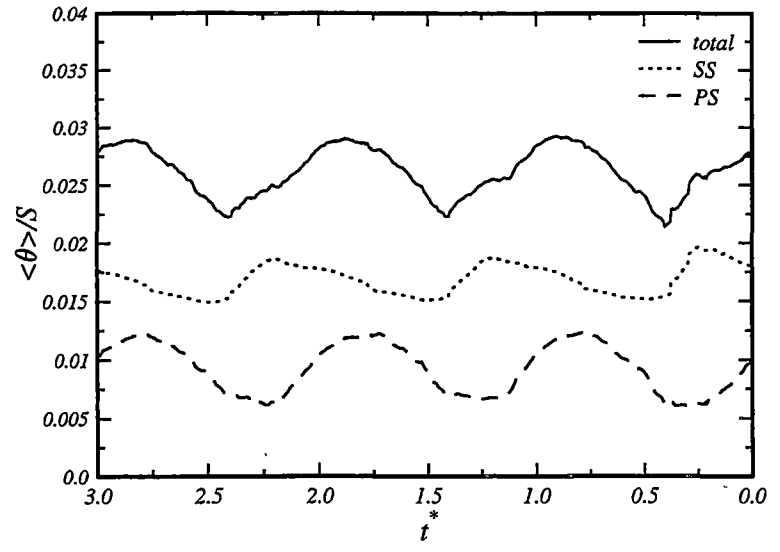

(a) $\phi = 0.600, Re_c = 120000$

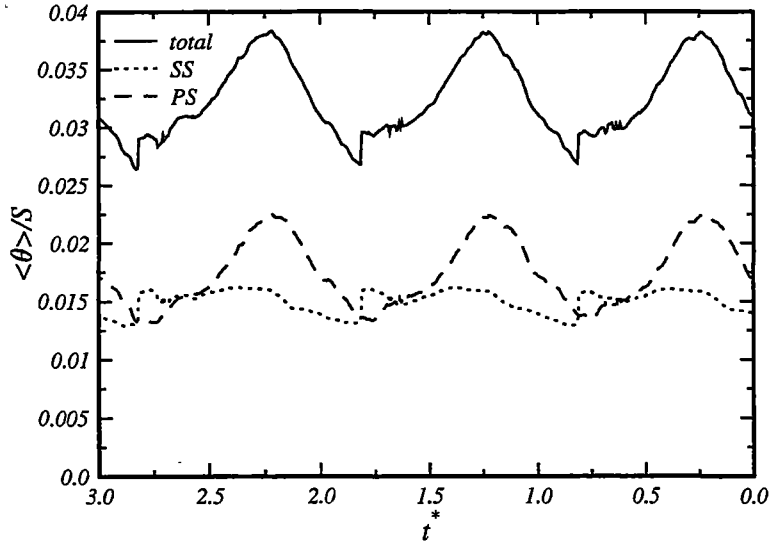

(b) $\phi = 0.840, Re_c = 120000$

Figure 6.3: Ensemble averaged wake momentum thickness 1.5% chord axially downstream of stator trailing edge. Suction surface (SS) part of wake, pressure surface (PS) part of wake and total wake thickness values shown separately.

relative rotor wake position will be further explored in later chapters.

Measurements of the unsteady wake momentum thickness downstream of the stator were also attempted and confirm the significant thickness variations of wakes as they leave the stator blade trailing edge. The boundary layer thickness variations for the suction and pressure surfaces can be at different phases at the trailing edge depending on the blade pressure distribution. If the two boundary layers can be arranged so that their peak thicknesses arrive at the trailing edge out of phase then a more uniform total wake thickness will result. It remains to be confirmed that this would be the most desirable arrangement for a designer to aim for (even if there is enough flexibility in a given design to attempt it).

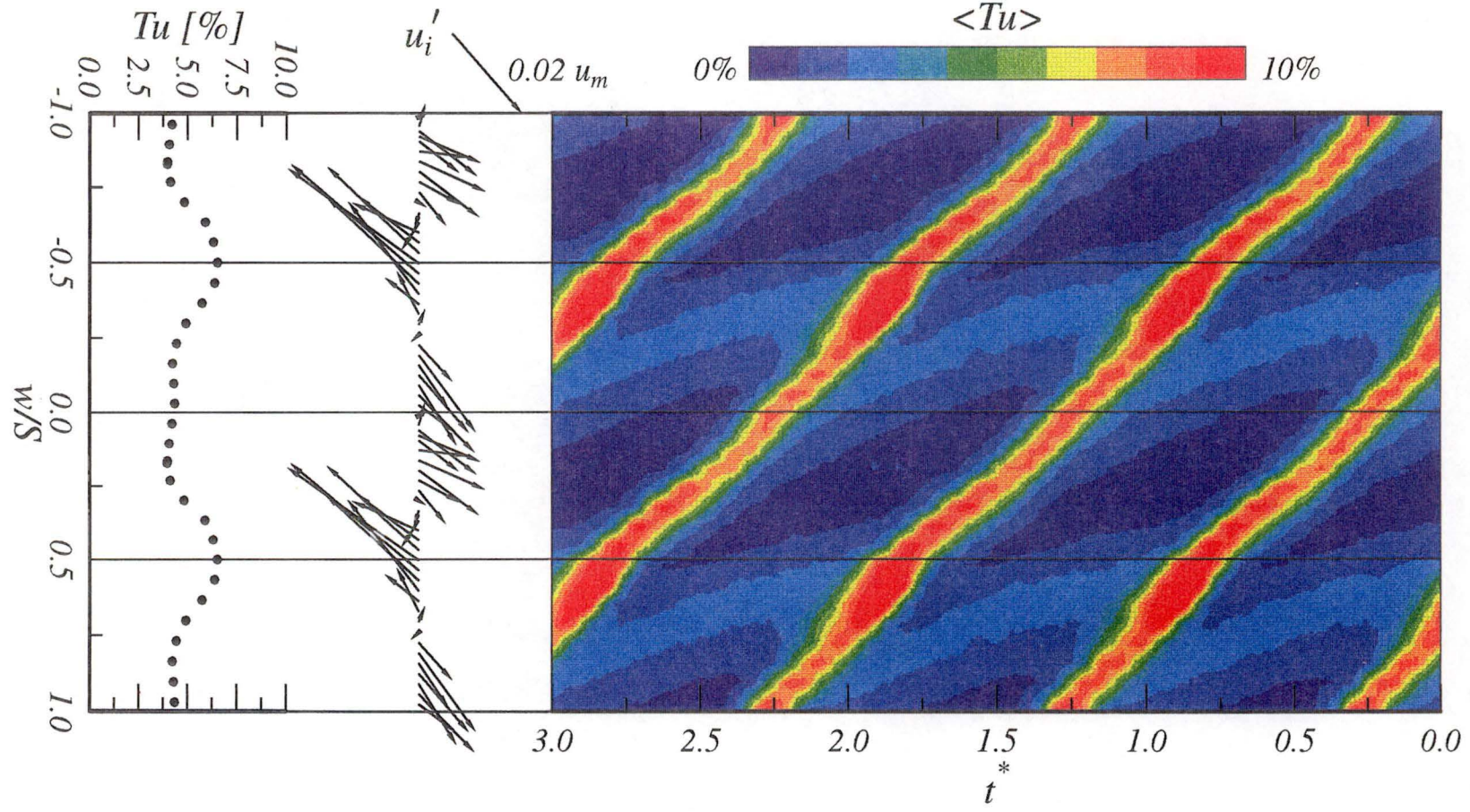

Figure 6.4: Long term time average turbulence Tu, time mean defect velocity vectors and contours of ensemble average turbulence $<Tu>$ measured 59% chord axially upstream of stator leading edge. $Re_c = 120000$, $\phi = 0.600$

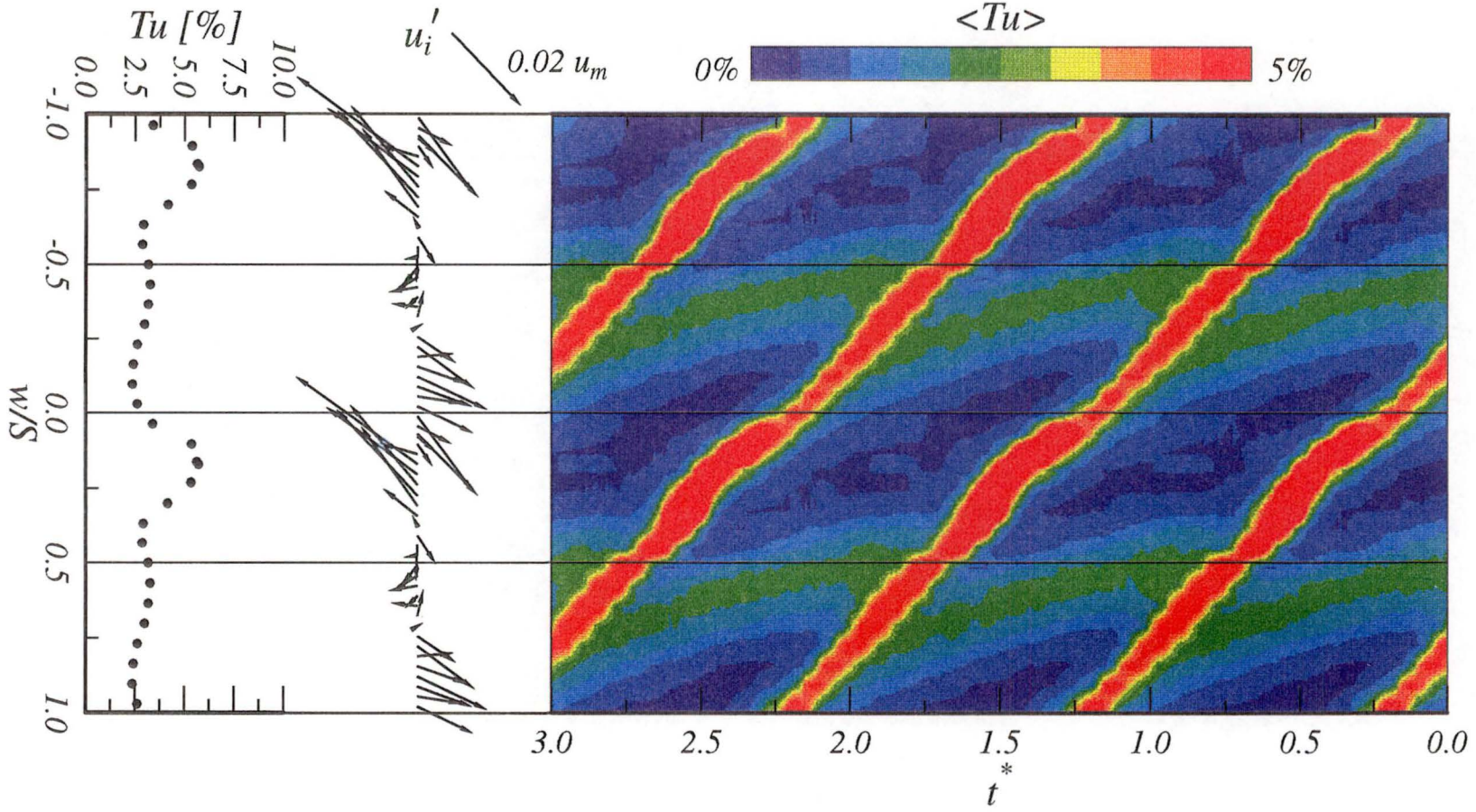

Figure 6.5: Long term time average turbulence Tu, time mean defect velocity vectors and contours of ensemble average turbulence $<Tu>$ measured 59% chord axially upstream of stator leading edge. $Re_c = 120000$, $\phi = 0.675$

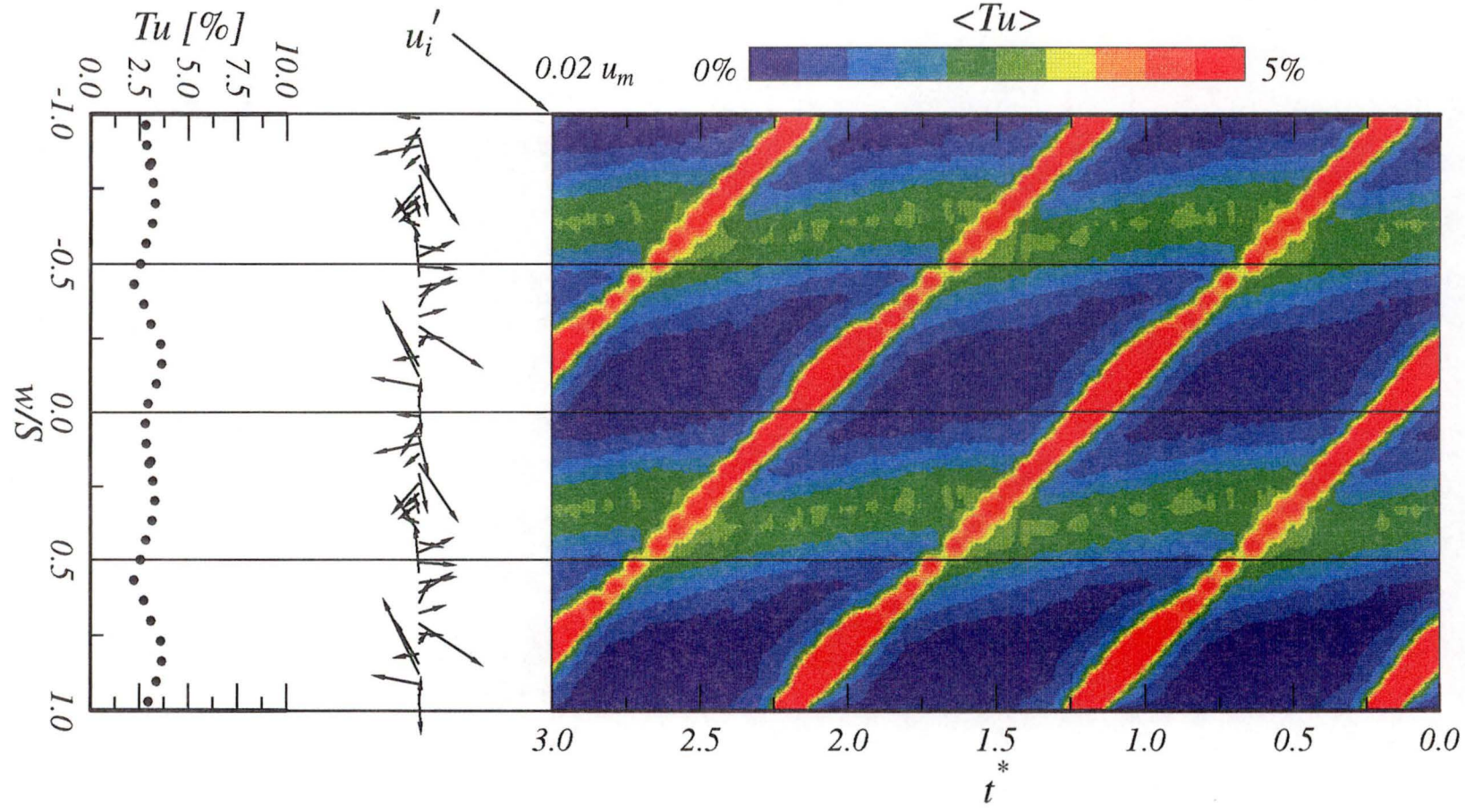

Figure 6.6: Long term time average turbulence Tu, time mean defect velocity vectors and contours of ensemble average turbulence $<Tu>$ measured 59% chord axially upstream of stator leading edge. $Re_c = 120000$, $\phi = 0.840$

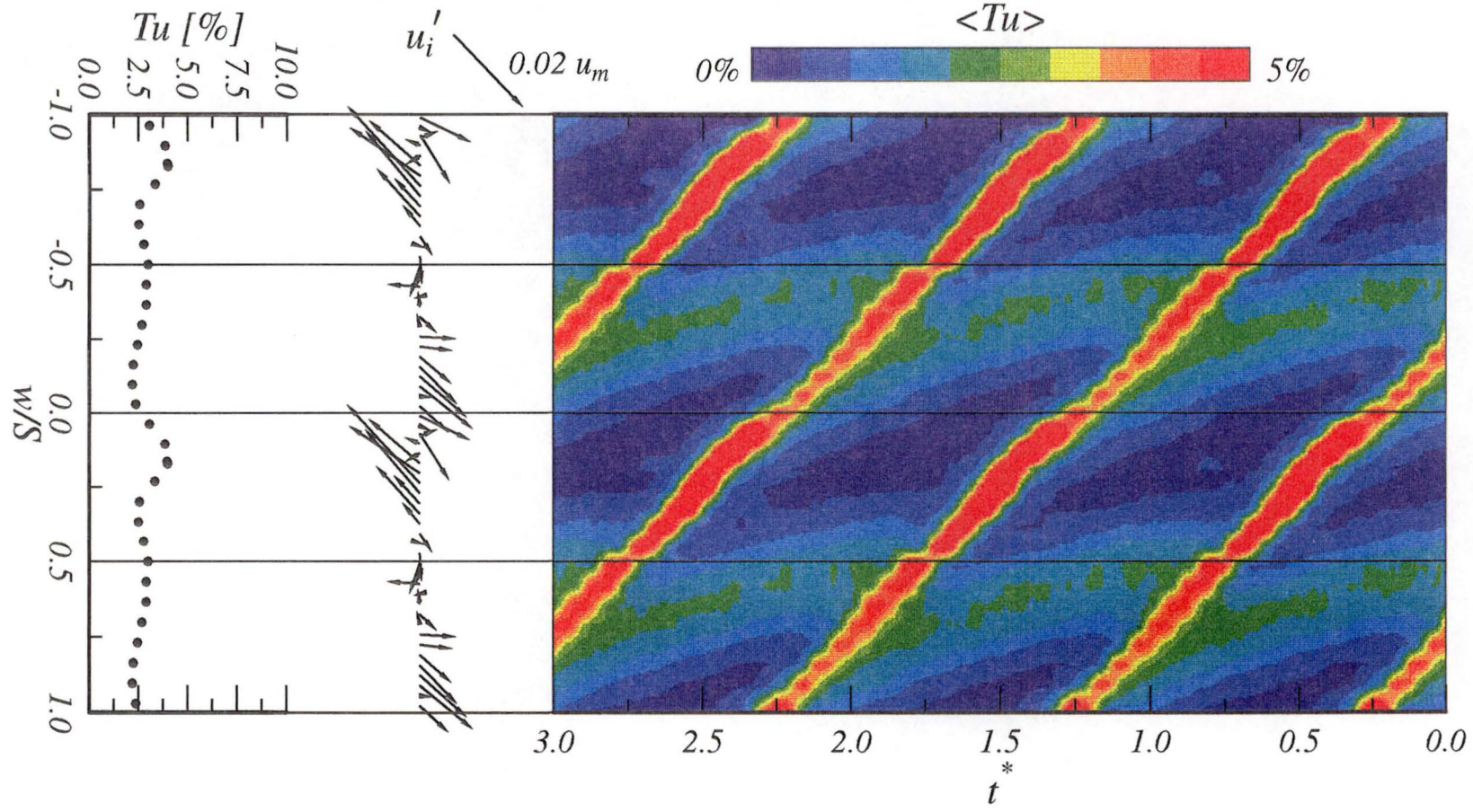

Figure 6.7: Long term time average turbulence Tu, time mean defect velocity vectors and contours of ensemble average turbulence $<Tu>$ measured 59% chord axially upstream of stator leading edge. $Re_c = 170000$, $\phi = 0.675$

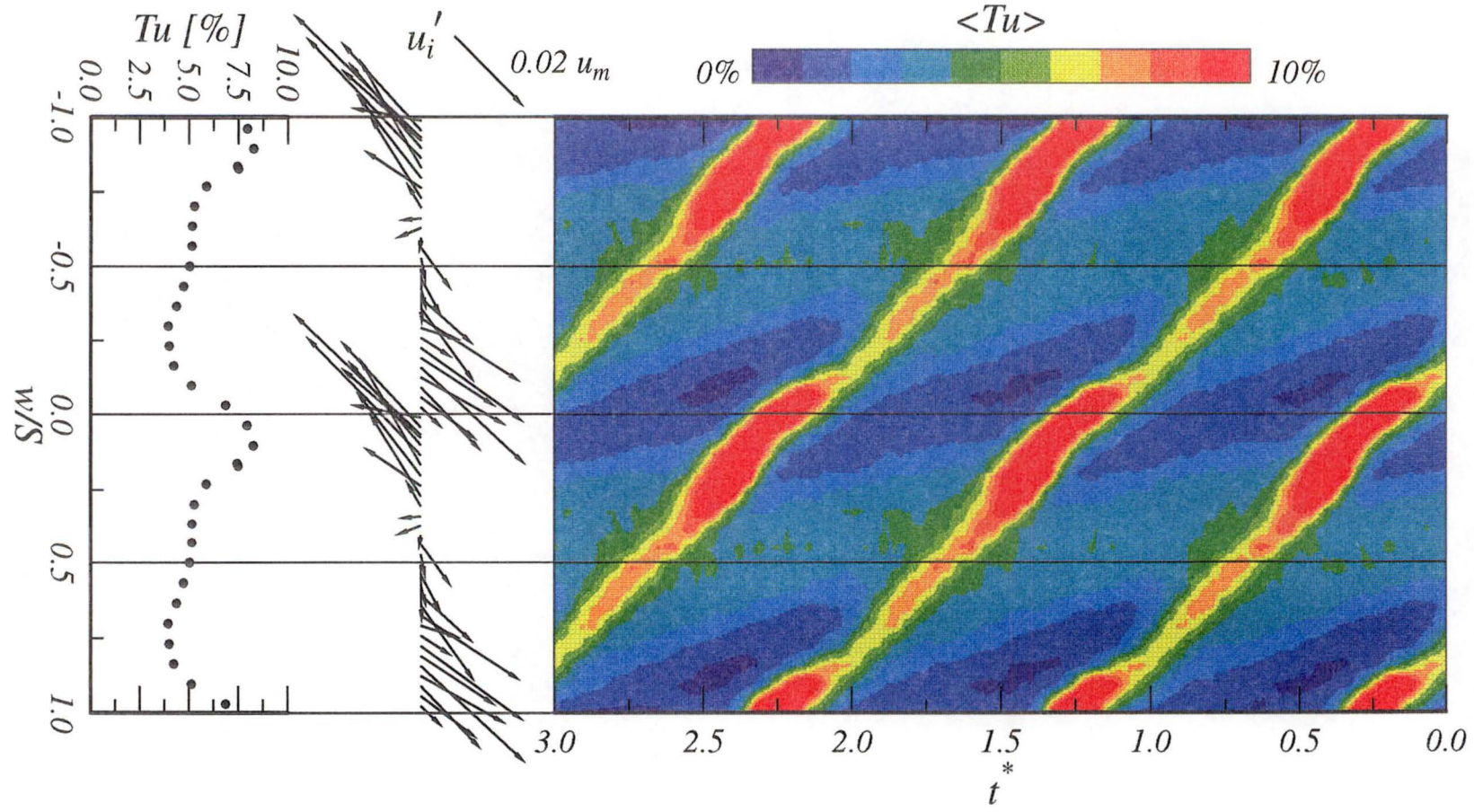

Figure 6.8: Long term time average turbulence Tu, time mean defect velocity vectors and contours of ensemble average turbulence $<Tu>$ measured 59% chord axially upstream of stator leading edge. $Re_c = 60000$, $\phi = 0.675$

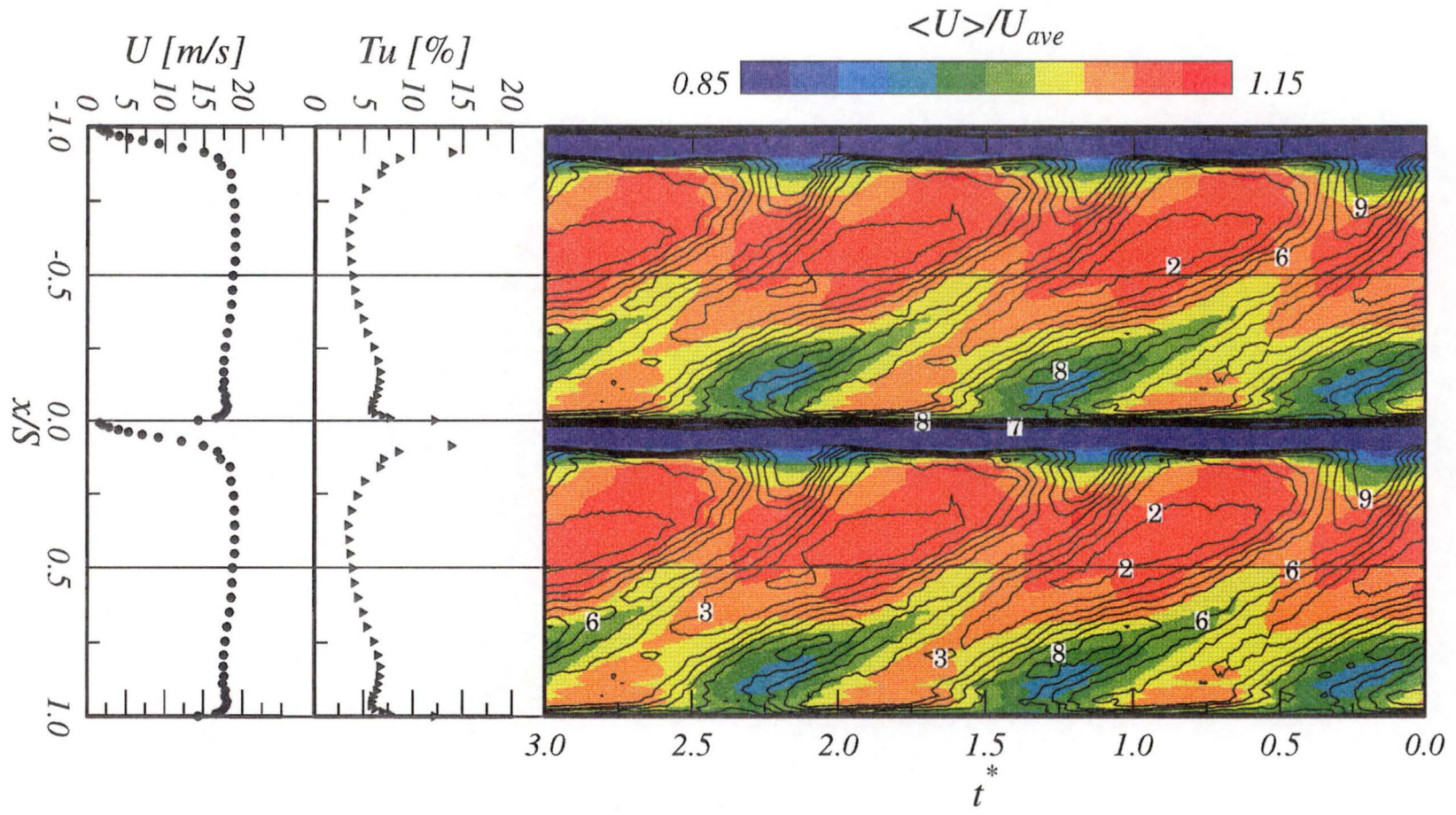

Figure 6.9: Time average velocity U, turbulence Tu. Colour contours of ensemble average velocity $<U>$ with contours of ensemble averaged turbulence $<Tu>$ overlaid. Measurements 1.5 % chord axially downstream of stator trailing edge. $Re_c = 120000$, $\phi = 0.600$

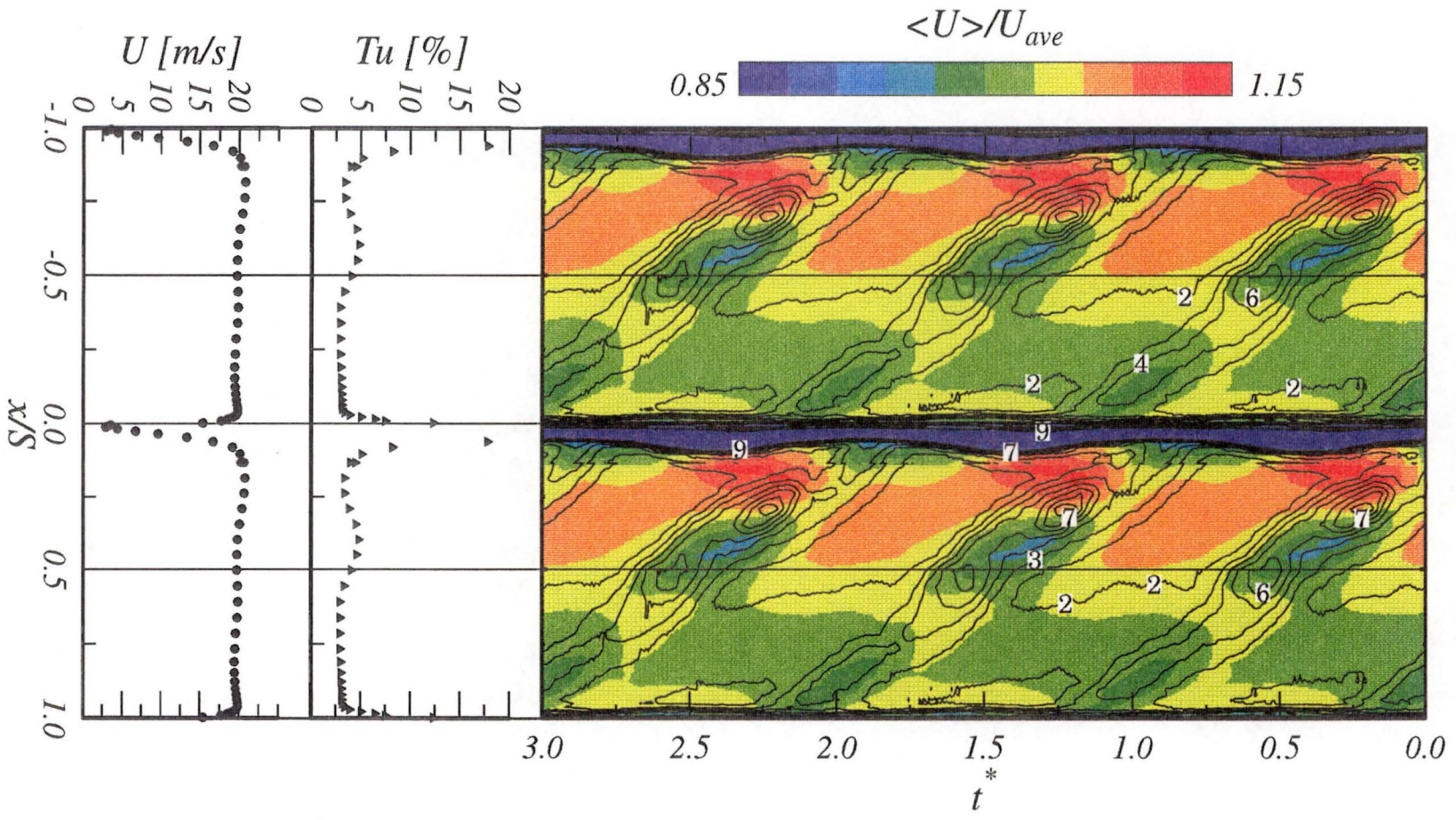

Figure 6.10: Time average velocity U, turbulence Tu. Colour contours of ensemble average velocity $<U>$ with contours of ensemble averaged turbulence $<Tu>$ overlaid. Measurements 1.5 % chord axially downstream of stator trailing edge. $Re_c = 120000$, $\phi = 0.675$

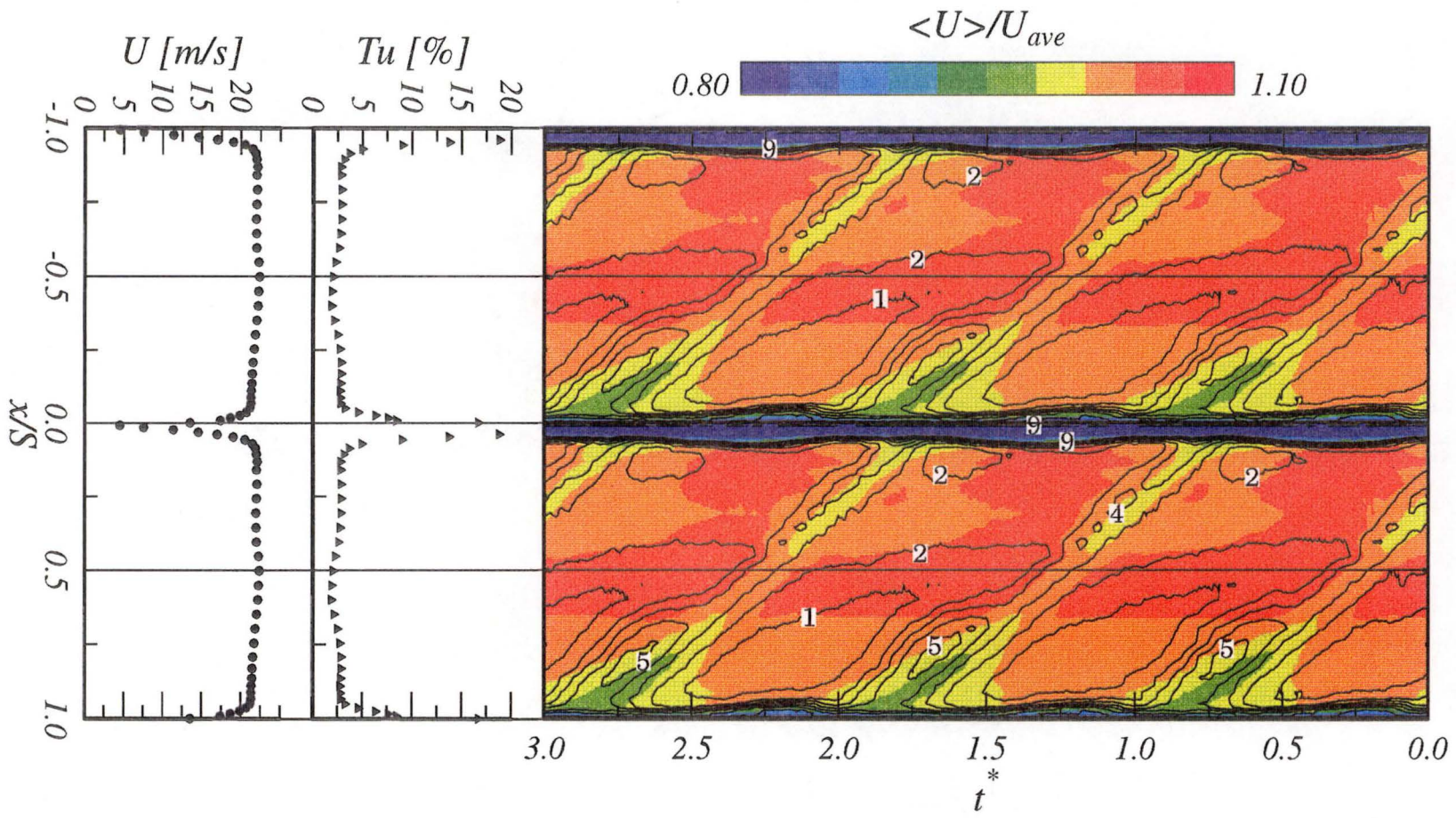

Figure 6.11: Time average velocity U, turbulence Tu. Colour contours of ensemble average velocity $<U>$ with contours of ensemble averaged turbulence $<Tu>$ overlaid. Measurements 1.5 % chord axially downstream of stator trailing edge. $Re_c = 120000$, $\phi = 0.840$

Chapter 7

Intermittency measurement

7.1 Introduction

Constant temperature thermal anemometers, used with either hot-wire or hot-film probes, have sufficient spatial and temporal resolution to follow flow perturbations associated with turbulence. Intermittency detection is the process of characterising the flow as either turbulent or non-turbulent on the basis of the signal from such an instrument. Intermittency γ is defined as the percentage of time turbulent flow is observed at the measurement point.

Reliable intermittency detection allows information such as the transition onset point and transition length to be measured in a consistent and unambiguous manner. Dey and Narasimha [22] present an extensive review of transition length measurement techniques and suggest methods of converting results from these different methods to a consistent basis. They note that minima in surface heat transfer or pitot-pressure, which are often used to define the transition onset point, may occur some distance downstream of the point where turbulent spots are first observed. Accurate assessment of the extent and position of the transition region is only possible where intermittency data is presented.

The current work is aimed at measuring *transitional* intermittency, which is the intermittency associated with the unsteady switching between laminar and turbulent states commonly observed over the length of flow where a boundary layer progresses from a continuously laminar state to a continuously turbulent one. Intermittency is also observed in other situations: many methods described in the literature have been developed for measuring the *edge intermittency* of a fully turbulent boundary layer (Corrsin and Kistler [15], Hedley and Keffer [50]) which describes the boundary between the turbulent flow in the boundary layer and non-turbulent flow from the freestream. Intermittency detection schemes are also used for identifying coherent structures in fully turbulent flow (Blackwelder and Kaplan [9] and Falco and Gendrich [31]). Successful coherent structure or edge intermittency detection algorithms may need modification, or may not work at all in transitional intermittency applications, especially in the presence of changing pressure gradients and boundary layer separation.

For the present work an intermittency measurement technique which would work over the entire surface of a compressor blade was needed. An automatic system was required to process the large volume of data which had been acquired. Minimisation

of manual intervention reduces the subjectivity which is inherent in any intermittency detection algorithm. Many of the existing methods have not been widely applied to the range of pressure gradients and extremes of mean wall shear stress level experienced in this situation.

7.2 Review of some different approaches

Hedley and Keffer [50] and Schon and Charnay [109] provide comprehensive reviews of the intermittency detection process. Narasimha [90] reviews transitional intermittency measurement techniques. Some more recent methods, notably those which make use of the probability density function of the signal, have also been considered in the current work.

Kurtosis method

Townsend [126] defined intermittency as the mean fractional duration of turbulent flow at any given point. Based on the theory of local isotropy Townsend presented expressions for intermittency in terms of the flatness (kurtosis) or the alternatively the skew of the signal from a hot-wire. For intermittent flow with a kurtosis $T(u)$, the intermittency γ is given by

$$\gamma = \frac{T'(u)}{T(u)} \tag{7.1}$$

where $T'(u)$ is the value of kurtosis for steady homogeneous turbulent flow. If the velocity signal was normally distributed then $T'(u) = 3.0$ would be expected. Townsend quotes mean experimental values for this term of 3.5 based on measurements in turbulent flow. This simple theory fails in situations where the probability distribution of either the turbulent or non-turbulent part of the signal deviates significantly from a Gaussian form.

This method has been applied to the surface hot-film data presented in Chapter 8. Results are poor at low intermittency, but are useful for comparison with other methods in the mid to high intermittency range.

Direct method

Townsend [127] described a more direct method for determining intermittency from the velocity signal from an anemometer. An electronic circuit is used to derive a new signal in the form of a random square wave which instantaneously takes the value one in turbulent flow and zero in non-turbulent flow. Intermittency is then found by averaging the square wave over time. Townsend's circuit essentially consisted of an amplifier which emphasised the high frequency component and a rectifier. Townsend observed that this method required a high number of velocity fluctuations in each patch of turbulent flow to give accurate results.

The direct method was used successfully by Corrsin and Kistler [15] and has since found favour with many workers (Hedley and Keffer [50]). In general the early methods were based on custom assembled analogue electronic circuitry. These devices were convenient to use 'on-line' once properly calibrated, but modifications to the algorithm

were difficult. A relatively modern version of an analogue intermittency meter (as used by Gostelow et al. [38]) is described by Alt [4]. Volino and Simon [130] have also recently applied an analogue circuit to the detection of turbulence in a curved plate boundary layer with transitional Taylor-Görtler vortices.

Digital implementations of the intermittency meter have emerged with the advent of inexpensive digital computers. Early software implementations such as the method of Hedley and Keffer [50] were relatively direct translations of the existing analogue algorithms. Digital intermittency detection allows for the development of a wide range of new algorithms. Storage of data and re-processing allows different algorithms and different settings to be compared on the same dataset.

Direct methods can be further divided according to the nature of the algorithm applied and the threshold level selection methods used.

The signal used

Intermittency can be measured using data from one or more velocity, temperature or shear stress gauges. The boundary layers in the current investigation were too thin to accept more than a single hot-wire. Some powerful methods (e.g. Volino and Simon [129]) which use signals from multiple wires were not considered for this reason.

Both hot-wire and surface hot-film signals have been used to measure intermittency in the current work, although the hot-wire has only been used at a single streamwise position. Narasimha [90] suggests that hot-films are possibly more appropriate for measuring transitional intermittency because confusion caused by edge intermittency is minimised. This generalisation cannot hold in separated flow such as the experiments of Malkiel [79] and others where the intermittency distribution of transitional flow is continuously varying and peaks at the centre of the shear layer. Hot-wire traverses in the current work (Chapter 9) show that the peak intermittency also moves away from the wall for attached boundary layers with strong adverse pressure gradients. Hot-film probes under a separated, transitioning shear layer will not register turbulent events until the flow starts to re-attach, and care is needed in interpreting such data.

Common features of direct algorithms

The basic features common to many intermittency detection algorithms are described below in the terminology of Hedley and Keffer.

- *Sensitizing.* The raw velocity (or shear stress etc.) signal is processed to produce a *detector function.* This step aims to accentuate the differences between the probability density functions of the turbulent and non-turbulent parts of the flow.

- *Smoothing.* The detector function will usually need to be smoothed to remove spikes or dropouts and produce a *criterion function.* A spike is a short spurious region of high detector function in a non-turbulent region and a dropout is a short low level area in a turbulent zone. Judgement is required when discriminating between genuine state changes and spikes or dropouts. A characteristic windowing period is commonly selected to aid this process.

- *Thresholding.* The criterion function is now compared to an adjustable threshold level. Regions where the threshold level is exceeded are logged as turbulent.

All three steps need careful consideration if a successful method is to be developed. These processes need to be matched and the success of any method can only be measured by the level of agreement of the results with the user's own subjective judgement.

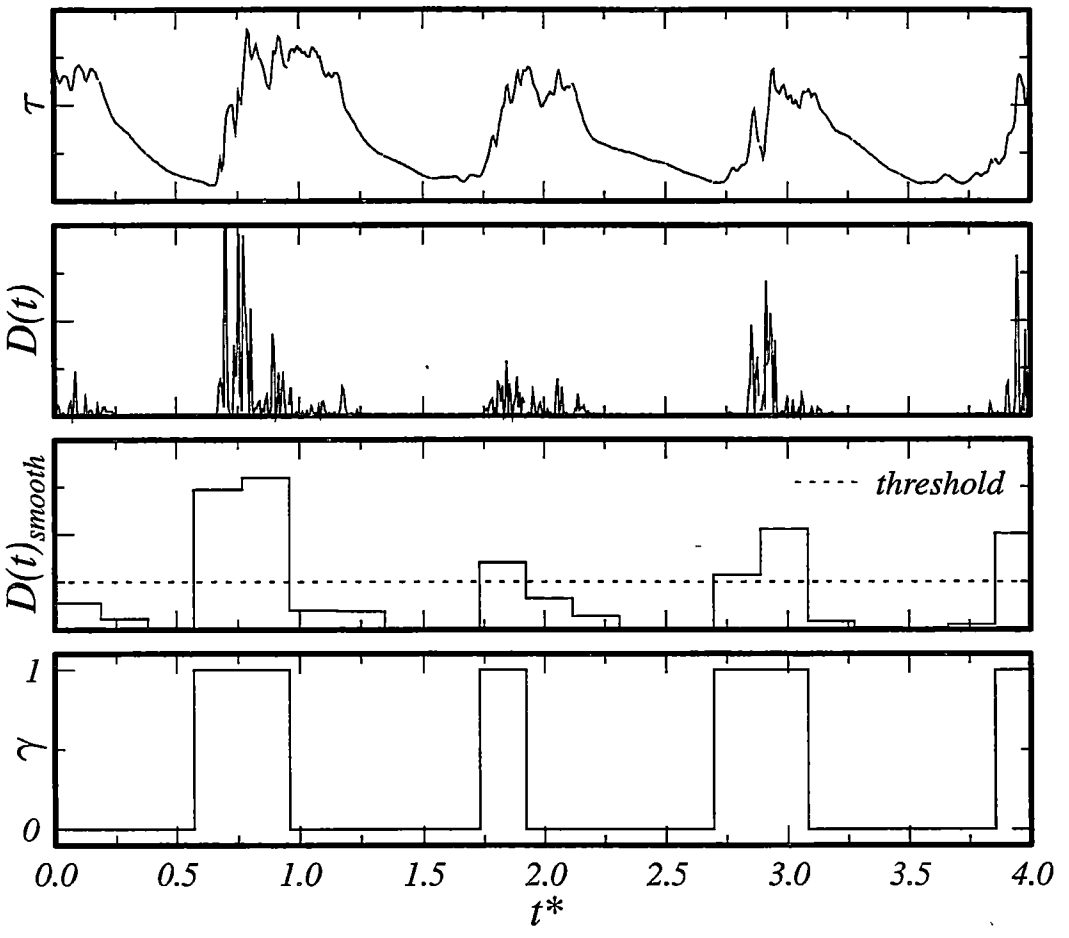

Figure 7.1: Illustration of a simple turbulent intermittency detection algorithm applied to a single surface hot-film signal.

Fig. 7.1 demonstrates a simple intermittency detection algorithm. In this case the signal being processed is the output from a surface hot-film gauge with regular wake-generated turbulent spots. The raw signal τ is sensitised to produce the detector function $D(t)$. In this example $D(t) = (d\tau/dt)^2$. The detector function has been smoothed to give the criterion function, $D(t)_{smooth}$, by simply averaging every 32 data points. An arbitrarily chosen threshold level was then selected and the intermittency γ calculated by comparing the smoothed detector function with the threshold.

7.3 Detector functions (Sensitising)

Hedley and Keffer list a variety of detector functions which have been used by several workers. $|\delta u/\delta t|$ and $(\delta u/\delta t)^2$ have been commonly used for schemes based on a single velocity signal.

There are several characteristics which can be used to identify turbulent flow. One approach is to use signals associated with the Reynolds stresses. The term uv or one of its derivatives is commonly used by workers with boundary layers thick enough for two component hot-wire systems. In a typical transitional boundary layer, ratios of $\overline{uv}$ in the turbulent region to $\overline{uv}$ in the non-turbulent region as high as 164 have been measured by Schon and Charnay [109]. Evidently $\overline{uv}$ is a very suitable function for turbulence detection. An alternative for workers limited to measurements of a single velocity component is to use the turbulent kinetic energy. The ratio of $\overline{u^2}$ in turbulent flow to the non-turbulent level is typically only around 10 indicating the inferiority of this detector function. Blair [10] found excellent agreement when comparing results using $(\delta u/\delta t)^2$ from a single wire with results obtained using $(\delta uv/\delta t)^2$ from an X-wire at the same flow conditions.

Falco and Gendrich [31] used a detector function $u(\delta u/\delta t)$ which is the time rate of change of the streamwise component of turbulent kinetic energy. They demonstrate a good correlation between this term and uv. This detector function has the advantage over alternatives such as u^2 or $(\delta u/\delta t)^2$ that when u is low $\delta u/\delta t$ is generally high (and vice versa) as may be seen by considering a sinusoidal velocity fluctuation and its derivative. This feature reduces (but does not eliminate) dropouts in the detector function during turbulent events and hence less smoothing of this detector function should be required.

7.4 Smoothing

The smoothing process helps to separate the probability density functions of the turbulent and non-turbulent parts of the criterion function by removing spikes and dropouts. This in turn improves the accuracy of the intermittency measurement.

The smoothing process at its simplest consists of averaging the detector function over a series of short window times or bins (Hedley and Keffer [50]). This simple binning process has the disadvantage of increasing the coarseness of the discretisation of the criterion function in time (see Fig. 7.1). All detected turbulent events are an integral number of window periods long under this scheme. Also, all changes of state will be forced to occur at times equal to an integral number of windows from the start time. These limitations are relatively unimportant for determination of time average intermittency, but the degradation of the temporal resolution is a disadvantage when phase-locked averaging is attempted.

A simple, although more computationally intensive, alternative is to allow the window to slide across the detector function one data point at a time in a manner similar to that used by Blackwelder and Kaplan [9]. This method gives a useful improvement in the resolution of the intermittency results in time. The front of a turbulent spot, however, coincides with a very rapid rise in velocity or shear stress. The sliding window method will smear this short-duration event across a window period. (Consider a

step change in detector function). The location of the front in time will then only be accurately measured by the intermittency detection routine if the threshold is correctly chosen, and the necessary threshold value may vary for different turbulence fronts.

Falco and Gendrich [31] combined the thresholding and smoothing steps in a single searching algorithm. This kind of scheme is capable of locating the front of a turbulent patch very accurately by examining the raw detector function. Smoothing is then applied after a candidate patch of turbulence has been identified. If the duration of the detected event is too short then it is discarded. Similarly dropouts in turbulent flow are accepted or rejected depending on the length of the event relative to the window time.

The peak-valley counting (PVC) method of Zohar [145] uses a different smoothing process. In this method, the raw signal is processed to produce a train of peaks and valleys corresponding the extremum points of the velocity signal. When the peak-valley pulse train is first derived it contains many false peaks and valleys. Zohar applies a series of tests (such as disqualifying adjacent peaks or valleys) to remove the false peaks and valleys. This is analogous to the smoothing process described for other methods where false spikes and dropouts are removed. The final test used by Zohar was a combined threshold condition for frequency and amplitude.

The length of the window t_w (the smoothing time constant) needs to be chosen carefully. Sensitivity to the window time varies for different intermittency algorithms. Non-dimensional window times have been suggested by various workers and provide a useful basis for comparing and selecting appropriate window times.

Non-dimensional window times

The time scale used to non-dimensionalise the intermittency detection smoothing time t_w must be chosen from a range of possibilities. Two commonly quoted parameters arising from the theory of turbulence are the Kolmogorov and Taylor microscales. The Kolmogorov length micro scale η is associated with the energy dissipating eddies (Bradshaw [12]).

$$\eta = (\nu/\epsilon)^{\frac{1}{4}} \tag{7.2}$$

where, assuming isotropy, the turbulent dissipation ϵ is given by

$$\epsilon = 15\nu\overline{(\delta u/\delta x)^2} \tag{7.3}$$

The term $(\delta u/\delta x)$ is estimated (by Taylor's hypothesis) to be $\frac{1}{U}(\delta u/\delta t)$ where U is the local mean velocity. The timescale t_K for the Kolmogorov eddies may then be estimated according to

$$t_K = U^{-\frac{1}{2}} \left(\frac{\nu^2}{15\overline{(\frac{\delta u}{\delta t})^2}} \right)^{\frac{1}{4}} \tag{7.4}$$

The Taylor microscale λ is a length associated with the energy containing eddies and is given by (Bradshaw [12])

$$\lambda = \left(\frac{\overline{u^2}}{\overline{(\frac{\delta u}{\delta x})^2}} \right)^{\frac{1}{2}} \tag{7.5}$$

Table 7.1: Typical windowing periods for intermittency measurement (t_w) in terms of appropriate timescales

	t_w/t_K	t_w/t_T	t_w/t_{bl}	t_w/t_v
Blair [10]	150	10	2.5	–
Hedley & Keffer [50]	40	0.8	0.04	8.2
Falco & Gendrich [31]	–	–	0.34-0.51	6
Krogstad & Kaspersen [69]	–	–	0.14	35

Again, using Taylor's hypothesis, a timescale t_T associated with the Taylor microscale is obtained as

$$t_T = \left(\frac{\overline{u^2}}{\overline{(\frac{\delta u}{\delta t})^2}} \right)^{\frac{1}{2}} \tag{7.6}$$

Both t_K and t_T are only meaningful in the turbulent portion of the flow and should properly be calculated using zonal parameters. This limits their usefulness in choosing a window time since their calculation requires prior knowledge of the intermittency function.

Characteristic times suitable for non-dimensionalising the windowing period can also be defined in terms of the boundary layer parameters. A convective timescale associated with the largest eddies possible in the boundary layer t_{bl} is defined as

$$t_{bl} = \delta / U \tag{7.7}$$

where U is the freestream velocity. Alternatively a viscous timescale t_v may be defined by

$$t_v = \nu / u_\tau^2 \tag{7.8}$$

where u_τ is the wall friction velocity. This parameter is clearly not applicable in separating flow.

Table 7.1 lists in non-dimensional form some window times which have been successfully used by various workers. Of these workers only Blair was concerned with transitional intermittency. The other workers were concerned with near-wall bursting (Falco and Gendrich [31]), edge intermittency (Hedley and Keffer [50]) or coherent structures (Krogstad and Kaspersen [69]) and consequently worked in fully developed turbulent boundary layers. Blair's windowing times are considerably longer than those used by the other workers and this is probably due to the need to detect larger eddies associated with the freshly generated turbulent patches of the transitional boundary layer. Scatter in the values chosen by the other workers will be partly due to the slightly different areas of interest and partly due to different sensitivities to window period for the different detection schemes.

7.5 Threshold level selection

The threshold level has a direct effect on the measured intermittency for most possible intermittency detection schemes. A transitional intermittency detection scheme needs

to have a threshold level which is below all likely values of the criterion function in fully turbulent flow (to give 100% intermittency) and above all likely values in non-turbulent flow to give zero intermittency. In flows with arbitrary pressure gradients these requirements can be conflicting if a unique threshold value is used. As in the case of the window time, one approach is to define a non-dimensional threshold level.

Non-dimensional threshold parameters

The dimensional threshold level chosen, T_r, depends on the detector function used and the type of intermittency detection scheme. Walker and Wu [140] used a detector function based on a windowed average value of $(\delta u/\delta t)_{RMS}$. Results using a constant threshold level were compared with those obtained using a non-dimensional threshold parameter C_{tr} given by

$$C_{tr} = \frac{T_r(\text{units of } (\delta u/\delta t)_{RMS})}{\left(\frac{U^2}{\delta}\right)} \tag{7.9}$$

where C_{tr} was taken as a constant value of 0.15. This dimensionless threshold was found to give acceptable intermittency detection over a wider range of Reynolds numbers than the constant threshold level.

Falco and Gendrich [31] used a detector function $u(\delta u/\delta t)$. They defined their non-dimensional threshold C_{tr} in terms of the long-term RMS value of the detector function

$$C_{tr} = \frac{T_r(\text{units of } u(\delta u/\delta t))}{\left(u\frac{\delta u}{\delta t}\right)_{RMS}} \tag{7.10}$$

These workers found that values for C_{tr} in the range 0.1 to 0.4 gave identification of coherent structures in turbulence which most closely agreed with the results of an independent visual inspection of the data.

When a simplified version of Falco and Gendrich's method was applied to hot-wire measurements of a transitional boundary layer, (Chapter 9), Walker and Solomon [137] found that a much higher value of C_{tr} was required (2.0 was used). This agrees with Blair [10], who also described his threshold levels in terms of the long-term RMS of his detector function. The C_{tr} value used by Blair was in agreement with the Walker and Solomon value. The requirement for higher non-dimensional threshold levels when measuring transitional flows than when detecting coherent structures is consistent with the need for longer non-dimensional windowing periods discussed above.

Dual slope methods

Another method which has been proposed for determining the correct threshold level is the dual-slope method. This is an inconvenient method which requires intermittency to be calculated for a range of different threshold levels. The 'correct' threshold is found by examining the plot of threshold vs. intermittency for a clear break-point, or the point of maximum curvature. Kuan and Wang [70] suggest that two straight lines can be fitted to the curve either side of the point of maximum curvature and that the threshold should be taken at the intersection of these lines. The results from the

current work suggests that this procedure is not always possible (Fig. 7.4). Hedley and Keffer [50] failed to find a universal sharp break point in the intermittency vs. threshold curve for all points in the boundary layer. Schneider [108] also found the dual-slope method inapplicable to some of his measurements in a transitional boundary layer.

PDF based methods

After a signal has been divided into turbulent and non-turbulent parts conditional processing can be performed. Probability density functions (PDF) for the laminar and turbulent parts of the signal are easily produced. PDF-based threshold selection schemes have been proposed by several different workers (Schneider [108], Hazarika and Hirsch [49], Ramesh et al. [99] and Kalfas and Elder [66]).

The techniques of Hazarika and Hirsch [49] and Ramesh et al. [99] are based on the assumption that the signal from the intermittently turbulent flow region is a combination of two Gaussian functions with significantly different standard deviations. It is proposed by these workers that the threshold level which gives the minimum probability of incorrect identifications (i.e. the minimum overlap of the turbulent and non-turbulent PDF's) is the level at the intersection of the two probability density functions. Useful results are obtained from this assumption even though the distributions may not be truly Gaussian[1].

7.6 Methods applied to hot-film and hot-wire results

A range of intermittency detection methods were applied to the signals obtained in the current work. The first unsteady signals obtained by the author in the research compressor were the hot-wire boundary layer traverse results of Chapter 9. These were processed by various methods, the most successful of which was a simplified version of Falco and Gendrich's Turbulent Energy Recognition Algorithm (TERA).

The surface hot-film signals presented a greater intermittency detection challenge because of the wide range of conditions the films were subjected to over the whole blade surface. At the leading edge there are very high shear stress levels associated with the very thin boundary layer. Further along the blade the shear stress levels fall as the laminar boundary layer becomes thicker. The normally expected rise in shear stress through transition is somewhat masked by the effects of the strong adverse pressure gradient on the blade suction surface. The presence of separation bubbles further complicates the situation.

TERA

The Turbulent Energy Recognition Algorithm (TERA) of Falco and Gendrich [31] was developed as a turbulent burst detection procedure. The original method was capable of differentiating between bursts and ejections. This refinement was omitted when

[1]Kuo and Corrsin [71] measured the flatness factors of the first and second derivatives of the velocity fluctuation signal in fully turbulent flow and found that although the velocity signal was close to Gaussian the distributions for the derivatives have higher and higher flatness factors as the turbulence Reynolds number increases. It was suggested that a log-normal distribution may give a better description of the probability density functions of these higher order signals.

the procedure was adapted for transitional intermittency measurement by Walker and Solomon [137].

Pseudo-code for the simplified Falco and Gendrich algorithm is given in Table 7.2. The detector function $D(t)$ is described at n time-steps, $t_i = t_0 + i\Delta t$. The threshold is given by T_r and the window period is t_w. t_d is the time since the end of the previously detected event. The pseudo-code assumes the intermittency signal γ is initialised to zero (non-turbulent) at all time-steps.

This method was found to be generally successful when applied to the hot-wire results of Chapter 9, using $u(\delta u/\delta t)$ as the detector function. A modified form of TERA was used in initial attempts to process the surface hot-film (Chapter 8) data. The detector function adopted for the surface hot-film data was $|(\delta\tau/\delta t)|$ where τ is the processed hot-film signal (quasi shear stress). When applied to the hot-film data, the $D(t)_{ave}$ condition caused difficulties. The average value would stay high too long after the turbulent part of a turbulent spot had passed, causing erroneous identification of the relaxing laminar flow behind the turbulent spot as turbulent. One attempt to reduce this problem was made by using the condition $(KD(t)_{ave} > T_r)$ to continue the turbulence identification, where K was some constant less than one. This was not successful because some spots were more badly affected by the $D(t)_{ave}$ problem than others. Consequently an alternative intermittency detection scheme (PVC / PDF) was developed.

7.7 PVC / PDF

For the processing of the surface hot-film data of Chapter 8, a new intermittency detection algorithm was developed. The procedure adopted borrows from the peak-valley counting (PVC) method of Zohar [145] and uses a PDF-based threshold detection algorithm similar to that of Hazarika and Hirsch [49].

The new intermittency detection algorithm is outlined in pseudo-code form in Table 7.3. The detector function used with the hot-film data was $D(t) = (\delta\tau/\delta t)$. Zohar produced his peak-valley signal and then removed spurious peaks or valleys. Instead, the current method applies the threshold to the signal before finding peaks and valleys, this prevents many of the spurious peaks and valleys from being identified in the first place. (Once applied in this way the threshold is not used again in the current method.) As in the TERA case the intermittency signal γ is initialised to zero (non-turbulent) at every time-step. Regions where peaks and valleys are found close together (closer than t_w) are tentatively identified as turbulent. This process fills in dropouts. A second pass is made to remove any regions of turbulence shorter than t_w (spikes).

Threshold selection is relatively easy when the turbulent and non-turbulent parts of the detector function have significantly different standard deviations. Hazarika and Hirsch [49] suggest this ratio may be an order of magnitude for bypass transition. Fig. 7.2 shows that in the case of the surface hot-film signals the ratio of standard deviation of the turbulent part of the detector function to the standard deviation of the laminar part is below 10 at all point on the blade surface. Partly for this reason attempts to specify threshold levels manually over the blade surface gave unsatisfactory results. Fig. 7.6 (a) shows a surface distance - time plot of the phase-locked average

Table 7.2: Pseudo-code for TERA

```
while (i < n) do
    if (D(t) > T_r) then
        t_d = (i − i_end)Δt
        if (t_d > t_w) then
            (assume a new event is starting)
            i_start = i
        else
            (assume this is a continuation of previous event)
            i_start = i_end
        endif
        while (event_continues) do
            (calculate the average value of D(t) over the window, D(t)_ave)
            if (D(t)_ave > T_r) or (D(t) > T_r) then
                event_continues = true
            else
                i_end = i
                event_continues = false
            endif
            i = i + 1 (next point)
        enddo
        t_d = (i_start − i_end)Δt
        if (t_d > t_w) then
            (fill γ with '1' back to i_start)
            i_end = i
        else
            (event was too short, ignore)
            i_end = i_start
        endif
    endif
    i = i + 1 (next point)
enddo
```

Table 7.3: Pseudo-code for peak-valley counting

(Smooth signal, if required)
do $(i = 1, n)$
    (apply threshold to detector function)
    if $(D(t) < T_r)$ then $D(t) = 0$.
enddo
do $(i = 1, n)$
    (find peaks and valleys)
    if (peak in $D(t)$ at t_i) then $PVC(i) = 1$
    if (valley in $D(t)$ at t_i) then $PVC(i) = -1$
    otherwise $PVC(i) = 0$
enddo
do $(i = 1, n)$
    (fill in all possible turbulent areas)
    if $(PVC(i) <> 0)$ then
        $t_d = (i - i_{start})\Delta t$
        if $(t_d < t_w)$ then
            (set $\gamma = 1$ from t_i back to t_{start})
        endif
        $i_{start} = i$
    endif
    $i = i + 1$ (next point)
enddo
(Now remove all spikes, where $\gamma = 1$ over periods less than t_w)

intermittency over the whole blade surface. This plot shows uneven growth in the turbulent region (shown in red) along the blade surface, especially on the suction surface.

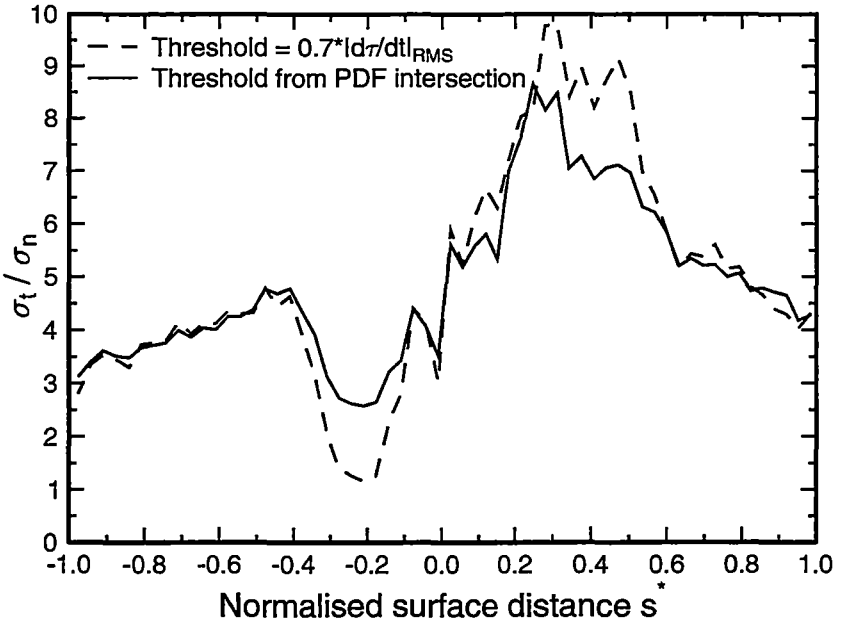

Figure 7.2: Ratio of standard deviations of turbulent and non-turbulent components of the detector function

After trying several different dimensionless thresholds a threshold selection scheme based on the PDF method described by Hazarika and Hirsch [49] was tried. For the current work an iterative approach was used to find the best threshold. Starting with a threshold level of $0.7(\delta\tau/\delta t)_{RMS}$ an initial intermittency result was used to conditionally process the detector function. Probability density functions were produced for the turbulent and non-turbulent parts of the detector function and these were fitted (as well as possible) by Gaussian distributions. The intersection of the two Gaussian curves was then used as the threshold level for the next iteration. This refinement process made a relatively small difference to the long term intermittency (Fig. 7.3) but did give a useful improvement in the quality of the predictions for individual traces. The resulting time - distance plot of intermittency (Fig. 7.6 (b)) shows a much smoother growth of turbulent zones than the results obtained with the manual threshold levels. The threshold refinement scheme did not work well at the leading edge because the effects of the passage of the wake over the thin laminar boundary layer here were erroneously identified as turbulence. A lower limit were applied to the threshold level to reduce this problem.

The sensitivity of the new method to variations in the threshold and window times was investigated and some typical results are presented in Fig. 7.4 and Fig. 7.5. The variation of intermittency with the threshold level is clearly not suitable for application of the dual-slope method at $s^* = 0.79$. The intermittency gradually increases with window level. A constant window time of 400 μs (12% of the blade passing period at $Re_c = 120000$) was found to give reasonable results over the whole blade. Curves of

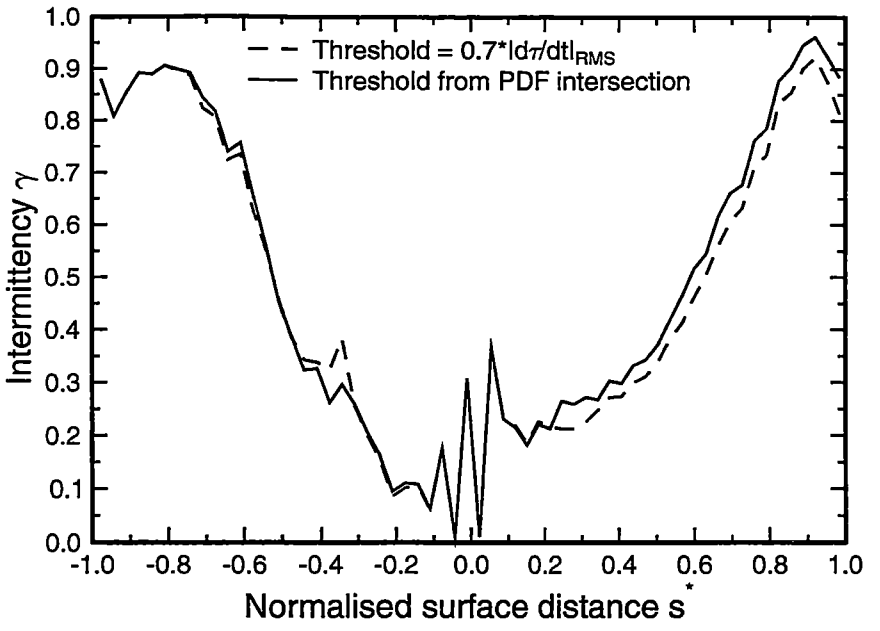

Figure 7.3: Effectiveness of the PDF threshold refinement technique

intermittency vs. window period show a decrease in slope at around this level.

7.8 Relaxing flow detection

A simple *relaxing flow* detection algorithm was implemented to further investigate this particular characteristic of the shear stress signals obtained from turbulent spots in a transitional boundary layer. The logic for the relaxing flow detector was applied sequentially after the intermittency processing described in Table 7.3. Pseudo-code for the relaxing flow detection scheme is given in Table 7.4. The signal *REL* is initialised to '0' at every time-step prior to running the detection algorithm. The detector then fills in all regions where the quasi shear stress signal is decreasing following a turbulent to non-turbulent transition.

This simple approach was found to give very reasonable results. Fig. 7.7 demonstrates the effectiveness of the intermittency detection scheme on some typical individual surface hot-film results. Regions identified as turbulent are indicated in red, non-turbulent regions are shown in blue. Green indicates the relaxing flow areas (which are also non-turbulent). A window time of 450 μs was used and the blade passing period for this case was about 3.4 ms. (Note that the window time is applied to the whole of the non-turbulent part of the signal, not just that shown in blue, so that in some cases areas of blue shorter than one window period are possible provided they are preceded by a green section of sufficient duration.) In some cases turbulent flow is not followed by relaxing flow, because the relaxing flow region was either too short and disallowed or non-existent.

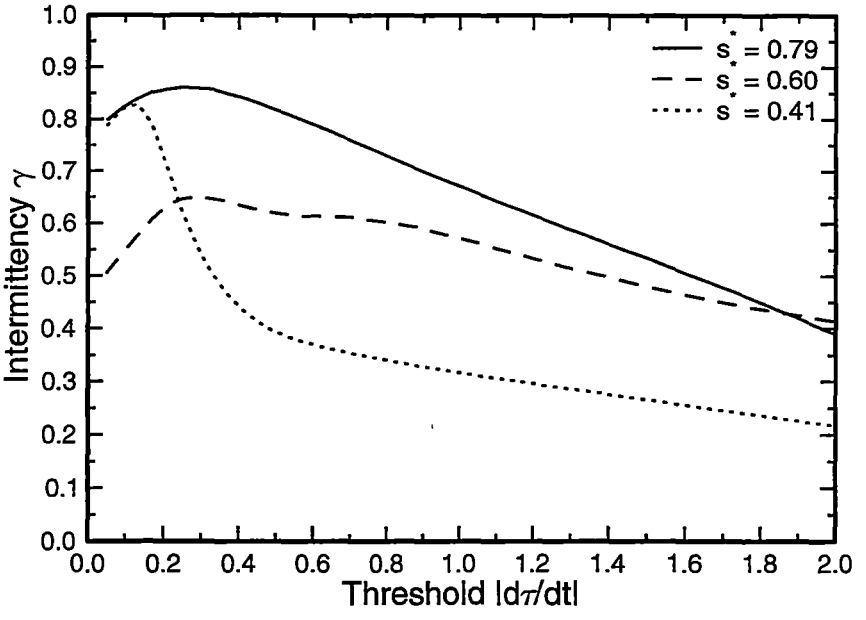

Figure 7.4: Effect of threshold variation on intermittency

7.9 Conclusions

The transitional intermittency detection schemes which have been adopted in the current work use dimensionless parameters for the selection of window times and threshold levels. This gives these methods an improved level of generality. It should be noted however that the universality of intermittency detection schemes can be dependent on the frequency response of the instrument and the sampling frequency used. Poor frequency response which affects spectrum of the signal can seriously degrade the performance of the intermittency detection algorithm.

Transitional intermittency detection algorithms require longer dimensionless window times and higher dimensionless threshold levels than coherent structure or edge intermittency detection schemes which operate in fully turbulent boundary layers.

A range of methods were applied to the unsteady measurements taken in the compressor during the current work. The turbulent energy recognition algorithm of Falco and Gendrich [31] was found to be particularly successful for processing the hot-wire results of Chapter 9. The shear stress measurements from the surface mounted hot-film array of Chapter 8, however, needed a different scheme in order to achieve reasonably uniform results over the whole blade surface.

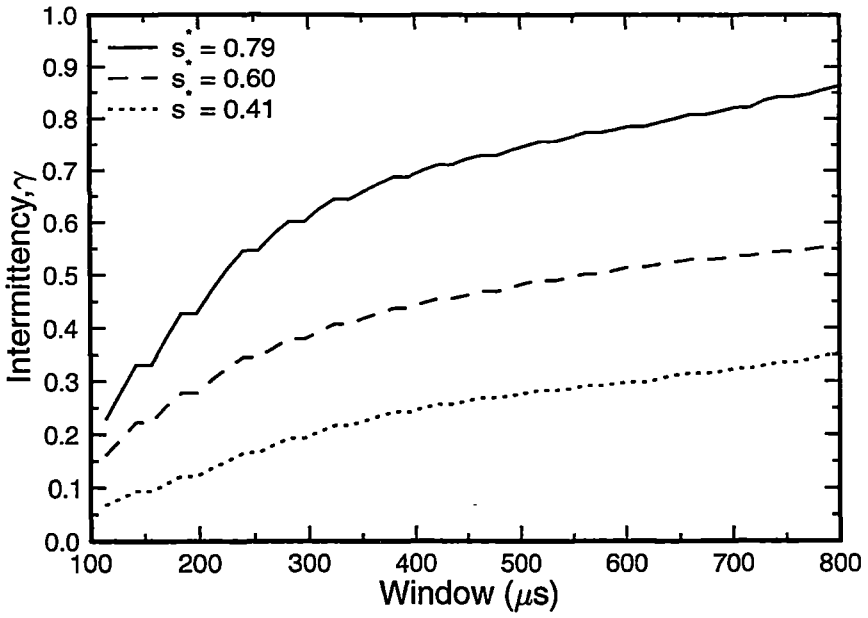

Figure 7.5: Effect of window variation on intermittency

Table 7.4: Steps involved in relaxing flow detection

(First process signal to produce a γ signal - Table. 7.3)
do $(i = 1, n)$
    if $(\gamma(i) < \gamma(i-1))$ then
        (found turbulent to non-turbulent transition)
        $REL(i) = 1$
    else
        $REL(i) = 0$
enddo
do $(i = 1, n)$
    if $(REL(i) = 1)$ then
        while $(D(t) < 0)$ do
            $REL(i) = 1$
            $i = i + 1$
        enddo
    endif
enddo
(Now go through and cull out regions where the length of relaxing flow is shorter than t_w)

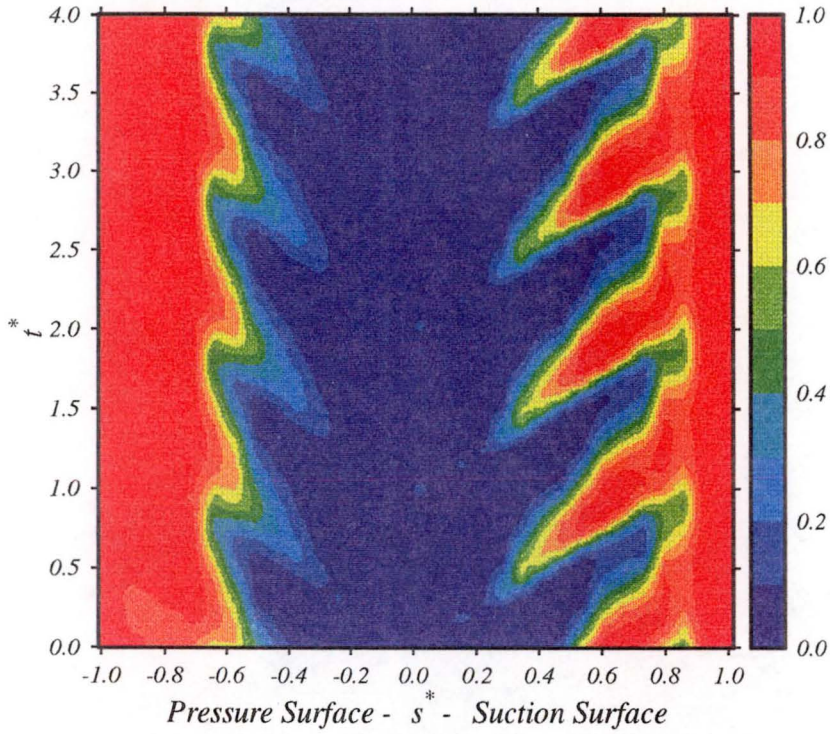

(a) Manual threshold levels

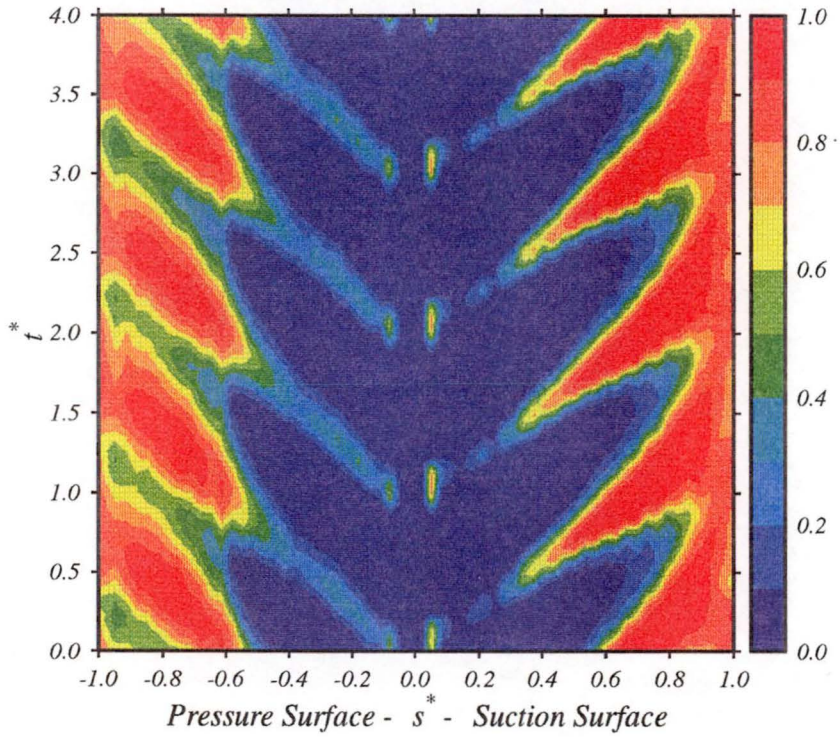

(b) PDF Threshold levels

Figure 7.6: Time-distance contour plot: ensemble average intermittency, comparison of threshold methods. $Re_c = 120000$, $\phi = 0.675$

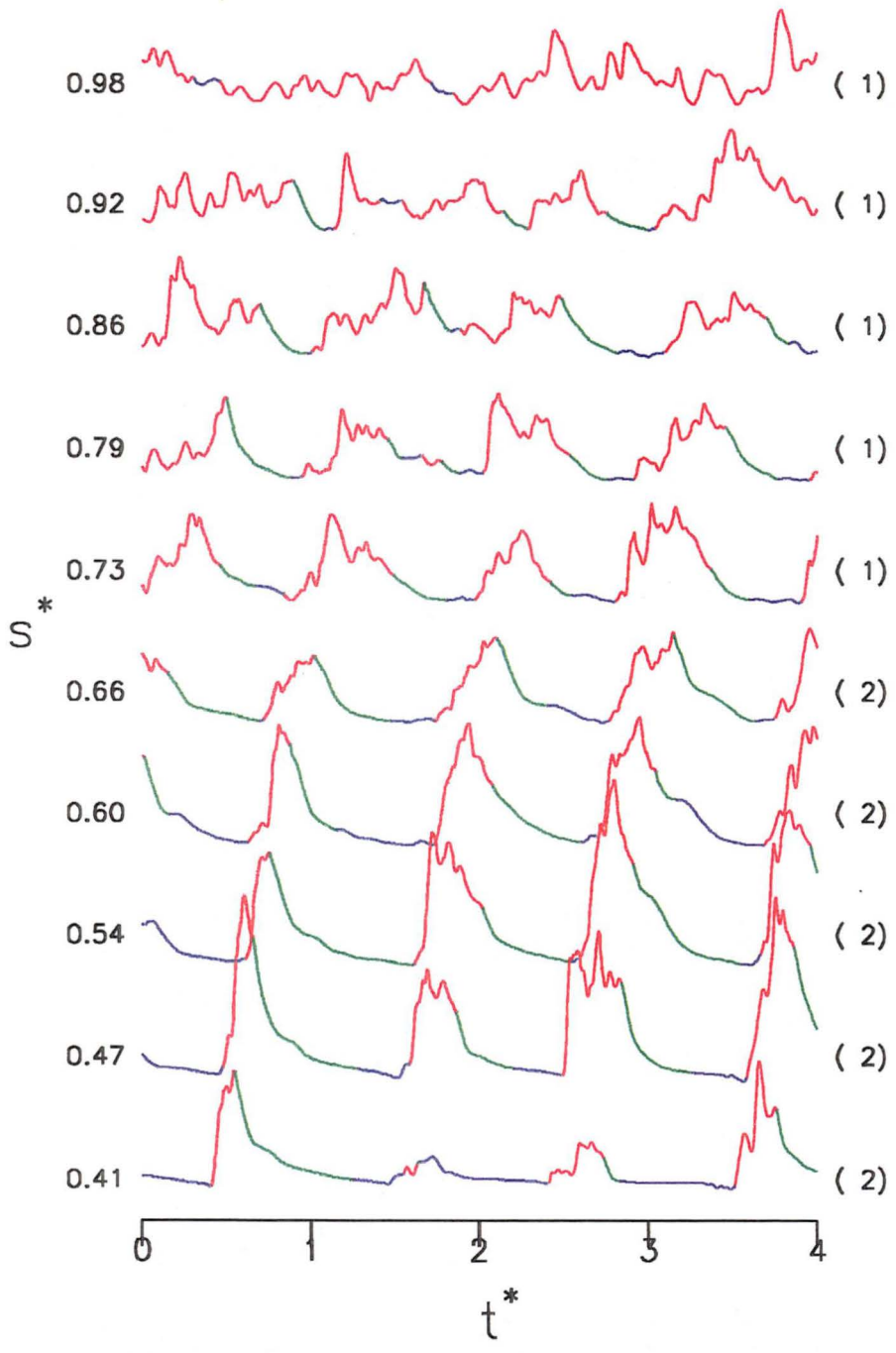

Figure 7.7: Typical individual quasi shear stress records at fractional positions s^* over the stator blade suction surface plotted against dimensionless time t^*. Line colour indicates local flow state as determined by the intermittency detection algorithm: red for turbulent, green for laminar and relaxing and blue for remaining laminar. The grouping number at the right indicates sets of traces which were measured simultaneously. $Re_c = 120000$, $\phi = 0.675$

Chapter 8

Hot-film survey results

8.1 Introduction

Multi-element surface hot-film arrays can provide much useful information about the state of a developing boundary layer. Appendix C reviews some operation techniques commonly applied with this type of instrument and details the procedure followed in the current work. The sensors in the current investigation were operated using TSI IFA-100 model anemometer bridges and signal conditioners. Few workers have attempted a full calibration in terms of wall shear stress with surface hot-films and this has not been tried here. Instead the semi-quantitative approach of Hodson [53] has been used. Information about the instantaneous state of the boundary layer can be obtained from the relative amplitudes and frequencies of the observed raw signal fluctuations. When coupled with the intermittency detection techniques discussed in Chapter 7 the state of the boundary layer can be quantitatively described. Turbulent spot propagation speeds can also be measured without the need for full calibration.

8.2 The surface hot-film array

The Senflex brand surface hot-film array consisted of a 0.05 mm thick polyimide sheet with electron beam deposited nickel sensors. The sensor elements were manufactured with a pitch of 2.54 mm and there were 61 sensors in total. The sensors were arranged in-line and the film was wrapped around the blade to place the sensors at mid-blade height (Fig. 8.8). The film fitted the blade smoothly and no large air-bubbles were trapped under the film. The analysis of Chapter 5 shows that the effect of the film on the blade surface pressure distribution is negligible. The signal wires were connected to the sensor array close to the blade root and led out through a hole in the blade root to a connection box. The blade profile was slightly altered where the sensor wires were attached to the film but this region of disturbance, which was partly immersed in the hub wall boundary layer, was not expected to alter the flow significantly at mid-blade height. Fig. 8.1 shows the distribution of sensors around the blade profile; coordinates for the sensor locations are given in Appendix A.

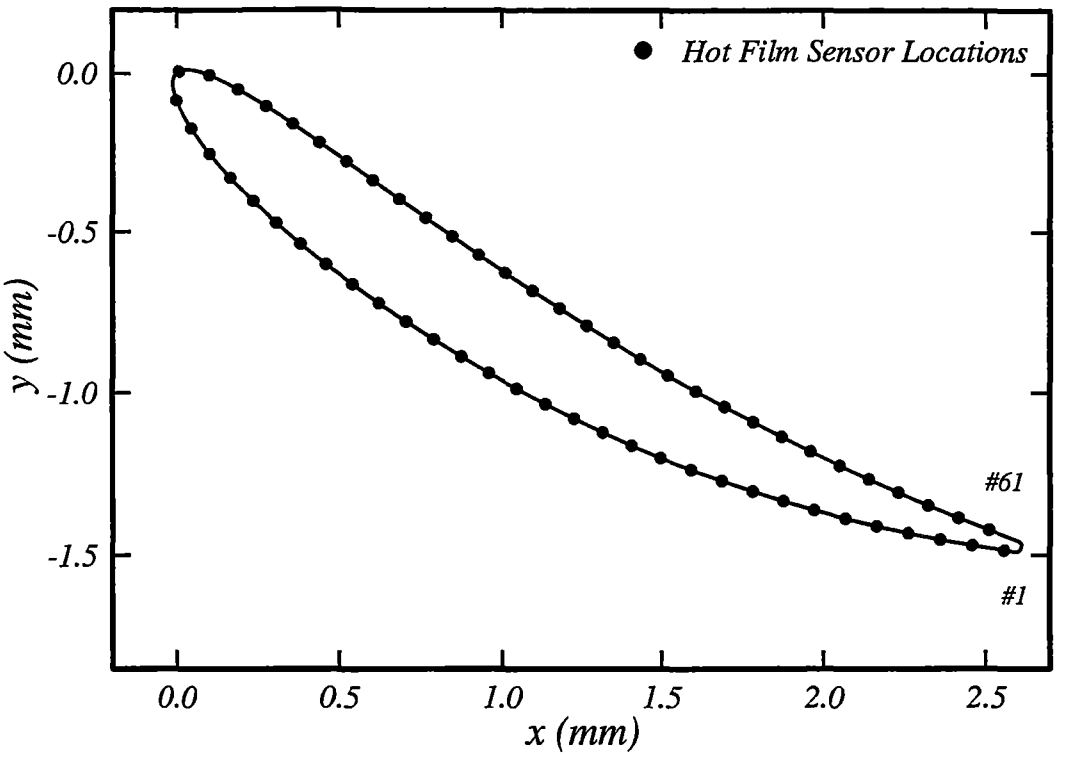

Figure 8.1: Position of the surface hot-film sensing elements on the surface hot-film instrumented stator blade

8.3 Data acquisition

The number of films which could be operated simultaneously was limited by the available number of constant temperature anemometer channels. For the first set of measurements three anemometers were available; later two more were acquired to give a total of five. To minimise possible sensor-sensor interference during simultaneous operation, every second sensor was used. An estimate of the level of cross channel interference was obtained by observing the output from a downstream film while a square wave was applied to the upstream film (this square wave was simply the frequency test signal from the anemometer). Even using adjacent films the effect on the downstream sensor output was minimal. Results for the whole blade were achieved by interleaving results from the odd numbered films with results from the even numbered films.

Each time measurements from a different set of sensors were required, it was necessary to stop the compressor, physically change the anemometer connections and re-tune the bridges (to allow for the different cold resistances of the different individual sensors). Using five anemometer channels, a complete survey of the unsteady shear stress on the blade surface could be achieved with 12 compressor runs.

Each anemometer output was AC coupled with a high-pass cut-off frequency of 0.1 Hz. The signal was also low-pass filtered with a cut-off frequency of 20 kHz to avoid aliasing. A sampling rate of 50 kHz per channel was chosen. (At $Re_c = 120000$,

the blade passing frequency is 296 Hz at standard atmospheric conditions.) Time mean values of the anemometer bridge voltage were also recorded to allow comparison of relative shear stress levels between sensors.

An analogue to digital converter (ADC) with a maximum throughput of 1 MHz and a resolution of 12 bit was used to digitise the anemometer output signals. A simultaneous sample and hold buffer on the ADC was used to ensure truly simultaneous sampling. Signal conditioner gains of between 50 and 100 were used to match the voltage range of the anemometer output to the ADC input and give the best possible signal to noise ratio. The data was taken in blocks with lengths set at integral powers of 2 to simplify any future digital Fourier transform processing and optimise digital storage utilisation. The block length was chosen to be the lowest integral power of two which would cover at least 5 blade passing periods. This gave 1024 samples at $Re_c \geq 120000$ and 2048 samples at $Re_c = 60000$.

The shaft zero marker reference signal was used to synchronise ensemble sampling and ensure that each repeated trace in the ensemble corresponded to the passage of the same group of rotor blades. At first 256 and later 512 repeats were taken at each sensor. Binary data storage required for all sensors on the blade at one operating condition was approximately 60 Mb (or 120 Mb at low speed). All the raw unsteady data was stored to allow re-processing. Availability of the raw data was especially valuable for comparative evaluation of different intermittency detection methods (Chapter 7).

8.4 Interpretation of anemometer output

Surface mounted hot-films have a relatively large heat flux to the substrate and the blade below. The time lags inherent in this process make accurate calibration difficult in unsteady flow. Following Hodson [53] and later workers a dimensionless term, quasi shear stress (τ), has been derived from the raw anemometer output signal. Quasi shear stress τ is proportional to the true wall shear stress τ_w (at least in steady flow)

$$\tau_w \propto \left(\frac{E^2 - E_0^2}{E_0^2} \right)^3 = \tau \tag{8.1}$$

Use of the zero-flow anemometer voltage E_0 in the numerator of the above expression gives τ a true zero. Note, however, that the hot-film cannot sense direction and gives a rectified version of the true signal if there is any flow reversal. See Appendix C for a more complete description of the quasi shear stress expression.

Fig. 8.2 (a) shows some typical raw voltage traces from the sensor at $s^* = 0.60$. Fig. 8.2 (b) shows the same signals re-processed to give quasi shear stress. The effect of the processing is to strongly enhance the peaks of the signal. τ gives a much better indication of the approach of the boundary layer to separation than the raw voltage E because the processed signal has a true zero.

The location of all the hot-film measurements in time and space are expressed non-dimensionally in terms of s^* and t^*. s^* is surface distance measured from the leading edge normalised by the maximum surface distance for the surface in question. Positive values of s^* denote sensor locations on the blade suction surface and negative s^* values indicate pressure surface sensors. t^* is time normalised by the blade passing period.

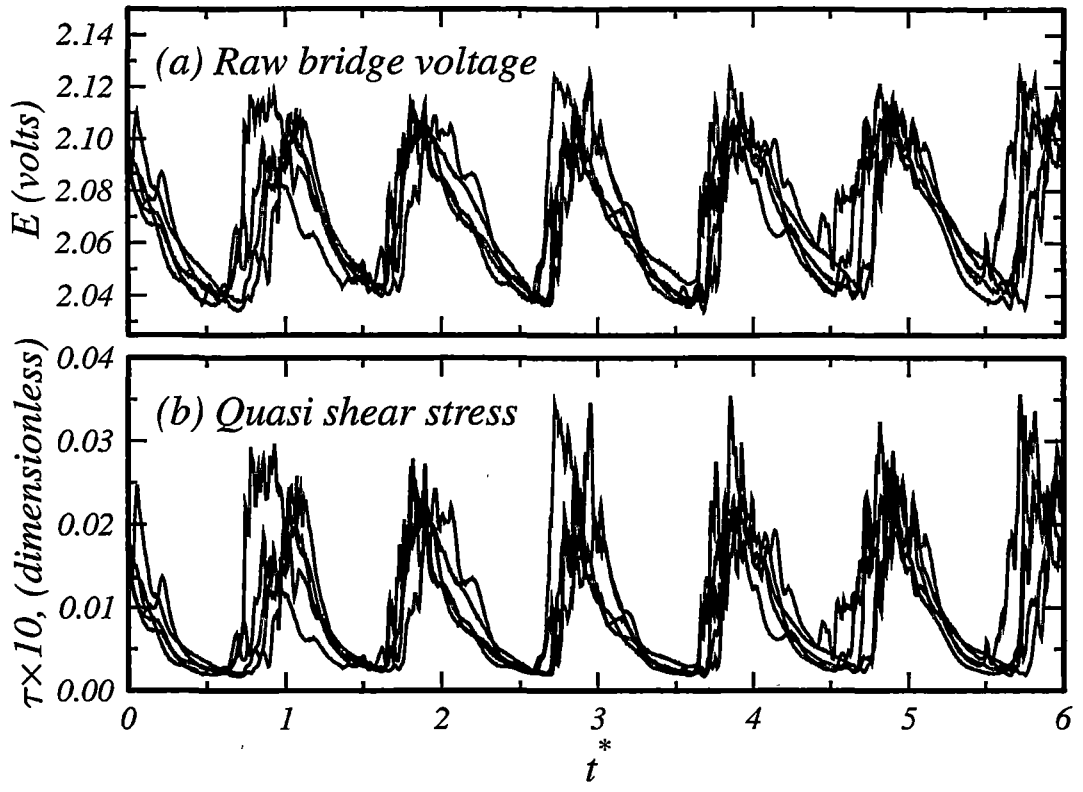

Figure 8.2: Five individual hot-film records at $s^* = 0.60$ on the suction surface. $Re_c = 120000, i = 1.24°$

8.5 Surface hot-film test cases

The surface hot-film test cases were introduced in Table 4.1. There were three series of hot-film measurements taken in the current investigation. First, the effect of Reynolds number was studied. With the machine operated at a constant flow coefficient of $\phi = 0.675$ measurements were taken at three different Reynolds numbers. Secondly, the machine was operated at constant Reynolds number ($Re_c = 120000$) and the flow coefficient was set to give two off-design incidence test cases either side of the $\phi = 0.675$ case. These two series, each of three cases with one overlapping, give a total of five test cases.

A third series of test cases was taken with one of the rotor blades removed and replaced with a counterweight which was hidden to the flow. This *blade-out* series was taken at constant Reynolds number ($Re_c = 120000$) with the same flow coefficients as for the incidence series described above. For the purposes of the current investigation any change in average flow angle caused by the reduced blade count has been neglected. No flow angle measurements were made with the rotor blade removed.

The three series of test cases are summarised in Table 8.5 which includes details of the unsteady data acquisition parameters.

Table 8.1: Surface hot-film test cases, # channels is the number of sensors operated simultaneously, # samples is the number of samples in a single trace and # in ensemble is the total number of traces in each ensemble of phase-locked data.

Reynolds number series, $\phi = 0.675$			
Re_c	60000	120000	170000
$i°$	0.23	1.24	1.41
Re_1	58000	117000	166000
# channels	5	5	3,5*
# samples	2048	1024	1024
# in ensemble	512	512	256,512*

Incidence series, $Re_c = 120000$			
ϕ	0.600	0.675	0.840
$i°$	4.11	1.24	-6.11
Re_1	110000	117000	130000
# channels	5	5	5
# samples	1024	1024	1024
# in ensemble	512	512	512

Blade-out series, $Re_c = 120000$			
ϕ	0.600	0.675	0.840
(Angles not measured)			
# channels	5	5	5
# samples	1024	1024	1024
# in ensemble	512	512	512

* In all cases odd and even numbered films were operated in separate compressor runs. In this particular case the odd numbered films were operated with three simultaneous channels and 256 traces per ensemble.

8.6 Long term average values and envelope curves

Variations of long-term average quasi shear stress are shown in Fig. 8.3 for the Reynolds number series and Fig. 8.4 for the incidence series. The long-term average quasi shear stress $\bar{\tau}$ gives a general indication of the development, transition and separation of the boundary layer. A logarithmic scale has been used to accommodate the wide range of shear stress values. The long dashed lines show the maximum and minimum values of the phase-locked average quasi shear stress $<\tau>$. In a random flow these lines should coincide and where there is strong periodicity in the flow there will be a significant difference in the maximum and minimum values of $<\tau>$. The short dashed lines show the maximum and minimum values of instantaneous quasi shear stress τ. These will only coincide for a laminar flow where the signal fluctuation level is low. The separation of minimum and maximum values of this parameter reflect both periodic and random unsteadiness in the signal.

The saw-toothed nature of the curves in Fig. 8.3 (c) are the result of the interlacing of measurements from separate runs of the compressor. While this procedure gave acceptable results for the other test cases, at low Reynolds number repeatability of the compressor set point is not as good. A slight change in operating condition can have a large change in the amount of intermittent separation at the low Reynolds number.

All five test cases show a local minimum of $\bar{\tau}$ in the stagnation region at the leading edge followed by strong acceleration up to about $s^* = 0.05$ on both pressure and suction surfaces. On the suction surface ($s^* > 0$) in all cases there is a general tendency for $\bar{\tau}$ to fall as the pressure gradient becomes increasingly adverse towards the trailing edge. This is resisted by the progress of wake-induced transition around mid-chord, but even the resulting turbulent layer is unable to withstand the strong gradients for $s^* > 0.9$, where $\bar{\tau}$ falls rapidly and turbulent separation is approached. With reducing incidence the rearward movement of the transition zone induced by the changing surface pressure distribution (see Fig. 5.3) eventually results in the development of laminar separation on the suction surface; this is particularly evident in the negative incidence case of Fig. 8.4 (c) which shows local minima in all curves around $s^* = 0.7$. The minimum value of τ for the incidence series (Fig. 8.4) is around 10^{-5}. Values below 10^{-4} are probably associated with separation.

On the pressure surface, the values of $\bar{\tau}$ generally fall in response to the positive pressure gradient near the leading edge, but subsequently increase in the region of accelerating flow and transition over the rearward part of the blade. The sharp local minimum in $\bar{\tau}$ at $s^* = -0.08$ for $i = -6.11°$ (Fig. 8.4 (c)) indicates the presence of a leading edge separation bubble. The gauge nearest the trailing edge on the pressure surface exhibits a sharp decrease in shear stress at all incidence values.

Regions of high periodicity are indicated by a significant separation of the minimum and maximum phase-locked average quasi shear stress $<\tau>$ values. At the trailing and leading edges where the flow is essentially fully turbulent or fully laminar, the minimum and maximum $<\tau>$ curves (long dash) are close together indicating a lack of periodicity. The onset of wake-induced transition approximately coincides with the streamwise location where the periodicity first develops. On the suction surface of the Reynolds number series (Fig. 8.3) this point moves rearward with decreasing Reynolds number. On the pressure surface (for both series) the separation of the minimum and maximum $<\tau>$ values is less pronounced. The pressure surface periodicity onset

points also move further rearward with decreasing Reynolds number. Increasing negative incidence (Fig. 8.4) gives a reduced adverse pressure gradient and the onset of wake-induced transition is delayed. The $i = 1.24°$ case shows the most pronounced periodicity. There is also a considerable degree of periodicity in the reattaching flow on the suction surface in Fig. 8.4 (c) around $s^* = 0.7$ and following the leading edge separation bubble on the pressure surface of that case. This suggests that separated flow transition is also influenced by wake passing. The end of wake-induced transition cannot be reliably inferred from the phase-locked average τ envelope curves because periodicity may persist in the turbulent boundary layer some distance downstream of the end of transition.

Divergence of the envelope curves for instantaneous values of τ (short dash) is largely dependent on random fluctuations of quasi shear stress. Although masked by the strong gradients of $\bar{\tau}$, this divergence commences quite close to the leading edge, where it probably reflects potential flow interactions associated with freestream turbulence. It subsequently increases to reach a maximum around the centre of the transition zone and decreases to a lower value thereafter, although this is less evident on the suction surface where the flow is strongly decelerating. The ratio of divergence in the instantaneous τ envelopes to that of the ensemble average envelopes is noticeably greater where transition occurs through a separation bubble.

8.7 Individual traces

Individual traces from every second hot-film blade are shown in figures 8.18 to 8.22 and for the $\phi = 0.675$ blade-out case in Fig..8.23. The instantaneous data from each channel has been normalised by the long term mean value of quasi shear stress for that channel. This causes the low apparent fluctuations at the leading edge where the average shear stress values are high, and high apparent fluctuations where the average shear stress is low and the flow is close to separation. Only results for odd-numbered films are shown, partly for space reasons but also to allow tracking of simultaneous events. Sets of sensors which were used simultaneously are indicated by the bracketed grouping numbers at the right of each trace.

The traces have colours assigned to various sections depending on the results of the intermittency detection algorithm. Red indicates turbulence, green relaxing non-turbulent flow, and blue is laminar flow. For the purposes of calculating intermittency γ, the relaxing flow (green) is counted as laminar (see Chapter 7).

The intermittency detection algorithm has undergone various modifications since it was first applied to these results. At the leading edge some τ fluctuations caused by unsteadiness in the freestream have been spuriously identified as boundary layer turbulence. The Reynolds number series was first presented in Solomon and Walker [120] where intermittency detection was made using a manual threshold method. This was laborious but did enable high thresholds to be set at the leading edge to prevent the spurious detections. In that work the time-space diagrams were produced from odd-numbered sensor measurements only, so the interlacing problem for the $Re_c = 60000$ case was avoided. The time-space intermittency plots obtained with manual thresholding showed a degree of inconsistency from one sensor to the next. The incidence series (first produced for Solomon and Walker [118]) used an automatic (PDF-based)

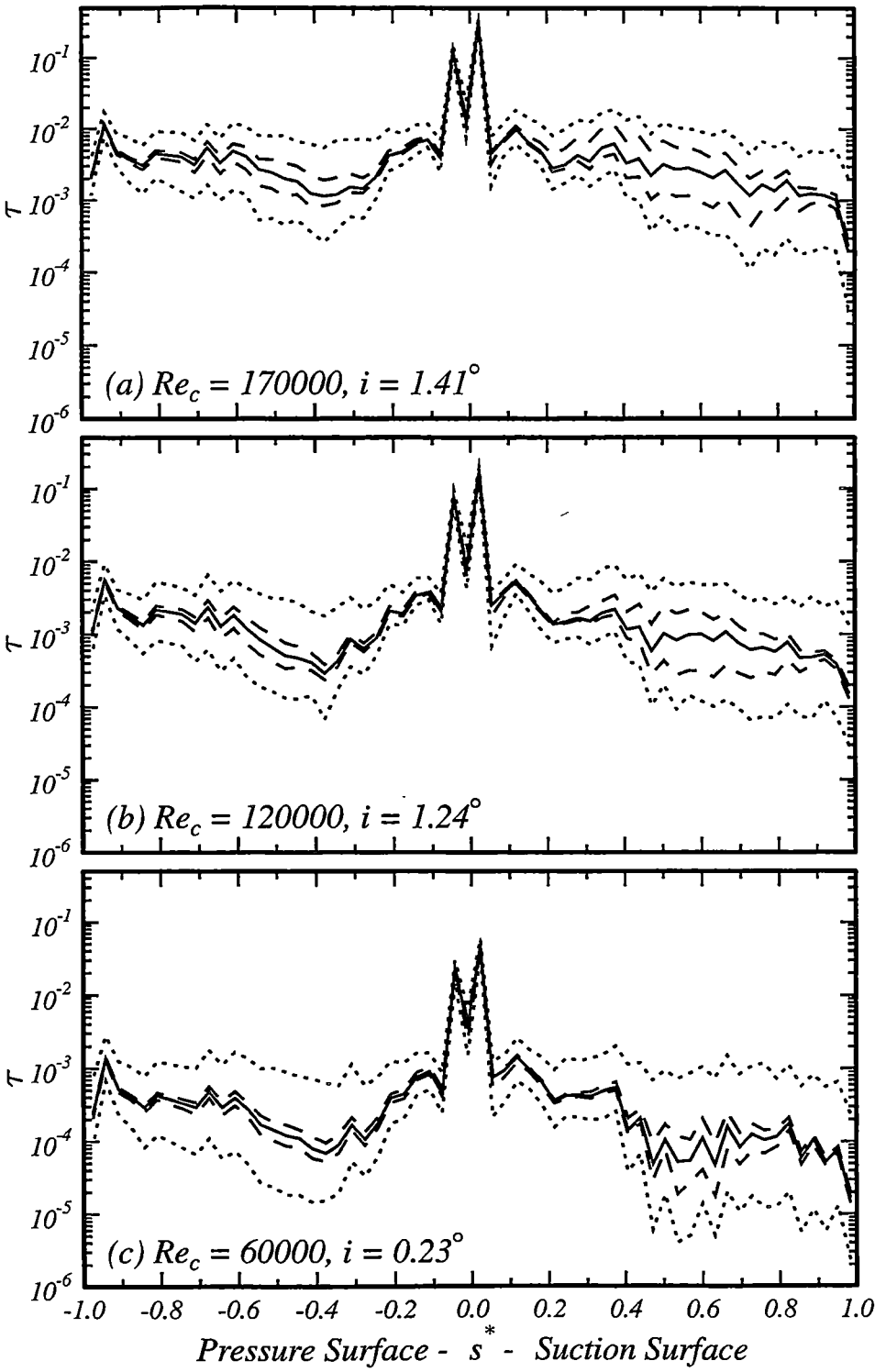

Figure 8.3: Variation of long-term mean (solid line), maximum and minimum ensemble means (long dash) and maximum and minimum instantaneous values (short dash) of quasi shear stress, τ. Reynolds number series. $\phi = 0.675$

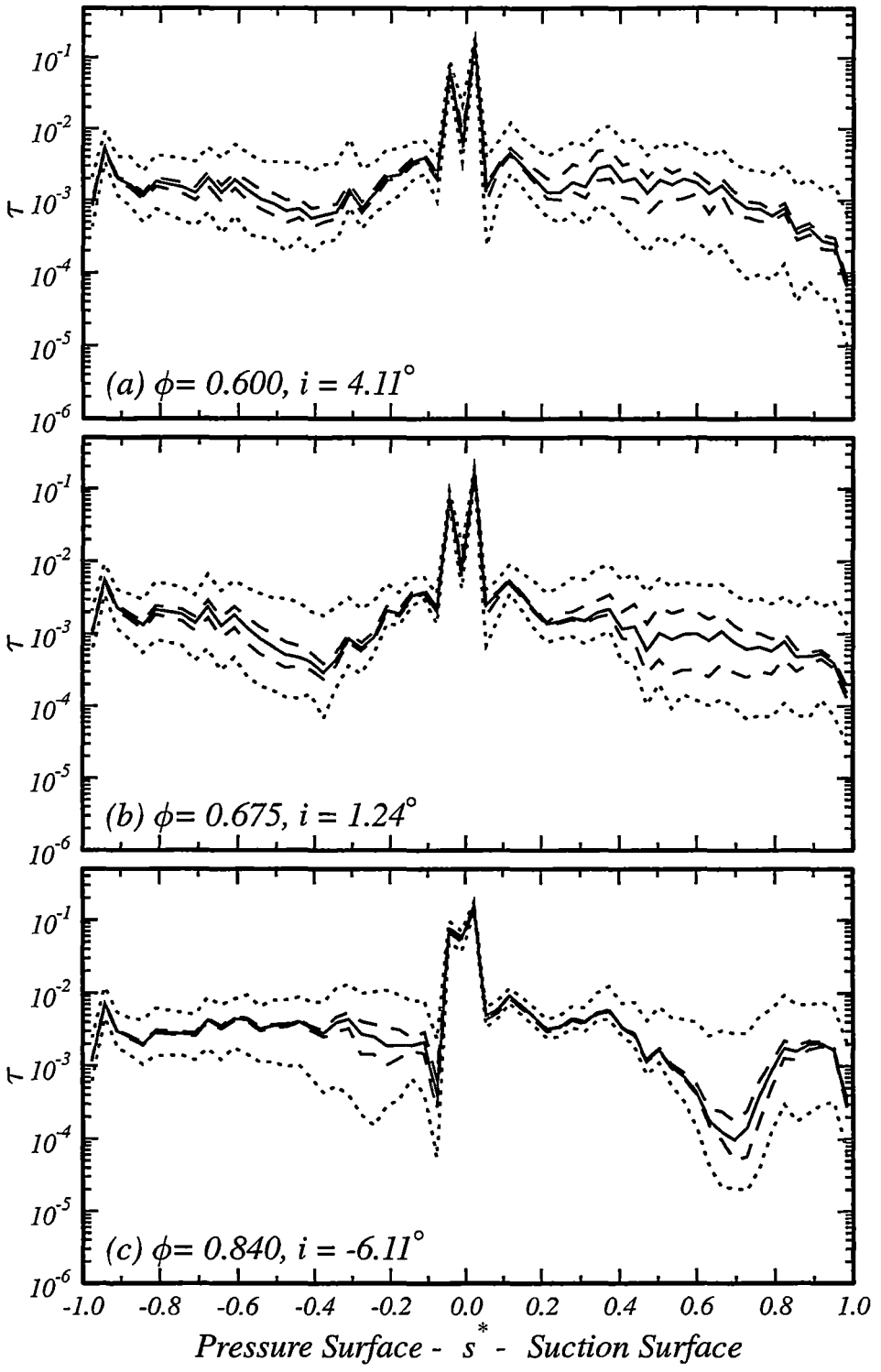

Figure 8.4: Variation of long-term mean (solid line), maximum and minimum ensemble means (long dash) and maximum and minimum instantaneous values (short dash) of quasi shear stress, τ. Incidence series. $Re_c = 120000$

Table 8.2: Extent of transitional regions (s^*_{start}–s^*_{end}). Hot-film values were estimated using Fig. 8.5 and Fig. 8.6. Calculated values were obtained from a boundary layer code using the experimental pressure distributions. Calculated values correspond to $\gamma_{0.05}$–$\gamma_{0.95}$.

	Measured, hot-film		Calculated			Measured, stethoscope
Re_c	between wakes	wake-induced	$Tu = 2\%$	$Tu = 10\%$	separation	time average
Suction surface						
170000	60–95	25–50	78–	34–51	–	not taken
120000	61–95	23–57	87–	43–59	39	40–65
60000	62–	26–	–	77–	44	not taken
Pressure surface						
170000	50–90	33–58	–	43–76	–	not taken
120000	55–	39–60	–	70–	–	45–70
60000	38–	12–60	–	–	52	not taken

	Measured, hot-film		Calculated			Measured, stethoscope
ϕ	between wakes	wake-induced	$Tu = 2\%$	$Tu = 10\%$	separation	time average
Suction surface						
0.600	22–92	7–37	78–	37–51	34	20–55
0.675	61–95	23–57	87–	43–59	39	40–65
0.840	72–92	59–80	73–88	46–81	62	68–90
Pressure surface						
0.600	58–	33–60	–	–	52	?–?
0.675	55–	39–60	–	70–	–	45–70
0.840	12–38	0–10	51–69	39–50	20	25–45

threshold selection scheme which gave much improved consistency from sensor to sensor. The intermittency identification for the current work is essentially this method modified to include the relaxing flow detection and to slightly reduce the detections at the leading edge. In general, the current threshold selection method performs better for the incidence series and is less successful at the extremes of the Reynolds number series.

Fig. 8.21 (Re_c = 170000, ϕ = 0.675) shows strong evidence of the development of wake-induced transition on the suction surface (upper part of the figure). The first turbulent spots develop in the region s^* = 0.21 to s^* = 0.28 (the earliest spots are not well detected by the intermittency scheme in this particular case). These two traces belong to different sets of simultaneously acquired records. At s^* = 0.21 the most advanced disturbance is at t^* = 3.4, at s^* = 0.28 the disturbance from the preceding wake is the most developed. Variability between these two records suggests that on different revolutions the wake from the same rotor blade can cause transition at slightly different streamwise locations. This variability is caused by unsteadiness in the freestream and/or the wake unsteadiness. Further back on the suction surface the turbulent spots are regular in appearance.

The turbulent spots on the suction surface in Fig. 8.21 are characterised by a rapid rise in quasi shear stress, followed by a section of turbulent flow. The length of the turbulent zone grows as the spots progress in the streamwise direction. At the rear of the turbulent spots the turbulence ends abruptly. Following the passage of the turbulent spot the shear stress relaxes back towards the laminar level. In the current case the next disturbance usually arrives shortly after the relaxing flow has reached the laminar level. There is little evidence of the regular Tollmien-Schlichting waves normally associated with natural transition except possibly following the relaxing flow at s^* = 0.60. At s^* = 0.92 there remains the occasional detection of relaxing flow but by s^* = 0.98 periodicity is difficult to detect in the raw signal and the flow is fully turbulent.

On the pressure surface the wake-induced turbulent patches are far less regular. At s^* = 0.44, for example, four rather crumbly looking spots are quite well developed but at t^* = 3 the only effect of the wake was to produce a few small disturbance waves. The pressure surface spots do not show the rapid rise in τ at the leading edge that the suction surface spots induced. Between the spots on the pressure surface there is far more instability wave activity than on the suction surface. The pressure surface turbulent spots hardly seem to have any well defined relaxing flow region at all; rather the turbulence seems to subside.

As the Reynolds number is reduced, Fig. 8.19 (Re_c = 120000,ϕ = 0.675) shows a generally similar behavior. On the suction surface the turbulent spots start later on the blade surface (s^* = 0.34). A few laminar and relaxing non-turbulent detections persist to the trailing edge in this case. Again, the pressure surface spots have a less well defined character. At the lowest Reynolds number (Fig. 8.22) transition is further delayed. In the s^* = 0.47 trace there are only two fairly well developed spots. Few of the spots in the low Reynolds number case have well defined relaxing flow regions. Further back on the blade there are still large areas of non-turbulent flow. The pressure surface spots are now also relatively few and do not seem to be particularly well synchronised to wake passing events.

The high positive incidence case, Fig. 8.18 (Re_c = 120000,ϕ = 0.600) differs from

the baseline case (Fig. 8.19) with wake-induced transition starting very close to the leading edge. Transition is essentially complete by $s^* = 0.79$. In this case the spots seem weaker and the relaxation time constant (rate at which the shear stress returns to the laminar level) is a smaller fraction of the blade passing period. Following relaxing flow regions in the traces at $s^* = 0.28$ and $s^* = 0.34$, small wave packets are developing between the wake-induced turbulent spots. These may be partly due to the onset of natural transition in an intermittently separating flow between the wake-induced turbulent spots.

The negative incidence case is uninteresting on the suction surface where the flow is laminar and attached up to around $s^* = 0.60$. A boundary layer calculation predicted separation at $s^* = 0.62$ and this is supported by the very low τ levels around this point observed in Fig. 8.4 (c). At $s^* = 0.73$ the reattachment process is well under way and is clearly influenced by the regular wake disturbances. Each wake disturbance has promoted early transition and reattachment of the separated shear layer. (Again, there is some randomness in this process with some wakes being more effective in promoting transition than others.) The turbulence generated by the wake-induced separated flow transition process seems to merge rapidly and by $s^* = 0.86$ there is little discernible periodicity in the turbulent flow. On the pressure surface the boundary layer is tripped at the leading edge by a short separation bubble. As in the case of the reattaching turbulent flow on the suction surface periodicity does not persist far along the pressure surface.

8.8 Time-distance diagrams

Time-distance (t-s) plots are a convenient way of representing the trajectories of wakes, disturbances and turbulent spots as they propagate along a surface. Here normalised surface distance and time, s^* and t^*, have been used.

Wake trajectories were constructed by assuming that the wakes propagate at the local freestream velocity, U (see Chapter 5). The trajectories of particles travelling at 0.88, 0.7, 0.5 and 0.35 times the freestream velocity have also been plotted. These trajectories are almost linear except at the leading edge and have a greater slope on the pressure surface due to the lower freestream velocity there. A particle travelling with infinite velocity will follow a horizontal path on the t-s plot and the lowest trajectory on each plot is the $1.0U$ trajectory.

The values of $0.88U$ and $0.5U$ correspond to typical leading and trailing edge velocities of a turbulent spot in zero pressure gradient, as described by Schubauer and Kelbanoff [110]; $0.7U$ is an approximate mean velocity of propagation for such a spot and for wake-induced turbulent strips (Mayle [81]). The speed of $0.35U$ is a typical convection velocity for Tollmien-Schlichting waves.

All signals were processed with a time-delay which was chosen to make $t^* = 0$ on the graphs coincide with the passage of the wake centre over the gauge nearest the leading edge. This time was determined by examining the ensemble mean and RMS traces for the gauge in question. There was only a slight variation in the non-dimensional wake arrival time for the different flow cases.

8.9 Phase-locked statistics

Detailed definitions of ensemble properties are given in the Nomenclature. A range of ensemble statistics can be derived from the hot-film data, some of which are better suited to interpreting the transitional state of the boundary layer than others.

Ensemble average quasi shear stress

Figures 8.9 and 8.10 show the phase-locked average quasi shear stress in the time-space plane. As in the case of Figs. 8.3 and 8.4, a logarithmic scale has been used to encompass the broad range of shear stress values. Data has been plotted over 2.5 wake passing periods. The Reynolds number series Fig. 8.9 shows a general decrease in shear stress level as the Reynolds number is reduced. At the leading edge ($s^* = 0.0$) all cases show the high levels associated with the thin boundary layer there as observed in Fig. 8.3 and Fig. 8.4.

Strong periodicity is evident on the suction surface in the two higher Reynolds number cases and a weaker periodicity is visible on the pressure surface. On the suction surface, the highest levels of $<\tau>$ occur where the first turbulent spots are forming. Regular avenues of high $<\tau>$ levels spread back along the blade surface indicating the location of the wake-induced transitional strips. As the turbulent spots become more developed the shear stress levels of the spots decreases with the thickening turbulent boundary layer and the adverse pressure gradient. In these figures the highest $<\tau>$ levels associated with the most vigorous parts of the wake-induced patches are bordered by the $0.7U$ and $0.5U$ t-s trajectory lines. Development of the transitional strip clearly lags the passage of the wake in the freestream (under the $1.0U$ t-s trajectory). Towards the trailing edge the periodicity reduces as the turbulent spots merge to form a fully turbulent boundary layer. On the pressure surface the periodicity is not as strong and the avenues of raised $<\tau>$ are less well defined.

The high positive incidence case in Fig. 8.10 (a) shows a similar behaviour to the baseline case (Fig. 8.10 (b)) until around $s^* = 0.8$ on the suction surface. Here the very low shear stress levels indicate a turbulent separation. In the high negative incidence cases (Fig. 8.10 (c)) a steady laminar separation is observed at $s^* = 0.6$. The reattachment line is modulated in time, varying in the range $s^* = 0.75$ to $s^* = 0.85$. On the pressure surface a thin region of low $<\tau>$ at $s^* = -0.05$ is evidence of a leading edge separation. Periodicity in the flow follows the reattachment on the pressure surface back to $s^* = -0.3$.

In both Fig. 8.9 and Fig. 8.10 there are vertical streaks at constant s^* which are caused by sensitivity variations between adjacent sensors. The extreme range of τ values also makes interpretation of the boundary layer development difficult. Consequently some alternative phase-locked average statistics were investigated.

Alternative statistics

Plots of the RMS output from surface film gauges have commonly been used by several workers including Addison and Hodson [2] and Halstead et al. [46]. Upstream of transition the RMS level is low. Through transition the long term RMS of τ rises to a maximum somewhere around $\gamma = 0.5$, then decays as the amount of switching between

laminar and turbulent states reduces. Halstead et al. [46] suggested that at $\gamma = 0.5$ RMS would peak and the skew of the signal would reach zero. At lower intermittency there would be positive skew (because the signal is biased towards the laminar level) and at $\gamma > 0.5$ negative skew may be expected. Maximum positive and negative skew would be expected at $\gamma = 0.25$ and $\gamma = 0.75$ respectively and zero skew in fully laminar and fully turbulent flow. These assumptions will only hold exactly if the laminar and turbulent parts of the intermittent signal have similar standard deviations and zero (or equal and opposite) skews. In the current investigation significant areas of high positive skew were found where the boundary layer was close to separation but still laminar. Also there were few areas which showed the high levels of negative skew expected in a boundary layer in the latter stages of transition. These observations may be a consequence of the lower Reynolds number of the current investigation but highlight a need for care in inferring intermittency from skew alone.

Interpretation of phase-locked average RMS data can vary depending on the normalisation method (if any) used. Halstead et al. [46] found $<\tau>_{RMS}/\bar{\tau}$ (with normalisation) more useful for their turbine data and $<\tau>_{RMS}$ (without normalisation) more useful for their compressor test cases. These different methods highlight different features of the flow (especially near separation where $\bar{\tau}$ tends to zero).

Fig. 8.15 shows the results of some different statistical processing treatments of the data. The top figure shows un-normalised $<\tau>_{RMS}$. High mean levels of τ at the leading edge also give high $<\tau>_{RMS}$ values in the un-normalised plot. This plot also shows some vertical streaks caused by differing sensor sensitivities. High levels of $<\tau>_{RMS}$ are evident where the switching between laminar and turbulent levels is the highest in the early part of the transition zone. Towards the rear of the blade $<\tau>_{RMS}$ falls to low levels with the increasing boundary layer thickness and adverse pressure gradient. Discrimination between the turbulent and non-turbulent areas is not as clear. Precise location of the wake-induced turbulent strips from this figure is difficult.

Fig. 8.15 (b) shows an alternative method where $<\tau>_{RMS}$ was normalised using $<\tau>$. This approach removes the high levels at leading edge where $<\tau>_{RMS}$ is small relative to the local τ values. The increase in $<\tau>_{RMS}$ in the streamwise direction now gives a clearer indication of the onset of transition. On the pressure surface the development of turbulent patches is followed by a decay in the relative RMS level as the boundary layer becomes continuously turbulent. This normalisation procedure gives a misleading picture on the suction surface. Here very low levels of $<\tau>$ associated with intermittent separation between the turbulent patches leads to very high levels of the normalised $<\tau>_{RMS}$. The first wake-induced turbulent patch on the suction surface is shown by the high $<\tau>_{RMS}/<\tau>$ levels forming around $s^* = 0.3$. As this turbulence develops the levels fall. Then at around $s^* = 0.6$ and $t^* = 1.0$ a new peak in $<\tau>_{RMS}/<\tau>$ is observed where the intermittently separating background flow is undergoing transition.

Fig. 8.15 (c) shows ensemble average kurtosis plotted in the way suggested by Townsend [126] (see Chapter 7) to represent intermittency. Until $s^* = \pm 0.4$ the picture is confused. Further back however, wedges of turbulent flow can be seen developing between the $0.7U$ and $0.5U$ t-s trajectories. Comparison with the phase-locked average intermittency presented later in Fig. 8.13 (b) is reasonable away from the leading edge.

RMS quasi shear stress

In general the most useful normalisation procedure for $<\tau>_{RMS}$ is to use the local long term average of τ and plot $<\tau>_{RMS}/\bar{\tau}$. This gives low disturbance levels at the leading edge, minimises the vertical streaks caused by sensor variations and lessens the problem of separation causing high apparent normalised disturbance levels. Fig. 8.11 and Fig. 8.12 show this statistic for the Reynolds number and incidence series.

At the highest Reynolds number Fig. 8.11 (a) shows periodicity staring around the leading edge on both surfaces. Transition onset has probably not commenced until $<\tau>_{RMS}/\bar{\tau} = 0.3$–$0.4$. The peaks in this plot do not correspond with the most continuously turbulent parts of the flow. On the suction surface two distinct bands of high $<\tau>_{RMS}/\bar{\tau}$ level follow the $0.5U$ and $0.88U$ t-s trajectory lines closely from transition onset towards the trailing edge. These correspond to the points where the switching between laminar and turbulent levels (measured across the ensemble) is the highest and probably indicate the 50% intermittency regions. The high levels of unsteadiness in the region of the $0.88U$ t-s trajectory line are partly due to randomness in the arrival times of the turbulent spots. A small fluctuation in spot arrival time can cause a large apparent unsteadiness at points in the ensemble close to the average arrival time. Continuous turbulence gives a lower RMS τ level.

Reduction in Reynolds number produces a delayed onset of wake-induced transition. The lowest Reynolds number case shows high levels of normalised RMS τ, partly because of the lower $\bar{\tau}$ levels and increased susceptibility to laminar separation. The different nature of the pressure surface turbulent patches is now clearly evident. The more rounded shape of the regions of high $<\tau>_{RMS}/\bar{\tau}$ on the pressure surface are indicative of a reduced synchronisation of the turbulent breakdown with wake passage.

At high positive incidence (Fig. 8.12 (a)) the normalised RMS τ plot is dominated on the suction surface by the high levels starting at $t^* = 0.0,1.0,2.0$, $s^* = 0.45$. These disturbances are not correctly placed to be wake-induced and are probably the result of intermittent separation starting in this area. The negative incidence case (Fig. 8.11 (c)) shows some small amount of periodicity on the suction surface growing to around $s^* = 0.60$. This is the effect of the wake disturbance on the laminar boundary layer. After $s^* = 0.60$, where the boundary layer is at the onset of separation, there are very high levels of $<\tau>_{RMS}/\bar{\tau}$ which persist through the separation. Similar behaviour exists around the leading edge separation on the pressure surface.

The plots of RMS τ do not clearly discriminate between high disturbance levels caused by boundary layer turbulence and high disturbance levels caused by switching between laminar and turbulent shear stress levels. Low levels of $\bar{\tau}$ around separation further complicate interpretation of these plots.

Ensemble intermittency

Phase-locked average intermittency quantitatively describes the transitional state of the boundary layer. Intermittency is an essential parameter in several commonly used boundary layer transition models. Processing the surface hot-film data to produce intermittency helps resolve some of the data interpretation problems which were experienced with the plots of mean and RMS τ. In adverse pressure gradients and in separating flows the peak intermittency level in the boundary layer moves away from

the wall (see Chapter 7 and Chapter 9). Intermittency levels determined from surface hot-film sensors may tend to underestimate the progress of transition in adverse boundary layer flows. In separated flow regions the hot-film sensors do not register transition in the shear layer until reattachment commences.

Time-space contour plots of phase-locked average intermittency are presented for the Reynolds number series in Fig. 8.13 and for the incidence series in Fig. 8.14. High intermittency levels associated with mostly continuous turbulence are indicated in red and low intermittency levels associated with non-turbulent flow are shown in blue. The boundary layer state information from the intermittency detection algorithm in these figures is the same as was shown in the individual traces except that a phase-locked average picture has been constructed.

Fig. 8.13 (b) shows the regular development and growth of turbulent spots on the suction surface. The leading edge of the (average) spot travels at around $0.7U$ between $s^* = 0.4$–0.6 and then seems to speed up closer to $1.0U$. This apparent speed-up may be the result of natural or separated flow transition developing in the region where the relaxing flow from the previous spot is at its weakest. The leading-edge of the wedge of turbulent turbulent flow on the suction surface shows a gradual rise in intermittency; formation of the earliest turbulent spots is an intermittent process. On the pressure surface spots of a very different nature have produced an average spot with a rounded upstream section and moderately high intermittency levels between wake-induced spots. The rounded shape of the upstream part of the pressure surface spot is caused by increased levels of temporal randomness in spot formation.

At the higher Reynolds number in Fig. 8.13 (a) the transition on the pressure surface is earlier than at the middle Reynolds number and transition is completed earlier. On the suction surface the intermittency detection scheme has failed to register spots at $s^* = 0.21$–0.28; comparison of the individual traces in Fig. 8.21 with Fig. 8.19 confirms the expected result that wake-induced transition occurs earlier at higher Reynolds number. The thicker 'nose' of the average spot at $s^* = 0.4$ is a result of the detection algorithm missing the youngest spots. The end of transition at the highest Reynolds number is at a similar location to the mid-Reynolds number case. The ragged appearance of the leading edge of the average spot in Fig. 8.13 (a) downstream of $s^* = 0.5$ is the result of transition between the wake-induced spots.

The low Reynolds number case (Fig. 8.13 (c)) is clearly corrupted by the interlacing of measurements from different compressor runs. The general picture seems similar to the other cases but the intermittency detector only registers high intermittency over relatively small areas.

Fig. 8.14 (a) shows the high positive incidence test case. There is a small amount of vertical banding on the suction surface associated with sensor sensitivity variations. Wake-induced transition on the suction surface occurs earlier in this case and the transition finishes earlier. Intermittency levels between the wake-induced spots are higher in this case indicating an increased probability of other transition modes. Trailing edge separation leads to very low indicated intermittency in this region. Prior to separation at the trailing edge there is distinct periodicity in the almost fully turbulent flow. Trailing edge separation seems to occur earliest between the $0.7U$ and $0.88U$ t-s trajectory lines. This is the expected location of the turbulence from the turbulent spots which were formed closest to the leading edge (described as the oldest turbulence by Cumpsty et al. [20]).

The negative incidence case in Fig. 8.14 (c) shows a radically different picture from the other cases. On the suction surface the turbulent reattachment line is clearly evident and shows evidence of periodic modulation of reattachment caused by the passing wakes and their effects on the separated shear layer. On the pressure surface the passing wakes cause transition at the leading edge and thereby suppress the pressure surface leading edge separation bubble. Between the wakes, intermittency does not rise to 1.0 until $s^* = 0.3$–0.4. This may be the result of a redeveloping leading edge separation in the intervals between wake passing events where turbulence levels are lower.

Minimum, maximum and average values of intermittency data for each of these test cases has been plotted against surface distance in Fig. 8.6 and Fig. 8.5. The maximum value of phase-locked average intermittency at any stream-wise location will generally correspond to the development of wake-induced turbulent spots. The minimum values are associated with transition between the wake-induced transitional strips. As in Fig. 8.3 and Fig. 8.4 separation between the minimum and maximum values indicates the level of periodicity. All these figures show some high levels around the leading edge caused by some incorrect detections. In most cases transition along the wake-induced path (the maximum level curve) shows a steep rise but not an instantaneous jump. Transition between wakes is usually more gradual. The high incidence case Fig. 8.5 (a) shows a rapid rise close to the leading edge on the suction surface. The different behaviour of the negative incidence case is clearly visible.

Relaxing flow regions

The intermittency detection algorithm was further developed to include a relaxing flow detector (Chapter 7). The probability of relaxing flow is plotted in the time-space plane for the incidence series in Fig. 8.16. As may be expected there is very little relaxing flow for the negative incidence case in Fig. 8.16 (c). The other two cases show high probability of relaxing flow on the suction surface. Nowhere is the relaxing flow probability as high as 1.0. The leading edge of the relaxing flow region follows the $0.5U$ t-s trajectory line in both cases. On the pressure surfaces the relaxing flow regions are less intense and this reflects the lower regularity of these spots. The high incidence spots are weaker and transition starts closer to the leading edge. These trends are confirmed by the relaxing flow plot in Fig. 8.16 (a).

Schubauer and Klebanoff [110] hypothesised that the calmed regions they observed following their turbulent spots were a consequence of the low relative velocity (about $0.35U$) of Tollmien-Schlichting waves. They suggested that the flow following the trailing edge of the spot (travelling at about $0.5U$) was inaccessible to the instability waves and hence remained calmed. The results of Fig. 8.16 show that the trailing edge of the relaxing flow region travels more slowly than the likely T-S wave speed and would in fact be accessible to T-S waves. Instead it is proposed that the 'calmed flow' is calm because the raised shear stress levels which persist following the passage of a turbulent spot stabilise the boundary layer. The relaxing flow causes an absence of instability waves rather than the absence of instability waves causing the calmed region.

The t-s trajectories of the spot leading edges, spot trailing edges and relaxing flow regions can be derived from the ensemble averaged intermittency and ensemble relaxing flow plots. Fig. 8.17 shows these trajectories for the baseline test case. The spot leading edge trajectory in Fig. 8.17 (a) shows the highest peak probability levels, indicating

that the spot leading edge is the most regular of these features in time. The average slope of the spot leading edge trajectory varies between $0.7U$ and $1.0U$, although the higher speeds closer to the blade trailing edge may be due to contamination from other transition modes. The spot trailing edge trajectory (which also corresponds to the leading edge of the relaxing flow region) in Fig. 8.17 (b) closely follows the $0.5U$ t-s trajectory line.

The trailing edge of the relaxing flow region is not well defined and downstream of $s^* = 0.5$ there are two distinct areas of high probability of relaxing flow ending. The upper path is the end of long relaxing flow regions. A significant number of turbulent spots have only have short (or non-existent) relaxing flow zones and these form the second path. The upper trajectory shows a distinct kink on the suction surface around $s^* = 0.5$ and this is a result of the relaxing flow zone being prematurely ended by the arrival of the next wake-induced turbulent spot. Trends on the pressure surface are similar but the amount of randomness of the locations of the features in time is increased.

8.10 Observed and calculated transition locations

Transition onset and completion locations along the wake-influenced path and away from wakes have been estimated from the measurements using Fig. 8.6 and Fig. 8.5. These onset and transition location were typically taken as the streamwise locations where $\gamma = 0.1$ and 0.9 but are of limited certainty in some cases. The transition locations are tabulated in Table 8.2.

Boundary layer calculations were made using the boundary layer code described in Chapter 11. As this is a steady boundary layer code a crude approximation of the effect of passing wakes was made by performing the boundary layer calculation at a high (10%) and low (2%) freestream turbulence levels. These levels are typical of the levels in wakes and between wakes observed in Chapter 6. Start and end of transition from the calculations have been taken as the streamwise locations where $\gamma = 0.05$ and 0.95. Laminar separation locations have also been given. The laminar boundary layer calculation was marched through separation regions with shape factor H held constant at 3.7.

A further check of the time-average transition location was made using a total-head tube immersed in the boundary layer and directed into the flow. This tube was connected to microphone and the signal was amplified and played back through a loudspeaker. A distinct increase of noise level was associated with transition onset but there was a tendency for tones at the blade passing period to drown out turbulence noise in parts of the boundary layer with high levels of periodicity. This technique was used in the earlier work of Walker [132] as the principal means of identifying the location of transitional flow regions on the blade surface. The present observations indicate that the stethoscope technique identifies the centre of the transition region reasonably well, but significantly underestimates the total length of the transition zone. Similar comments have been made by Dey and Narasimha [22] in relation to the surface pitot technique.

On the suction surface, overall comparison between calculated transition onset and finish locations are better for the wake disturbed transition. Between wakes transition

onset is predicted too late in all cases except at $\phi = 0.840$ which was the negative incidence case. The calculations between the wakes might give better agreement if a higher turbulence level were selected but it is likely that a more sophisticated model which can allow for relaxing flow and intermittent separation will be required.

8.11 Blade-out case

In order to study the effect of changing the rotor blade passing frequency one of the rotor blades was replaced with a counterweight. Typical individual traces for this case are shown in Fig. 8.23. Normal wake disturbances propagate from the leading edge at $t^* = 0.0$ and 1.0 but the wake which would have hit the leading edge at $t^* = 2.0$ is missing. Turbulent spots from the wake starting at $t^* = 0.0$ grow as for the normal case (Fig. 8.19); the suction surface spots have relatively long relaxing flow regions which are interrupted by the turbulent spots induced by the wake which passed the leading edge at $t^* = 1.0$. The spots from the $t^* = 1.0$ wake are similar in character but now the relaxing flow from these spots has time to reach the laminar shear stress level because it is not interrupted by the next wake. Rearward of $s^* = 0.5$, instability waves and breakdown to turbulence are evident in the flow between the $t^* = 1.0$ and $t^* = 3.0$ wake-induced spots. These disturbances first develop where the non-relaxing laminar flow has been established longest (i.e. just before the next turbulent spot arrives). For this reason the wake-induced turbulence developing from $t^* = 3.0$ at the leading edge seems to grow in the negative time direction.

Phase-locked average contour plots of RMS τ, intermittency and relaxing flow are presented in Fig. 8.24. In both these figures the change of transition mode when the wake spacing is increased is evident. On the pressure surface the flow is laminar to the trailing edge when the boundary layer in the space where the wake is missing. As the turbulent spots develop further on the suction surface, the relaxing flow region seems to grow shorter and the transition of the background boundary layer happens sooner after the passage of the wake-induced turbulent spots. The boundary layer calculations and very low levels of τ between wake-induced spots for this case suggest the transition of the background boundary layer is occurring through intermittent separation. This is very similar to the description of a wake-disturbed flow with a mid-chord separation bubble presented by Cumpsty et al. [20]. The turbulent spots at $s^* = 0.6$ have the strongest relaxing flow regions which are most effective in suppressing the transition of the background boundary layer.

The blade-out test case shows the strong similarity between the development of wake-induced turbulent patches on the compressor blade suction surface with the development of artificially triggered turbulent spots in an adverse pressure gradient flat plate boundary layer observed by Gostelow et al. [40, 42]. In the Gostelow experiment a turbulent spot was generated upstream of the point of natural transition onset. As the turbulent spot moves into the natural transition zone the calmed region delays transition of the natural boundary layer for some time following the passage of the turbulent spot. As in the blade-out case, the end of the calmed region is eventually reached and the natural state of transition of the background boundary layer re-establishes itself.

8.12 Conclusions

Unsteady surface hot-film measurements of boundary layer development are able to resolve the different processes which take place at different parts of the wake passing period. Some of the difficulties in interpreting the unsteady surface hot-film data have been examined. Using intermittency and relaxing flow detection algorithms, useful quantitative data can be extracted from uncalibrated surface hot-film gauges.

The current study is in qualitative agreement with the work of Halstead et al. [46] which included test cases at higher Reynolds numbers and had more blade-rows upstream. The current work is also in general agreement with the work of Cumpsty et al. [20]. In the compressor-baseline case of Halstead et al. [46] (reproduced in Fig. 8.7) the calmed region associated with weaker wake disturbances was ineffective in suppressing transition at region '4' and allowed breakdowns to occur there occasionally. This type of behaviour was not observed in the current data except possibly at high positive incidence. This is probably a result of the different relative wake-induced and natural transition locations for the two cases (in the current work region B ends before the transition between wakes starts). The transitional nature of the wake-induced transitional strip (region B) in the Halstead et al. [46] was confirmed in the current work but was not emphasised by Cumpsty et al. The unsteady data from the current work should prove useful in validating unsteady CFD codes as has been attempted with the Halstead data.

The results presented in this chapter have shown that:

- Wake-induced turbulent spots first develop at a random position in space and time, and not every passing wake necessarily causes a breakdown every cycle. These observations agree with Halstead et al. [46].
- Relaxing flow (calmed) regions are a consequence of the stabilising effect of the high shear levels immediately following the trailing edge of a turbulent spot. The whole calmed region is not inaccessible to T-S waves on the propagation velocity argument of Schubauer and Klebanoff [110].
- The wake-induced turbulent spots lag the passage of the wake in the freestream.
- Wake turbulence influences the transition of separated flow and can cause a periodic variation of separation bubble length.
- Turbulent spots which develop on the pressure surface in the current work are very different in character to the suction surface spots. This may either be due to the different surface pressure distributions on either side of the blade or may be the result of the difference in sign of the wake-jet effect.

Unsteady boundary layer transition involves the complex interplay of different transition modes. Wake-induced transitional strips dominate most of the current test cases but separated flow transition and bypass transition in the flow between wakes also need to be considered. In instances where the turbulent spots are strong and regular, significant regions of relaxing flow can exist. Relaxing flow plays an important part in stabilising the flow between the wake-induced turbulent strips and delaying the onset of separation. Schulte [112] explores the possibilities of exploiting properties of unsteady

relaxing flow on a turbine blade to achieve increased blade loadings and reduced blade counts.

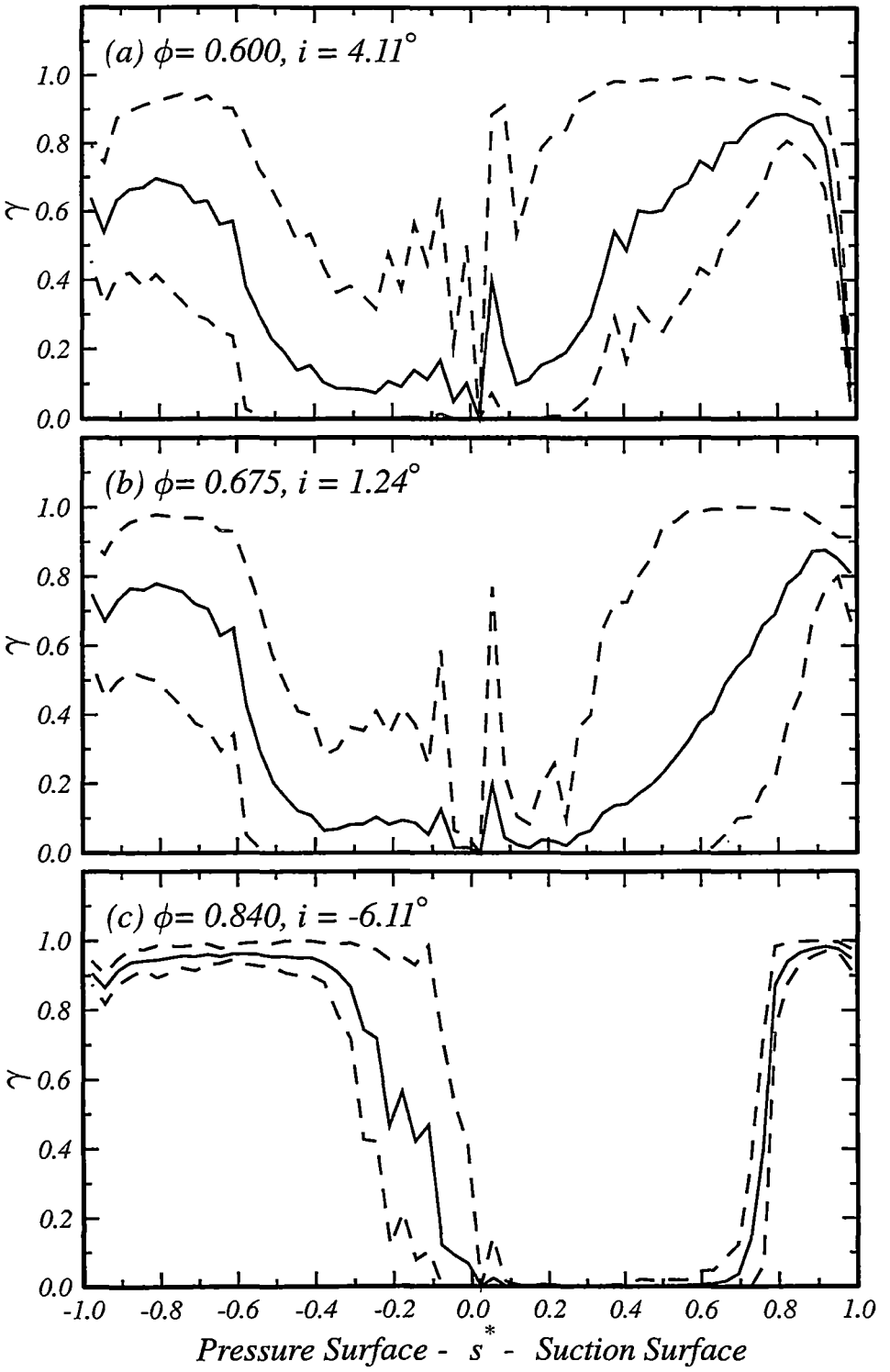

Figure 8.5: Variation of long term mean (solid line) and maximum and minimum ensemble means (dash) of intermittency. Incidence series. $Re_c = 120000$

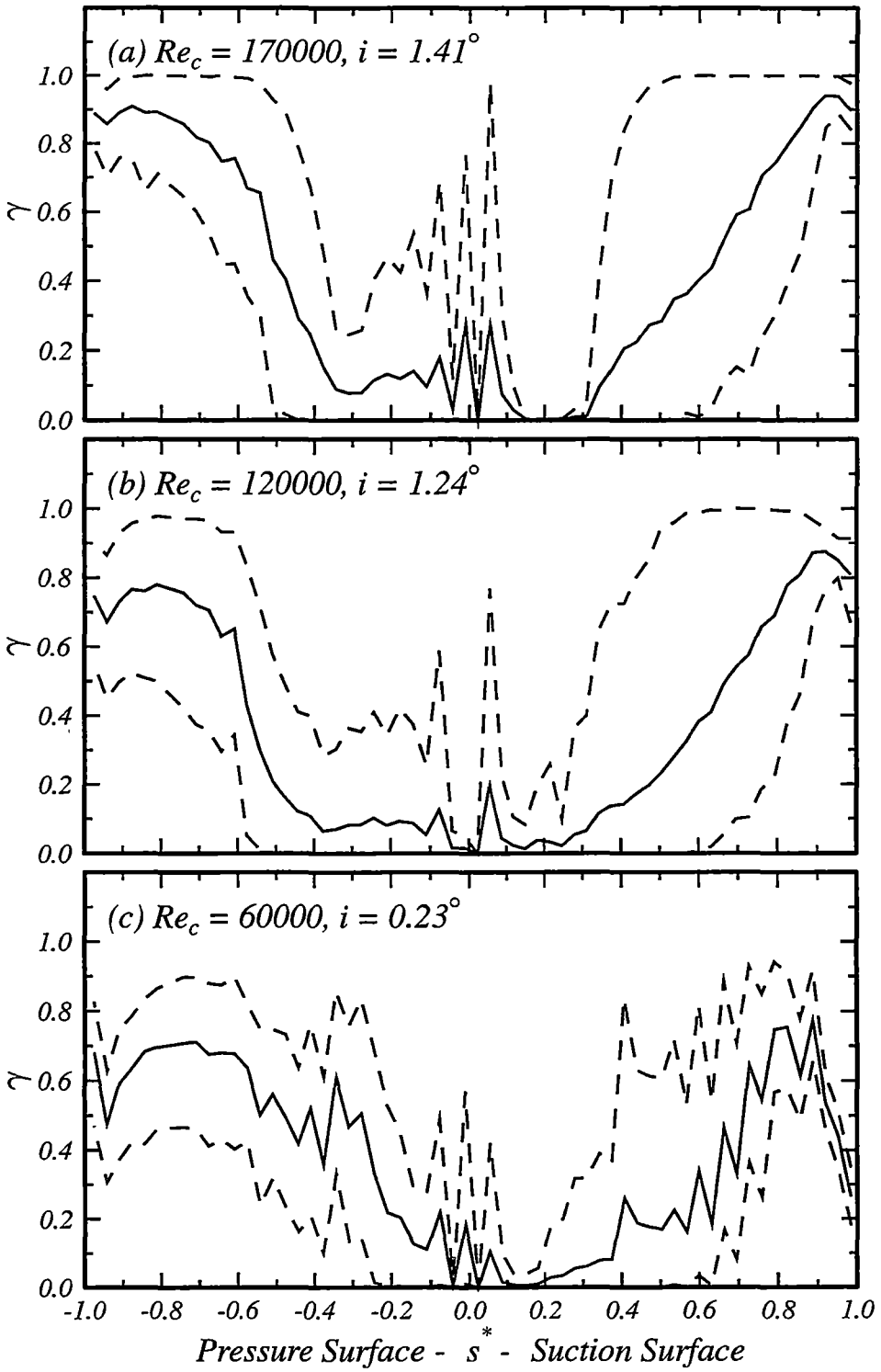

Figure 8.6: Variation of long term mean (solid line) and maximum and minimum ensemble means (dash) of intermittency. Reynolds number series. $\phi = 0.675$

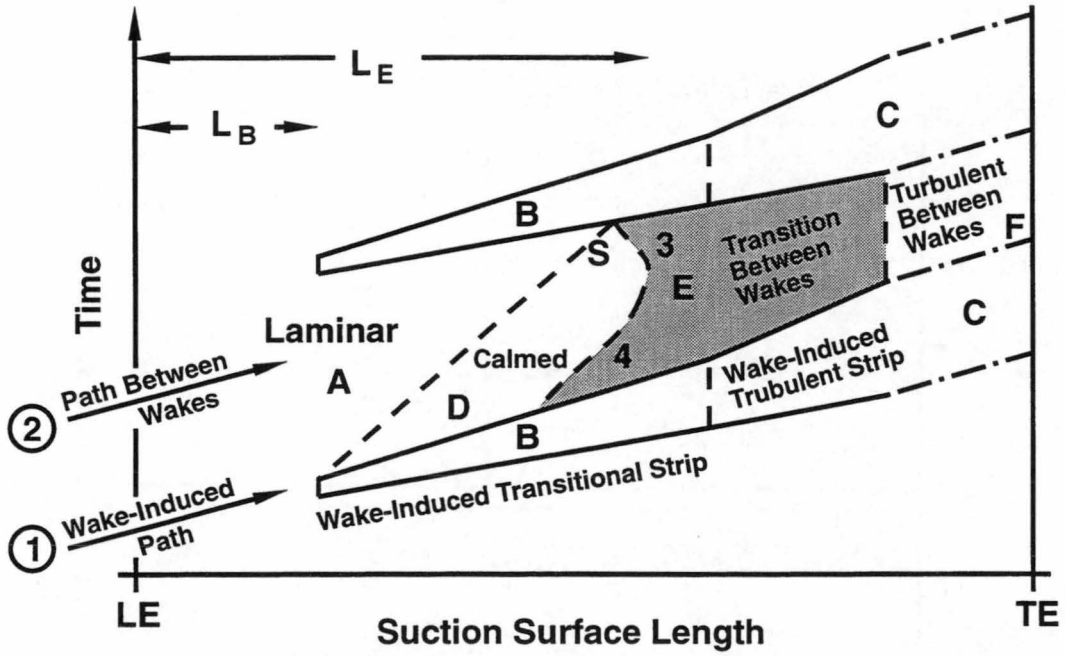

Figure 8.7: Unsteady boundary layer development on an axial compressor blade (Halstead et al. (1995))

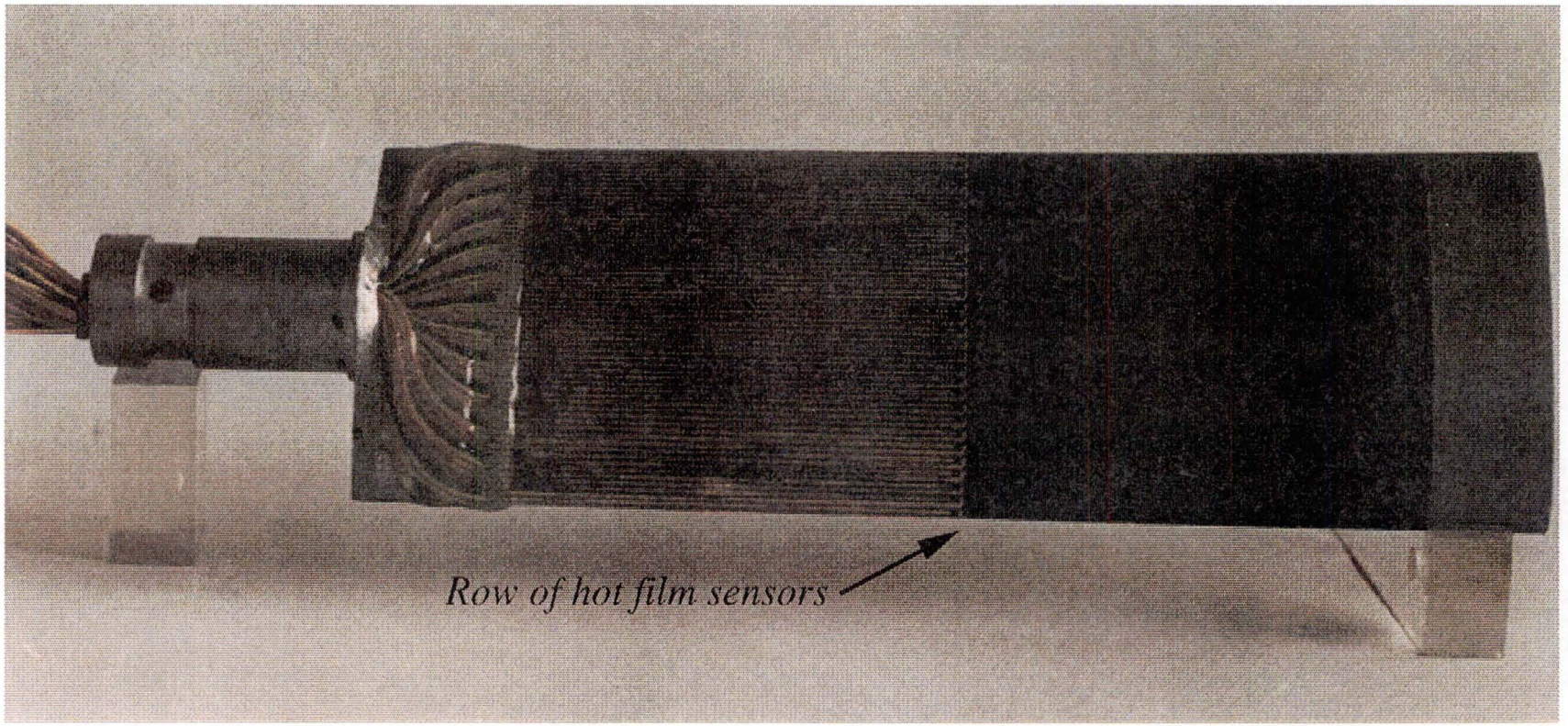

Figure 8.8: Hot-film instrumented blade

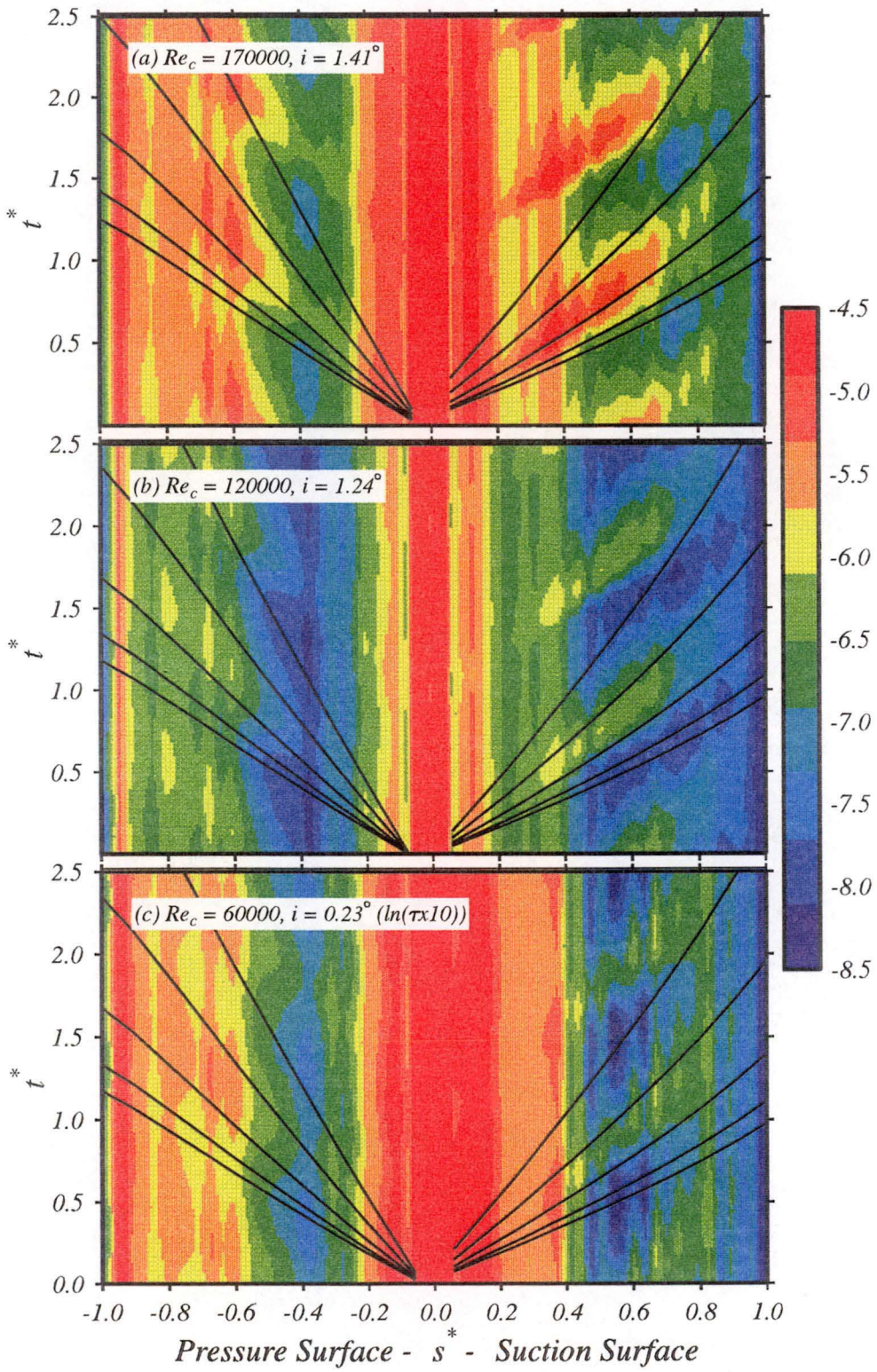

Figure 8.9: Time-distance contour plot: log ensemble average quasi shear stress. Particle trajectories for $1.0U$, $0.88U$, $0.7U$, $0.5U$, $0.35U$ overlaid. Note change of scale for case (c). Reynolds number series. $\phi = 0.675$

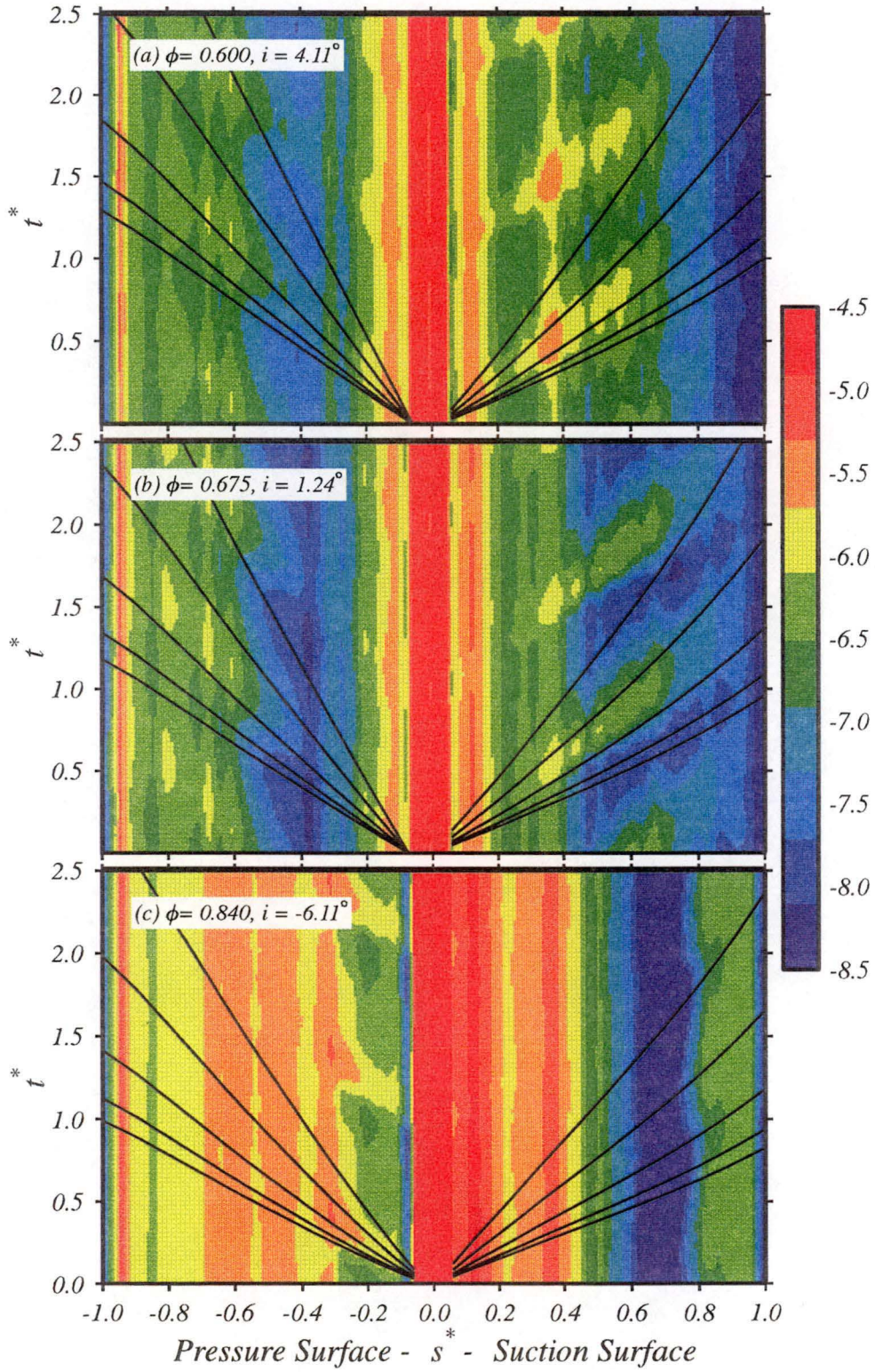

Figure 8.10: Time-distance contour plot: log ensemble average quasi shear stress. Particle trajectories for $1.0U$, $0.88U$, $0.7U$, $0.5U$, $0.35U$ overlaid. Incidence series. $Re_c = 120000$

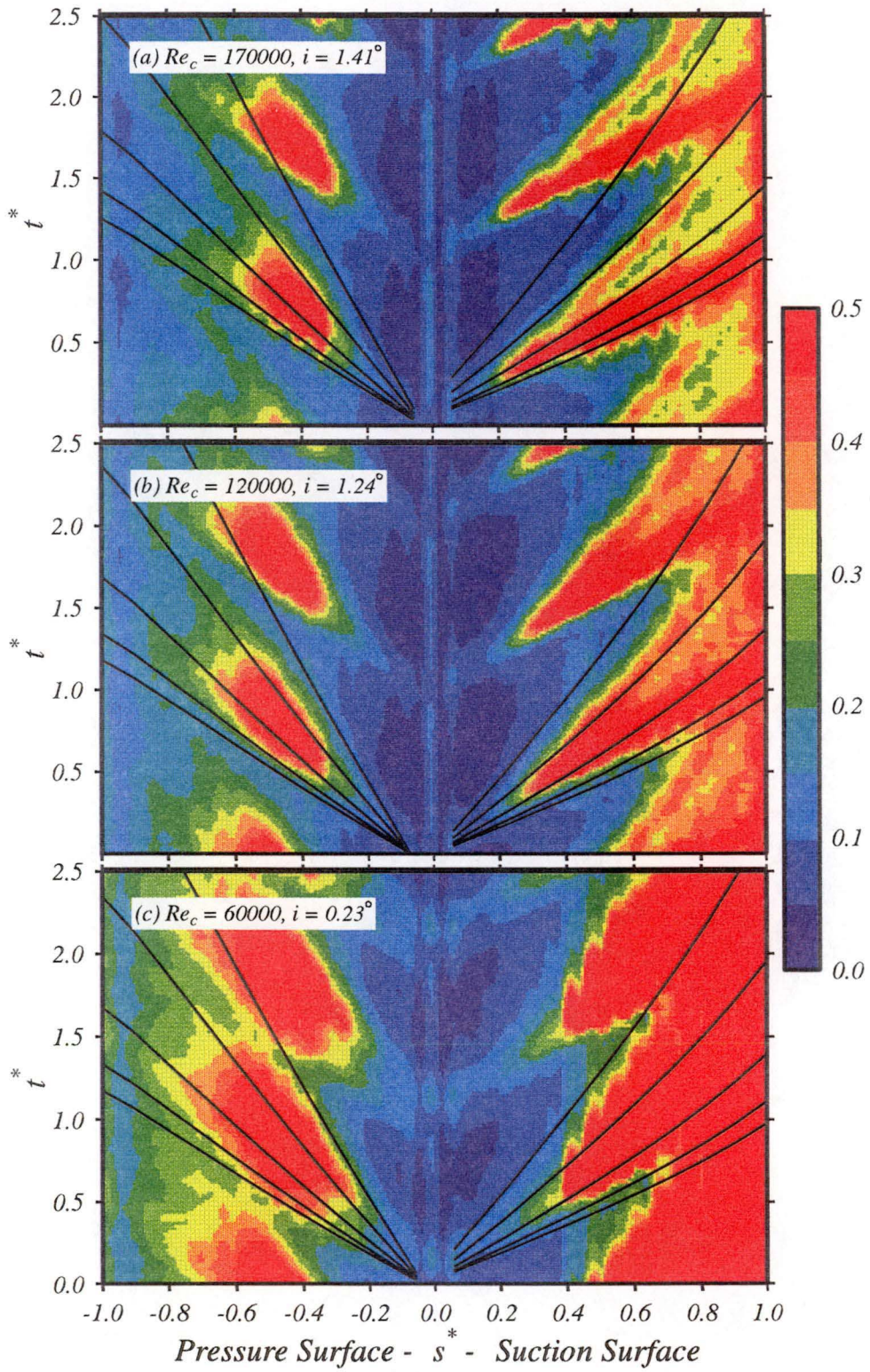

Figure 8.11: Time-distance contour plot: ensemble average RMS quasi shear stress (normalised by local $\overline{\tau}$). Particle trajectories for $1.0U$, $0.88U$, $0.7U$, $0.5U$, $0.35U$ overlaid. Reynolds number series. $\phi = 0.675$

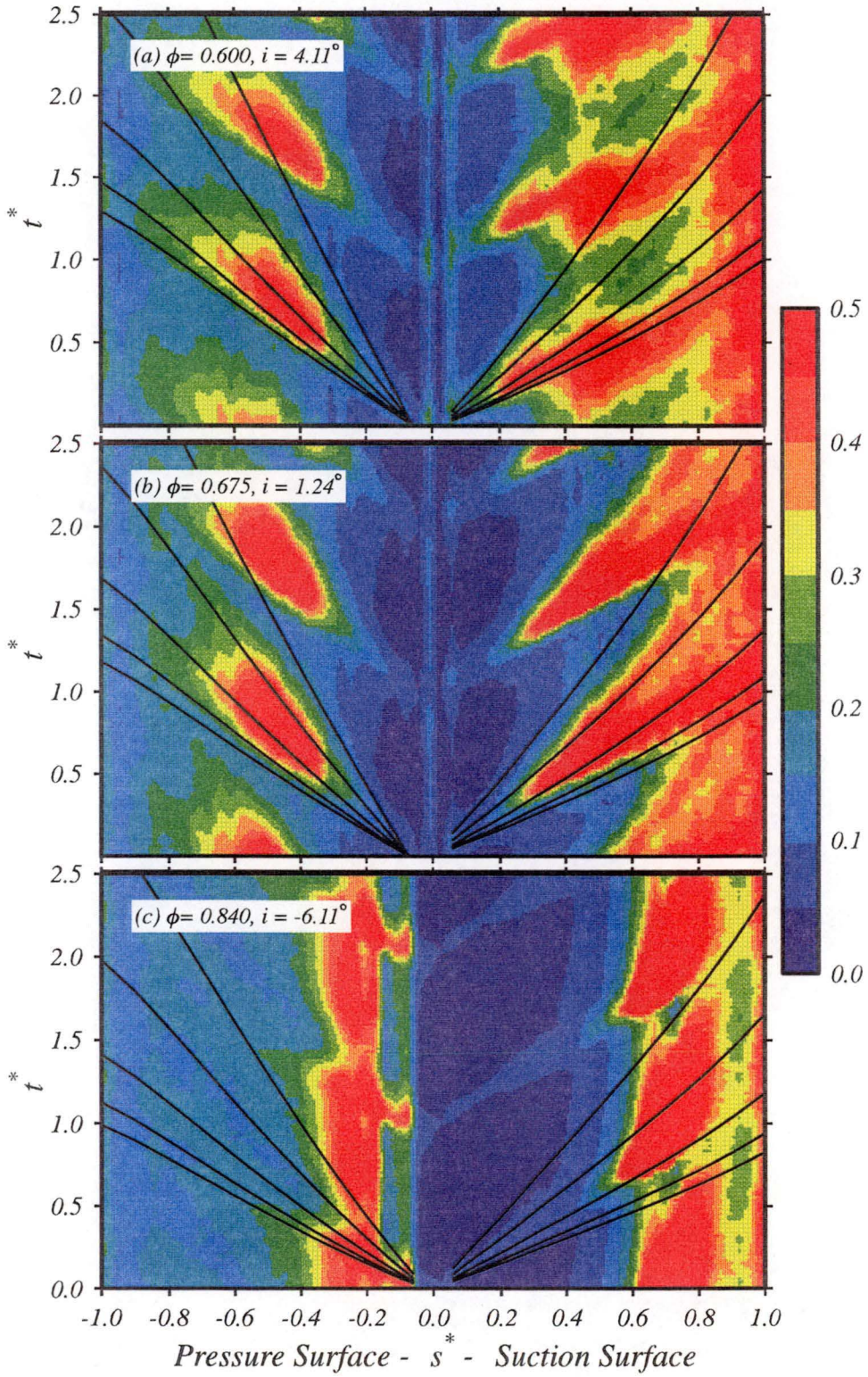

Figure 8.12: Time-distance contour plot: ensemble average RMS quasi shear stress (normalised by local $\overline{\tau}$). Particle trajectories for $1.0U$, $0.88U$, $0.7U$, $0.5U$, $0.35U$ overlaid. Incidence series. $Re_c = 120000$

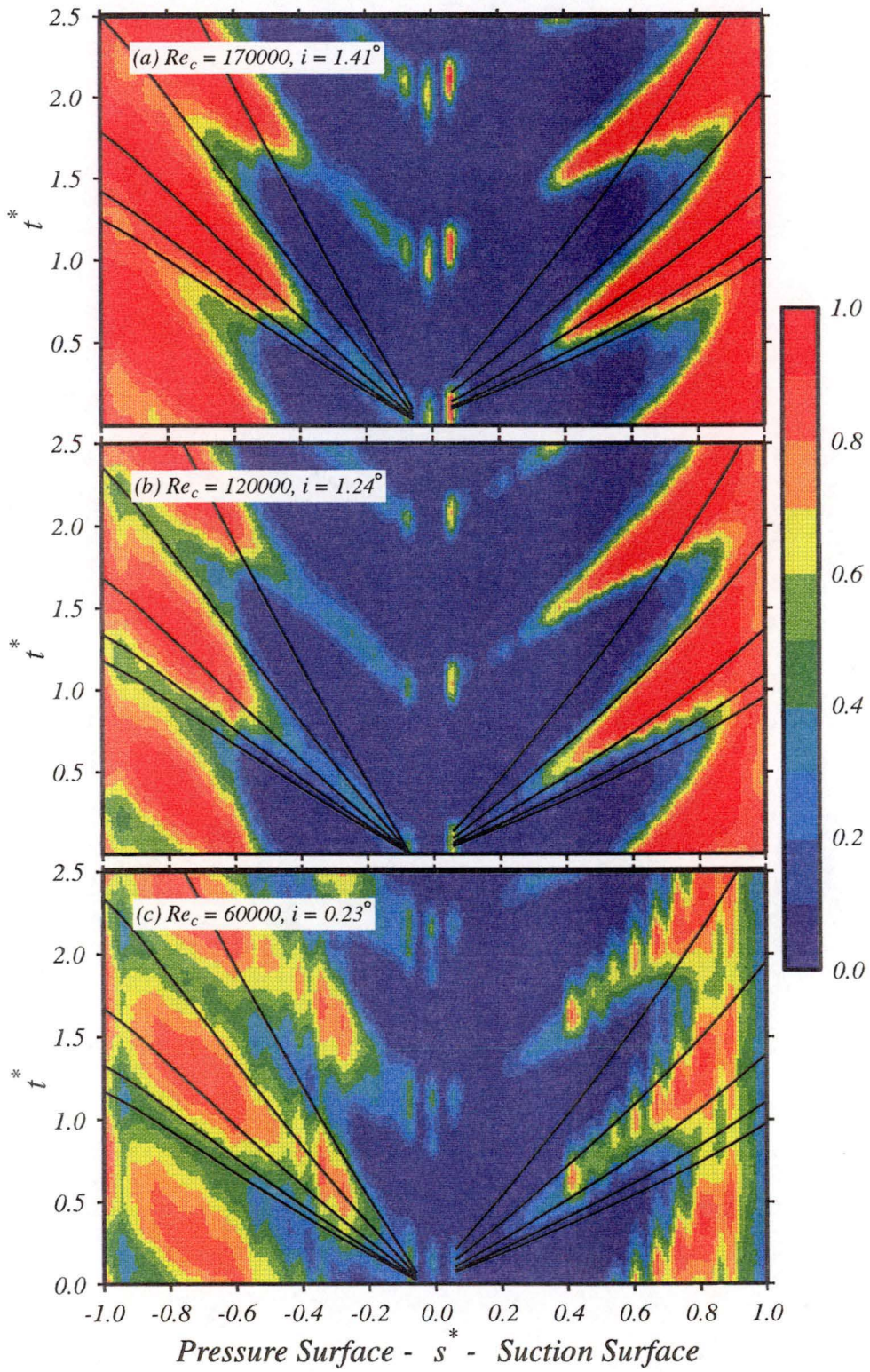

Figure 8.13: Time-distance contour plot: ensemble average intermittency. Particle trajectories for $1.0U$, $0.88U$, $0.7U$, $0.5U$, $0.35U$ overlaid. Reynolds number series. $\phi = 0.675$

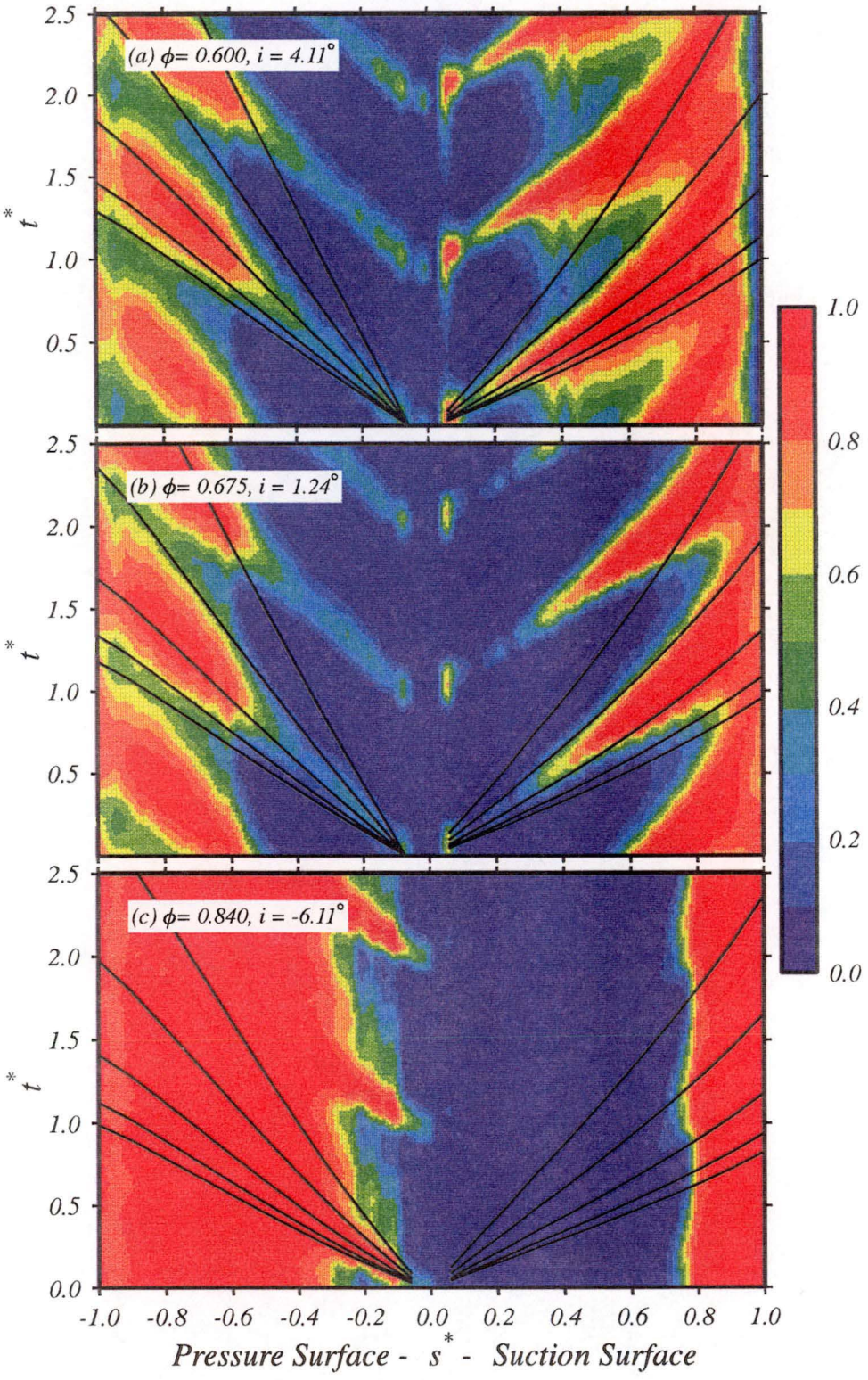

Figure 8.14: Time-distance contour plot: ensemble average intermittency. Particle trajectories for $1.0U$, $0.88U$, $0.7U$, $0.5U$, $0.35U$ overlaid. Incidence series. $Re_c = 120000$

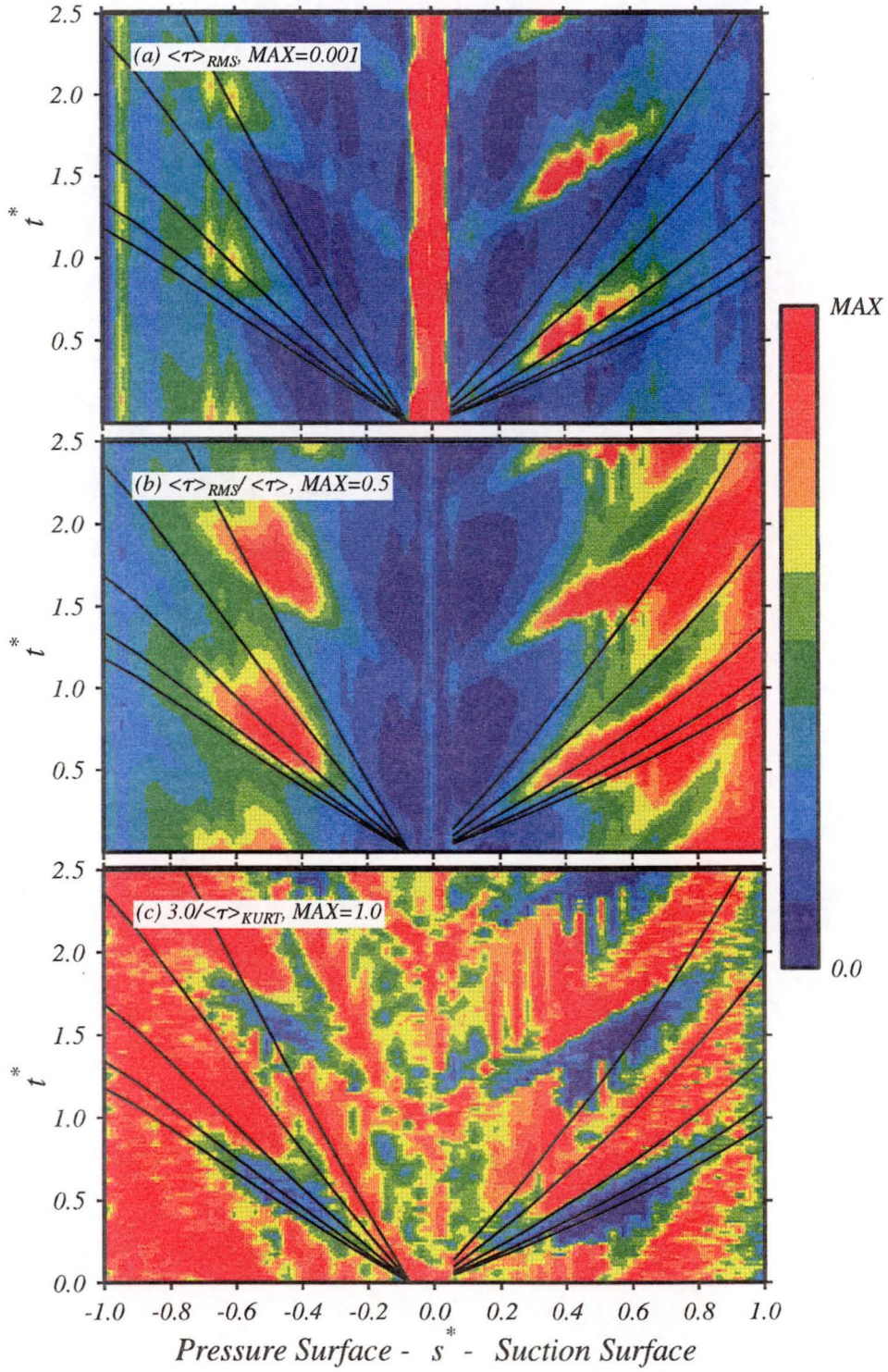

Figure 8.15: Time-distance contour plot: comparison of data processing methods. Particle trajectories for $1.0U$, $0.88U$, $0.7U$, $0.5U$, $0.35U$ overlaid. All plots generated from same test data. $Re_c = 120000$, $\phi = 0.675$

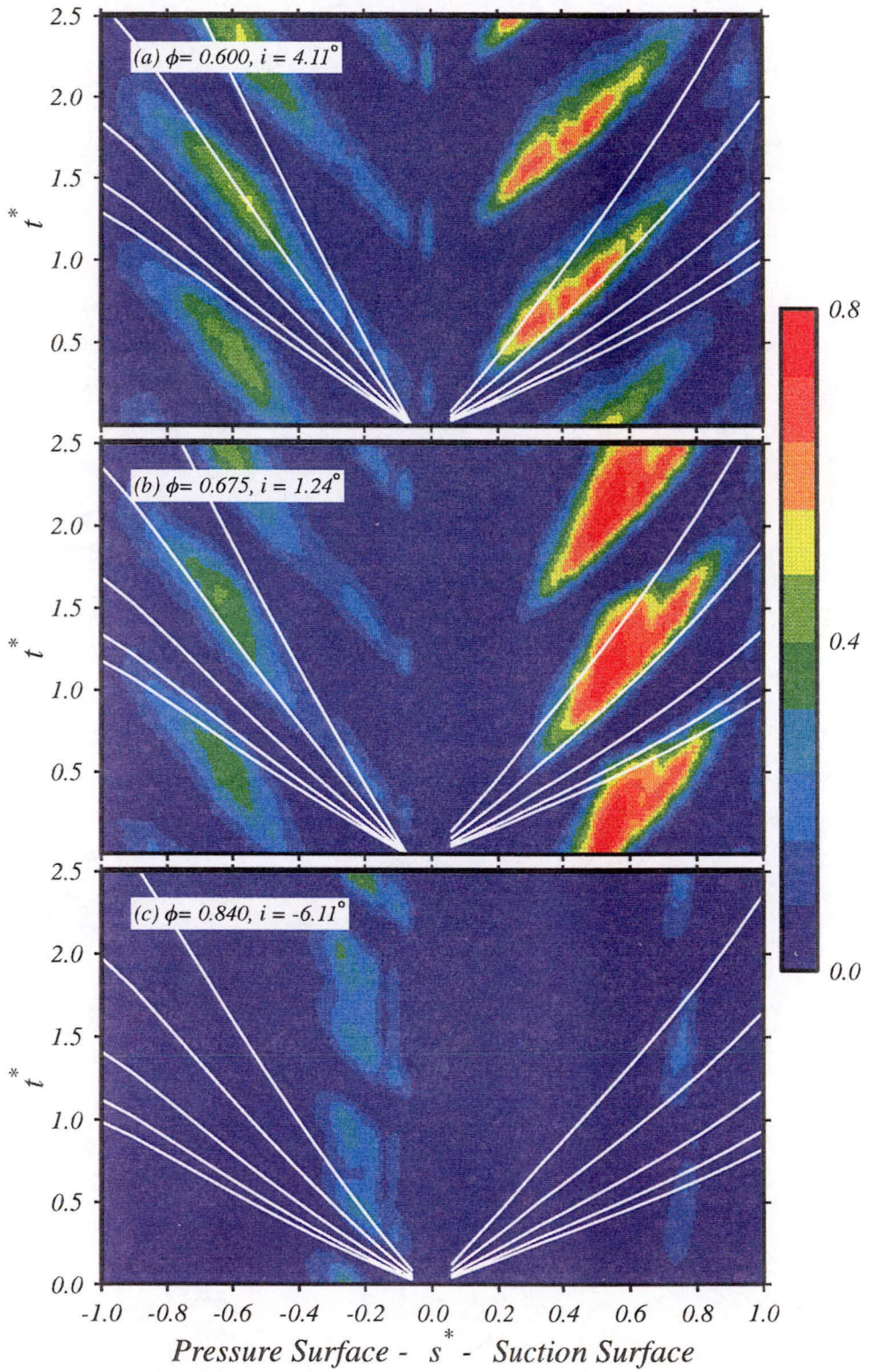

Figure 8.16: Time-distance contour plot: ensemble average probability of relaxing flow. Particle trajectories for $1.0U$, $0.88U$, $0.7U$, $0.5U$, $0.35U$ overlaid. Incidence series. $Re_c = 120000$

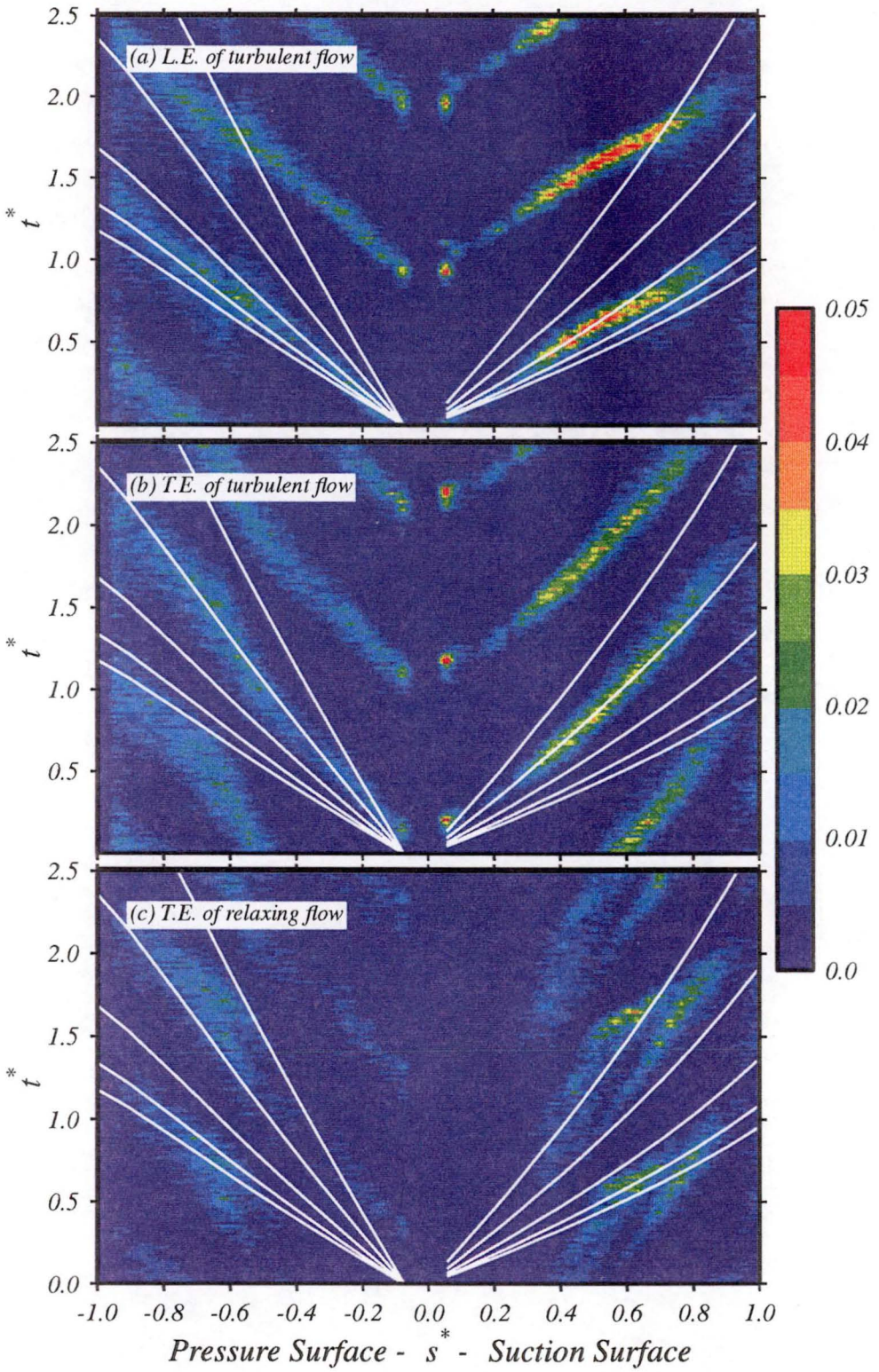

Figure 8.17: Time-distance contour plot: ensemble average probability of boundary layer state change. Particle trajectories for $1.0U$, $0.88U$, $0.7U$, $0.5U$, $0.35U$ overlaid. All plots generated from same test data. $Re_c = 120000$, $\phi = 0.675$

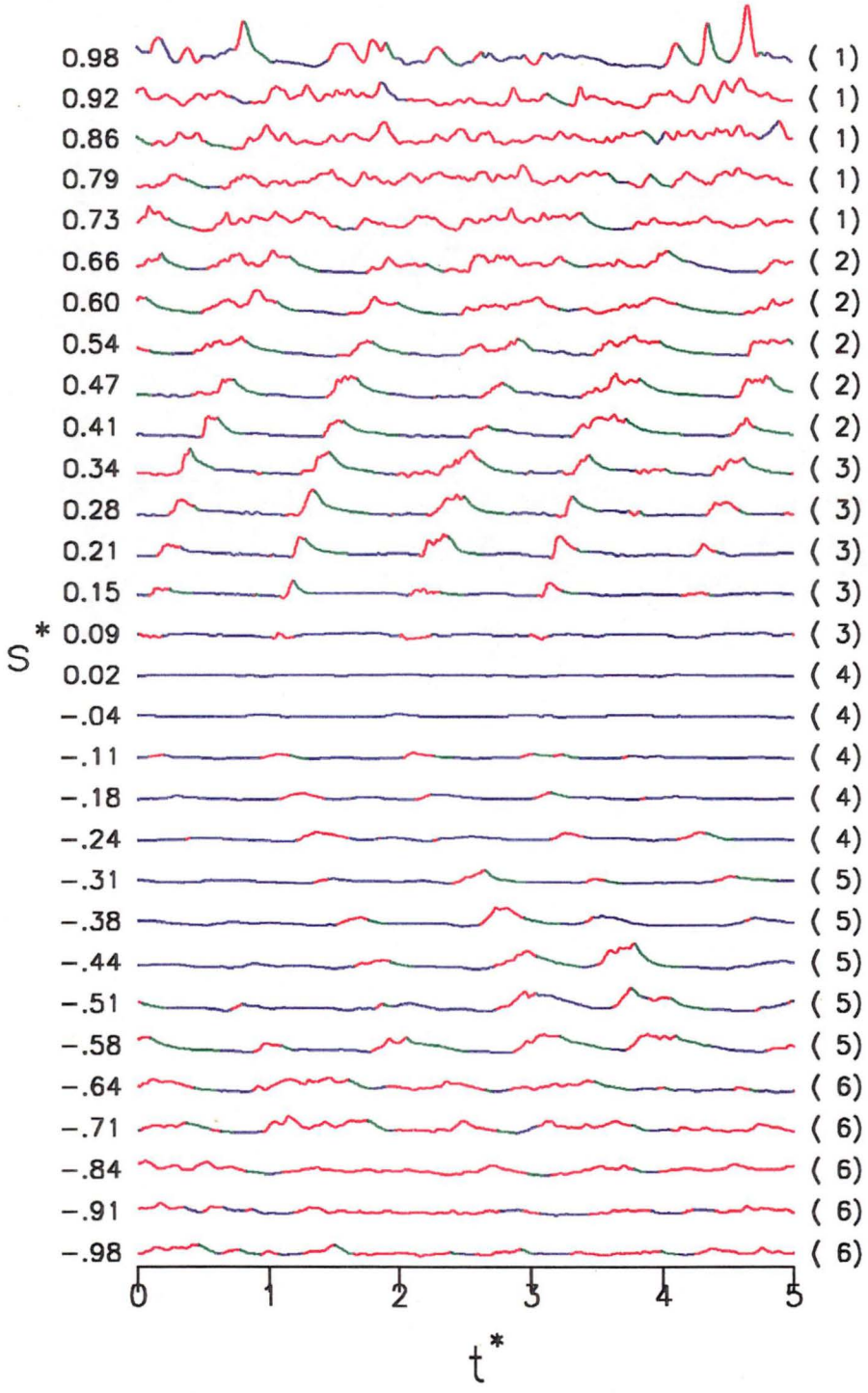

Figure 8.18: Typical individual quasi shear stress records at fractional positions s^* over the stator blade suction surface plotted against dimensionless time t^*. Line colour indicates local flow state as determined by the intermittency detection algorithm: red for turbulent, green for laminar and relaxing and blue for remaining laminar. The grouping number at the right indicates sets of traces which were measured simultaneously. $Re_c = 120000$, $\phi = 0.600$

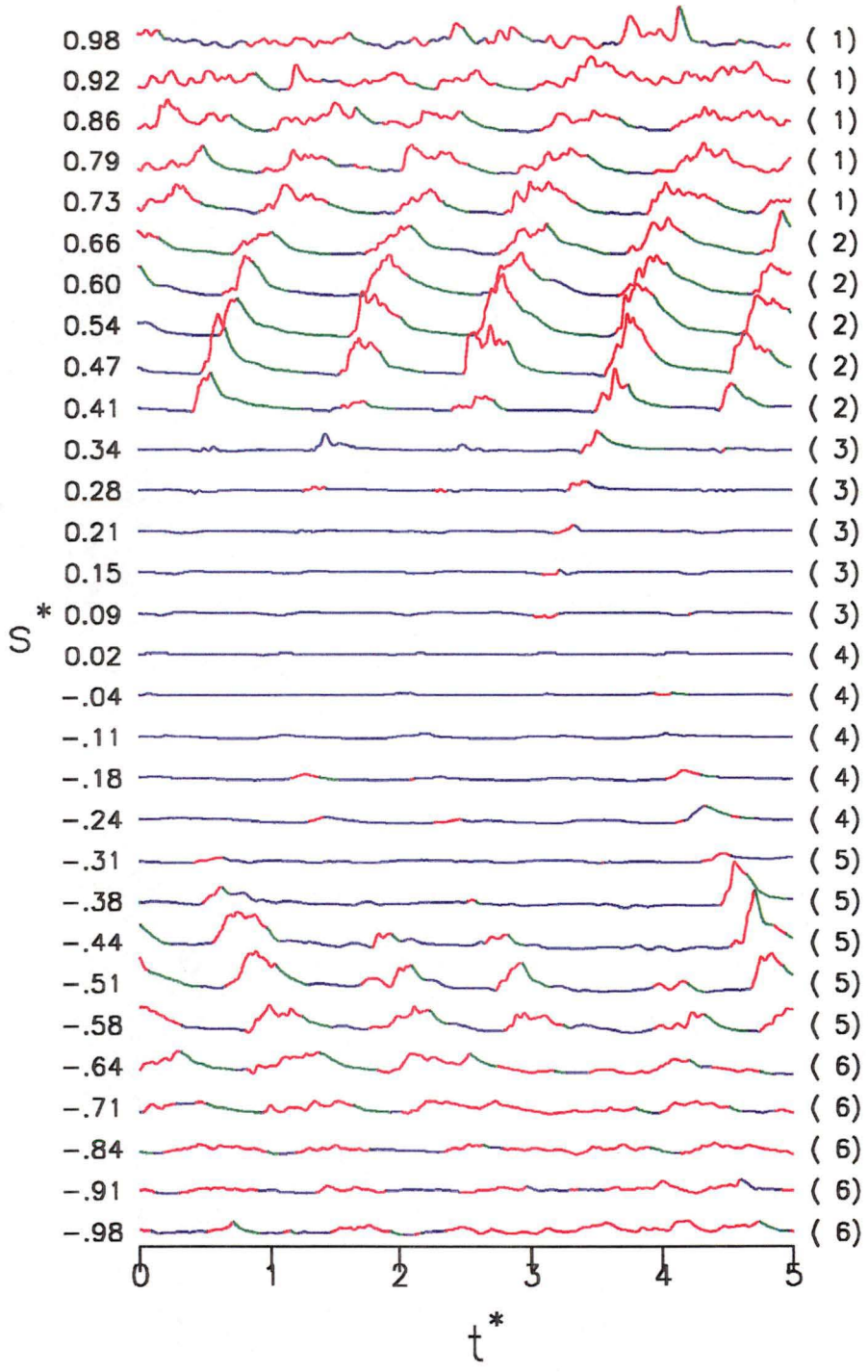

Figure 8.19: Typical individual quasi shear stress records at fractional positions s^* over the stator blade suction surface plotted against dimensionless time t^*. Line colour indicates local flow state as determined by the intermittency detection algorithm: red for turbulent, green for laminar and relaxing and blue for remaining laminar. The grouping number at the right indicates sets of traces which were measured simultaneously. $Re_c = 120000$, $\phi = 0.675$

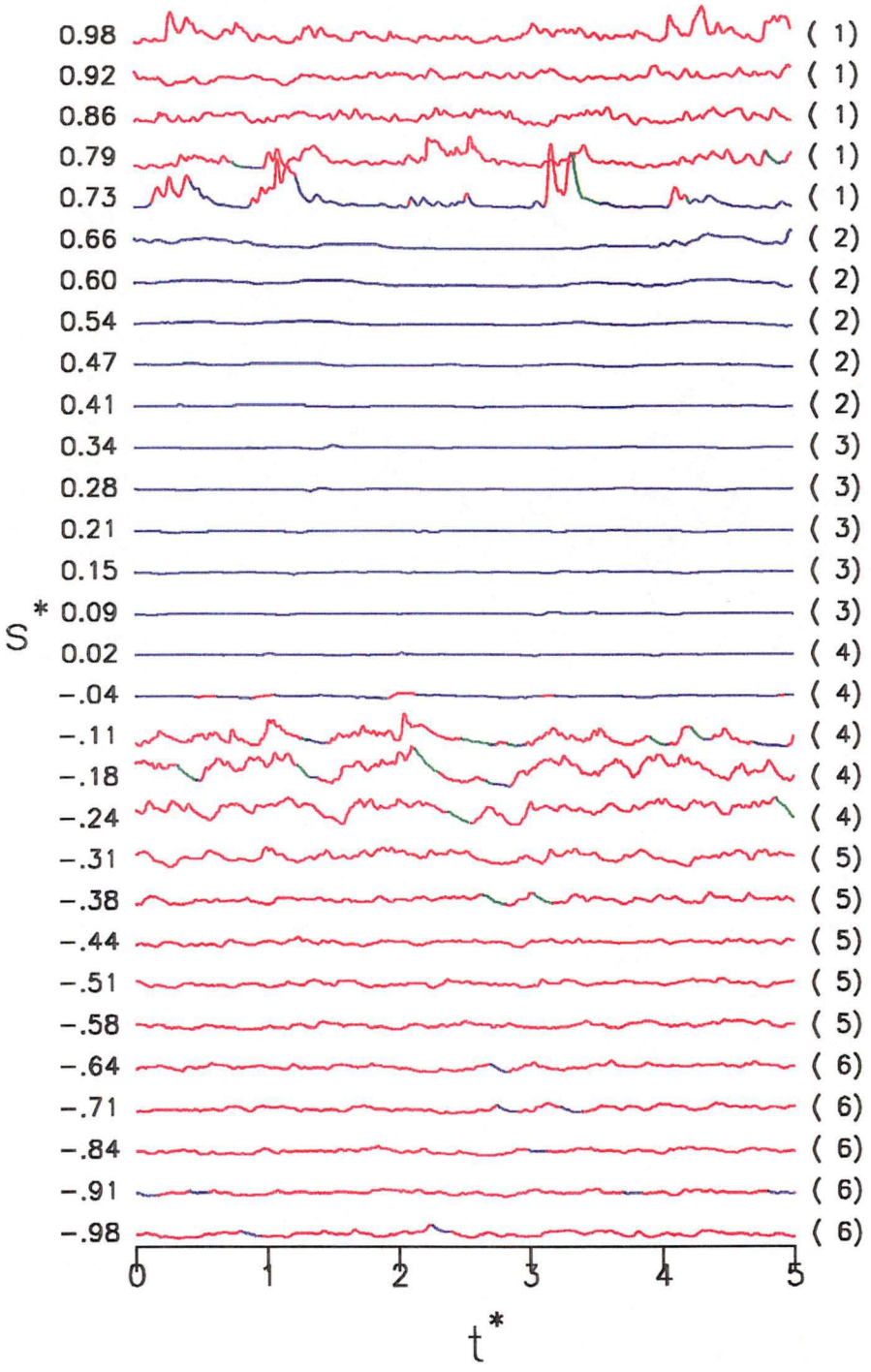

Figure 8.20: Typical individual quasi shear stress records at fractional positions s^* over the stator blade suction surface plotted against dimensionless time t^*. Line colour indicates local flow state as determined by the intermittency detection algorithm: red for turbulent, green for laminar and relaxing and blue for remaining laminar. The grouping number at the right indicates sets of traces which were measured simultaneously. $Re_c = 120000$, $\phi = 0.840$

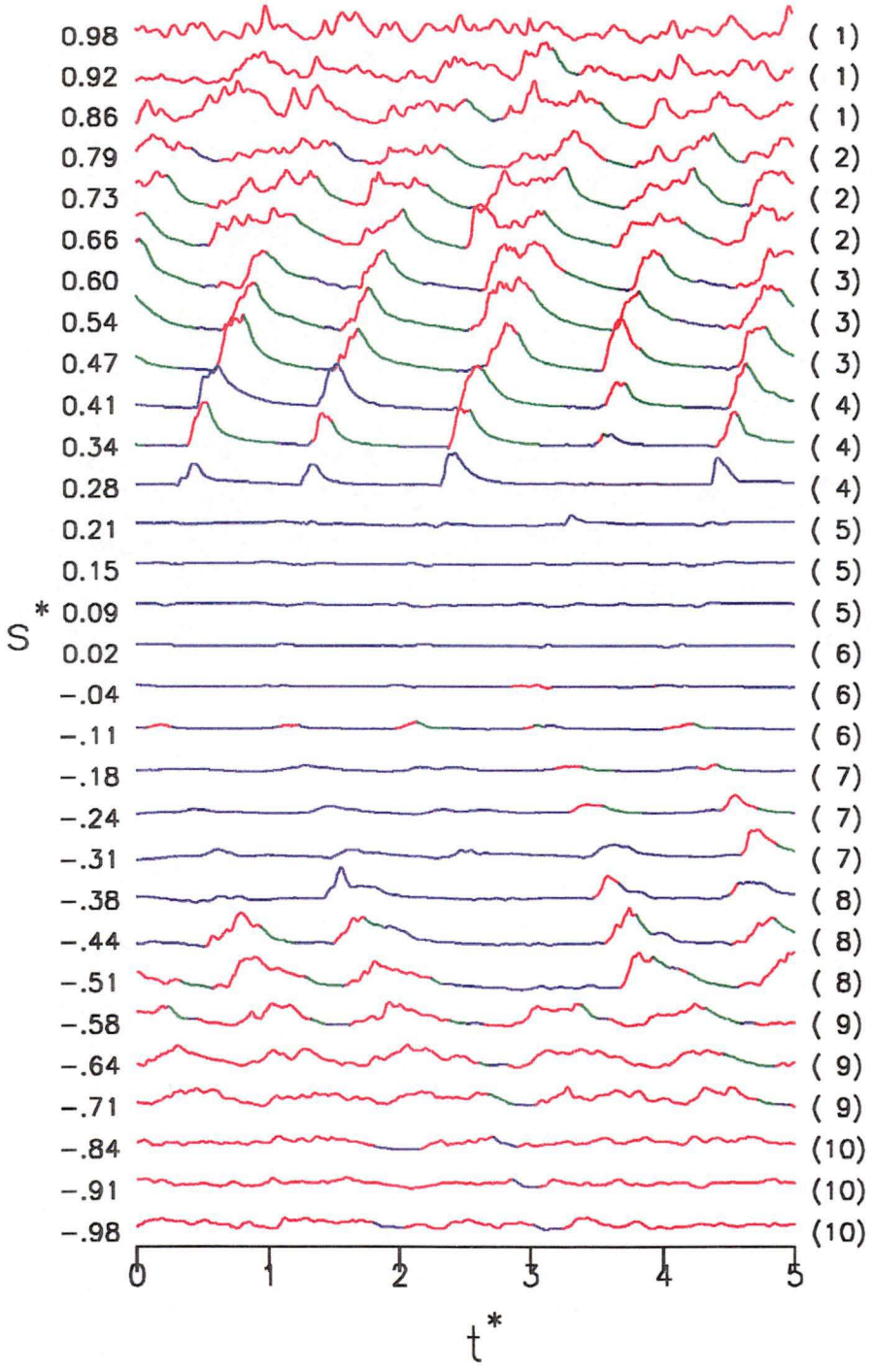

Figure 8.21: Typical individual quasi shear stress records at fractional positions s^* over the stator blade suction surface plotted against dimensionless time t^*. Line colour indicates local flow state as determined by the intermittency detection algorithm: red for turbulent, green for laminar and relaxing and blue for remaining laminar. The grouping number at the right indicates sets of traces which were measured simultaneously. $Re_c = 170000$, $\phi = 0.675$

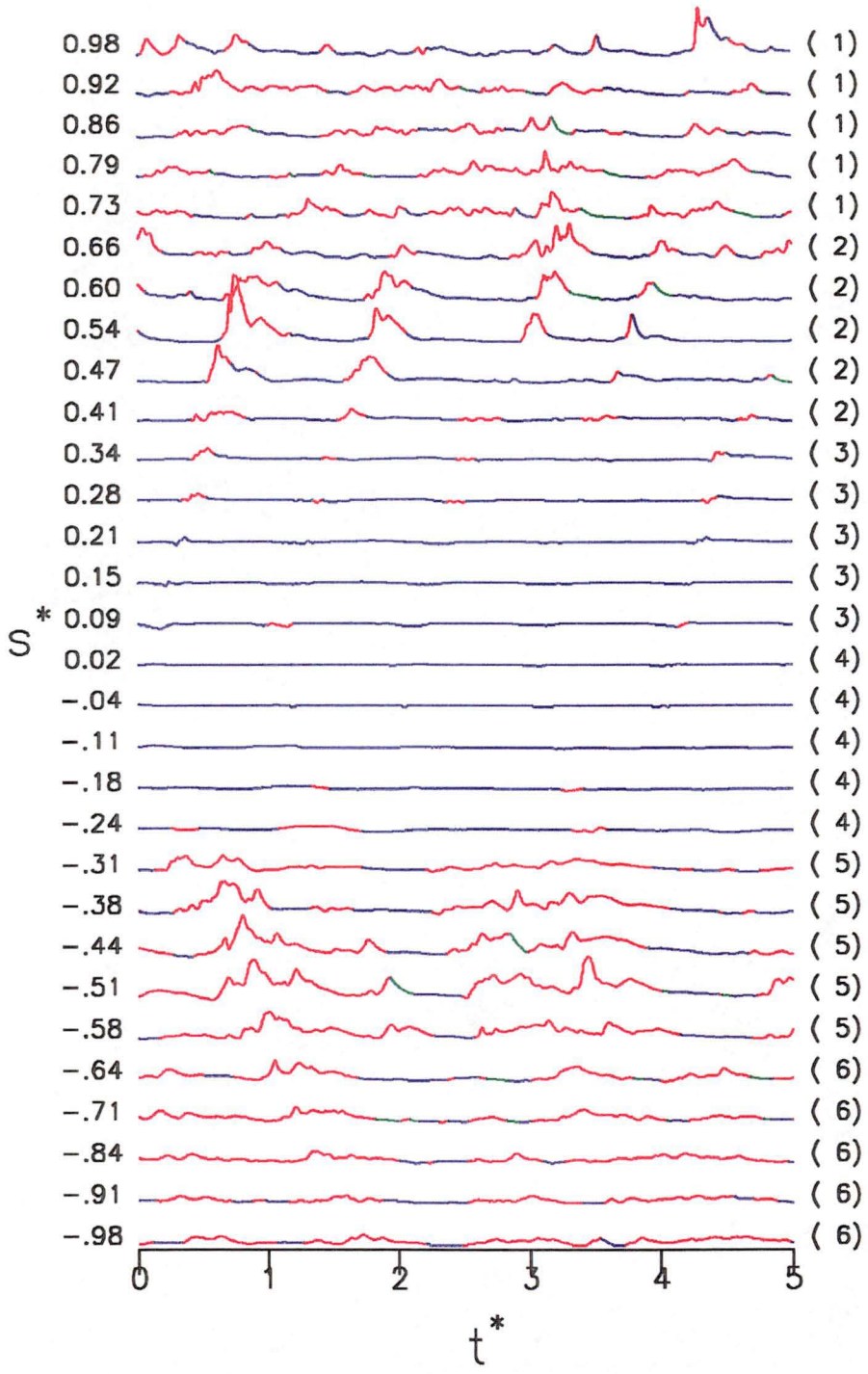

Figure 8.22: Typical individual quasi shear stress records at fractional positions s^* over the stator blade suction surface plotted against dimensionless time t^*. Line colour indicates local flow state as determined by the intermittency detection algorithm: red for turbulent, green for laminar and relaxing and blue for remaining laminar. The grouping number at the right indicates sets of traces which were measured simultaneously. $Re_c = 60000$, $\phi = 0.675$

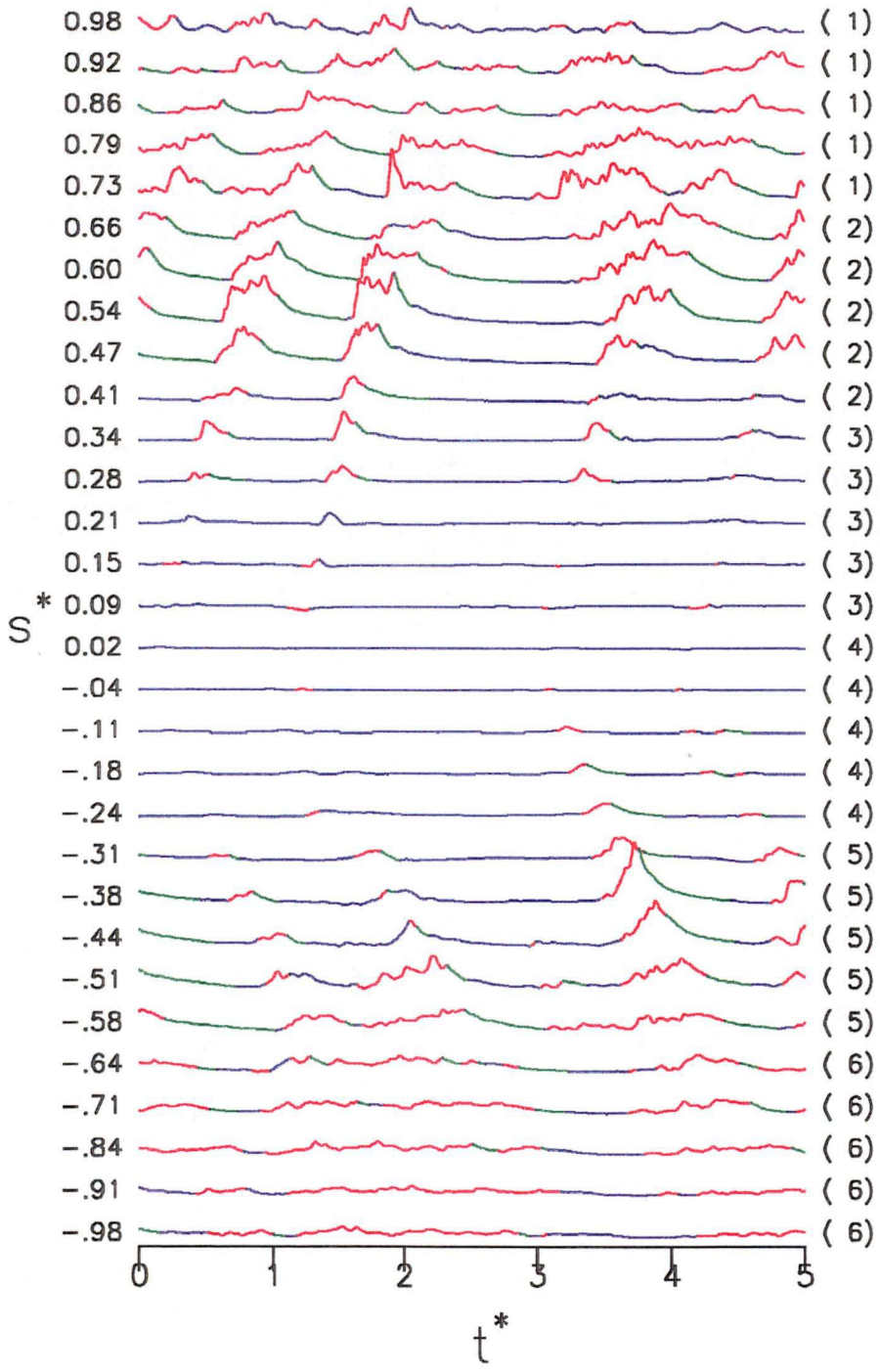

Figure 8.23: Typical individual quasi shear stress records at fractional positions s^* over the stator blade suction surface plotted against dimensionless time t^*. Line colour indicates local flow state as determined by the intermittency detection algorithm: red for turbulent, green for laminar and relaxing and blue for remaining laminar. Blade-out case. $Re_c = 120000$, $\phi = 0.675$

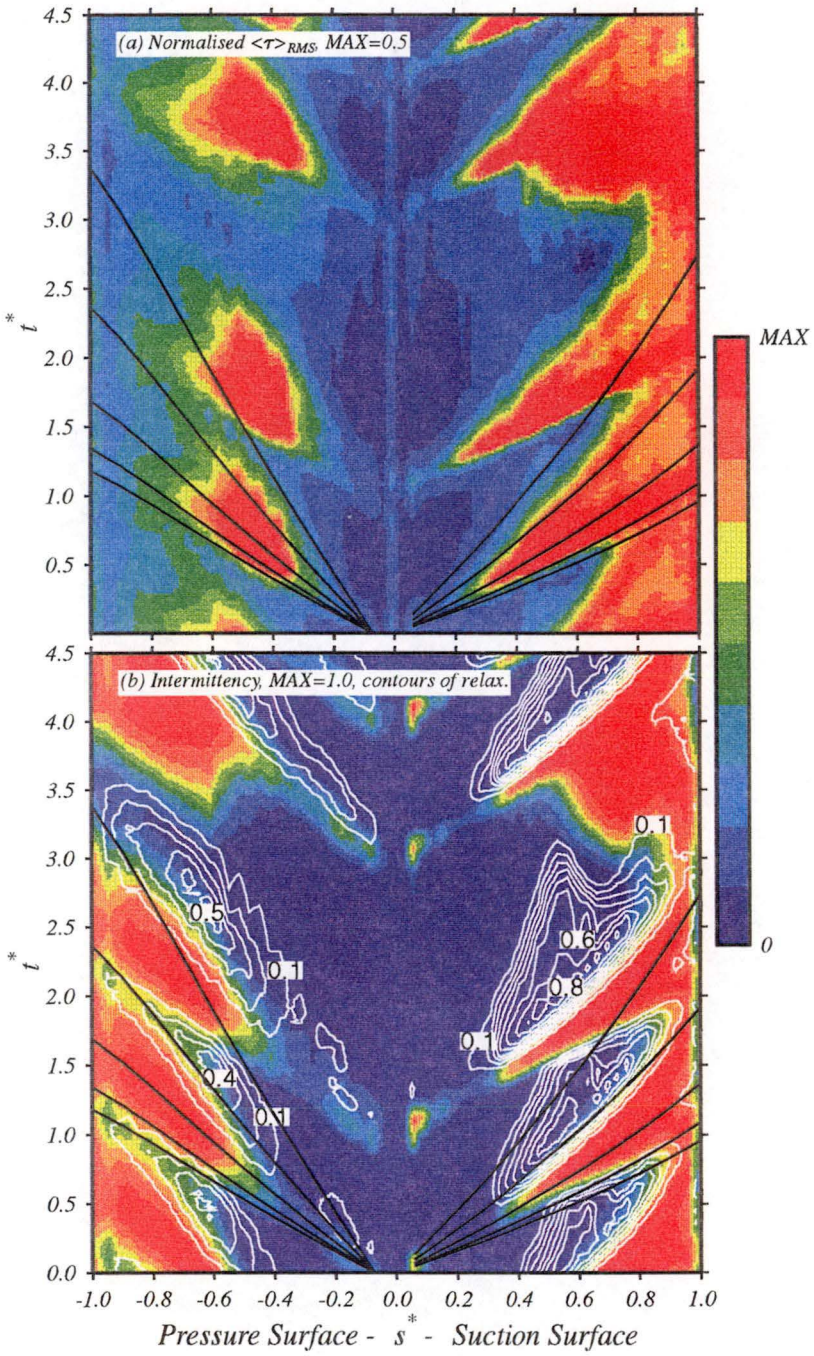

Figure 8.24: Time-distance contour plot: ensemble RMS quasi shear stress (a) and ensemble average intermittency (b). Blade-out case. Contours of relaxing flow probability (intervals of 0.1) overlaid in (b). $Re_c = 120000$, $\phi = 0.675$

Chapter 9

Hot-wire measurements of the stator blade boundary layer

9.1 Introduction

This hot-wire investigation was preliminary in nature and limited to a single chordwise position on the blade suction surface but reveals some features of the unsteady boundary layer flow which cannot be observed using the surface mounted hot-film sensors. Results are presented for a range of incidence values at a constant Reynolds number. Changes in incidence altered the severity of the adverse pressure gradient on the blade suction surface and moved the transition locations relative to the measurement station.

Time average velocity and intermittency profiles are presented. These are characteristic of boundary layers close to separation and the peak intermittency levels are away from the wall. Phase-locked average unsteadiness measurements are also presented. Peak unsteadiness levels in the boundary layer lag the passage of the wake in the freestream.

9.2 Hot-wire boundary layer traverse

A single hot-wire probe was mounted in the research compressor. The sensing wire was axially aligned to coincide with the 60% chord point on the suction surface of one of the stator blades. The probe support was inserted into the stator passage from downstream at a slight angle to the flow and was secured at right-angles to a mounting inserted through the outer casing downstream of the blade-row. The probe was fixed circumferentially relative to the casing and the blade surface boundary layer was traversed past the probe by circumferentially rotating the stator blade row.

The hot-wire boundary layer traverses were taken at incidence values chosen to provide transitional states ranging from laminar to almost fully turbulent at the probe traverse location. The incidence and flow-coefficient values for the test cases are given in Table 9.1. Boundary layer thickness is difficult to define and measure in the current situation due to the significant velocity variation across the passage caused by the potential flow field. The quoted values for δ at $u/U = 0.99$ are the best estimates from the available data. The boundary layer values shown here are time-averaged.

The data presented here was all taken at a constant Reynolds number of $Re_c =$

Table 9.1: Hot-wire boundary layer traverse test cases. Traverse at $x/c = 0.6$, $Re_c = 90000$ and $a/S = 0.5$

ϕ	$i°$	H	Re_θ	Tu [%]	δ_{99} [mm]
0.609	3.2	2.17	339	5.0	2.8
0.704	-1.0	3.37	197	3.3	1.4
0.726	-2.0	3.77	186	2.9	1.4
0.752	-3.4	3.92	160	3.4	1.2
0.791	-5.1	3.70	161	2.6	1.1

90000. The relative IGV-stator blade row circumferential position was $a/S = 0.5$ (see Fig. 3.3). Some additional detail and further results from this test series can be found in Walker et al. [139]. Test cases at another relative IGV-stator position were presented in Walker and Solomon [138]. The incidence values quoted in these papers pre-date the discovery of an error in the rotor blade angle setting (see Appendix A) and corrected incidence values have been quoted here.

The hot-wire was calibrated in a small closed circuit wind tunnel prior to use in the compressor. Periodic in-situ calibration drift checks were made during the measurement series by moving the wire to a reference location in the compressor well outside the suction surface boundary layer. The signal from the anemometer bridge was processed digitally as discussed in Appendix C. Wills' [142] wall correction was applied to correct for heat loss to the aluminimum blade surface. A DISA type 55P05 hot-wire probe was used with a DISA type 55M10 constant temperature anemometer bridge. The probe sensing wire nominal diameter was 5 μm and the length to diameter ratio was approximately 250. The anemometer signal was digitised at a rate of 100kHz and a 50kHz low-pass filter was used to reduce aliasing. The unsteady data was DC coupled and an TSI-IFA type 100 signal conditioning unit was used to match the signal level to the input of the analogue to digital converter.

Each unsteady velocity record consisted of 1300 samples which corresponds to just over three rotor blade passing events at the chosen data sampling rate and compressor operating speed. Phase-locked averaging was performed on 100 records acquired at each measurement location. The number of measurement stations inside the boundary layer ranged from 11 to 15.

Because of the nature of the traversing method used, the hot-wire traverse plane was not perpendicular to the blade surface. The normal distance from the wire to the blade surface was found by correcting for a 22.5° incline of the blade surface from axial at the measurement location. Correction was also made for deflection of the blade at operating speed using data from Walker [132]. The hot-wire sensor position relative to the stator surface was determined using a 2.5 μm dial gauge mounted outside the compressor casing. The position zero was measured to 5 μm but uncertainty of the position of the sensor wire on the probe tip limited y-position accuracy to 0.05 mm. The diameter of the sensing wire support tips limited the minimum sensor-blade distance to around 0.1 mm.

9.3 Results

The trend of suction surface velocity gradient with incidence for the current Reynolds number is similar to that presented for $Re_c = 120000$ in Fig. 5.3. At high positive incidence (low flow-coefficient ϕ) there is a strong adverse pressure gradient on the suction surface starting downstream of the velocity peak which is close to $s^* = 0.05$. This strong positive pressure gradient promotes earlier transition than at lower incidence values (both in the wake-induced path and between wakes) as demonstrated in the previous chapter in Fig. 8.13.

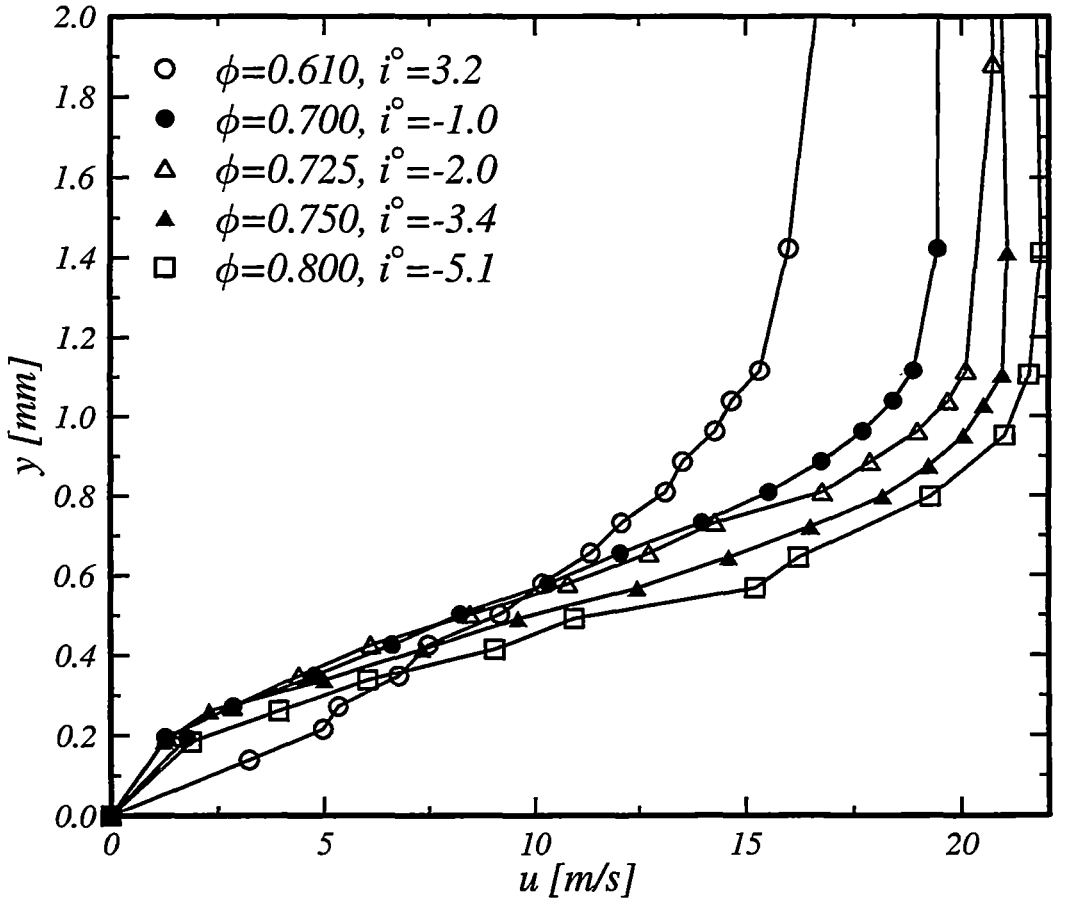

Figure 9.1: Mean velocity profiles u [m/s] at $x/c = 0.6$ from hot-wire traverse data. $Re_c = 90000$, $a/S = 0.5$

Fig. 9.1 shows the measured time-mean velocity profiles over the incidence range. The positive incidence case has a boundary layer profile which is attached and approaching a fully turbulent boundary layer. The lower incidence cases show points of inflection and have profiles closer to those of a separated laminar shear layer. As the incidence is reduced, the strength of the adverse pressure gradient also reduces; this in turn delays transition onset and as the boundary layer at the measurement station becomes more laminar (on average) it becomes more susceptible to separation.

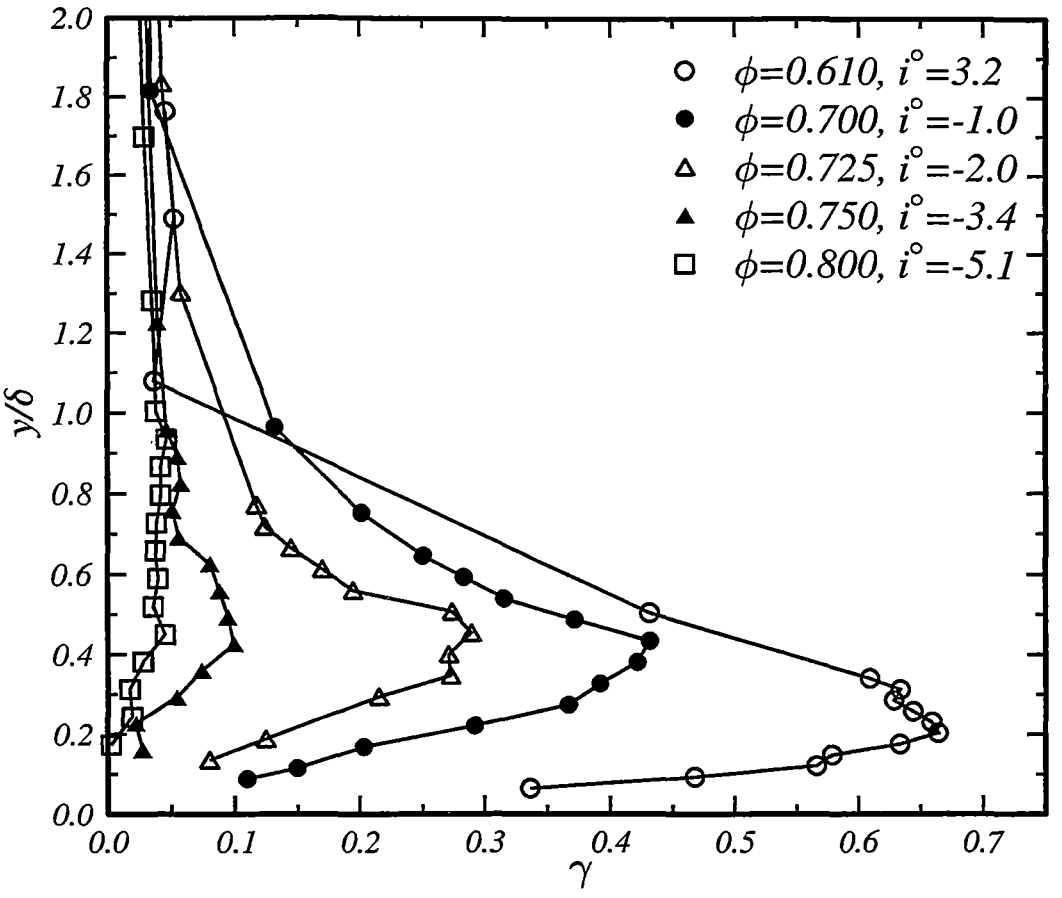

Figure 9.2: Mean intermittency γ profiles at $x/c = 0.6$ from hot-wire traverse data. $Re_c = 90000$, $a/S = 0.5$

The hot-wire traverse was processed to give intermittency data using a simplified version of the TERA method of Falco and Gendrich [31] (see Chapter 7). Profiles of time-mean intermittency across the boundary layer are presented in Fig. 9.2. For the $i = -5.1°$ case the boundary layer is laminar and (from Fig. 9.1) close to separation. The intermittency profile in the $i = -3.4°$ case shows the commencement of transition with the peak intermittency away from the wall at $y/\delta = 0.4$. With increasing incidence the peak intermittency level at the measurement point increases and moves closer to the wall as the boundary layer becomes more turbulent and (on average) more attached. The low values of time-average intermittency at the wall are caused by a combination of the effect of adverse pressure gradient on intermittency distribution and the intermittent separation of the boundary layer between the passage of wake-induced turbulent spots.

Unsteady RMS velocity data for three of the test cases is shown in Fig. 9.3 (presented as $<u>_{RMS}/U$ [%]). The data is plotted against normalised time t^*. Wake passing events in the freestream are shown by raised disturbance levels in the freestream at $t^* = 0.2, 1.2$ and 2.2. Fig. 9.3 (a) shows high disturbance levels in the boundary

layer following the passage of the wake in the freestream. The highest levels of disturbance in the wake-induced turbulent patch lag the passage of the wake. At about 0.75 times the blade passing period following the wake the disturbance levels in the boundary layer drop as the trailing edge of the turbulent spot passes. The remaining peak disturbance levels in the boundary level move away from the wall suggesting the intermittent growth of separation which persists until just after the next turbulent spot arrives to re-energise the boundary layer.

The $i = -2.0°$ case shows a decrease in unsteadiness level and in spot size. At the highest negative incidence case in Fig. 9.3 (c), the wake disturbances are still of similar level but disturbance levels in the boundary layer are low.

9.4 Conclusions

The unsteady boundary layer traverse data shows that in the adverse pressure gradient experienced on the stator blade suction surface, the turbulence associated with the passage of the rotor wake in the freestream leads the passage of the most turbulent part of the turbulent patch in the boundary layer. Thus the lag in the wake-induced turbulent strips observed in the surface hot-film tests of Chapter 8 is not merely a surface phenomenon.

Intermittency values close to the wall are lower than those at the critical height in the boundary layer. This highlights the care which should be taken when interpreting the surface hot-film data in adverse pressure gradients.

The turbulent structures observed in the boundary layer show significant similarities with the artificially induced turbulent spots of Gostelow et al. [39]. This gives some hope that the development of the transitional boundary layer on the compressor blade can be modelled using information about the behaviour of turbulent spots obtained from these and other similar fundamental studies in controlled environments. Modelling of turbulent spot development is discussed in the following chapters.

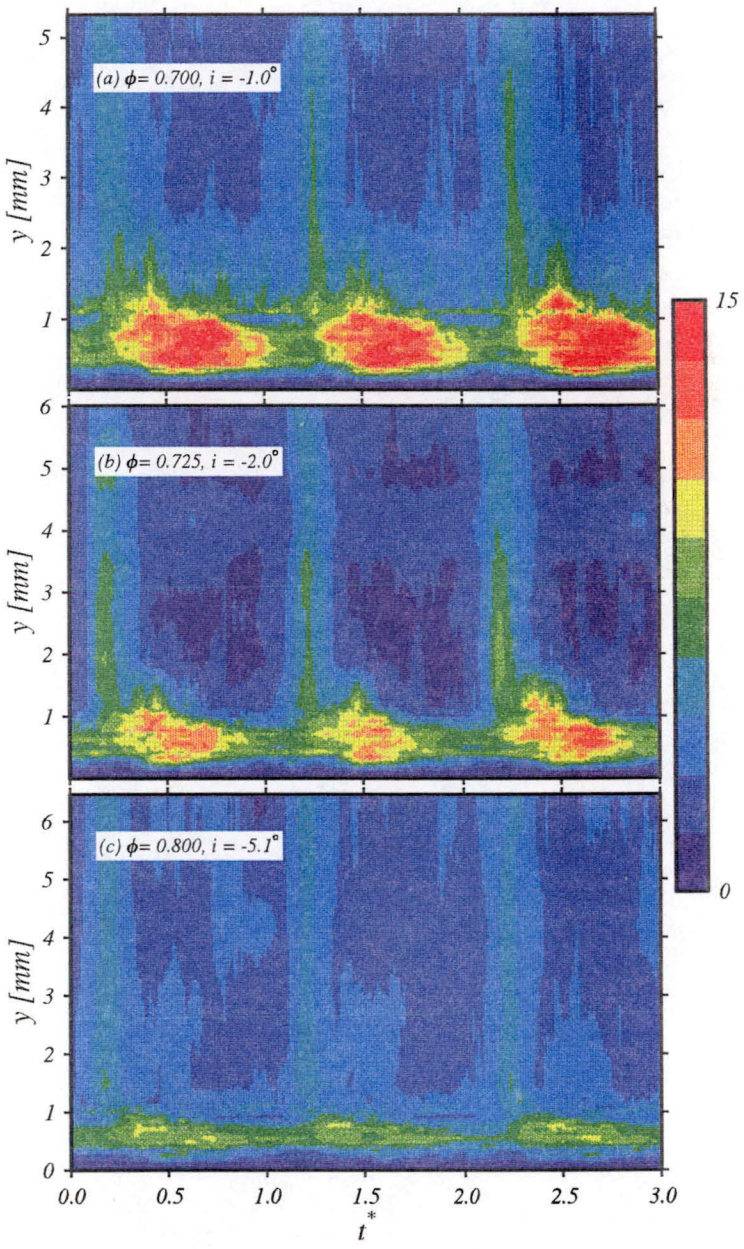

Figure 9.3: Contours of ensemble-average $<u>_{RMS}/U$ [%] in the y–t^* plane at $x/c = 0.6$ from hot-wire traverse data (selected cases)

Chapter 10

Predicting transitional flow

10.1 Introduction

The preceding chapters have demonstrated the highly complex nature of transitional boundary layer flow disturbed by passing wakes. This chapter investigates some of the commonly available methods for predicting transition onset and transition length in a turbomachinery environment. Historically, the unsteadiness associated with wake passing was either ignored or allowed for by artificially raising the (time-average) turbulence level. One goal of the current work was to improve codes which are commonly used interactively in the blade design process. When developing blade sections, designers typically use a boundary layer code (integral or differential) which is coupled with an inviscid flow solver.

Transition modelling has evolved as the importance of the transition region to flow development has become more widely recognised. Transition modelling can be conveniently divided into the two problems of finding the transition onset point and then the length of the transitional zone (or the streamwise distribution of intermittency). Historically the models have developed as follows:

- Point transition at the leading edge
- Point transition at the suction peak
- Point transition at a predicted (by correlation) onset location
- Length transition at a predicted (by correlation) onset location

For high Reynolds number applications in steady flow, where the transition length is a small proportion of the boundary layer length, a point transition assumption may suffice. The lower Reynolds numbers found in gas turbine engines are likely to give a significant proportion of transitional flow on blade surfaces, especially in the LP-turbine. Wake passing also lengthens the transition zone by causing earlier transition in wake-affected zones and delaying transition in the inter-wake regions. The importance of transition modelling to turbomachinery blading design has been established by Hourmouziadis [59], Mayle [80] and others.

The different modes of transition were introduced in Chapter 2.1. On turbomachinery blading, transition is usually assumed to occur through the *bypass* mode. Bypass

transition is a general term which refers to any transition mode which occurs before natural transition can affect the boundary layer. Bypass in turbomachinery is primarily attributed to the relatively high disturbance levels commonly encountered. Other bypass mechanisms exist: on some high Reynolds number blading transition caused by surface roughness can be important. Factors such as noise, vibration, heat transfer and surface curvature can also affect the transition process.

Natural transition is of importance in low disturbance level flows such as found in external aerodynamics problems. Linear stability theory has found widespread engineering application through semi-empirical e^n-type amplification ratio methods of Smith and Gamberioni [116] and Van Ingen [128] (see Mack [78]). A new model using parabolised stability equations seems to offer a promising theoretically based approach to the prediction of transition in low disturbance level flows (Bertolotti et al. [7]). By contrast, prediction of bypass transition is heavily reliant on empirical correlations.

The current experimental work has revealed the important influence of unsteadiness on the flow. A full unsteady flow solver was beyond the scope of the current work (and remains impractical for interactive use by designers). Periodic unsteadiness in the flow allows for the possibility of *multimoded* transition (Mayle [80]) where different transition modes are possible at different dimensionless times in the same flow. Prediction of unsteady transition onset locations using a quasi-steady method was attempted in Chapter 8.

None of the currently available techniques for calculating transitional flow with wake passing allow for the changes in spot spreading behaviour with pressure gradient which was observed by Gostelow et al. [40]. To this author's knowledge only Schulte [112] has attempted the development of a transitional intermittency model which allows for the relaxing flow which follows turbulent spots.

10.2 Natural transition

An introduction to the stability of boundary layer flows may be found in Schlichting [107] or White [141]. Natural transition arising from instability to small two-dimensional disturbances is of limited direct importance to transition in turbomachinery although it may play a role in multimoded transition. Linear stability theory provides a reasonable model of the natural transition process. Some of the results from linear stability theory are also applicable in bypass transition.

Schlichting commences his discussion of boundary layer transition with a description of the Reynolds pipe-flow experiment. This work introduced the concept of a critical Reynolds number beyond which transition would occur. Even in this geometrically simple flow, the critical Reynolds number has been found to vary widely (from around $Re_{crit} = 2000$ to $Re_{crit} = 40000$) depending on the disturbance level of the inlet flow.

Linear stability theory

Linear stability theory considers the growth of small perturbations in a two-dimensional parallel mean flow. These sinusoidal instability waves are commonly referred to as Tollmien-Schlichting (T-S) waves. The stream function assumed for the disturbance is

of the form

$$\psi(x,y,t) = \phi(y)e^{i(\alpha x - \beta t)} \tag{10.1}$$

where α is real and β is complex. The wavelength of the disturbance is $2\pi/\alpha$ and the circular frequency is the real part of β. The complex part of β is the amplification factor of the disturbance. Substitution of the perturbation velocities obtained from this stream function into the Navier Stokes equations leads to the the Orr-Somerfield equation

$$(U-c)(\phi'' - \alpha^2\phi) - U''\phi = -\frac{i}{\alpha Re} \tag{10.2}$$

Assuming α and Re are given then Eqn. (10.2) with appropriate boundary conditions yields a complex eigenvalue, the real part of which is the phase velocity of the disturbance and the imaginary part the amplification factor. Perturbations which have an amplification factor of zero neither grow or decay and are termed neutrally stable. The locus of such points, plotted in a wavenumber versus Reynolds number plane, defines the boundary between stable and unstable flow, or the neutral stability curve.

Linear stability analysis can be extended to non-parallel, three-dimensional and compressible flows as described by Mack[78]. Alternatively, the Orr-Somerfield equation can be simplified to obtain an inviscid instability equation. This equation can be used to show that velocity profiles with a point of inflection are unstable. Flows which exhibit this frictionless instability have neutral stability curves where the unstable region continues as Re tends to infinity. The result that inflectional profiles are unstable has been used to propose a criterion for turbulent spot formation in bypass transition (see Section 10.3).

Schubauer and Skramstad [111] were first to provide conclusive experimental evidence supporting the linear stability theory. Typical turbulence levels in these experiments varied from 0.035% to 0.014% over the speed range of the wind tunnel, a large component of which was due to noise from the fan. In adverse pressure gradient flows T-S waves have increased amplitude and frequency. Walker and Gostelow [136] were able to observe strong T-S wave activity in a 0.3% turbulence adverse pressure gradient flow.

The e^n-type methods based on linear stability theory are widely applied in external aerodynamics. The method involves the calculation of amplification ratios of disturbances and accounts for history of the flow. Selection of the critical amplification ratio is empirical; values in the range 7-10 are commonly used. The exact formulation of the e^n method is computationally time consuming and simplified methods have been developed (Dini et al. [24]). The two-dimensional MISES viscous-inviscid coupled cascade flow solver of Youngren and Drela [144] uses a simplified e^n transition method. Calculations using this code to predict the flow on the stator blade of the current machine suggest that n values lower than those used for low disturbance flows are needed to give transition onset locations which are close to the experimental values. It may be possible to correlate the 'n' factor with freestream disturbance level to produce a method capable of predicting bypass transition; but as amplification of disturbance waves is not commonly observed with bypass transition (see Blair [10]) such an approach would not be physically correct.

10.3 Bypass transition

High freestream turbulence levels can cause onset of turbulent spots well upstream of the location where development of amplified T-S waves would otherwise occur. Morkovin [87] termed this behaviour bypass transition. On turbomachinery blading, failure to predict bypass transition may lead to late prediction of transition onset and consequently underestimated loss. Alternatively late transition may cause laminar separation to be predicted when in fact bypass transition would have prevented it.

Transition in elevated freestream turbulence flows has been studied both experimentally and with numerical modelling. Recent experimental studies include the work of Abu-Ghannam and Shaw [1], Blair [10], Suder et al. [125], Gosetelow et al. [38] and Coupland (Rolls-Royce) [16]. Numerical studies of bypass transition include the direct numerical simulation (DNS) work of Yang and Voke [143]. Low Reynolds number turbulence models have also been modified to enable them to predict bypass transition (an example is presented by Savill [106]). The latter models assume bypass transition is caused by diffusion of freestream turbulence into the boundary layer. Recent work by Johnson and Ercan [65] and Mayle and Schulz [84] recognise that this is not the correct mechanism for bypass transition and instead suggest that fluctuations in the laminar boundary layer are produced by fluctuating pressures in the freestream.

Laminar boundary layer with high freestream turbulence

Various prediction methods for high freestream turbulence transitional flows overestimate shape factor H in the laminar flow just prior to transition onset. This may be the result of late transition onset prediction, as a few turbulent spots upstream of the calculated onset point could reduce the shape factor. Alternatively raised freestream turbulence levels may modify the behaviour of the laminar boundary layer (which remains laminar although highly disturbed). Dyban et al. [28] observed increased skin friction and decreased shape factor in laminar boundary layers in a high disturbance environment. Hart [48] found this effect to be very small in a 2.8% freestream turbulence flow. Some low Reynolds number turbulence models (perhaps with overestimated diffusion of turbulence into the laminar boundary layer) do predict this phenomenon.

Bypass transition onset prediction

An extensive experimental study of the effects of freestream turbulence and pressure gradient on transition was performed by Abu-Ghannam and Shaw [1]. A correlation for bypass transition onset was developed from their results and the earlier correlation of Hall and Gibbings [44]. The Abu-Ghannam and Shaw (AGS) correlation for transition onset has a lower limit as $Re_\theta = 163$ which corresponds to the minimum Reynolds number for which linearised stability theory predicts amplification of small disturbances in a zero pressure gradient flow. This assumption is not valid in adverse pressure gradients where stability theory predicts lower critical Re_θ values. Also, the relevance of linear stability theory to bypass transition is in question. Abu-Ghannam and Shaw used the 'rapid rise' in surface velocity from a surface pitot tube or hot-wire to find the transition onset point. Dey and Narasimha [22] point out that this does not necessarily correspond to the location where spots first form, as a small number of spots must be

present to change the velocity distribution. Another problem with the AGS correlation is that they attempted to account for flow history by correlating freestream turbulence effects with the average turbulence level between the inlet level and the local level at the transition point. This value is not well defined in an arbitrary pressure gradient. Despite these objections, this correlation is widely used to predict bypass transition on turbomachinery blading with fair success.

An alternative transition onset correlation has been proposed by Mayle [80] who suggests that for the turbulence levels found in gas turbines ($> 3\%$) the transition onset point is practically independent of the pressure gradient. Mayle recommends a correlation of the form

$$Re_{\theta t} = 400 Tu^{-5/8} \tag{10.3}$$

A very similar result was obtained by Hourmouziadis [59].

Sharma et al. [115] observed that at transition onset (defined as $\gamma = 0.1$ in this case) the maximum value of disturbance level u_{RMS} in the boundary layer was 3 times the wall friction velocity. Sharma et al. combined this observation with the hypothesis (due to Liepmann) that transition onset occurred when the maximum Reynolds stress in the laminar boundary layer equals the wall shear stress to devise a transition onset criterion. Johnson [64] proposed an alternative criterion for the start of bypass transition based on the local turbulence level in the boundary layer near the wall. Using a simple analysis Johnson demonstrates that when $u_{RMS}/\bar{u}$ exceeds 23 percent, instantaneously inflectional velocity profiles will exist in the boundary layer. Johnson suggests that this condition may correspond to the initiation of hairpin vortices and formation of turbulent spots.

Use of these disturbance level-based transition onset criteria to predict bypass transition requires calculation of the disturbance levels in the boundary layer in question. Johnson and Ercan [65] present a model for the growth of near-wall disturbances in high freestream turbulence level flows in which the growth rate is correlated with the wall skin friction coefficient. Combined with Johnson's breakdown criterion a transition model is developed. Mayle and Schulz [84] have proposed a model where the growth of disturbances imposed on the laminar boundary layer by fluctuating pressure forces is calculated using a laminar kinetic energy equation. This model has been tentatively used with the Sharma-Liepmann onset criterion. Both the Johnson-Ercan and the Mayle-Schulz models are new and relatively untested but they do give hope that current empiricism in bypass transition prediction can be reduced.

10.4 Transition length prediction (steady flow)

Once the transition onset location is determined the length of transitional flow (or the rate at which transition takes place) is required. Empirical correlations have been proposed for predicting transition length. Dhawan and Narasimha [23] correlated transition length with the surface distance Reynolds number for zero pressure gradient flow. Abu-Ghannam and Shaw [1] adopted this model and provided a correlation for the growth of momentum thickness through the transition zone, based on the momentum thickness at transition onset. More representative models for the development of the intermittent boundary layer are based on the turbulent spot model of Emmons [29].

Walker [134] developed an alternative minimum transition length model in which turbulent spots were assumed to be regularly formed on each primary T-S wave cycle. The corresponding transition length was determined by calculating the length of flow required for adjacent turbulent spots to merge.

Turbulent spots

Prior to the observations of Emmons [29] the transition region was assumed to be a jagged fluctuating front across the flow (Narasimha [90]). Emmons [29] found that transition of the boundary layer on a nearly horizontal water table occurred through the growth of 'islands' of turbulence surrounded by laminar flow. These *turbulent spots* were visible in the disturbed surface of the water and appeared at random times and locations on the surface. The spot model of transition was confirmed by the observations of Schubauer and Klebanoff [110]. The probability of turbulent flow at a point in space (and time for unsteady flows) is defined as the intermittency γ.

Emmons' spot model

Emmons [29] developed a statistically based theory for calculating the streamwise intermittency distribution for a transitional boundary layer. The intermittency at any point $P(x, y, t)$ is given by

$$\gamma(P) = 1 - \exp\Big[-\int_{R(P)} g(x', y', t')\, dV\Big] \tag{10.4}$$

where $R(P)$ is the dependence cone for point P (i.e. the time-space volume in which turbulent spots must form in order to cause turbulent flow at point P) and g is the function describing the probability that a turbulent spot will be formed at (x', y', t'). Emmons initially assumed that the probability of turbulent spot formation was equal everywhere in the plate to give $g(x', y', t') = \text{consant}$.

Narasimha's concentrated breakdown hypothesis

Narasimha [89] found that Eqn. (10.4) gave better agreement with experiment when it was assumed that spots form at a preferred streamwise location. This *concentrated breakdown hypothesis* gives an expression for g in steady 2-D flow of the form

$$g(x) = n\delta(x - x_t) \tag{10.5}$$

where x_t is the streamwise transition onset location and δ is Dirac's delta function. n is the spot generation rate (spots formed per unit time per unit span at x_t).

The concentrated breakdown hypothesis can be criticised on the basis that if breakdowns are possible at x_t then they must be more likely downstream of x_t where the boundary layer is less stable. Dhawan and Narasimha [23] demonstrate that if breakdown locations are assumed to have a normal distribution centred on x_t, the resulting intermittency distributions are not significantly different to those given by Eqn. (10.5). LaGraff et al. [72] also test an intermittency model which uses a distributed breakdown assumption. Schulte [112] provides a possible explanation for the success of the concentrated breakdown hypothesis based on the calmed region which follows developing

spots. Schulte suggests that once a few spots are formed around x_t their calmed regions inhibit further breakdowns in the surrounding laminar flow.

Universal intermittency distribution

Given a spot propagation parameter σ, which Narasimha [90] defines as the base area of the propagation cone at a unit distance from the apex, and assuming that the vertices of the propagation cone follow straight-line trajectories, Narasimha combined Emmons' intermittency expression Eqn. (10.4) with the concentrated breakdown hypothesis to give a universal intermittency distribution. The following expression is a generalised form of Narasimha's original universal intermittency distribution

$$\gamma = \begin{cases} 1 - \exp[-(x - x_t)^2 n\sigma/U] & \text{for } (x \geq x_t) \\ 0 & \text{for } (x \leq x_t) \end{cases} \tag{10.6}$$

The transition length is determined from this expression by the values of $n\sigma$ and U. The spot generation and propagation information $n\sigma$ can be obtained from any of the various transition length correlations which are available. Eqn. (10.6) describes a characteristic shape for the intermittency distribution which is fully described when $n\sigma$, U and x_t are specified. This expression has proven highly successful and generally describes transition in zero and constant pressure gradient flows very well. However, this expression cannot account for any changes in flow conditions (velocity, pressure gradient) downstream of x_t which may alter the transition process. Methods for making such allowances are described in Chapter 11.

10.5 Wake-induced transition

Emmons spot model Eqn. (10.4) is valid in both steady and unsteady flows. The universal intermittency distribution and Narashimha's concentrated breakdown hypothesis cannot be applied to unsteady flow (except in a quasi-steady way) without modification. The results of Chapter 8 clearly indicate that a different transition model is required in wake-induced transitional flows.

The results of Pfeil et al. [96] implied that a simple wake-induced transition model could be developed where time-averaged intermittency is found by assuming wake-induced transitional strips grow with constant leading and trailing edge velocities aU and bU from the wake-induced transition onset point x_{tw}. Wake-induced strips are formed with a wake passing period of T. Funazaki et al. [35] express this simple model as

$$\gamma(x) = \left(\frac{1}{bU} - \frac{1}{aU}\right) \frac{x - x_{tw}}{T} \tag{10.7}$$

This model takes no account of other transition modes. Hodson [55] uses a similarly simple model to predict the effects of wake passing on profile loss.

Another theory for wake-induced transition has been proposed by Mayle and Dullenkopf [82]. This model, based on Emmons' theory, accounts for spot production via both the natural and wake-induced modes to calculate the time-average intermittency distribution in the wake-disturbed flow. Wakes are assumed to form turbulent strips

which then grow independently of the wakes. Calmed regions and their inhibition of spot development are not allowed for in this model (which treats the development of the two transition modes separately). The model also assumes that spot production in the wakes disturbed flow is very intense, which is not always well supported by the observations of Chapter 8 (especially on the pressure surface). Application of this model requires prior knowledge of the transition onset locations (natural and wake-induced) and the spot production rates for the two modes. Mayle and Dullenkopf [82] demonstrate some very good agreement of their model with experimental data. Mayle and Dullenkopf [83] simplified the previous model to produce a wake-induced transition model where time-averaged intermittency depends on the onset point of wake-induced transition and the wake passing period only. Difficulty in predicting the correct onset locations for wake-induced transition remain a problem with this method (Funazaki et al. [35]).

Addison and Hodson [3] describe a model where the unsteady transition onset location is determined from correlations developed in steady flow. An unsteady boundary layer code is used to calculate the unsteady variation of boundary layer parameters and a simple wake-spreading model is used to find the unsteady freestream turbulence levels. The transition onset model used (Abu-Ghannam and Shaw [1]) predicts that freestream turbulence will dominate the transition process. Schulte [112] has recently proposed a transition model which recognises the importance of the relaxing non-turbulent flow region behind a spot. In this model the spot generation rate is corrected to prevent spot formation in the relaxing flow.

The wake-induced transition models described above assume that the turbulent fluctuations in the wake dominate the spot formation process, rather than the periodic velocity fluctuations associated with the wake velocity defect. It does seem likely that the turbulence in the wakes is the dominant factor but no allowance has been made for any effects the velocity defect and jet-wake may have on the unsteady transition process. None of these models describe or predict the differences in spot development observed on the suction and pressure surfaces of the compressor stator blade in the current study.

10.6 Conclusions

Bypass mode transition is likely to dominate the transition of blade surface boundary layers in turbomachinery where freestream disturbance levels are generally high. Natural shear layer instability processes may also play a role in the region between wake-induced transitional strips and in laminar separation regions.

Designers are currently heavily reliant on empirical correlations for the prediction of bypass transition. Ongoing work (Mayle and Schulz [84] and Johnson and Ercan [65]) suggests calculation of the development of unsteadiness in the disturbed laminar boundary layer may provide an improved prediction technique.

Prediction of the length of both wake-induced and steady transitional flow is also largely based on empirical results. Until recently no account has been made of the calmed region and its important effect on spot generation. Better understanding of the behaviour of individual turbulent spots will help to develop more realistic transition length calculation methods.

Wake-induced transition models are still in their infancy. Most of the models proposed to date neglect the effect of periodic velocity fluctuations and assume that wake-induced transition is dominated by freestream turbulence levels. The applicability of transition onset and spot generation rate correlations derived from steady flow data to the unsteady situation has not been thoroughly demonstrated.

Chapter 11

Transition length modelling for turbomachine design

11.1 Introduction

A new method for calculating intermittency in transitional boundary layers in steady flow with rapidly changing pressure gradients has been developed. Previous methods have assumed that turbulent spot propagation velocities and spot spreading angles are not altered by pressure gradient. A recent compilation of experimental spot spreading and propagation data made by Gostelow et al. [40] shows that adverse pressure gradients significantly affect these parameters. This information has been incorporated into a new boundary layer transition length model which is sensitive to local changes in pressure gradient through the transition zone. The new model is simple enough for use in integral boundary layer codes but is able to calculate transitional flows with rapidly changing pressure gradients and predict sub-transitional behaviour.

Development of the new model and its incorporation into an integral boundary layer code is described in this chapter. This model is a development of the Chen and Thyson [14] technique. Sanz and Platzer [104] have applied this model to transition in laminar separation bubbles on aerofoils in steady and oscillatory motion (with modification to limit the behaviour of the model at the extreme λ_θ values in the separated flow). In its current form the model is not valid for unsteady flows with wake passing, although it has been used in a quasi-steady mode to produce the boundary layer predictions of Chapter 8.

The new model is particularly useful in some typical turbine blade surface pressure distributions where transition onset occurs before the velocity peak. In this situation, previous methods would calculate the transition length based on the favourable pressure gradient at onset and fail to allow for the significant shortening of transition which should occur as the newly transitional boundary layer advances into the adverse pressure gradient region.

11.2 Sub-transition

In transitional boundary layer flows with changing pressure gradient, the intermittency distribution can depart from Narasimha's universal intermittency distribution

(Eqn. (10.6)). Narasimha et al. [91] present several test cases which are not well described using the universal intermittency distribution. If a flow observes the universal intermittency equation (and $n\sigma/U$ is constant) then the function

$$F(\gamma) = \sqrt{-\ln(1-\gamma)} \tag{11.1}$$

will describe a straight line. Chen and Thyson [14] proposed a method of calculating transitional flow (described in more detail below) which relates the spot propagation velocities to the local freestream velocity. Narasimha et al. [91] demonstrate that this effect is too small to account for the shapes of the observed intermittency distributions. In Narasimha [90] deviations from the universal intermittency distribution are termed *sub-transitions*. The $F(\gamma)$ plots of Narasimha et al. [91] seem to be piecewise linear but these authors make no suggestions about how to calculate a-priori the slopes or breakpoints of the linear segments.

The term sub-transition has also been used to describe the departure from the universal intermittency distribution often observed in experimental data at low intermittencies (Gostelow et al. [38]). This effect is smaller than that caused by pressure gradient variation observed by Narasimha et al. [91] and it is possible that this discrepancy is a consequence of the concentrated breakdown assumption. Changes of the intermittency distribution for $\gamma < 0.1$ of similar shape and magnitude were obtained by Dhawan and Narasimha [23] when a normally distributed breakdown assumption was used in place of the concentrated breakdown assumption. A distributed breakdown model was also presented by LaGraff et al. [72].

The relatively small change in intermittency distribution which results from replacing concentrated breakdown with distributed breakdown does not seem to justify the additional complication, but this situation may change in wake disturbed flow where the breakdown location moves periodically anyway. The sub-transition caused by changing pressure gradient part way through transition does seem to cause serious deviation from the universal intermittency distribution and so methods for predicting this effect are investigated below.

11.3 New spot propagation data

Gostelow et al. [40] have made measurements of the development of triggered turbulent spots in strong adverse pressure gradients. These results were also compared with those obtained over a range of pressure gradients by other workers. The compiled results reveal a large variation in the spot spreading and propagation parameters with adverse pressure gradients.

The actual geometry of a turbulent spot is complex (Schubauer and Klebanoff [110], Gad-el-Hak et al. [36]) and simplifications are required to permit the development of an intermittency model. The simplification adopted here is to assume the turbulent spot has a triangular plan-form and to ignore any shape variations normal to the surface. This triangular spot model has been used by McCormick [85], Chen and Thyson [14] and others (Fig. 11.1). The simplified model allows the geometry of a turbulent spot to be represented by three parameters, the leading edge velocity aU, the trailing edge velocity bU and the spreading half angle α. These expressions implicitly assume that the spot velocities are functions of the freestream velocity U.

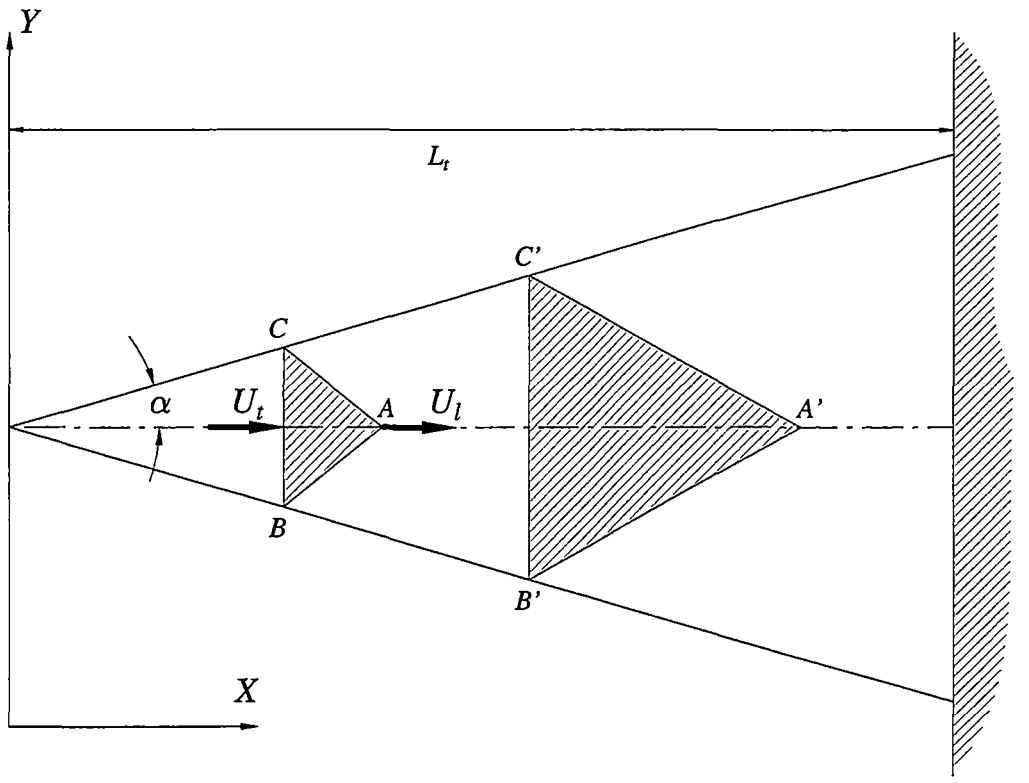

Figure 11.1: Plan view of the triangular spot model at times t and t' (after McCormick [85])

The compiled spot spreading angle data from Gostelow et al. [40] is presented in Fig. 11.2. This data can be conveniently combined with the spot velocity data to produce a spot spreading parameter σ defined as

$$\sigma = \tan\alpha(b^{-1} - a^{-1}) \tag{11.2}$$

Use of this expression reduces to two the required number of parameters for describing a turbulent spot. The compiled spot spreading angle data is presented in Fig. 11.2 and the spot propagation parameter data is shown in Fig. 11.3.

Both the spreading angle α and the propagation parameter σ show large increases with adverse pressure gradient. Data for favourable pressure gradient flows is limited but the variation seems relatively small. Correlations were made to this compiled data using a least squares algorithm (Eqn. (11.3) and Eqn. (11.4)). Expressions with asymptotic behaviour outside the range of the available data were chosen to limit computational problems where extrapolation may be required. The currently available data is insufficiently detailed to reveal any trend with freestream turbulence.

$$\alpha = 4 + (22.14/(0.79 + 2.72\exp(47.63\lambda_\theta))) \tag{11.3}$$

$$\sigma = 0.03 + (0.37/(0.48 + 3.0\exp(52.9\lambda_\theta))) \tag{11.4}$$

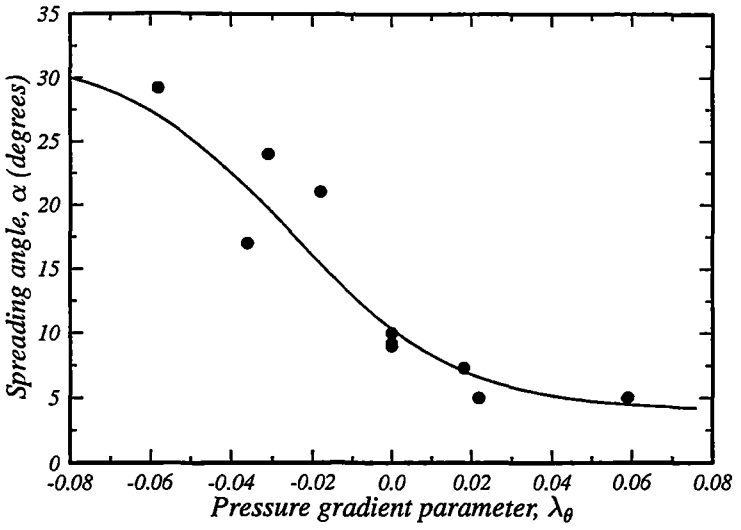

Figure 11.2: Fit to turbulent spot spreading data from various sources compiled by Gostelow et al. [40].

11.4 Spot generation rate correlations

Transition length data can be correlated in a variety of ways. Narasimha [90] demonstrates that the most appropriate non-dimensional breakdown parameter is of the form

$$N = n\sigma\theta_t^3/\nu \tag{11.5}$$

Dey and Narasimha [22] tested a range of transition length correlations. For zero pressure gradient flows with levels of freestream turbulence above around 0.3%, N was found to be constant. Pressure gradient effects were only considered for favourable pressure gradients and correlated with the pressure gradient parameter at transition onset, $\lambda_{\theta t}$. The correlation proposed was

$$N = \begin{cases} 0.7 \times 10^{-3} & (\lambda_{\theta t} \leq 0), \\ 0.7 \times 10^{-3} + 0.24(\lambda_{\theta t})^2 & (0 < \lambda_{\theta t} \leq 0.10) \end{cases} \tag{11.6}$$

The effects of freestream turbulence level and adverse pressure gradient on transition length were studied in a extensive experimental investigation by Gostelow et al. [38]. Their transition length data was correlated in several ways including the use of Narasimha's breakdown parameter N. The correlation given in Gostelow et al. [38] has been extended to favourable pressure gradients using a function suggested by Fraser et al. [32]. A correlation of this form was used in Solomon et al. [120]; later testing has suggested that when coupled with the alteration of the spreading angle and propagation parameter in favourable pressure gradients the resultant lengthening of the transition zone may be too extreme. The form of this correlation (including the modification of Fraser et al.) is then

$$N = \begin{cases} 0.86 \times 10^{-3} \exp(2.134\lambda_\theta \ln(Tu) - 59.23\lambda_\theta - 0.564\ln(Tu)) & \text{for } \lambda_\theta \leq 0, \\ 0.86 \times 10^{-3} \exp(-59.23\lambda_\theta) & \text{for } \lambda_\theta > 0. \end{cases} \tag{11.7}$$

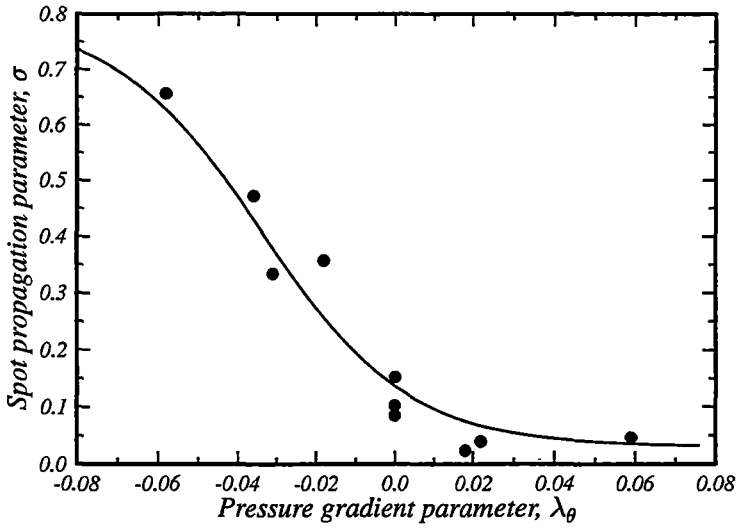

Figure 11.3: Fit to turbulent spot propagation data from various sources compiled by Gostelow et al. [40].

Chen and Thyson [14] presented a spot generation rate correlation of the form

$$G\nu^2/U^3 = Re_{\theta t}^{-2.68}\left(\frac{1}{60+4.68M^{1.92}}\right)^2 \tag{11.8}$$

where $Re_{\theta t}$ is the momentum thickness Reynolds number at transition onset and M is the Mach number. By noting that Chen and Thyson's G equals Narasimha's $n\sigma$ and multiplying by $Re_{\theta t}^3$, the Chen Thyson correlation can be re-expressed in terms of N as follows

$$N = Re_{\theta t}^{0.32}\left(\frac{1}{60+4.68M^{1.92}}\right)^2 \tag{11.9}$$

11.5 Transitional intermittency distribution

The universal intermittency distribution (Eqn. (10.6)) is a simple transition model which seems to give reasonable results in constant pressure flows. This intermittency distribution can be used with any of the N correlations described above. Since these correlations are based on local parameters at transition onset, the transition length is fixed by conditions at this point and nothing the flow does downstream of the onset location will alter it.

Chen and Thyson

Another popular method of estimating the transitional intermittency distribution has been developed by Chen and Thyson [14]. This method uses both the probability theory of Emmons and the concentrated breakdown hypothesis of Narasimha, but also adjusts

the transition length in response to changes in the local freestream velocity. The Chen and Thyson [14] intermittency distribution is given (for 2-D flow) by

$$\gamma = 1 - \exp\left[-n\sigma(x - x_t)\int_{x_t}^{x}\left(\frac{dx}{U}\right)\right] \tag{11.10}$$

The combined spot generation rate and propagation parameter $n\sigma$ is determined from the local conditions at transition onset using one of the N correlations above. This expression allows for convective effects on spot growth associated with changing velocity downstream of the transition onset point. While this model may be expected to be an improvement on the Narasimha expression, it still has not made allowance for the strong changes of σ which occur in adverse pressure gradients.

New method

A new method has been developed to address the shortcomings of the Narasimha and Chen and Thyson methods when applied to arbitrary pressure gradients. The basic features of the new model are as follows:

(a) the concentrated breakdown hypothesis of Narasimha is retained;

(b) the spot inception rate is assumed to depend only on the local conditions at transition onset, x_t;

(c) the spreading rate of turbulent spots is allowed to vary continuously through the transition zone in response to changes in the local pressure gradient parameter λ_θ for the surrounding laminar flow.

The new model does not allow for any relaxing flow behind turbulent spots. The model also assumes the spot propagation and spreading parameters respond instantaneously to changes in local flow parameters, although some lag may be expected in practice.

Derivation of the new model (which closely follows the analysis of Chen and Thyson) is described in Appendix B. The resulting intermittency distribution is given by

$$\gamma = 1 - \exp\left[-n\int_{x_t}^{x}\frac{\sigma}{\tan(\alpha)}\left(\frac{dx}{U}\right)\int_{x_t}^{x}\tan(\alpha)\,dx\right] \tag{11.11}$$

Notice that the spot generation rate n and spot propagation parameter σ must now be obtained separately. For the present study N and σ are determined from the correlations Eqn. (11.7) and Eqn. (11.4) using the values of λ_θ and Tu at transition onset x_t. The spot formation rate n is then obtained from Eqn. (11.5). A direct correlation in terms of n would simplify the process further. It is felt that sufficient information now exists for such a correlation to be attempted.

For the new method the assumptions of constant spreading angle and propagation rates have been abandoned. The new empirical correlations for the spot propagation parameters replace the usual transition length correlations. Changes in the propagation parameters as a result of changes in pressure gradient (and freestream velocity) lengthen or shorten the transition zone as required.

11.6 Testing the new transition model

The integral boundary layer code of Dey and Narasimha [22] (with modifications) has proven a useful test bed for a variety of transition length calculation methods. The method uses a modified Thwaites method for the laminar boundary layer and a lag-entrainment method [43] for the turbulent boundary layer. Within the transition zone the laminar and turbulent solutions are combined as follows:

$$\delta^* = (1-\gamma)\delta_L^* + \gamma\delta_T^* \tag{11.12}$$

$$\theta = \gamma(1-\gamma)\int_0^\delta [u_L(1-u_T) + u_T(1-u_L)]dy + (1-\gamma)^2\theta_L + \gamma^2\theta_T \tag{11.13}$$

$$C_f = (1-\gamma)C_{fL} + \gamma C_{fT} \tag{11.14}$$

where the subscripts L and T refer to laminar and turbulent values respectively. The value of intermittency γ is determined from one of the transition models described above.

The turbulent boundary layer solution is started at x_t assuming continuity of momentum thickness. The laminar and turbulent portions of the layer are assumed to develop without affecting each other. The current method uses the steady flow 2-D momentum integral equation and hence neglects $d\gamma/dx$ terms. Dey (private communication, 1996) suggests that the neglected terms largely balance each other and the net error is small. Since the start point for the turbulent boundary layer (x_t) is unaffected by the transition length model, and the turbulent boundary layer is grown independently of the laminar layer, the current transition length calculation has no effect on the (turbulent) momentum thickness at the end of the transition zone. It is possible to develop more complicated models where the $d\gamma/dx$ terms are included and the laminar and turbulent boundary layer solutions are coupled (e.g. Steelant and Dick [124]). Unless the important effects of relaxing flow and possibly intermittent separation can also be accounted for, such additional complication is not likely to improve predictions significantly.

In some cases, the laminar part of the solution may separate. In order to continue the solution, the limits $H_L = 3.70$ and $C_{fL} = 0$ were applied. This crude approach will only cause small errors provided the intermittency is large (and hence the contribution of θ_L small) at the laminar separation point. In the real flow it is likely that relaxing flow would inhibit separation of the laminar layer.

Turbulence values used in the correlations were obtained from a frozen turbulence assumption. This assumption is not fully valid in flows were there is significant decay of freestream turbulence.

Transition models compared

Three transition length models have been compared. The aim here is to compare the relative effectiveness of the transition models given by Eqn. (10.6), Eqn. (11.10) and Eqn. (11.11) and so all models have been applied using the same non-dimensional breakdown correlation, Eqn. (11.7). Solutions using Eqn. (10.6) have been identified

as Dey, Narasimha (even though the Gostelow-Fraser spot breakdown rate equation Eqn. (11.7) is used). Solutions using Eqn. (11.10) are identified as Chen and Thyson; again Eqn. (11.7) has been used instead of the original Chen and Thyson breakdown rate correlation.

The new model was developed in an attempt to explain the departures from the Narasimha universal intermittency distribution observed by Narasimha et al. [91]. These are logical test cases for the new method. These test cases are flat plate boundary layers which had various pressure gradients imposed on them by using an adjustable liner in the roof of the wind-tunnel. All calculations were started at the same (specified) transition onset point x_t. Since all calculations use the same N correlation they should then all give the same transition length in zero pressure gradient flow. In Figures 11.4 to 11.6 intermittency is plotted in $F(\gamma)$ form to highlight deviations from the universal intermittency distributions.

Fig. 11.4 shows a comparison of the three models on boundary layer flow DAU1 which is initially zero pressure gradient, followed by a strong deceleration part-way through transition. Even in this strong adverse pressure gradient the Chen-Thyson model does not deviate far from the Dey-Narasimha curve. Clearly Chen and Thyson's method of adjusting spot velocity with local velocity cannot account for the effects of the of experimental velocity distribution. The new model reacts appropriately to the adverse pressure gradient, increasing the spot growth rate and reducing the transition length relative to the other two models.

Case DFU1 with an acceleration applied part way through the transition zone is shown in Fig. 11.5. The Chen-Thyson and Dey-Narasimha models have transition lengths determined by the pressure gradient at the transition onset point and under-predict the transition length. The new model starts with the same spot generation rate n as the other two but as it enters the favourable pressure gradient σ and α fall and the model lengthens transition.

Case DFU3 shown in Fig. 11.6 is nominally an accelerating flow case but the main slope change in the experimental $F(\gamma)$ curve occurs at $x = 1500$ mm, after the change in pressure gradient. A slight amount of deceleration downstream of this point may be responsible for this particular deviation. The velocity distribution was extrapolated as shown to make the new model fit the experimental data. This is not a valid verification of the new model but may indicate the physical process responsible for the observed sub-transition.

Results for a further test case from the European Research Community on Flow Turbulence and Combustion (ERCOFTAC) communicated by Coupland [16] is shown in Fig. 11.7. This test case is also a flat plate with an imposed pressure gradient. The form of the surface pressure distribution was chosen to simulate a typical turbine blade suction surface boundary layer. The nominal turbulence level for this case is 3%. Intermittency measurements are not available for this case and so boundary layer parameters H and C_f have been plotted to allow comparison. Transition onset for this case was set at $x_t = 750$ mm for all computations. This is just upstream of the velocity peak in the favourable pressure gradient. As the flow enters the positive pressure gradient region, only the new method is able to react and predict a sufficiently short transition length to give fair agreement with the experiment. Kinks in H and C_f at $x = 1100$ mm are due to separation of the laminar boundary layer; these do not significantly affect the Re_θ curve as transition is well advanced by this stage.

11.7 Conclusions

A new transition length model has been developed and tested on a range of experimentally measured flows. The advantage of the new method over previously existing techniques is its ability to react to changes in pressure gradient which may occur partway through transition in an arbitrary velocity distribution.

The correlations for turbulent spot spreading angle α and σ are currently based on a relatively small amount of data. The range of data is especially limited for favourable pressure gradients. A more direct correlation for spot generation rate n, not involving the spot propagation parameter σ, should be attempted and may lead to an improvement in the new method. The current model assumes the spot is always triangular, which may not be a good assumption in all pressure gradients. The relaxing flow following turbulent spots, which was shown in Chapter 8 to have stabilising effects, should be incorporated into a transition length model if possible.

Wake-induced transitional effects have not been considered here. None of the currently available wake-induced transition models make allowance for pressure gradient effects on spot spreading and propagation.

The new model is able to predict the sub-transition behaviour observed in flows with rapidly changing pressure gradients. The magnitude of these effects has been demonstrated to be consistent with changes in spot spreading and propagation parameters with pressure gradient indicated by the compiled experimental data of Gostelow et al. [40].

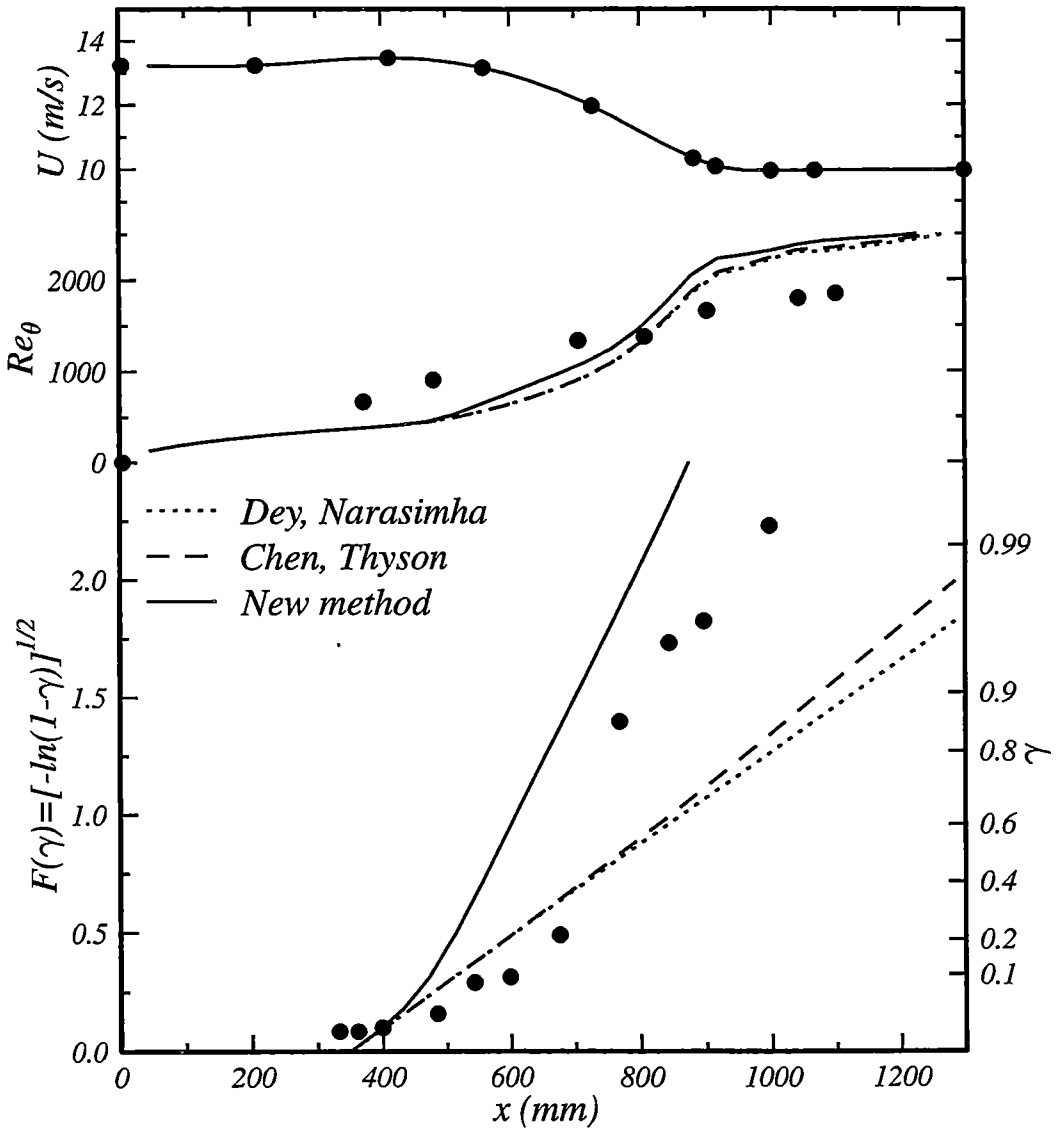

Figure 11.4: Comparison of transition models, case DAU1 from Narasimha et al. [91]

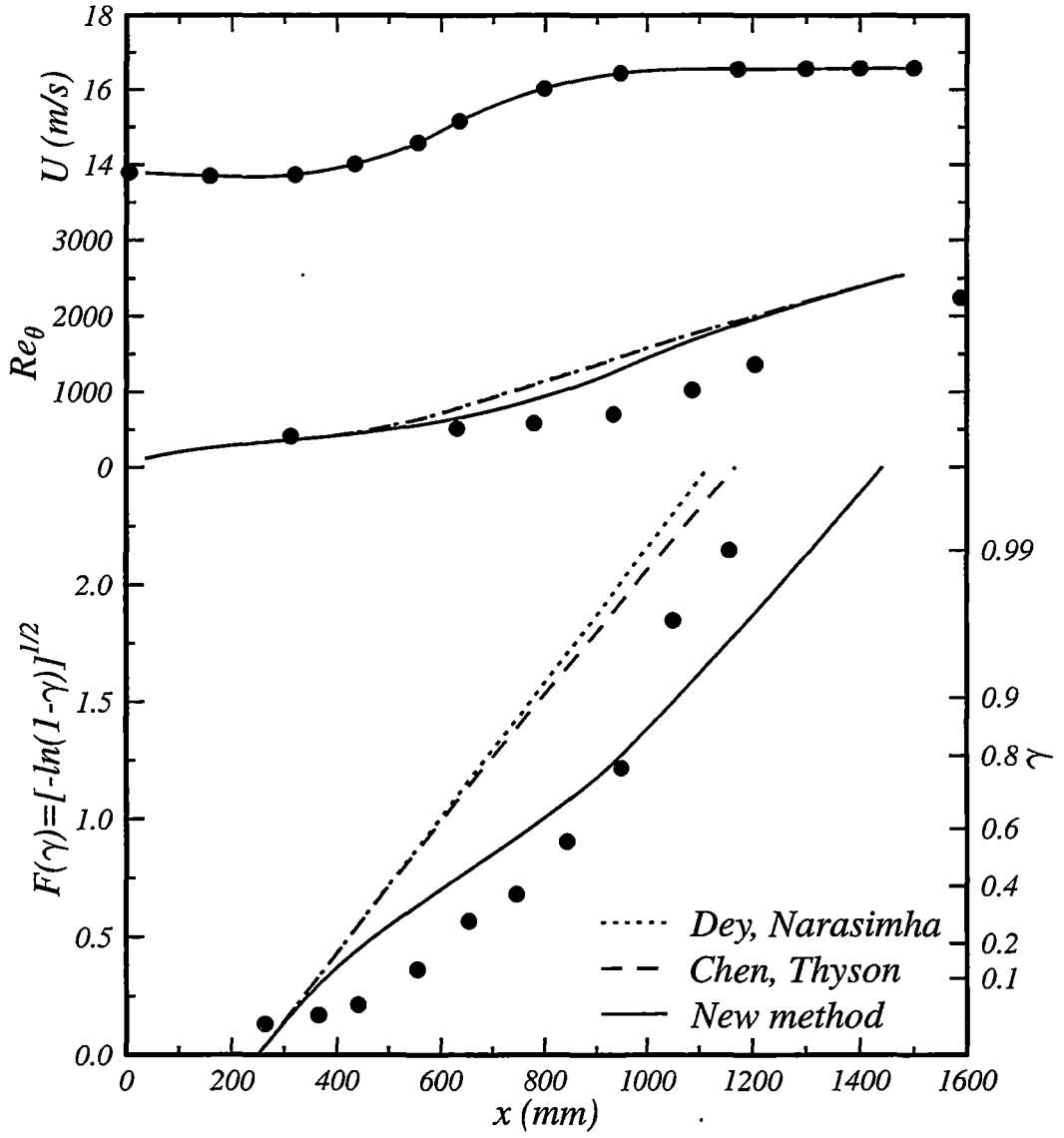

Figure 11.5: Comparison of transition models, case DFU1 from Narasimha et al. [91]

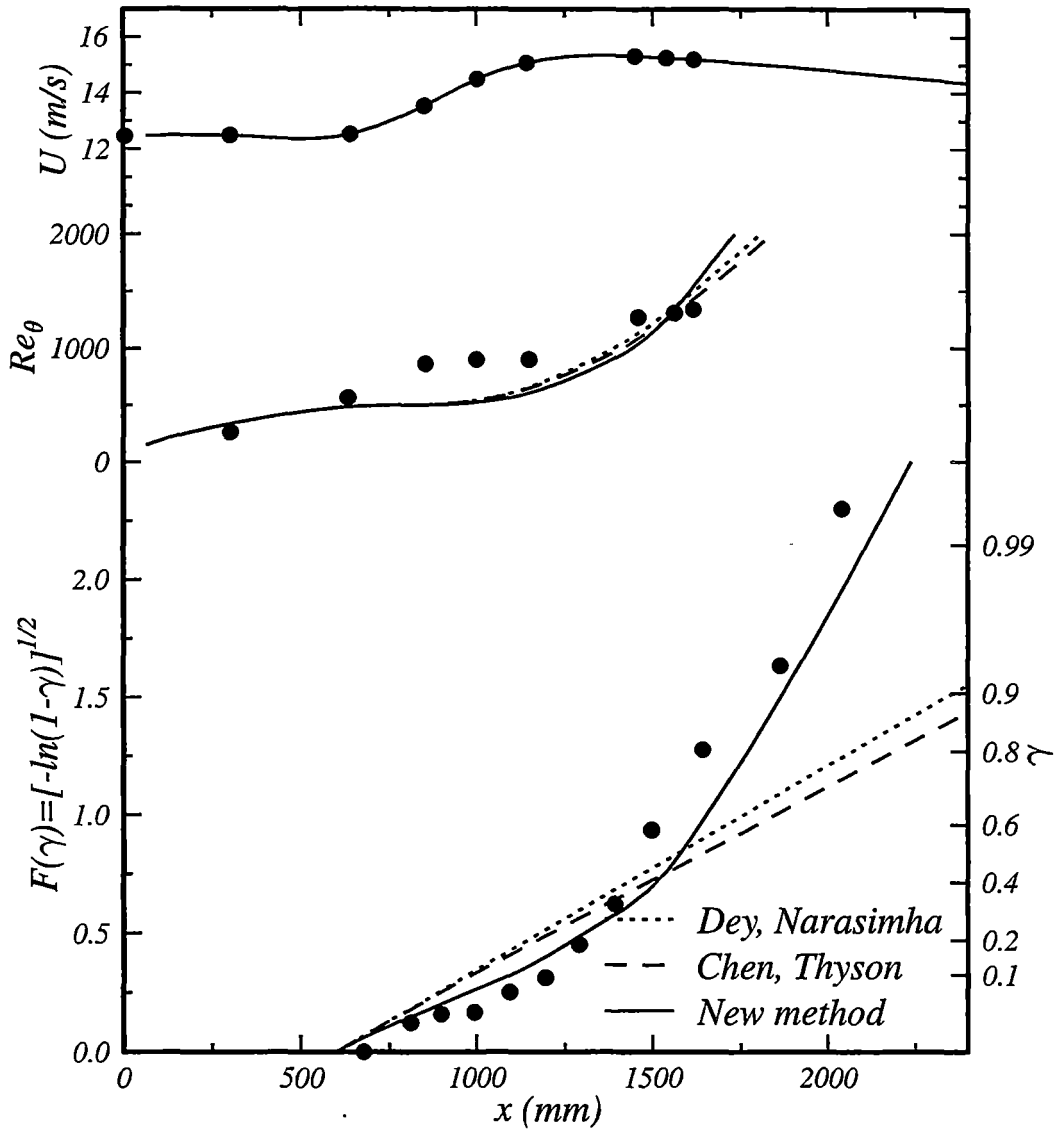

Figure 11.6: Comparison of transition models, case DFU3 from Narasimha et al. [91]

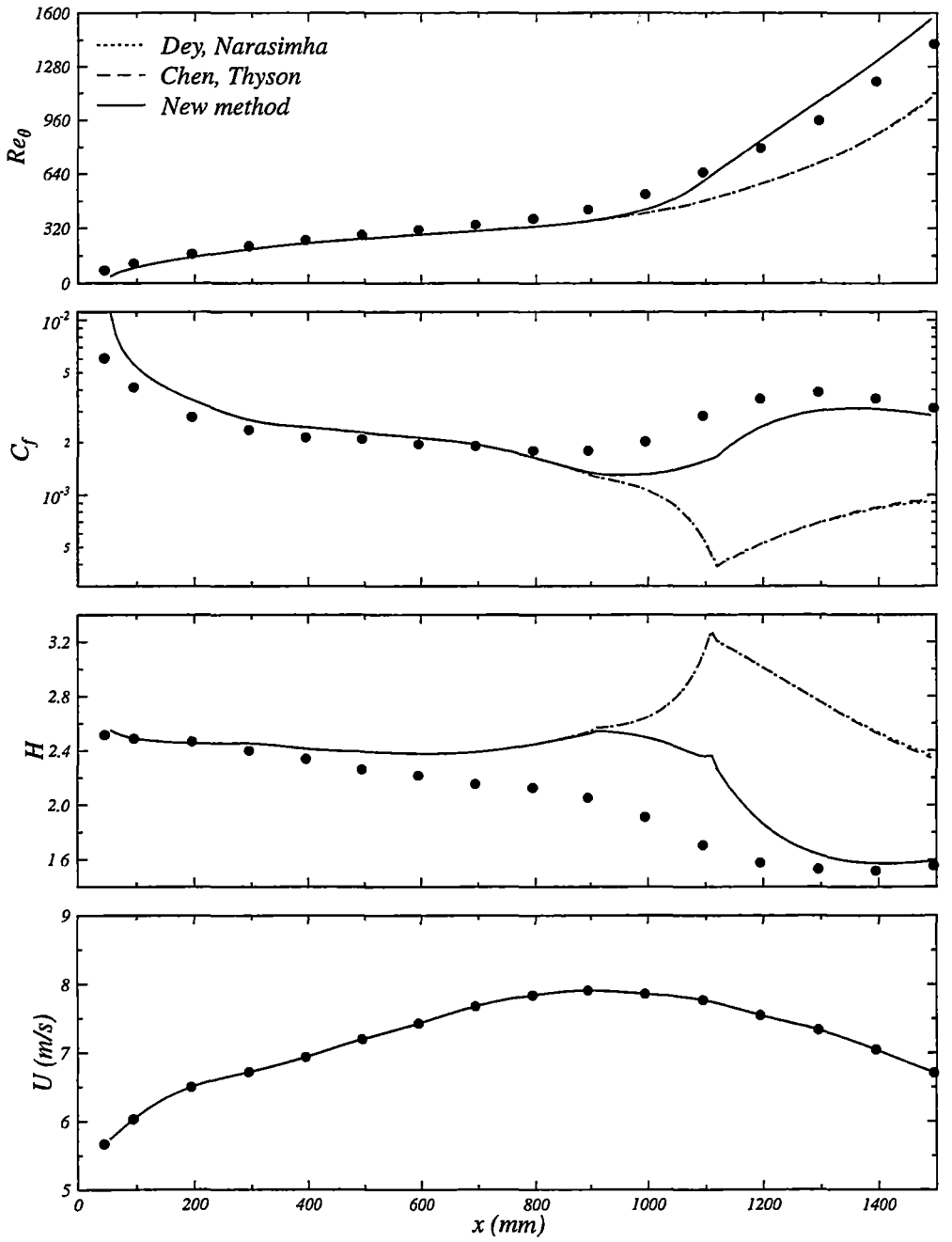

Figure 11.7: Comparison of transition models, ERCOFTAC case T3C2 from Coupland [16]

Chapter 12

Conclusions

This study has explored the complex nature of boundary layer transition on a axial compressor blade under the influence of passing wakes. The boundary layer development on the stator blade of the current machine is influenced by the moving wakes from the upstream rotor and the stationary wakes from the upstream inlet guide vanes. The disturbance field seen by the stator row includes all the dominant viscous flow influences experienced by an embedded stage in a multi-stage machine. The blade-row spacings in the research compressor are large enough for potential flow effects to be minimal.

An automatic control system was developed for the research compressor. This allows the machine to be run at constant Reynolds number with a minimum of operator intervention. Time-average stator blade surface pressure distributions and stator blade flow inlet angles were measured. The surface pressure distributions show the development of a laminar separation bubble and turbulent reattachment on the suction surface at high negative incidence and low Reynolds number. The majority of test cases in the current investigation are at Reynolds numbers above the critical Reynolds number for a C4 profile, and complete laminar separation without reattachment did not occur in any of the test cases.

Time-average cross-passage traverse measurements were made upstream of the stator row using pressure probes and a single hot-wire. These measurements revealed significant variations in velocity and time-average turbulence level across the passage. Phase-locked average measurements indicated that although the IGV wake was responsible for a small part of this variation, periodic fluctuations in the rotor wake thickness had a larger effect. These thickness variations are likely to be largely due to the influence of the passing IGV wakes on the rotor blade boundary layer. The variation is also consistent with interruption of cross-passage transport of rotor wake fluid in the rotor-stator gap by the Lockhart-Walker mechanism.

Unsteady measurements downstream of the stator blade show large periodic variations of stator wake thickness. Again these are mostly due to the effect of rotor wake-passing on the stator blade boundary layers. The rotor wake downstream of the stator shows evidence of the Kerrebrock-Mikolajczak mechanism redistributing rotor wake fluid as the wake traverses the stator passage. Wakes seen by an embedded stage in a turbomachine can show significant periodic thickness variations which are currently not allowed for in experimental or numerical wake passing simulations. Periodic thick-

ness variations of the rotor and stator boundary layers are not necessarily in phase. More uniform wakes may result if the pressure and suction surface boundary layer thickness variations are out of phase.

Turbulence level measurements in the rotor-stator gap show typical time-average values of about 3%. Phase-locked average values are very high in the rotor wake region (above 10%), between 2 and 3% in the IGV wakes, but below 1% between wakes. Bypass transition onset locations are strongly dependent upon the turbulence level and so prediction of unsteady transition in any turbomachine will require knowledge of the unsteady variation of turbulence levels.

A surface mounted hot-film array was wrapped around the stator blade and used to investigate the unsteady boundary layer behaviour. Although the sensors were not directly calibrated for shear stress, sufficient information was available from the sensors to judge the boundary layer state. Intermittency processing algorithms were developed to provide quantitative information about the progress of unsteady transition. A peak-valley counting intermittency detection method was developed and proved successful over a wide range of conditions. The intermittency detection algorithm was extended to detect relaxing flow behind the developing turbulent spots. Test cases with one of the rotor blades removed showed the full decay of the relaxing flow and the re-establishment of the laminar boundary layer.

Wake-induced transition of the blade surface boundary layers occurs predominantly through the bypass mode. It seems likely, but has not yet been conclusively shown, that wake turbulence is the primary cause of wake-induced transition. Wake velocity defects, the sign of the wake jet-effect and boundary layer pressure gradients could also modify the wake-induced transition process. Turbulent spot generation on the stator pressure surface was markedly different in character from that on the suction surface, suggesting that pressure gradient and/or jet-wake sign cannot be neglected when predicting wake-induced transition onset.

Evidence of instability waves associated with natural transition was found in the inter-wake region in some cases. Cases with mid-chord and leading edge separation bubbles indicated that transition in separated flows is also influenced by the wakes. A general wake-induced transition model must be able to predict multiple transition modes.

The phase-locked hot-film results clearly show the development of wake-induced turbulent spots. This work is complementary to and largely agrees with the work of Halstead et al. [46], Cumpsty et al. [20] and Schulte and Hodson [114]. The wake-induced breakdown process is random in nature, different wakes causing spots in slightly different places at slightly different times. Once formed, the turbulent spots develop independently of the position of the wake in the freestream. The leading edge of a spot slightly lags the wake centreline. The wake-induced transition starts further upstream than would be predicted for steady transition (using the time-averaged turbulence level).

The calmed regions following a turbulent spot have been shown to result from the stabilising effect of the high shear stress levels at the rear of a spot. It is not simply a zone which is inaccessible to Tollmien-Schlichting waves. The raised shear stress level of the calmed region allows it to traverse stronger adverse pressure gradients without separating than an undisturbed laminar boundary layer could. A full understanding of the strength and extent of this effect may allow low Reynolds number blading to be

developed with increased loading.

A stator blade suction surface boundary layer traverse with a single hot-wire sensor demonstrated that intermittency levels at the surface underestimate the peak level across the shear layer in strong adverse pressure gradient flows. The developing turbulent structures are similar to triggered turbulent spots observed by Gostelow et al. [40, 42]. Fundamental studies of turbulent spot development by these workers and others have recently shown that turbulent spot spreading angles and propagation parameters are dramatically increased by adverse pressure gradients.

A new steady-flow transition model has been developed for calculation of flows with rapidly changing pressure gradients through the transition zone. This model can predict the sub-transition behaviour observed by Narasimha et al. [91]. The ability of the new model to lengthen or shorten transition appropriately in response to arbitrary local changes in pressure gradient can be important in certain turbomachinery flows. Other models which base their transition length on the conditions at transition onset alone will over predict the transition length if the flow subsequently moves into a region of increased positive pressure gradient.

12.1 Recommendations for future work

The transition length prediction method described in Chapter 11 uses correlations for the turbulent spot spreading angle and growth rate which are based on a limited amount of data. Further information (especially in favourable pressure gradients) is required to improve the model. The influence of freestream turbulence on these parameters should also be investigated.

Modelling of the transition region in unsteady flow has not yet reached an advanced state. Only the model of Schulte [112] attempts to allow for the relaxing flow region and no unsteady model accounts for effects of pressure gradient on transition lengths. Further work in this area should include an investigation into methods for predicting a periodically separating transitional flow.

The current work has demonstrated the importance of unsteady boundary layer transition to turbomachinery blade surface boundary layers. It has been suggested that these effects could be exploited to increase blade loadings and possibly reduce losses. Achieving these results will require a better understanding of the calmed region and a reliable technique for predicting wake-induced transition onset location. The difference between the pressure and suction surface results in the current work need to be more fully explained because they may indicate the likelihood of a different wake-induced transition mechanism on turbine blade suction surfaces.

Axial blade-row spacings in the research compressor are much larger than commonly found in commercial machines. The turbulence levels in a 1.5-stage machine are also inevitably lower than those in embedded stages of a multi-stage machine. Decreasing axial spacing will increase the strength of wakes seen by following blade rows and thereby increase unsteady transition effects. Higher turbulence levels may offset this by promoting earlier transition onset between the wake-induced turbulent patches. Both of these effects should be investigated further.

Appendix A

Blade profiles and sensor locations

A.1 Setting of blade angles

The tangent chord to the rotor or stator blade pressure surface at mid blade makes an angle of 30.3° to the axial direction when the blade has been set to the design stagger (29.5°). This was determined by plotting the design co-ordinates at ten times full scale. A special tool was used to provide a straight edge set at an adjustable angle at mid blade height. The blades were each compared against this in turn and the angles were adjusted if necessary. An optical protractor (graduated to 5 minutes of angle) was used to set the angle of the straight edge.

Due to an error which occurred in a re-build prior to the current work, the rotor blades were actually set with a tangent chord of 28.3°. Since no re-build was necessary until the instrumented stator blade was installed this error went unnoticed-noticed through the early part of the work and so it was decided to continue with the incorrect rotor blade settings. Consequently the values of rotor stagger are two degrees less than the design values, i.e. the rotor had a mid-blade stagger of 27.5°. The stator blades were found to be correctly set at the design angle (29.5°).

A.2 Blade shape

A definition of the C4 blade shape is given by the expression below. The coefficients for the defining polynomials were obtained from Howell [61].

$$\pm y = \begin{cases} 1.5492\sqrt{x} - 0.06563x - 0.002528x^2 + 0.00002811x^3 & \text{for } x \leq 30 \\ 3.866 + 0.07871x - 0.001467x^2 + 0.000003448x^3 & \text{for } x > 30 \end{cases} \quad \text{(A.1)}$$

where x and y are in % chord. At $x = 30\%$ chord the point of maximum thickness ($\pm 5\%$ chord) is reached; this is the point of intersection of the two polynomials and the slope of both reaches zero here. The radius of curvature at the leading edge is 1.2% chord. A trailing edge circle with a radius of 0.575344% chord is exactly tangent and intersects the rear polynomial at $x = 99.488\%$ chord.

A simple code was used to transform the co-ordinates of the above expressions to obtain the actual blade co-ordinates for an aerofoil with the design camber and stagger.

Walker (private communication) has shown by plotting at ten times full scale that the results from this code are in very close agreement with the original coordinates used to manufacture the blades.

The same code has been modified to obtain accurate positions for the hot-film sensors and the pressure tappings. Surface distances have also been calculated for use with boundary layer codes. The boundary layer calculations have been performed on the plane section at mid-blade height assuming there is no radial motion.

A.3 Hot-film instrumented blade sensor locations

Nominal chord for all blades was 3.0 inches (76.2 mm) however measurement of the instrumented blade at mid blade height gave $c = 75.7$ mm and hence a maximum surface distance of $S_{c,max} = 76.6$ mm. The sensor pitch was 2.54 mm (as given by the manufacturer). This value was assumed to be unchanged by the process of wrapping and adhering the array to the blade. The distance from the trailing edge to the first sensor was measured; then using the blade profile code the expected position of the last sensor relative to the trailing edge on the other side was calculated. The result agreed with the measured value to within the level of accuracy of the measurements (0.3% c). Table A.1 gives the (x, y) coordinates of the sensors (referenced to $0, 0$ at the leading edge) and the surface distances to the sensors from the leading edge. The leading edge was defined as the end of the camber line.

A.4 Pressure tapping locations

Table A.2 gives the location of the pressure tappings. The x/c positions are accurate to at least the tapping diameter (0.5 mm). Conversion from x/c to surface distance and coordinates was made as for the hot-film instrumented blade.

Table A.1: Hot-film sensor positions for instrumented blade, $c = 75.7$ mm, $\theta = 31.1°$ and $\xi = 29.5°$. $S_1 = S_c/S_{c,max}$ and $S_2 = S_u/S_{u,max}$ on the suction surface and $S_2 = S_l/S_{l,max}$ on the pressure surface where $S_{u,max} = 79.23$ mm, and $S_{l,max} = 76.27$ mm and $S_{c,max} = 76.64$ mm.

Suction Surface				
#	S_1	S_2	$x[mm]$	$y[mm]$
1	0.9836	0.9840	64.53	37.48
2	0.9508	0.9519	62.02	37.09
3	0.9180	0.9199	59.52	36.64
4	0.8853	0.8878	57.03	36.14
5	0.8527	0.8557	54.55	35.59
6	0.8200	0.8237	52.09	34.99
7	0.7875	0.7916	49.63	34.33
8	0.7549	0.7596	47.20	33.61
9	0.7224	0.7275	44.77	32.85
10	0.6899	0.6955	42.37	32.03
11	0.6575	0.6634	39.99	31.16
12	0.6251	0.6313	37.62	30.23
13	0.5927	0.5993	35.28	29.25
14	0.5603	0.5672	32.96	28.22
15	0.5280	0.5352	30.66	27.13
16	0.4957	0.5031	28.39	25.99
17	0.4633	0.4711	26.15	24.79
18	0.4310	0.4390	23.94	23.55
19	0.3987	0.4069	21.76	22.25
20	0.3665	0.3749	19.60	20.90
21	0.3342	0.3428	17.49	19.49
22	0.3019	0.3108	15.40	18.04
23	0.2696	0.2787	13.36	16.53
24	0.2373	0.2467	11.36	14.97
25	0.2051	0.2146	9.40	13.35
26	0.1728	0.1825	7.51	11.66
27	0.1405	0.1505	5.69	9.89
28	0.1083	0.1184	3.95	8.03
29	0.0762	0.0864	2.34	6.07
30	0.0444	0.0543	0.90	3.98
31	0.0139	0.0223	-0.17	1.68

Pressure Surface				
#	S_1	S_2	$x[mm]$	$y[mm]$
32	0.0039	0.0102	0.71	-0.29
33	0.0328	0.0435	3.14	0.37
34	0.0653	0.0768	5.37	1.58
35	0.0986	0.1101	7.51	2.95
36	0.1323	0.1434	9.59	4.40
37	0.1662	0.1767	11.65	5.89
38	0.2001	0.2100	13.70	7.40
39	0.2341	0.2433	15.74	8.91
40	0.2682	0.2766	17.78	10.41
41	0.3022	0.3099	19.84	11.90
42	0.3363	0.3432	21.91	13.37
43	0.3703	0.3765	24.00	14.82
44	0.4044	0.4098	26.10	16.25
45	0.4384	0.4431	28.22	17.65
46	0.4724	0.4764	30.35	19.03
47	0.5063	0.5097	32.50	20.38
48	0.5402	0.5430	34.67	21.70
49	0.5741	0.5763	36.85	23.00
50	0.6079	0.6096	39.05	24.28
51	0.6417	0.6429	41.26	25.52
52	0.6755	0.6762	43.49	26.73
53	0.7091	0.7095	45.74	27.92
54	0.7427	0.7428	48.00	29.08
55	0.7763	0.7761	50.28	30.20
56	0.8097	0.8094	52.57	31.29
57	0.8432	0.8427	54.88	32.35
58	0.8765	0.8760	57.20	33.38
59	0.9098	0.9093	59.54	34.37
60	0.9430	0.9426	61.89	35.33
61	0.9761	0.9759	64.26	36.25

Table A.2: Pressure tapping positions , $c = 75.7$ mm, $\theta = 31.1°$ and $\xi = 29.5°$. $S_1 = S_c/S_{c,max}$ and $S_2 = S_u/S_{u,max}$ on the suction surface and $S_3 = S_l/S_{l,max}$ on the pressure surface where $S_{u,max} = 79.23$ mm, and $S_{l,max} = 76.27$ mm and $S_{c,max} = 76.64$ mm.

Pressure tappings							
#	S_1	S_2	$x[mm]$	$y[mm]$	S_3	$x[mm]$	$y[mm]$
1	0.0000	0.0000	0.00	0.00	0.0000	0.00	0.00
2	0.0479	0.0580	1.05	4.22	0.0592	4.20	0.91
3	0.0965	0.1067	3.35	7.33	0.1080	7.37	2.86
4	0.1456	0.1556	5.97	10.17	0.1565	10.40	4.98
5	0.1952	0.2048	8.82	12.84	0.2052	13.40	7.18
6	0.2453	0.2546	11.85	15.36	0.2542	16.41	9.40
7	0.2958	0.3047	15.02	17.76	0.3036	19.45	11.62
8	0.3466	0.3552	18.30	20.04	0.3533	22.54	13.82
9	0.3976	0.4058	21.68	22.20	0.4032	25.68	15.97
10	0.5000	0.5074	28.70	26.14	0.5035	32.10	20.13
11	0.6024	0.6089	35.98	29.55	0.6042	38.69	24.07
12	0.7042	0.7095	43.42	32.40	0.7047	45.41	27.75
13	0.8048	0.8087	50.94	34.68	0.8045	52.23	31.13
14	0.9035	0.9056	58.42	36.43	0.9030	59.10	34.19

Appendix B

Derivation of the general intermittency expression

This derivation closely follows that given by Chen and Thyson [14], but allows the spot leading and trailing edge velocities and the spot spreading angle to vary with streamwise distance. The expression may be extended to axisymmetric flow as demonstrated by Chen and Thyson. The expression derived reduces to the original Chen and Tyson model when α, U_l, U_t are taken as constant. If U is taken as constant then the Chen and Thyson model itself reduces to the Narasimha universal intermittency distribution, although the correlations for spot generation and propagation rates suggested by the different authors vary.

Consider a spot which is propagating in x, t, y space where x is the streamwise direction, y the spanwise direction and t is time. We assume the simplified triangular spot model (Section 11.3). Fig. 11.1 shows a plan view of the spot in the x, y plane at times t and t'. The velocity triangle for the vertices of the model spot is plotted in Fig. B.1. Distance from point o in the diagram represents magnitude of velocity relative to the surface.

Point A at the front of the spot travels in the streamwise direction at the spot leading edge velocity U_l. The point on the trailing edge midway between B and C travels at the trailing edge velocity U_t. All other points around the edge of the spot also have a spanwise velocity component which is a function of U_l, U_t and α, the spot spreading half angle.

At time t the streamwise positions of the vertices of a spot originating at (x_0, t_0, y_0) are given by

$$x(B,C) = x_0 + \int_{t_0}^{t} U_t(x,t)\,dt \tag{B.1}$$

$$x(A) = x_0 + \int_{t_0}^{t} U_l(x,t)\,dt \tag{B.2}$$

$$\pm y(B,C) = \int_{t_0}^{t} \tan\alpha(x,t) U_t(x,t)\,dt \tag{B.3}$$

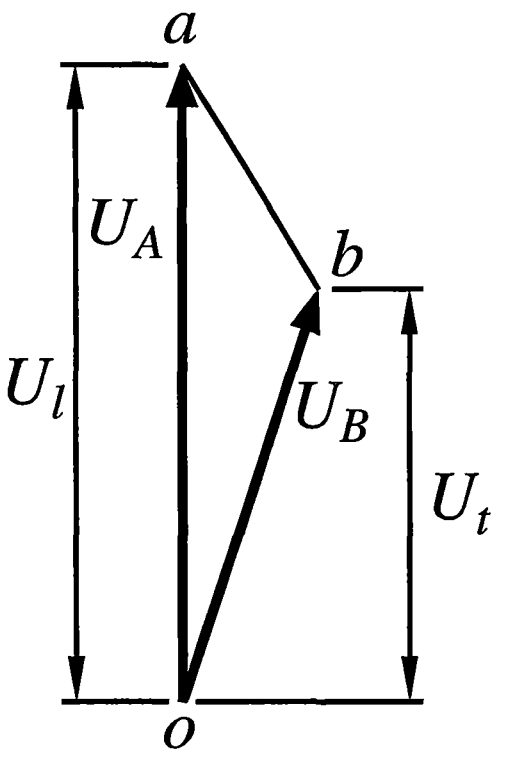

Figure B.1: Velocity triangle for simple turbulent spot model.

Hence the angle formed at the leading edge of the spot, $\angle BAC$ is

$$\angle BAC = 2\arctan\left(\frac{y(B,C)}{x(A)-x(B,C)}\right) \tag{B.4}$$

which is a function of α, U_l and U_t in general.

Fig. B.2 shows a triangular spot in x,t,y space. The trajectories of points A,B and C are shown as straight lines although this is not necessarily so as recognised by Emmons [29] and is not an assumption of the derivation which follows. The vertical shaded area in the y,t plane is the base of the dependence volume for point P_0; any turbulent flow from new or existing spots which pass through this plane will lead to turbulent flow at P_0. Similarly, if there is turbulent flow at P_0 then all points in the horizontal shaded area in the x,y plane will have turbulent flow. This area is the base of the propagation volume for P_0. If U_l, U_t and α are all constant then then dependence and propagation volumes become conical as shown.

Now consider the trajectories of the vertices of a spot growing downstream of $P_0 = (x_0, y_0, t_0)$ as functions of the streamwise position. Point A travels the path given by

$$y = y_0 \tag{B.5a}$$

$$t = t_0 + \int_{x_0}^{x} \frac{dx}{U_l(x)} \tag{B.5b}$$

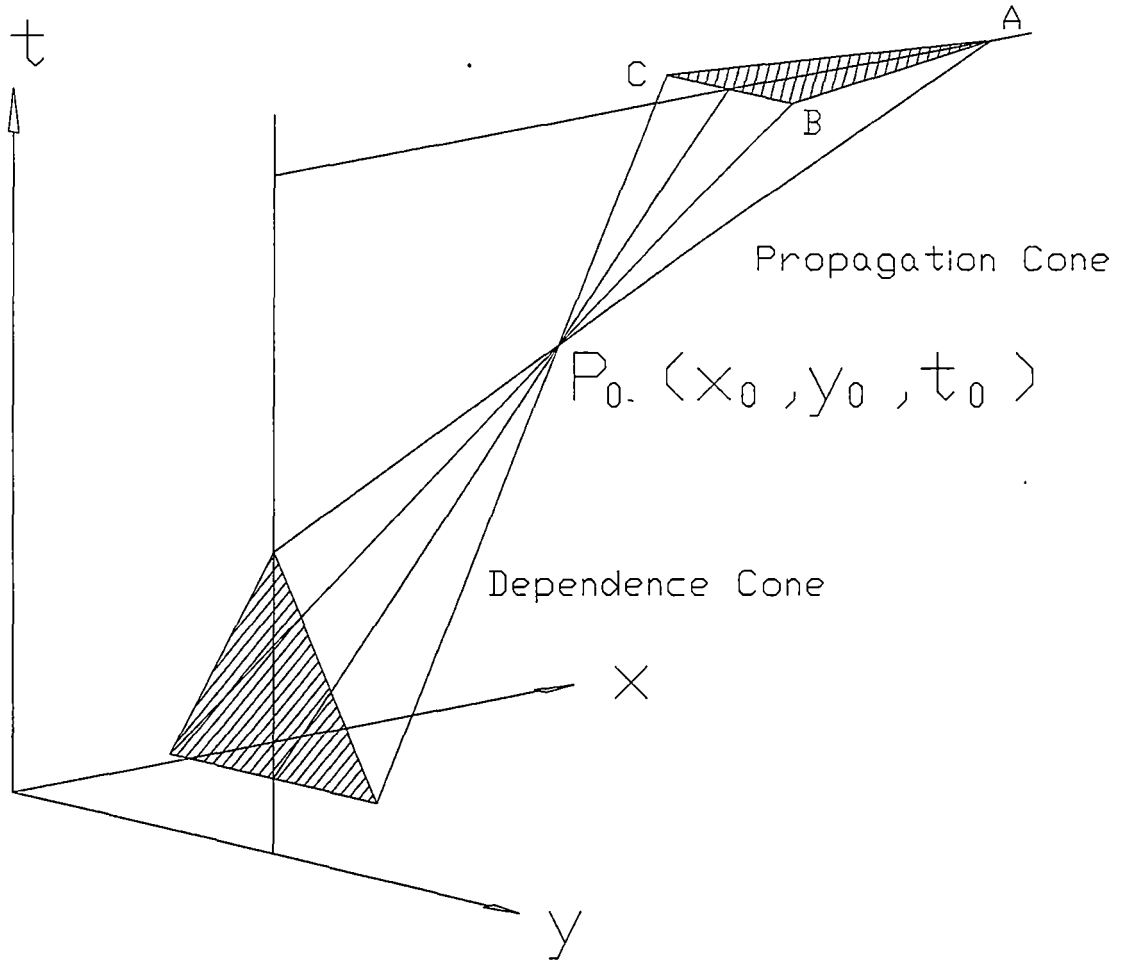

Figure B.2: Propagation and dependence volumes for a triangular spot

Points B and C follow the path

$$y = y_0 \pm \int_{x_0}^{x} \tan\alpha(x)\, dx \tag{B.6a}$$

$$t = t_0 + \int_{x_0}^{x} \frac{dx}{U_t(x)} \tag{B.6b}$$

The current problem is to evaluate Emmons' expression for intermittency

$$\gamma(P) = 1 - \exp[-\int_{R(P)} g(x,y,t)\, dV] \tag{10.4}$$

(see Chapter 11) in the general case where spot propagation parameters α, U_l and U_t are influenced by local boundary layer conditions.

If transition occurs at $x = x_0$ then the integral term of Eqn. (10.4) at some point $P(x,t,y)$ downstream of $P_0(x_0,t_0,y_0)$ can be written as

$$\int_R g\, dV = \int_{x_0}^{x} g A_d\, dx \tag{B.7}$$

where A_d is the area (in the y, t plane) of the base of the dependence volume R for point P and g is the source rate density function. (This volume is not shown in Fig. B.2 but will be similar in form to the dependence volume for P_0 which is shown).

Equations (B.5b),(B.6a) and (B.6b) are now re-arranged to find A_d at all points between x and x_0. We introduce a new variable x' which will vary from x back to x_0. Interchanging the constant and variable terms in Eqn. (B.5b) and putting $x_0 = x'$, $y_0 = y'$ and $z_0 = z'$ yields

$$t' = t - \int_{x'}^{x} \frac{dx'}{U_l(x')} \tag{B.8}$$

If this process is followed for the other spot trajectory equations then the required (triangular) area will be found to be

$$A_d(x') = \frac{1}{2}\left(2\int_{x'}^{x} \tan\alpha\, dx'\right)\left(\int_{x'}^{x}\left(\frac{1}{U_t} - \frac{1}{U_l}\right) dx'\right) \tag{B.9}$$

$$= \int_{x'}^{x} \tan\alpha\, dx' \int_{x'}^{x}\left(\frac{1}{U_t} - \frac{1}{U_l}\right) dx' \tag{B.10}$$

where U_l, U_t and α are all functions of x'.

This expression may now be used with Eqn. (B.7) and an appropriate function for $g(x')$. For the current work the concentrated breakdown hypothesis (Section 10.5) has been found to be adequate. This gives

$$g(x) = n\delta(x - x_0) \tag{B.11}$$

When this is substituted into Eqn. (B.7) all A_d values away from $x' = x_0$ become irrelevant because the function $\delta(x - x_0)$ is zero except at this point. Eqn. (B.7) then becomes

$$\int_R g\, dV = nA_d(x_0) \tag{B.12}$$

The complete expression for intermittency at a point $P(x, t, y)$ downstream of the onset plane (x_0, t_0) is then obtained from equations (10.4), (B.10) and (B.12) as

$$\gamma(P) = 1 - \exp\left[n\int_{x_0}^{x} \tan\alpha\, dx \int_{x_0}^{x}\left(\frac{1}{U_t} - \frac{1}{U_l}\right) dx\right] \tag{B.13}$$

Note that it has not been necessary to make any assumptions about the form of functions for the spot propagation parameters α, U_l and U_t.

The simple triangular turbulent spot model used here does not fully represent the observations of turbulent spots of Schubauer and Kelbanoff [110]. Experimental observations of the turbulent spot show that the leading edge velocity of the spot is approximately the same, whatever the offset of the probe from the spot centreline. The current simple model assumes a linear variation of the streamwise component of spot leading edge velocity from U_t at points B and C to U_l at point A. This assumption is necessary to maintain the triangular spot planform as is grows but will cause the average leading edge velocity of the spot to be underestimated. One possible solution to this difficulty is to adopt a turbulent spot model which allows for changes in the spot planform shape as the spot grows.

Appendix C

Hot-wire and hot-film techniques

C.1 Hot-wire techniques

All work was performed using single sensor hot-wire probes, usually type DISA 55P05. These have a nominal sensor length l of 1.25 mm and a nominal diameter d of 5 μm. The electrical resistance of these sensors at 20°C, R_{20}, was typically 3.5 Ω and the temperature coefficient of resistance α_{20} was 0.0036 % per degree C. Overheat ratios in the range 1.5 to 1.7 were used. At an overheat ratio of 1.65 the mean wire temperature was 200°C.

The hot-wire calibration curve used was based on King's law (see Goldstein [37]). Following the practice of Walker [132], a quadratic term has been added to the calibration curve. This has been found to slightly improve the calibration at low velocities. Using the definitions

$$Nu^* = Nu\left(\frac{T_f}{T_a}\right)^{-0.17} \tag{C.1}$$

$$= \frac{Q_w}{\pi l \Delta T k_f}\left(\frac{T_f}{T_a}\right)^{-0.17} \tag{C.2}$$

$$Re^* = Re^{0.45} \tag{C.3}$$

$$= \left(\frac{Ud}{\nu}\right)^{0.45} \tag{C.4}$$

the calibration curve is given by

$$Nu^* = C_1 + C_2 Re^* + C_3 (Re^*)^2 + C_{wall} \tag{C.5}$$

where C_1, C_2 and C_3 are the calibration coefficients. C_{wall} is a correction term to allow for the extra heat loss from a wire close to a wall. The heat loss from the sensor Q_w is obtained from the bridge voltage and sensor resistances. ΔT is the difference between the mean wire temperature and the atmospheric temperature and T_f is the average of the two.

A least squares fitting algorithm was applied to the data of Wills [142] to produce a correlation for C_{wall} of the form

$$0.18 \exp(y/17.1d) \tag{C.6}$$

where y is distance from the wall and d is the wire diameter. This expression is valid in the range $15 < y/d < 50$ and C_{wall} was set to zero for y values greater than $50d$.

Both steady and unsteady hot-wire data was processed using the above calibration curve. Use of dimensionless parameters in the expression ensure that changes in atmospheric temperature and pressure are accounted for through changes in kinematic viscosity ν and thermal conductivity k_f.

Drift and in-situ calibration

The calibration constants were determined for each wire by testing against a reference pitot tube in a small recirculating wind tunnel. The hot-wire was then mounted in the compressor at a reference location. Measurements at the reference location with a freshly calibrated wire were used as the basis of an in-situ calibration procedure. During operation of the wire in the compressor ageing effects and dirt build-up alter the calibration characteristics of the hot-wire. Periodically the wire was returned to the reference position and the amount of drift was estimated. Drift correction was applied by making the required (small) changes to the calibration coefficients. At the end of a test series the wire was returned to the recirculating wind tunnel to provide a final calibration check.

Frequency response

The frequency response of the hot-wire was determined using the square wave test of Freymuth and Fingerson [33]. Depending on the individual wire 3dB cutoff frequencies in the range 150-200 kHz were obtainable. The hot-wire signal was filtered at 20 kHz to avoid aliasing during digitisation.

C.2 Hot-film techniques

The surface hot-films elements are 1.5 mm wide and 0.1 mm long. They consist of a 0.25 μm thick layer of nickel deposited onto a 0.05 mm polymide sheet. The sensors had cold resistances of around 6 Ω and were operated at an overheat ratio of 1.5.

Various workers (Brown [13], Pope [97]) have shown that surface mounted hot-film sensors can be calibrated for skin friction measurements in laminar and turbulent flows. Direct calibration of the compressor blade mounted hot-film array was not attempted. Applying a suitable calibration flow to the film array which was glued to the blade surface would be difficult. Instead a semi-quantitative method developed by Hodson [53] has been used to process the hot-film data.

Bellhouse and Schultz [6] show that if the thermal boundary layer thickness is small compared with the velocity boundary layer thickness, and if the pressure gradient is small enough for the thermal boundary layer profile to be linear, then

$$(Q - Q_s) = k\tau_w^{1/3} \tag{C.7}$$

where Q is the total instantaneous power dissipated by the film and Q_s is the power loss to the substrate. For hot-films, Q_s can be of the same order as Q and must be accurately measured. Hodson [53] overcame this difficulty by assuming that Q_s is approximately

equal to the heat transfer under zero flow conditions, Q_0. The relationship between wall shear stress and anemometer bridge voltage E then becomes

$$\tau_w \propto \left(\frac{E^2 - E_0^2}{E_0^2}\right)^3 = \tau \tag{C.8}$$

The normalization by E_0^2 in this equation will remove the effects of differences in the sizes and resistances of individual sensors from the results, provided that the rate of heat transfer to the air and substrate have similar dependencies on these variables.

Halstead et al. [45] have reduced hot-film results using a non-dimensionalisation of the form

$$\tau = \left(\frac{E - E_0}{E_0}\right)^6 \tag{C.9}$$

and obtained reasonable results. Later work by Halstead et al. [46] used the Hodson expression.

Frequency response

The frequency response of the hot-films, determined using the square wave test, was around 30 kHz. This is much lower than the hot-wire because of the large component of heat transfer to the substrate. Again, a 20 kHz low pass filter was used to prevent aliasing.

Appendix D

Instrumentation accuracy

D.1 Pressure transducing system

A Datametrics Barocell 572 capacitive pressure transducing system with a 0–100 torr (13.33 kPa) range is used to measure differential pressure. This transducer has an internal volume of 5 cm^3, accuracy of $\pm 0.03\%$ and hysteresis of $\pm 0.003\%$ of full scale. The transducer has a thermal base to reduce temperature drift effects.

A Datametrics 1015 signal conditioner scales the voltage output into a -5–+5 v output suitable for input to the data acquisition system. The signal conditioner system is auto-ranging with a downrange point at 30% full scale. Maximum amplification gives a full scale range of 13.3Pa. Software was written to detect any auto-ranging events which may have occurred during a series of measurements at a test point. In that case the software would change the range as necessary and re-take the data.

The manufacturer specifies an overall system (including transducer) accuracy of $\pm 0.06\%$ of reading and $\pm 0.01\%$ of operating scale. Assuming the reading was always greater than 30% of full scale (due to the auto-ranging function) the maximum error is 0.07% of reading except at very low differential pressures (< 4 Pa). Throughout this discussion, errors are combined by the root-sum-squares method where appropriate.

A Metrabyte DAS 20 ADC board was used to digitise the signal. The accuracy of the ADC board was given as $\pm 0.01\%$ of reading and ± 1 LSB. For a 12-bit ADC with a minimum reading of 30% full scale, this gives an error of $\pm 0.08\%$ of reading.

Accuracy of the system including the ADC may then be expected to be of the order of $\pm 0.11\%$. This includes random and bias errors due to the sensor and electronics but does not yet include uncertainty due to random fluctuations in the pressure being measured. Also included in this number are zero offset errors. The zero-offset and full scale voltage outputs were measured (over 30 sec) prior to starting any set of readings. The results of these measurements were used to scale the measured voltage correctly and account for any offset or scale error in the ADC. A final check of the null reading (with both ports of the transducer connected together) was made at the start and end of a test series to eliminate errors from zero drift.

The system was tested against a Van Essen Betz-type projection micro manometer (S.N. 10964), which had an accuracy of ± 0.1 Pa, with acceptable results. With the manometer and transducer connected to the same reference pressure, 50 readings of pressure were taken by the data acquisition system and the mean and standard de-

viation of the sample calculated. A typical result from this work showed a standard deviation of 0.19 Pa at a pressure of 100 Pa, or a 95% confidence limit of 0.38%. This is somewhat larger than the error quoted by the manufacturer, probably due to drift in the reference pressure caused by temperature fluctuation and/or leakage. Averaging over the 50 readings gives a standard error of the mean is 0.03 Pa, or 0.03% where the standard error of the mean σ_m is defined as

$$\sigma_m = \frac{s}{\sqrt{n-1}} \tag{D.1}$$

and s is taken as the standard deviation of the sample of n observations.

Combining errors due to the level of uncertainty of the instrumentation and randomness of the measured pressure and expressing as 95% confidence values, the overall uncertainty σ_v is obtained as

$$\left(\frac{\sigma_v}{R}\right)^2 = \left(\frac{2\sigma_m}{R}\right)^2 + \left(\frac{0.11}{100}\right)^2 \tag{D.2}$$

For example (Chapter 3) a typical long term series of pressure measurements had a standard deviation of 0.8%. In this case the large number of samples ensures the standard error of the mean is small compared with the instrument uncertainty. The resulting 95% confidence value of the mean is ±0.11%.

Uncertainty expressed this way does not include errors due to changes in operating conditions longer than the total sampling period. Where a result is calculated from more than one pressure reading, errors arising from slightly different operating conditions between sampling the two ports are also not included. In some cases these errors were reduced by repeated alternate sampling of the ports in question.

D.2 Anemometry system

The TSI IFA-100 anemometry system has specifications as follows. The resistance measurement repeatability is typically 0.002Ω and the bridge resistance setting accuracy is ±0.002Ω. The signal conditioner has an offset accuracy of 0.15% and a gain accuracy of 0.15%. ADC uncertainties are as given above.

For a hot-wire, by far the largest source of uncertainty is due to calibration drift. For example, during the hot-wire measurements described in Chapter 4, the in-situ calibration technique revealed a drift of around 7% in the C_1 coefficient. Errors in velocity due to this shift alone can be estimated from

$$\frac{\Delta u}{U} = \frac{\delta u}{\delta C_1}\frac{\Delta C_1}{C_1}\frac{C_1}{U} \tag{D.3}$$

At $U = 20$ m/s this gives an error in U of 6.5%. Although correction was made for this drift one may still expect uncertainties of the order of 3% in the corrected measurements (because the time when the drift occurred is not precisely known).

For the surface hot-film array direct calibration was not performed. Sources of uncertainty in comparison of the derived quasi-shear stress signal with true wall shear stress are described in Chapter 8.

Bibliography

[1] Abu-Ghannam, B. J. and Shaw, R. Natural transition of boundary layers - the effects of pressure gradient and flow history. *Journal of Mechanical Engineering Science*, vol. 22, no. 5, pp. 213–228, 1980.

[2] Addison, J. S. and Hodson, H. P. Unsteady transition in an axial flow turbine, Part 1: Measurements on the turbine rotor. *ASME Journal of Turbomachinery*, vol. 112, pp. 206–214, 1990.

[3] Addison, J. S. and Hodson, H. P. Unsteady transition in an axial flow turbine, Part 2: Cascade measurements and modelling. *ASME Journal of Turbomachinery*, vol. 112, pp. 215–221, 1990.

[4] Alt, P. H. An intermittency meter for investigating boundary layer transition. Technical Report UTS/ME-17, School of Mechanical Engineering, The University of Technology, Sydney, Australia, Apr. 1988.

[5] Arndt, N. Blade row interaction in a multistage low-pressure turbine. *ASME Journal of Turbomachinery*, vol. 115, pp. 137–146, Jan. 1993.

[6] Bellhouse, B. J. and Schultz, D. L. Determination of mean and dynamic skin friction, separation and transition in low-speed flow with a thin film heated element. *Journal of Fluid Mechanics*, vol. 24, no. 2, pp. 379–400, Jul. 1966.

[7] Bertolotti, F. P., Herbert, T. and Spalart, P. R. Linear and nonlinear stability of the Blasius boundary layer. *Journal of Fluid Mechanics*, vol. 242, pp. 441–474, 1992.

[8] Binder, A., Förster, W., Kruse, H. and Rogge, H. An experimental investigation into the effect of wakes on the unsteady turbine rotor flow. *ASME Journal of Engineering for Gas Turbines and Power*, vol. 107, pp. 458–466, Apr. 1985.

[9] Blackwelder, R. F. and Kaplan, R. E. On the wall structure of the turbulent boundary layer. *Journal of Fluid Mechanics*, vol. 768, pp. 89–112, 1976.

[10] Blair, M. F. Boundary layer transition in accelerating flows with intense freestream turbulence. Tech. Report UTRC91-1, UTRC, East Hartford, Connecticut, 1991.

[11] Blight, F. G. and Howard, W. Tests on four aerofoil cascades Part 1: Deflection, drag and velocity distribution. Report E 74, Aeronautical Research Laboratories, Melbourne, Australia, Jul. 1952.

[12] Bradshaw, P. *An Introduction to Turbulence and its Measurement.* Pergamon, first edn., 1971.

[13] Brown, G. L. Theory and application of heated films for skin friction measurement. In *Proceedings of the 1967 Heat Transfer and Fluid Mechanics Institute*, pp. 361–381, 1967. Paper 18.

[14] Chen, K. K. and Thyson, N. A. Extension of Emmons' spot theory to flows on blunt bodies. *AIAA Journal*, vol. 9, no. 5, pp. 821–825, May 1971.

[15] Corrsin, S. and Kistler, A. L. Free-stream boundaries of turbulent flows. NACA TR 1244, 1955.

[16] Coupland, J. Private communication concerning Rolls-Royce Applied Science Laboratory flat plate transitional boundary layer results, Jan. 1993. Test cases used by the ERCOFTAC Special Interest Group on Transition.

[17] Crooks, P. V. and Howard, W. Low speed tests on three aerofoil cascades designed for prescribed surface velocity distributions. Report ME 76, Aeronautical Research Laboratories, Melbourne, Australia, Sep. 1954.

[18] Cumpsty, N. A. *Compressor Aerodynamics.* Longman Scientific & Technical, first edn., 1989.

[19] Cumpsty, N. A. Current aerodynamic issues for aircraft engines. In Davis, M. R. and Walker, G. J. (eds.), *Eleventh Australasian Fluid Mechanics Conference*, pp. 799–811. Hobart, Australia, Dec. 1992. Keynote Paper K–6.

[20] Cumpsty, N. A., Dong, Y. and Li, Y. S. Compressor blade boundary layers in the presence of wakes. Jun. 1995. ASME Paper 95-GT-443, International Gas Turbine and Aeroengine Congress and Exposition, Houston, Texas.

[21] Curtis, E. M., Hodson, H. P., Banieghbal, M. R., Denton, J. D. and Howell, R. J. Development of blade profiles for low pressure turbine applications. 1996. ASME Paper 96-GT-358, International Gas Turbine and Aeroengine Congress and Exposition, Birmingham, UK.

[22] Dey, J. and Narasimha, R. An integral method for the calculation of 2-D transitional boundary layers. Fluid Mechanics Report 88 FM 7, Indian Institute of Science, Bangalore, Dec. 1988.

[23] Dhawan, S. and Narasimha, R. Some properties of boundary layer flow during the transition from laminar to turbulent motion. *Journal of Fluid Mechanics*, vol. 3, pp. 418–436, 1958.

[24] Dini, P., Selig, M. S. and Maughmer, M. D. Simplified linear stability transition prediction method for separated boundary layers. *AIAA Journal*, vol. 30, no. 8, pp. 1953–1961, Aug. 1992.

[25] Dong, Y. and Cumpsty, N. A. Compressor blade boundary layers: Part 2 — Measurements with incident wakes. *ASME Journal of Turbomachinery*, vol. 112, pp. 231–240, 1990.

[26] Doorly, D. J. and Oldfield, M. L. G. Simulation of wake passing in a stationary turbine rotor cascade. *AIAA Journal of Propulsion and Power*, vol. 1, pp. 316–318, 1985.

[27] Dullenkopf, K., Schultz, A. and Wittig, S. The effect of incident wake conditions on the mean heat transfer of an airfoil. 1990. ASME Paper 90-GT-121.

[28] Dyban, Y. P., Epik, E. Y. and Suprun, T. T. Characteristics of the laminar boundary layer in the presence of elevated free-stream turbulence. *Fluid Mechanics – Soviet Research*, vol. 5, no. 4, pp. 30–36, 1976.

[29] Emmons, H. W. The laminar-turbulent transition in a boundary layer - Part I. *Journal of Aerospace Sciences*, vol. 18, no. 7, pp. 490–498, Jul. 1951.

[30] Evans, R. L. Turbulence and unsteadiness measurements downstream of a moving blade row. *ASME Journal of Engineering for Power*, pp. 131–139, 1975.

[31] Falco, R. E. and Gendrich, C. P. The turbulence burst detection algorithm of Z. Zarić. In Kline, S. J. and Afgan, N. H. (eds.), *Near-Wall Turbulence 1988 Zoran Zarić Memorial Conference*, pp. 911–931. Hemisphere, 1990.

[32] Fraser, C. J., Higazy, M. G. and Milne, J. S. End-stage boundary layer transition models for engineering calculations. *Proceedings of the Institution of Mechanical Engineers, Part C*, vol. 208, pp. 47–58, 1994.

[33] Freymuth, P. and Fingerson, L. M. Electronic testing of frequency response for thermal anemometers. *TSI Quarterly*, vol. 3, pp. 5–12, Nov./Dec. 1977. (Appendix A of TSI IFA-100 manual.).

[34] Funazaki, K. Unsteady boundary layers on a flat plate disturbed by periodic wakes : Part II - Measurements of unsteady boundary layers and discussion. 1994. ASME Paper 94-GT-430.

[35] Funazaki, K., Meguro, T. and Yamawaki, S. Studies on the unsteady boundary layer on a flat plate subjected to incident wakes. Forced transition models of the boundary layer. *JSME International Journal*, vol. 36, no. 4, pp. 532–539, 1993.

[36] Gad-el-Hak, M., Blackwelder, R. F. and Riely, J. J. On the growth of turbulent regions in laminar boundary layers. *Journal of Fluid Mechanics*, vol. 110, pp. 73–95, 1981.

[37] Goldstein, R. J. *Fluid Mechanics Measurements.* Hemisphere, 1983.

[38] Gostelow, J. P., Blunden, A. R. and Walker, G. J. Effects of free-stream turbulence and adverse pressure gradients on boundary layer transition. *ASME Journal of Turbomachinery*, vol. 116, pp. 392–404, 1994.

[39] Gostelow, J. P., Hong, G., Melwani, N. and Walker, G. J. Turbulent spot development under a moderate adverse pressure gradient. May 1993. ASME Paper 93-GT-377, International Gas Turbine Congress, Cincinnati, Ohio.

[40] Gostelow, J. P., Melwani, N. and Walker, G. J. Effects of a streamwise pressure gradient on turbulent spot development. 1995. ASME Paper 95-GT-303, International Gas Turbine Congress, Houston.

[41] Gostelow, J. P., Melwani, N., Walker, G. J. and Solomon, W. J. Effects of a self-similar adverse pressure distribution on turbulent spot development. 1995. AIAA 95-2254, AIAA 26th Fluid Dynamics Conference, San Diego.

[42] Gostelow, J. P., Walker, G. J., Solomon, W. J., Hong, G. and Melwani, N. Investigation of the calmed region behind a turbulent spot. Jun. 1996. ASME Paper 96-GT-489, International Gas Turbine and Aeroengine Congress and Exposition, Birmingham, UK.

[43] Green, J. E., Weeks, D. J. and Brooman, J. W. F. Prediction of turbulent boundary layers and wakes in compressible flow by a lag-entrainment method. Tech. Report 72231, RAE, Farnborough, 1973.

[44] Hall, D. J. and Gibbings, J. C. Influence of stream turbulence and pressure gradient on boundary layer transition. *Journal of Mechanical Engineering Science*, vol. 14, pp. 134–146, 1972.

[45] Halstead, D. E., Okiishi, T. H. and Wisler, D. C. Boundary-layer transition and separation on a turbine blade in plane cascade. 1990. AIAA Paper 90-2263.

[46] Halstead, D. E., Wisler, D. C., Okiishi, T. H., Walker, G. J., Hodson, H. P. and Shin, H. Boundary layer development in axial compressors and turbines: Parts 1–4. 1995. ASME Papers 95-GT-461–464.

[47] Han, J. C., Zhang, L. and Ou, S. Influence of unsteady wake on heat transfer from a gas turbine blade. *ASME Journal of Heat Transfer*, vol. 15, pp. 904–911, Nov. 1993.

[48] Hart, M. *Boundary Layers on Turbine Blades.* Ph.D. thesis, Churchill College Cambridge, Jul. 1985.

[49] Hazarika, B. K. and Hirsch, C. Transition over C4 leading edge and measurement of intermittency factor using PDF of hot-wire signal. 1995. ASME Paper 95-GT-294.

[50] Hedley, T. B. and Keffer, J. F. Some turbulent / non-turbulent properties of the outer intermittent region of a boundary layer. *Journal of Fluid Mechanics*, vol. 64, pp. 645–678, 1974.

[51] Ho, Y. and Lakshminarayana, B. Computation of unsteady viscous flow through turbomachinery blade row due to upstream rotor wakes. 1993. ASME Paper 93-GT-321.

[52] Hodson, H. P. Boundary layer and loss measurements on the rotor of an axial-flow turbine. *ASME Journal of Engineering for Gas Turbines and Power*, vol. 106, pp. 391–399, Apr. 1984.

[53] Hodson, H. P. Boundary layer transition and separation near the leading edge of a high speed turbine blade. *ASME Journal of Engineering for Gas Turbines and Power*, vol. 107, pp. 127–134, Apr. 1985.

[54] Hodson, H. P. Measurements of wake-generated unsteadiness in the rotor passages of axial flow turbines. *ASME Journal of Engineering for Gas Turbines and Power*, vol. 107, pp. 467–476, Apr. 1985.

[55] Hodson, H. P. Modeling unsteady transition and its effects on profile loss. *ASME Journal of Turbomachinery*, vol. 112, pp. 691–701, Oct. 1990.

[56] Hodson, H. P. and Addison, J. S. Wake-boundary layer interactions in an axial flow turbine rotor at off-design conditions. *ASME Journal of Turbomachinery*, vol. 111, pp. 181–192, Apr. 1989.

[57] Hodson, H. P. and Dawes, W. N. On the interpretation of measured profile losses in unsteady wake-turbine blade interaction studies. Jun. 1996. ASME Paper 95-GT-494, International Gas Turbine and Aeroengine Congress and Exposition, Birmingham, UK.

[58] Horton, H. P. A semi-empirical theory for the growth and bursting of laminar separation bubbles. Current Paper 1073, Aeronautical Research Council, 1969.

[59] Hourmouziadis, J. Aerodynamic design of low pressure turbines. In Fottner, L. (ed.), *AGARD Lecture Series No. 167, Blading Design for Axial Turbomachines*, pp. 8.1–8.40. AGARD, 1989.

[60] Howell, A. R. The present basis of axial flow compressor design: Part I– Cascade theory and performance. Tech. Rep. 2095, ARC R&M, 1942.

[61] Howell, A. R. Private Communication - to A. R. Oliver, University of Tasmania. Aug. 1973.

[62] Hughes, J. Axial flow compressors. Honours Thesis CM 95/34, Deptartment of Civil and Mechanical Engineering, University of Tasmania, Dec. 1995.

[63] Jang, H. M., Ekaterinaris, J. A., Platzer, M. F. and Cebeci, T. Essential ingredients for the computation of steady and unsteady blade boundary layers. *ASME Journal of Turbomachinery*, vol. 113, pp. 608–616, Oct. 1991.

[64] Johnson, M. W. A bypass transition model for boundary layers. Jun. 1993. ASME Paper 92-GT-90.

[65] Johnson, M. W. and Ercan, A. H. A boundary layer transition model. Jun. 1996. ASME Paper 96-GT-444, International Gas Turbine and Aeroengine Congress and Exposition, Birmingham, UK.

[66] Kalfas, A. I. and Elder, R. L. Determination of the intermittency distribution in the boundary layer of a flat plate with a C4 leading edge. Mar. 1995. ERCOFTAC Bulletin.

[67] Kerrebrock, J. L. and Mikolajczak, A. A. Intra-stator transport of rotor wakes and its effect on compressor performance. *ASME Journal of Engineering for Power*, vol. 92, pp. 359–368, Oct. 1970.

[68] Korakianitis, T. and Papagiannidis, P. Surface-curvature-distribution effects on turbine-cascade performance. *ASME Journal of Turbomachinery*, vol. 115, pp. 334–341, Apr. 1993.

[69] Krogstad, P. and Kaspersen, J. H. Methods to detect coherent structures, a comparison. In Davis, M. R. and Walker, G. J. (eds.), *Eleventh Australasian Fluid Mechanics Conference*, pp. 1262–1272. Hobart, Australia, Dec. 1992.

[70] Kuan, C. and Wang, T. Investigation of the intermittent behaviour of transtional bounadary layer using a conditional averaging technique. *Experimental Thermal and Fluid Science*, vol. 3, pp. 157–173, 1990.

[71] Kuo, A. Y. and Corrsin, S. Experiments on internal intermittency and fine structure distribution functions in fully turbulent fluid. *Journal of Fluid Mechanics*, vol. 50, pp. 285–319, 1971.

[72] LaGraff, J. E., Ashworth, D. A. and Schultz, D. L. Measurement and modelling of the gas turbine blade transition process as disturbed by wakes. *ASME Journal of Turbomachinery*, vol. 111, pp. 315–322, Jul. 1989.

[73] Lewis, R. I. *Vortex Element Methods for Fluid Dynamic Analysis of Engineering Systems*. Cambridge, first edn., 1991.

[74] Lieblein, S. Experimental flow in two-dimensional cascades. In Johnsen, I. A. and Bullock, R. O. (eds.), *Aerodynamic Design of Axial-Flow Compressors*, no. SP-36, pp. 183–226. NASA, 1965.

[75] Liu, X. and Rodi, W. Experiments on transitional boundary layers with wake-induced unsteadiness. *Journal of Fluid Mechanics*, vol. 231, pp. 229–256, 1991.

[76] Lockhart, R. C. and Walker, G. J. The influence of viscous interactions on the flow downstream of an axial compressor stage. Sep. 1974. Paper presented at the 2nd International Symposium on Air Breathing Engines, Sheffield UK.

[77] Loehrke, R. I., Morkovin, M. V. and Fejer, A. A. REVIEW–Transition in nonreversing oscillating boundary layers. *ASME Journal of Fluids Engineering*, vol. 97, pp. 534–549, Dec. 1975.

[78] Mack, L. M. Boundary-layer linear stability theory. In Michel, R. (ed.), *Special Course on Stability and Transition of Laminar Flow*, pp. 3.1–3.81. AGARD, Jun. 1984. Report No. 709.

[79] Malkiel, E. Transition in separating-reattaching boundary layer flows. In LaGraff, J. E. (ed.), *Minnowbrook Workshop on End-Stage Boundary Layer Transition*, pp. 1–7. Syracuse University, New York, Aug. 1993. Session 3a.

[80] Mayle, R. E. The role of laminar-turbulent transition in gas turbine engines. *ASME Journal of Turbomachinery*, vol. 113, pp. 509–537, Oct. 1991. The 1991 IGTI Scholar Lecture.

[81] Mayle, R. E. Unsteady multimode transition in gas turbine engines. 1992. AGARD PEP 80.

[82] Mayle, R. E. and Dullenkopf, K. A theory for wake-induced transition. *ASME Journal of Turbomachinery*, vol. 112, pp. 188–195, Apr. 1990.

[83] Mayle, R. E. and Dullenkopf, K. More on the turbulent-strip theory for wake-induced transition. *ASME Journal of Turbomachinery*, vol. 113, pp. 428–432, Jul. 1991.

[84] Mayle, R. E. and Schulz, A. The path to predicting bypass transition. 1996. ASME Paper 96-GT-199, International Gas Turbine and Aeroengine Congress and Exposition, Birmingham, UK.

[85] McCormick, M. E. An analysis of the formation of turbulent patches in the transition boundary layer. *ASME Journal of Applied Mechanics*, vol. 35, pp. 216–219, Jun. 1968.

[86] Meyer, R. X. The effect of wakes on the transient pressure and velocity distributions in turbomachines. *ASME Journal of Basic Engineering*, vol. 80, pp. 1544–1552, Oct. 1958.

[87] Morkovin, M. V. On the many faces of transition. In Wells, C. S. (ed.), *Viscous Drag Reduction*, pp. 1–31. Plenum Press, New York, Sep. 1969.

[88] Morkovin, M. V. Panoramic view of changes in vorticity distribution in transition instabilities and turbulence. In Reda, D. C., Reed, H. L. and Kobayashi, R. (eds.), *Boundary Layer Stability and Transition to Turbulence*, pp. 1–12. ASME, 1991. FED – Vol 114, Book No. G00602.

[89] Narasimha, R. On the distribution of intermittency in the transition region of a boundary layer. *Journal of Aerospace Sciences*, vol. 24, no. 9, pp. 711–712, Sep. 1957.

[90] Narasimha, R. The laminar-turbulent transition zone in the boundary layer. *Progress in Aerospace Science*, vol. 22, pp. 29–80, 1985.

[91] Narasimha, R., Devasia, K. J., Gururani, G. and Narayanan, M. A. B. Transitional intermittency in boundary layers subjected to pressure gradient. *Experiments in Fluids*, vol. 2, pp. 171–176, 1984.

[92] Obremski, H. J. and Fejer, A. A. Transition in oscillating boundary layer flows. *Journal of Fluid Mechanics*, vol. 29, pp. 93–111, 1967.

[93] Okiishi, T. H., Hathaway, M. D. and Hansen, J. L. A note on blade wake interaction influence on compressor stator row aerodynamic performance. *ASME Journal of Engineering for Gas Turbines and Power*, vol. 107, pp. 549–551, 1985.

[94] Oliver, A. R. Comparison between sand cast and machined blades in the vortex wind tunnel. Report ME 103, Aeronautical Research Laboratories, Melbourne, Australia, Sep. 1961.

[95] Orth, U. Unsteady boundary-layer transition in flow periodically disturbed by wakes. *ASME Journal of Turbomachinery*, vol. 115, pp. 707–713, Oct. 1993.

[96] Pfeil, H., Herbst, R. and Schröder, T. Investigation of the laminar-turbulent transition of boundary layers disturbed by wakes. *ASME Journal of Engineering for Power*, vol. 105, pp. 130–137, Jan. 1983.

[97] Pope, R. J. Skin-friction measurements in laminar and turbulent flows using heated thin-film gages. *AIAA Journal*, vol. 10, no. 6, pp. 729–730, 1972.

[98] Raj, R. and Lakshminarayana, B. Characteristics of the wake behind a cascade of airfoils. *Journal of Fluid Mechanics*, vol. 61, no. 4, pp. 707–730, 1973.

[99] Ramesh, O. N., Dey, J. and Prabhu, A. Transitional intermittency distribution in a three-dimenional constant pressure diverging flow. Fluid Mechanics Report 95 FM 5, Indian Institute of Science, Bangalore, Aug. 1995.

[100] Rhoden, H. G. Effects of Reynolds number on the flow of air through a cascade of compressor blades. ARC R&M 2919, 1952.

[101] Roberts, W. B. The effect of Reynolds number and laminar separation on axial compressor performance. *ASME Journal of Engineering for Power*, pp. 261–274, Apr. 1975.

[102] Rodi, W., Liu, X. and Schönung, B. Transitional boundary layers with wake-induced unsteadiness. In Cebeci, T. (ed.), *Numerical and Physical Aspects of Aerodynamic Flows*, pp. 1–11. California State University, Long Beach, California, Jan. 1989. Session 6.

[103] Sanger, N. L. The use of optimization techniques to design controlled-diffusion compressor blading. *ASME Journal of Engineering for Power*, vol. 105, pp. 256–264, Apr. 1983.

[104] Sanz, W. and Platzer, M. F. On the Navier-Stokes calculation of separation bubbles. 1996. ASME Paper 96-GT-487, International Gas Turbine and Aeroengine Congress and Exposition, Birmingham, UK.

[105] Savill, A. M. Test Case T3A,T3B: Free Stream Turbulence, Introduction. In Pironneau, O., Rodi, W., Ryhming, I. L., Savill, A. M. and Truong, T. V. (eds.), *Numerical Simulation of Unsteady Flows and Transition to Turbulence*, pp. 318–. Lausanne, Switzerland, Mar. 1990.

[106] Savill, A. M. The Savill-Launder-Younis (SLY) RST intermittency model for predicting transition. In Dick, E. (ed.), *ERCOFTAC Bulletin*, pp. 37–41. European Research Community on Flow Turbulence and Combustion, Mar. 1995.

[107] Schlichting, H. *Boundary Layer Theory.* McGraw-Hill, fourth edn., 1962.

[108] Schneider, S. P. Improved methods for measuring laminar-turbulent intermittency in boundary layers. *Experimental Thermal and Fluid Science*, vol. 18, pp. 370–375, 1995.

[109] Schon, J. P. and Charnay, G. Conditional sampling. In Richards, B. E. (ed.), *Measurement of Unsteady Fluid Dynamic Phenomena*. Hemisphere.

[110] Schubauer, G. B. and Klebanoff, P. S. Contributions on the mechanics of boundary layer transition. NACA TN 3489, Sep. 1955.

[111] Schubauer, G. B. and Skramstad, H. K. Laminar boundary layer oscillations and transition on a flat plate. NACA Tech. Rept. 909, 1948.

[112] Schulte, V. *Unsteady Separated Boundary Layers in Axial-Flow Turbomachinery*. Ph.D. thesis, Cambridge University Engineering Department, Aug. 1995.

[113] Schulte, V. and Hodson, H. P. Wake-separation bubble interaction in low pressure turbines. 1994. AIAA Paper 94-2931.

[114] Schulte, V. and Hodson, H. P. Unsteady wake-induced boundary layer transition in high lift LP turbines. 1996. ASME Paper 96-GT-486, International Gas Turbine and Aeroengine Congress and Exposition, Birmingham, UK.

[115] Sharma, O. P., Wells, R. A., Schlinker, R. H. and Bailey, D. A. Boundary layer development on turbine airfoil suction surfaces. *ASME Journal of Engineering for Power*, vol. 104, pp. 698–706, Jul. 1982.

[116] Smith, A. M. O. and Gamberioni, N. Transition, pressure gradient and stability theory. Report ES 26388, Douglas Aircraft Co., Inc., El Segundo, CA, 1956.

[117] Smith, L. H. Wake dispersion in turbomachines. *ASME Journal of Basic Engineering*, vol. 88, pp. 688–690, Sep. 1966.

[118] Solomon, W. J. and Walker, G. J. Incidence effects on wake-induced transition on an axial compressor blade. Sep. 1995. Proc. 12th International Symposium on Air Breathing Engines, Melbourne, Australia.

[119] Solomon, W. J. and Walker, G. J. Intermittency detection from surface film arrays on aerofoils in unsteady flow. In Bilger, R. W. (ed.), *Twelfth Australasian Fluid Mechanics Conference*, pp. 85–88. University of Sydney, Australia, Dec. 1995.

[120] Solomon, W. J. and Walker, G. J. Observations of wake-induced transition on an axial compressor blade. 1995. ASME Paper 95-GT-381.

[121] Solomon, W. J., Walker, G. J. and Gostelow, J. P. Transition length prediction for flows with rapidly changing pressure gradients. 1995. ASME Paper 95-GT-241 (Accepted for publication in the Transactions of the ASME).

[122] Solomon, W. J., Walker, G. J. and Gostelow, J. P. Transition zone predictions for rapidly varying flows. Dec. 1995. Transitional Boundary Layers in Aeronautics - Colloquium of the Royal Netherlands Academy of Arts and Sciences, Amsterdam.

[123] Squire, L. C. Interactions between wakes and boundary-layers. *Progress in Aerospace Science*, vol. 27, pp. 261–288, 1990.

[124] Steelant, J. and Dick, E. Modelling of bypass transition with conditioned Navier-Stokes equations coupled to an intermittency transport equation. *International Journal For Numerical Methods in Fluids*, vol. 22, pp. 1–28, 1996.

[125] Suder, K. H., O'Brien, J. E. and Reshotko, E. Experimental study of bypass transition in a boundary layer. NASA TM-100913, 1988.

[126] Townsend, A. A. Local isotropy in the turbulent wake of a cylinder. *Australian Journal of Scientific Research, Series A : Physical Sciences*, vol. 1, no. 2, pp. 161–174, Jun. 1948.

[127] Townsend, A. A. The fully developed turbulent wake of a circular cylinder. *Australian Journal of Scientific Research, Series A : Physical Sciences*, vol. 2, no. 4, pp. 451–468, Dec. 1949.

[128] Van Ingen, J. L. A suggested semi-empirical method for the calculation of the boundary layer transiton region. Report VTH-74, University of Technology, Delft, Holland, 1956.

[129] Volino, R. J. and Simon, T. W. An application of octant analysis to turbulent and transitional flow data. 1993. ASME Paper 93-GT-72.

[130] Volino, R. J. and Simon, T. W. Measurements in a transitional boundary layer with Görtler vortices. 1996. ASME Paper 96-GT-166, International Gas Turbine and Aeroengine Congress and Exposition, Birmingham, UK.

[131] Walker, G. J. Effect of wake-wake interactions on the generation of noise in axial-flow turbomachinery. Jun. 1972. First International Symposium on Air Breating Engines, Marseille, France.

[132] Walker, G. J. *An Investigation of the Boundary Layer Behaviour on the Blading of a Single-Stage Axial-Flow Compressor.* Ph.D. thesis, University of Tasmania, Nov. 1972.

[133] Walker, G. J. The unsteady nature of boundary layer transition on an axial compressor blade. 1974. ASME Paper 74-GT-135.

[134] Walker, G. J. Transitional flow on axial turbomachine blading. *AIAA Journal*, vol. 27, no. 5, pp. 595–602, May 1989.

[135] Walker, G. J. The role of laminar-turbulent transition in gas turbine engines — A discussion. *ASME Journal of Turbomachinery*, vol. 117, pp. 207–217, 1993.

[136] Walker, G. J. and Gostelow, J. P. Effects of adverse pressure gradients on the nature and length of boundary layer transition. *ASME Journal of Turbomachinery*, vol. 112, pp. 196–205, 1990.

[137] Walker, G. J. and Solomon, W. J. Turbulent intermittency measurement on an axial compressor blade. In Davis, M. R. and Walker, G. J. (eds.), *Eleventh Australasian Fluid Mechanics Conference*, pp. 1277–1280. Hobart, Australia, Dec. 1992.

[138] Walker, G. J. and Solomon, W. J. Boundary layer transition on an axial compressor stator blade–wake passing and freestream turbulence effects. In LaGraff, J. E. (ed.), *Minnowbrook Workshop on End-Stage Boundary Layer Transition.* Syracuse University, New York, Aug. 1993.

[139] Walker, G. J., Solomon, W. J. and Gostelow, J. P. Observations of wake-induced turbulent spots on an axial compressor blade. 1993. ASME Paper 93-GT-378.

[140] Walker, G. J. and Wu, J. Turbulent intermittency measurement for turbomachinery flows. Jun. 1991. First Joint ASME-JSME Fluids Engineering Conference, Portland, Oregon.

[141] White, F. M. *Viscous Fluid Flow.* McGraw-Hill, first edn., 1974.

[142] Wills, J. A. B. Correction of hot wire readings for proximity to a solid surface. *Journal of Fluid Mechanics*, vol. 12, pp. 388–396, 1962.

[143] Yang, Z. Y. and Voke, P. R. Large-eddy simulation of transition under turbulence. Technical Report ME-FD/93.12, University of Surrey, Dept. Mech. Eng, 1989.

[144] Youngren, H. and Drela, M. Viscous-inviscid method for preliminary design of transonic cascades. 1991. AIAA Joint Propulsion Conference.

[145] Zohar, Y. *Fine Scale Mixing in a Free Shear Layer.* Ph.D. thesis, University of Southern California, Apr. 1990. See also Y. Zohar and C-M. Ho. Dissipation scale and control of fine-scale turbulence in a plane mixing layer. *Journal of Fluid Mechanics.* 320, pp 139–161, 1996.